

Physical and Chemical Parameters Determining Bacterial Growth of Acid Mine Drainage
Sites in Southeast Ohio

A thesis presented to
the faculty of
the College of Arts and Sciences of Ohio University

In partial fulfillment
of the requirements for the degree
Master of Science

Sebastian D. Barkett

August 2020

© 2020 Sebastian D. Barkett. All Rights Reserved.

This thesis titled
Physical and Chemical Parameters Determining Bacterial Growth of Acid Mine Drainage
Sites in Southeast Ohio

by

SEBASTIAN D. BARKETT

has been approved for
the Department of Geological Sciences
and the College of Arts and Sciences by

Dina L. López

Professor of Geological Sciences

Florenz Plassmann

Dean, College of Arts and Sciences

ABSTRACT

BARCKETT, SEBASTIAN D., M.S., August 2020, Geological Sciences

Physical and Chemical Parameters Determining Bacterial Growth of Acid Mine Drainage Sites in Southeast Ohio

Director of Thesis: Dina L. López

This study focused on highlighting the connection between the physical, chemical, sedimentary, and microbial aspects of various acid mine drainage settings of contrasting chemistry. In addition, a comprehensive thesis model was suggested to explain the interconnected relationships of this data set. The first 30 meters were evaluated for Pine Run (Fe), Esco No. 40 (Fe and Al), York Clay No. 4 (Mn), and Sines No. 2 (Al) coal mines. The acidophilic microbial taxa evaluated were *Thiothrix* sp.(any), *Gallionella ferruginea*, and *Leptothrix discophora*. Through principal component analysis (PCA) and a Spearman correlation matrix (n=20) a number of correlations were found to describe our model. The results of this study indicate a strong relationship between distribution of total Fe, and SO₄, in the sediment due to physics of flow. Statistical analyses suggest precipitation of Mn into the sediments could occur at the medium-coarse sand (0.5-0.99 mm) grain size fraction and Fe likely precipitates as a larger grain size fraction than this. Both *Thiothrix* and *G. ferruginea* taxa shared a positive correlation with velocity, and *L. discophora* shared a negative correlation to flow velocity. Variable flow conditions within the first 30-meters of the mine opening can alter distribution of precipitates to deposit medium to coarse sand grain size fractions, reoxygenate waters, and alter pH to create supersaturated conditions for the minerals

basaluminite, amorphous $\text{Fe}(\text{OH})_3$, gibbsite, barite, and goethite. Results from this study also indicate *G. ferruginea* is likely favored in Fe contaminated systems, *L. discophora* could be the more abundant in Mn and Al contaminated mines, and SO_4 contaminated drainage favors *Thiothrix*. Geochemical modeling results agree with water quality tests and field observations for each site.

DEDICATION

A dedication to those who have made this work possible:

“One equal temper of heroic hearts

Made weak by time and fate, but strong in will

To strive, to seek, and not to yield”

-Alfred Tennyson (Ulysses)

TABLE OF CONTENTS

	Page
Abstract.....	3
Dedication.....	5
List of Tables	8
List of Figures.....	9
Chapter 1: Introduction.....	15
1.1 Introduction to Acid Mine Drainage.....	15
1.2 Objectives of this Research.....	18
1.3 Hypothesis and Research Questions.....	18
1.4 Structure of Thesis	19
Chapter 2: Generation of Acid Mine Drainage.....	20
2.1 Chemical Processes.....	20
2.2 Microbiological Processes	26
2.2.1 Acidophilic Microbial Taxa.....	31
2.3 Physical Processes	39
2.4 Acid Mine Drainage Sedimentological Processes	43
2.4.1 Sediment Transport.....	43
2.4.2 Mineralogy of AMD Sediments.....	44
Chapter 3: Site Selection and Geological Setting.....	49
3.1 Climate.....	52
3.2 Geology.....	52
Chapter 4: Methodology	58
4.1 Site Descriptions	58
4.2 Field Work	68
4.2.1 Field Parameters.....	68
4.2.2 Water Sampling	69
4.2.3 Sediment Sampling	69
4.2.4 Biological Sampling.....	70
4.3 Laboratory Work.....	72
4.3.1 Cations and Anions Analysis in Water Samples.....	72
4.3.2 Sediment Analysis	73

4.3.3 Microbial Ecology	74
4.4 Geochemical Modeling and Statistical Analysis	78
4.4.1 Simulations in PHREEQCI.....	78
4.4.2 Statistical Analysis.....	78
Chapter 5: Results.....	81
5.1 General Presentation of Data	81
5.2 Statistical Analysis of Data.....	94
5.2.1 Principle Component Analysis	94
5.2.2 Spearman Correlation Analysis	110
5.3 Analysis of Sediments and Geochemical Modeling.....	143
5.3.1 Sediment Grain Size	143
5.3.2 Sediment Grain Size vs All Parameters	145
5.3.3 PHREEQCI Simulations and Different Precipitates.....	152
5.4 Microbial Ecology	166
5.4.1 Descriptive Analysis	166
Chapter 6: Discussion	183
Chapter 7: Conclusions.....	190
References.....	195
Appendix.....	202

LIST OF TABLES

	Page
Table 1 AMD Mineral Information	48
Table 2 Field Parameters Data.....	82
Table 3 Water Ion Chemical Data	84
Table 4 Sediment Ion Chemical Data	86
Table 5 Microbial Data (colonization rates)	89
Table 6 Mineral Saturation Index Data.....	91
Table 7 Sediment Grain Size and LoI Data	92
Table 8 Sediment Sieve Mass Data	93
Table 10 Spearman's Matrix Field Parameters.....	112
Table 11 Spearman's Matrix Water Ion vs Field Parameters.....	114
Table 12 Spearman's Matrix Water Ions	120
Table 13 Spearman's Matrix Sediment Ions vs Field Parameters	122
Table 14 Spearman's Matrix Sediment Ions.....	125
Table 15 Spearman's Matrix Water Ion vs Sediment Ions	130
Table 16 Spearman's Matrix Field Parameters vs Bacterial Counts	134
Table 17 Spearman's Matrix Water Ions vs Bacterial Counts.....	138
Table 18 Spearman's Matrix Sediment Ions vs Bacterial Counts	141
Table 19 Mean Sediment Sizes.....	143
Table 20 Spearman's Matrix Mean Min and Max Grain Size vs All	146
Table 21 Spearman's Matrix Individual Sieve Fraction vs All	148
Table 22 Pine Run (Sunday Creek No. 9 and 12 coal mine) Bacterial Comparison	168
Table 23 Esco No. 40 Bacterial Comparison.....	170
Table 24 York Clay and Mining No. 4 Bacterial Comparison	174
Table 25 Sines No. 2 Bacterial Comparison.....	178
Table 26 Spearman's Matrix Fractional Percent vs All.....	227

LIST OF FIGURES

Figure 1 Map of watersheds that were examined for underground abandoned mine discharges overlaid with map of AMD afflicted surface areas (ODNR, 2019). ATH=Athens County, HOC=Hocking County, PER=Perry County.....	16
Figure 2 Map depicting the location of Esco No. 40 Coal mine in Monday Creek watershed adapted from Overly (1997)	23
Figure 3 Concentrations of total Fe and Mn at varying distances from the Esco No. 40 mine exit from 10/10/96 to 03/20/97 adapted from Overly, 1997.....	24
Figure 4 Concentrations of Al at varying distances from the Esco No. 40 mine exit from 10/10/96 to 03/20/97 adapted from Overly, 1997.....	25
Figure 5 Adapted from Overly 1997. Fluid velocity and colonization rates of different microbes at varying distances from the mine exit. Adapted from Overly 1997.	27
Figure 6 Instances of colonization of various microbes at varying distances from the Esco No. 40 mine exit. Adapted from Overly, 1997.	28
Figure 7 Fluid velocity and colonization rates of different microbes at varying distances from the mine exit. Adapted from Overly 1997.	29
Figure 8 Filamentous rosettes of Thiiothrix shown as a gram positive (1000X) (gram-variable).	32
Figure 9 Ferric-hydroxide stained Gallionella ferruginea viewed at 1000X located in the Pine Run mine drainage.	34
Figure 10 Rod shaped bacteria in chain conformation fitting the description of the Leptothrix genus found in the York Clay mine drainage (1000x).....	36
Figure 11 Rod-shaped gram-negative bacteria found in clusters of each slide fitting the description of Thiobacillus genus (1000x).	38
Figure 12 Rate of increasing DO levels along the Esco No. 40 effluent, 06/12/96 to 03/20/97 (Overly, 1997).....	42
Figure 13 Popular AMD mineral precipitates represented by the ranges in which they precipitate (Potter-McIntyre et al., 2018; Ruiz-Agudo et al., 2015; Lozano et al. 2018; Bénézeth et al., 2008; Yue et al., 2016; Lükewille et al., 1992; Mayanna et al., 2015; Bigham et al., 1996(a)).	47
Figure 14 View of selected mine sites and their respective data points within the boundaries of Monday and Sunday Creek watersheds on watersheddata.com. Brown data points are water samples not relevant to this study.....	50
Figure 15 Triangular diagram showing selected sampling points representing those that were discharging from underground mines and plotted to describe primary contaminant. Contrasting relative chemistry sites were selected.	51

Figure 16 Map showing the abandoned mine discharges that were sampled and their watersheds (watersheddata.com, 2019). Areas with acid mine land problems are also shown. (ODNR, 2019).	53
Figure 17 Location of sampling sites within Monday and Sunday Creek watersheds for Athens (ATH), Hocking (HOC) or Perry (PER) counties in Ohio.	54
Figure 18 Geologic progression of coal seams located in the Pottsville and Allegheny formation, highlighting the targeted coal seam of Southeast Ohio (Middle Kittanning... ..	55
Figure 19 Descriptions of the lithologies found in and directly above and below the Middle Kittanning No. 6 coal seam.	57
Figure 20 Location of Pine Run coal mine with relation to Shawnee, OH.	59
Figure 21 Site map depicting sampling sites at Sunday Creek No. 9 and 12 Mine (Pine Run). This figure was obtained using the ODNR mine viewer (accessed 10/30/2019). ..	60
Figure 22 Location of Esco mine in relation to New Straitsville, OH.....	61
Figure 23 Site map depicting the sampling sites at Esco No. 40 Mine Via the ODNR mine viewer (accessed 10/30/2019).	62
Figure 24 Location of York Clay coal mine in relation to Nelsonville, OH.	64
Figure 25 Site map depicting sampling sites at York Clay and Mining No. 4 Mine. Figure was obtained using the ODNR mine viewer (accessed 10/30/2019).	65
Figure 26 Location of Sines coal mine in relation to New Straitsville, OH.	66
Figure 27 Site map depicting sampling sites at Sines No. 2 Mine. Figure was obtained using the ODNR mine viewer (accessed 10/30/2019).	67
Figure 28 Slide contraptions implemented for collection of selected acidophilic microbial colonization rates at each site for all four mine locations.	71
Figure 29 View of microbial grid used to determine colonization rate for microbial species at 1000X magnification.	75
Figure 30 Example of microbial colony (cfu) count from a sampled biofilm at Sines No. 2 coal mine on LB nutrient agar.	77
Figure 31 Model illustrating the first principal component (PC1)	79
Figure 32 Overview of the result of PCA conducted on the water ions using the Unscramble x software, A) Scores plot, B) Correlation Loading, C) Influence plot, D) Explained Variance.	95
Figure 33 Expanded version of the correlation loading for principal component analysis on water ions.	96
Figure 34 Overview of the result of PCA conducted on water ions vs sediment ions using the Unscramble x software, A) Scores plot, B) Correlation Loading, C) Influence plot, D) Explained Variance.	98
Figure 35 Expanded version of the correlation loading for principal component analysis of water vs sediment ions.	99

Figure 36 Overview of the result of PCA conducted on field parameters vs microbes using the Unscramble x software, A) Scores plot, B) Correlation Loading, C) Influence plot, D) Explained Variance.	101
Figure 37 Expanded version of the correlation loading for principal component analysis of field parameters vs microbes.	102
Figure 38 Overview of the result of PCA conducted on water ions vs microbes using the Unscramble x software, A) Scores plot, B) Correlation Loading, C) Influence plot, D) Explained Variance.	105
Figure 39 Expanded version of the correlation loading for principal component analysis of water ions vs microbes.	106
Figure 40 Overview of the result of PCA conducted on sediment ions vs microbes using the Unscramble x software, A) Scores plot, B) Correlation Loading, C) Influence plot, D) Explained Variance.	108
Figure 41 Expanded version of the correlation loading for principal component analysis of sediment ions vs microbes.	109
Figure 42 Relationship between; i) correlation of conductivity vs concentration of SO ₄ in water, ii) correlation of pH vs concentration of Mg in water, iii) correlation of pH vs SO ₄ in water.	115
Figure 43 Relationship between; i) ORP vs concentration of Mg in water, ii) ORP vs concentration of Ni in water, iii) ORP vs concentration of Co in water, iv) ORP vs concentration of SO ₄ in water.	116
Figure 44 Relationship between variables; i) mean velocity vs K in sed, ii) mean velocity vs Zn in sed, iii) DO vs Mn in sed, iv) mean velocity vs Fe in sed.	123
Figure 45 Relationship between variables; i) Fe in sed vs SO ₄ in sed, ii) Ni in sed vs Li in sed, iii) Ga in sed vs Li in sed.	127
Figure 46 Relationships between variables; i) Ni in sed vs Mg in sed, ii) Li in sed vs Mg in sed, iii) Pb in sed vs Ca in sed, iv) Ga in sed vs Bi in sed.	128
Figure 47 Negative correlation between Ca in sed and NO ₃ in water.	132
Figure 48 Negative correlation between Mn in sed and Na in water.	132
Figure 49 Significant relationships between i)Thiothrix day 7 vs velocity, ii) Thiothrix day 19 vs velocity, and iii) Thiothrix average vs velocity.	135
Figure 50 Significant relationships between i)Thiothrix day 7 vs temperature, ii) Thiothrix day 19 vs temperature, and iii) Thiothrix average vs teperature.	136
Figure 51 Negative correlations for i) SO ₄ in water vs Thiothrix day-7 and ii) NO ₃ in water vs G. ferruginea day-19.	139
Figure 52 Significant relationships between i) SO ₄ in sed vs Thiothrix 19, ii) G ferruginea 19 vs SO ₄ in sediment, and iii)SO ₄ in sed vs G. ferruginea.	142

Figure 53 Plot of average grain size for all sites on a Hjølström curve adapted from Grabowski et al. (2011).....	144
Figure 54 Relationships between variables; i) mean grain size vs NO ₃ in water, ii) mean grain size vs Li in water, iii) mean grain size vs Gferr day 19.	150
Figure 55 Spatial variability in mineral saturation indexes of minerals in a state of supersaturation at 0, 8, 15, 23, and 30 meters from the Sunday Creek No. 9 and 12 mine opening, 10/23/19	154
Figure 56 Spatial variability in mineral saturation indexes of minerals in a state of supersaturation at 8, 15, 23, and 30 meters from the Esco No. 40 mine opening, 10/20/19.	156
Figure 57 Spatial variability in mineral saturation indexes of minerals in a state of supersaturation at 0, 25, 50, 75, and 100 feet from the York Clay mine opening, 10/20/19.	158
Figure 58 Spatial variability in mineral saturation indexes of minerals in a state of supersaturation at 0, 8, 15, 23, and 30 meters from the Sines No. 2 mine opening, 10/20/19.	160
Figure 59 Orange colored precipitates covering stream bed of the Esco No. 40 discharge, likely a form of iron III hydroxide precipitate. White mineral precipitate can also be noted likely precipitated hydroxylates alumino-sulfates.	161
Figure 60 Orange colored precipitate of stream bed at Sines No. 2 discharge. This is likely precipitated iron hydroxide (yellowboy).	162
Figure 61 Yellow and orange colored mineral precipitate thickly coating stream bed of the Pine Run (Sunday Creek No. 9 and 12) mine effluent creating a false bottom. This is likely a large portion of iron hydroxide (yellowboy) deposition from accumulated forms of iron hydroxide.....	163
Figure 62 White precipitate visible on the York Clay and Mining No. 4 effluent.	165
Figure 63 Complete yield of all suspended slides from each location. Red "X" indicating slides lost to flow or damage to slide.....	167
Figure 64 Gallionella ferruginea, single gram + cocci, and single gram + rods from the outflow of Sunday Creek No. 9 and 12 at Pine Run (1000x).	169
Figure 65 Thiobacillus Gram + rods (single) and cocci (clusters and single) isolated from Esco No. 40 outflow (1000x).....	171
Figure 66 Gallionella ferruginea gram - isolated from Esco No. 40 (1000x).....	172
Figure 67 Thiiothrix (gram -) and gram + stained flagellate rods identified from Esco No. 40 outflow slide contraptions (1000x).	173
Figure 68 Thiiothrix (gram -) and gram + stained flagellate rods identified from Esco No. 40 outflow slide contraptions (1000x).	173
Figure 69 L. discophora and (gram +) located in the effluent of York Clay and Mining No. 4 coal mine (1000x).	175

Figure 70 <i>Thiothrix</i> (gram -) and gram + flagellated rods located in the effluent of York Clay and Mining No. 4 coal mine (1000x).	176
Figure 71 <i>Thiobacillus</i> (gram variable) and Gram + cocci single, clustered, and chain conformation located in the mine effluent of York Clay and Mining No. 4 (1000x).	177
Figure 72 <i>Vibrios</i> (failed decolorization appearing gram +) found in the outflow of Sines No. 2 (1000x).	179
Figure 73 <i>L. discophora</i> (gram +) chain conformations and some single rod-shaped bacteria (gram +) found in the outflow of Sines No. 2 (1000x).	180
Figure 74 <i>Thiothrix</i> (gram +) flagellated rods, single rod shaped (gram variable), and clustered rods (gram -) from the Sines No. 2 outflow (1000x).	181
Figure 75 <i>L. discophora</i> (gram +) chain conformation rod shaped bacteria on slides of the Sines No. 2 effluent (previously identified in the Esco No. 40 mine effluent by Overly, 1997) (1000x).	182
Figure 76 fine (#140), medium (#60), and medium/coarse (#35) sand grain size fractions vs velocity and DO for each mine site.	185
Figure 77 Spatially variable velocity trends for each mine with source geology of the Middle Kittanning No. 6 coal seam, and histograms representing microbial colonization rates for 0, 8, 15, 23, and 30 meters from the mine opening.	187
Figure 78 Coarse (1-1.99 mm), coarse/medium (0.5-0.99 mm), and fine (0.105-0.24 mm) sand grain size fractions with correlation to <i>Thiothrix</i> and <i>G. ferruginea</i> taxa.	188
Figure 79 Hjulström plot of average sediment grain size fractions vs average velocities including hypothesized zones for <i>Thiothrix</i> , <i>G. ferruginea</i> , and <i>L. discophora</i>	189
Figure 80 Variations in conductivity of water exiting each of the underground mine locations at 0, 8, 15, 23, and 30 meters from discharge point, 10/20/2019 to 10/23/2019	203
Figure 81 Variability of TDS of waters at 0, 8, 15, 23, 30 meters from each mine opening, 10/20/19-10/23/19.	203
Figure 82 Variations in dissolved oxygen vs. velocity of waters exiting each abandoned underground coal mine location, 10/20/2019 to 10/23/2019.	203
Figure 83 Variations in temperature of water exiting each abandoned underground coal mine location, 10/20/2019 to 10/23/2019.	203
Figure 84 Variations in pH of water exiting each abandoned underground coal mine location, 10/20/2019 to 10/23/2019.	203
Figure 85 Variability in total iron concentrations of water exiting each abandoned underground mine effluent along flow path, 10/20/2019 or 10/23/2019.	203
Figure 86 Variations in total aluminum concentrations of water exiting each abandoned underground mine effluent along flow path, 10/20/2019 or 10/23/2019.	203

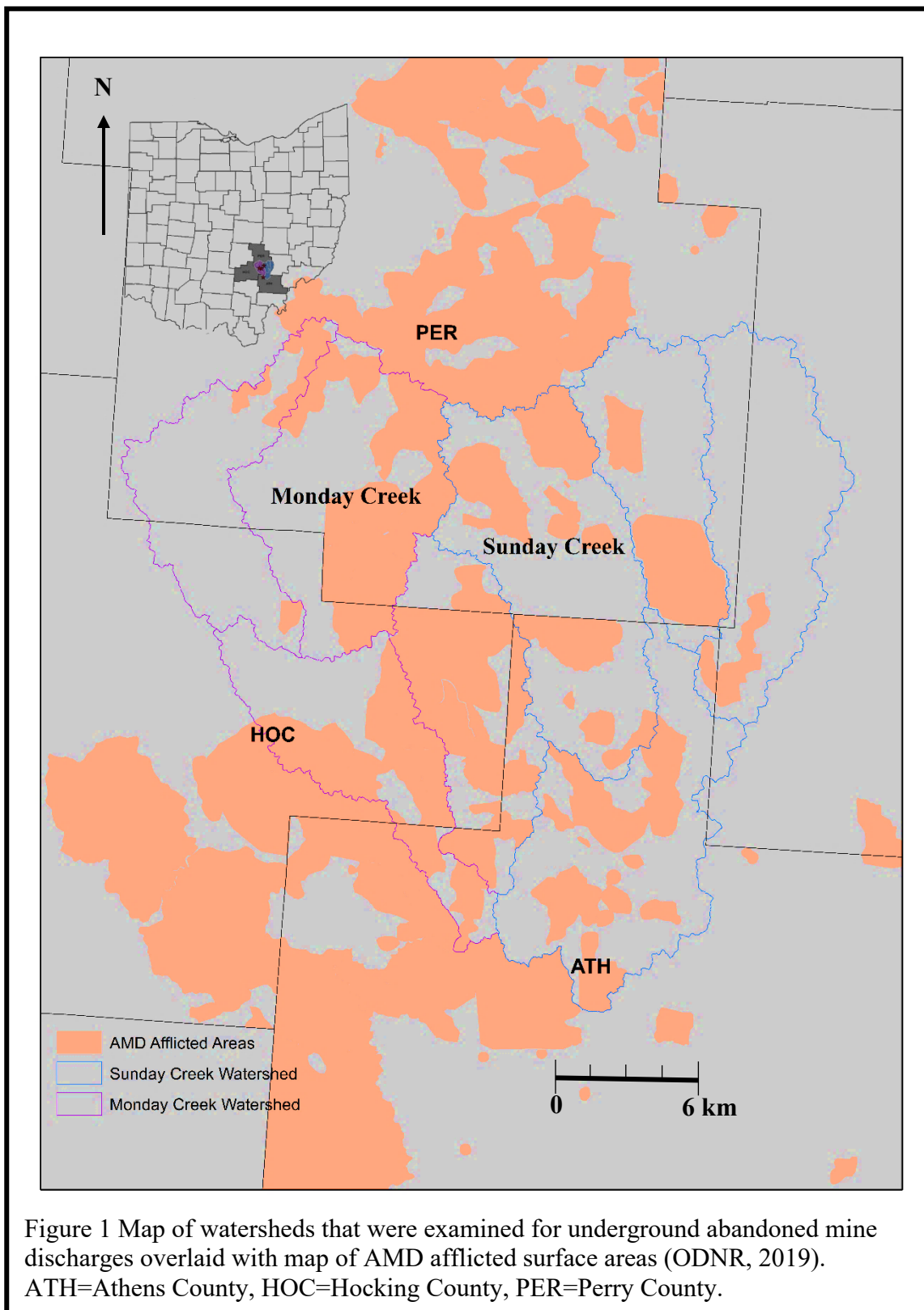
Figure 87 Variations in total manganese concentrations of water exiting each abandoned underground mine effluent along flow path, 10/20/2019 or 10/23/2019.....	203
Figure 88 Spatial Variability of Ferrous iron (Fe ²⁺) in the mine effluents at 0, 8, 15, 23, and 30 meters for each location plotted alongside total iron and velocity.....	203
Figure 89 Fluctuations in sulfate, iron, aluminum, manganese, and nitrate originating from the Sunday Creek No. 9 and 12 (Pine Run) Mine, 10/23/19.....	203
Figure 90 Fluctuations in sulfate, iron, aluminum, manganese, and nitrate originating from the Esco No. 40 Mine, 10/20/19.....	203
Figure 91 Fluctuations in sulfate, iron, aluminum, manganese, and nitrate originating from the York Clay Mine, 10/20/19.	203
Figure 92 Fluctuations in sulfate, iron, aluminum, manganese, and nitrate originating from the Sines No. 2 Mine, 10/20/19.....	203
Figure 93 Graph depicting percent finer by mass versus grain size	203

CHAPTER 1: INTRODUCTION

1.1 Introduction to Acid Mine Drainage

Acid mine drainage (AMD) outflow from abandoned underground mining complexes is one of the largest contributors to water pollution in the former coal producing areas of the Eastern United States. If there is not enough alkalinity in the rocks close to the coal seam, the main products of AMD are water with acidic pH, elevated sulfuric acid and sulfate concentrations, and high concentrations of heavy metals (Hoffert, 1947). Overall, the prevalence of coal mining is still highly significant as an extractive industry worldwide. However, the exploitation of coal mining prior to environmental regulation has left several abandoned mine sites throughout southern and eastern Ohio with accountability falling on watershed groups with oversight from the Ohio Department of Natural Resources (ODNR). Estimations from Earthworks (2013) indicate that every year, 40 abandoned mines in the United States can produce 17-27 billion gallons of polluted water each year.

In terms of environmental damage, AMD negatively impacts aquatic systems, surface, and groundwater resources, and causes increased treatment costs as well as corrosion of metal and concrete infrastructure. As a result, modern coal-mining operations must abide to strict guidelines in terms of mining and treatment practices. Unfortunately, the mining industry has operated for much longer than our understanding of the effects of AMD which has led to the large number of abandoned coal mines in Ohio. One region historically influenced by AMD is Monday and Sunday Creek Watersheds (Figure 1). Streams located within Monday and Sunday Creek pose as a



representative case study of the degradation of water quality and the ecology inhabiting and dependent on those streams.

Coal mining in Ohio is older than the state itself, with the first reported mining dated to the year 1800. Three billion tons of coal has been exploited. The industry has fluctuated greatly as it once employed up to 50,000 individuals (Crowell, 1995). Eventually the coal mining industry in Ohio decreased as other regions presented greater economic viability. Much of the flourishing coal yields were in a time of little environmental oversight, which has led to the environmental impacts that we note today in the vast number of abandoned underground regions that generate acid mine drainage continuously. These abandoned mines have been monitored and accounted for by watershed groups funded by the government to work on remediating watersheds negatively affected by Ohio's long coal mining history.

Overly (1997) examined the complex relationships taking place at Esco #40 mine through examining physical, chemical, and biological relationships of the mine drainage. This approach highlighted the importance of addressing environmental issues from an interdisciplinary standpoint and lead to the study outlined in this thesis. Lopez et al. (1999) previously monitored and collected chemistry and flow data for Esco No. 40 mine in the Snow Fork sub-watershed. This research also described the bacterial populations present within the unique water chemistry of the Esco #40 mine waters, and tried to explain the overall behavior of the system as an attempt to hypothesize the interactions noted between the biology, chemistry, and flow regime. An approach similar to Overly

(1997) will be adopted in this thesis and will differ only in its focus of examining four streams of contrasting chemistry.

1.2 Objectives of this Research

There are three primary objectives of this study:

1. To better describe the bacterial populations found within AMD systems and explain the variations found in species with respect to elevated levels of Al, Mn, and Fe.
2. To supplement the existing information about water chemistry, sediment analysis, volumetric flow, and biological data of four separate AMD impaired sites with differing levels of contaminant loadings for Al, Mn, and Fe.
3. To expand on the overall model proposed by Lopez et al. (1999) by comparing interactions of water chemistry, sediment analysis, physics of flow, and biological presence of three systems with varying primary metal contaminants, and one site with average values of the different contamination cations.

1.3 Hypothesis and Research Questions

Water chemistry, flow regime, and the microbiology of each site have a unique relationship determined by the ability of the microbiology to precipitate metal ions and the water chemistry sustaining an acceptable environment chemically and physically for the bacteria. The research question that will be answered with this research are:

1. How does physics of flow affect the distribution of metal contaminants in water and sediments as well as the presence of bacteria that utilize these contaminants?

2. Which bacteria genera and species favor Fe, Al, or Mn concentrated acid mine drainage and how does the water and sediment chemistry influence the proliferation of these bacteria?
3. Is there a common model that can explain the presence and utilization of metal contaminants by specific genera of bacteria in unique flow regimes and system chemistries?

1.4 Structure of Thesis

This thesis initially provides background on acid mine drainage processes which includes chemistry, microbiology, and physical parameters regarding AMD generation. After this is established, descriptions of my study site locations, climate, and geology will be addressed. Then a detailed description is provided of the methodologies used to sample and analyze the data used in this thesis. Finally, the thesis results, discussion, and the major conclusions will be presented addressing the research objectives and questions posed in subsections 1.2 and 1.3.

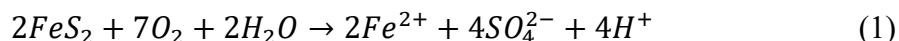
CHAPTER 2: GENERATION OF ACID MINE DRAINAGE

A number of factors influence the production of acid mine drainage. While chemistry dictates the products, numerous hydrologic, mineralogical, biological, and sedimentological factors can alter the rate of production, transport, and precipitation of these chemical products. In this chapter background on the chemistry, microbiology, sedimentology, and physical influences on acid mine drainage formation from underground mining complexes is presented.

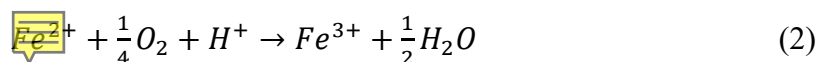
2.1 Chemical Processes

The generation of acid from underground mines is the product of oxidation of sulfide minerals when in contact with water and oxygen. Rates of AMD production are dependent on several factors. This includes the quantity, textures, and types of sulfide minerals exposed in the mine site, water, and oxygen availability. The most common of these sulfide minerals is pyrite (FeS_2). The pyrite present in these mines tends to be fine or small in grain size with respect to other sulfide minerals and occurs in clusters of euhedra, isolated and clustered framboids and spheres, cleat-and-fracture filling spaces, cell fillings, porous and spongy deposits, and replacement of plant debris throughout the coal seams (Parratt and Kullerud, 1979). Pyrite's texture is widely intricate which leaves several potential reaction sites for the AMD cycle to occur which increases its acid generating capabilities relative to the other sulfide minerals present. Therefore, pyrite is considered an ideal candidate when evaluating the potential influence of acid mine drainage and other sulfide weathering processes.

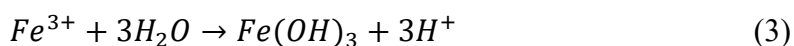
To begin discussing the acid generating reactions of AMD, we can look to the balanced chemical equation for the oxidation of pyrite which yields free hydrogen and sulfate ions:



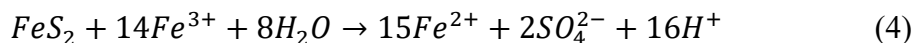
The conditions of reaction 1 yield an environment where the ferrous iron (Fe^{2+}) is greater than the ferric iron (Fe^{3+}). Should the environment provide sufficient oxidizing conditions, the ferrous iron will transition to a ferric species via this equation:



The oxidation of ferrous to ferric iron is the rate determining step as determined by Singer and Stumm (1970). Singer and Stumm performed kinetic tests that showed orders of magnitude difference in oxidation of pyrite dependent on the presence or absence of ferrous iron. The ferric iron (Fe^{3+}) generated begins to precipitate as $Fe(OH)_3$ also known as yellowboy which further generates acidity and decreases ferric iron concentrations:



The above equation shows the chemical reaction in which yellowboy precipitates. This step is ultimately pH dependent and the nonreacted ferric iron is then in equilibrium and free to oxidize more pyrite:



pH values of <4 are environments in which ferric iron become the primary source of oxidation of pyrite (Otwinski, 1994).

The acidic conditions of AMD mobilize several contaminants and other constituents that are contained within the coal material and containing bedrock. Lopez et al. (1999) performed a complete chemical analysis of contaminants during low and high flow conditions at **Esco** #40 mine (also referred to as Essex Mine, Figure 2). A number of ions were found here in high concentration such as iron, sulfate, aluminum, and manganese. These trends are presented in Figures 3 and 4. Iron and sulfate are sourced from the sulfide minerals, such as Pyrite. Al and Mn contamination leach into the water column from the shales and clay minerals found in the adjacent mine lithologies. A more comprehensive outline can be noted in section “3.2 Geology”. All contaminants were found in higher concentrations during low-flow conditions such as that of late summer and early fall. Contaminant concentrations decreased in fall, winter, spring, and early summer during higher flows. This trend also illustrates the relationship of reaction rates in AMD processes and flow of water within the mine. Total iron was noted to be higher in concentration halfway between the mine exit and its junction with the nearby river. Manganese also showed variability in concentration of the mine waters with a decreased concentration 7 and 45 meters from the exit. Aluminum had **peak** concentrations in October roughly 20 meters from the mine exit. Processes of precipitation, transport, and re-dissolution due to changing pH as oxidation occurs are responsible for the changes in concentration along the flow path.

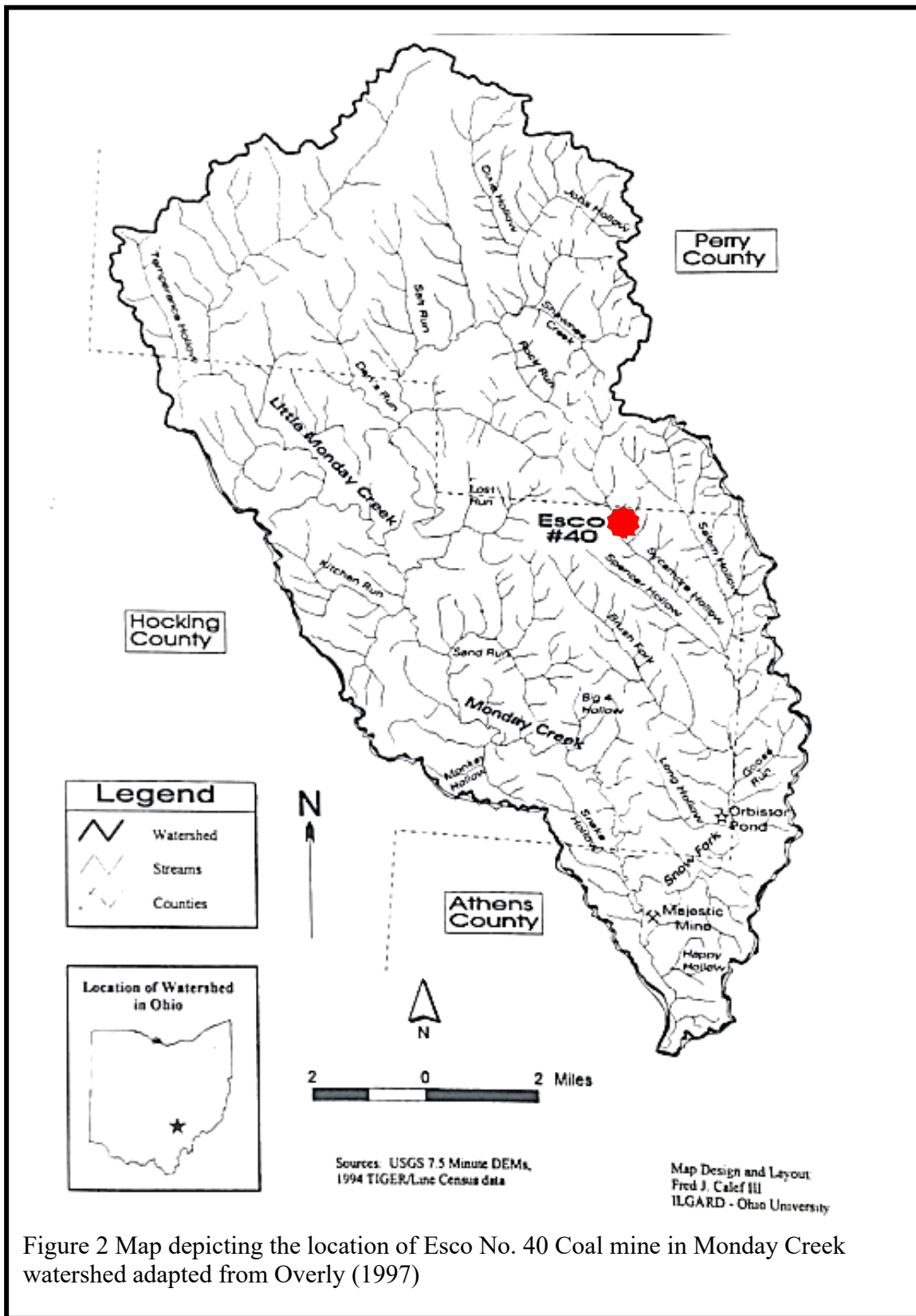


Figure 2 Map depicting the location of Esco No. 40 Coal mine in Monday Creek watershed adapted from Overly (1997)

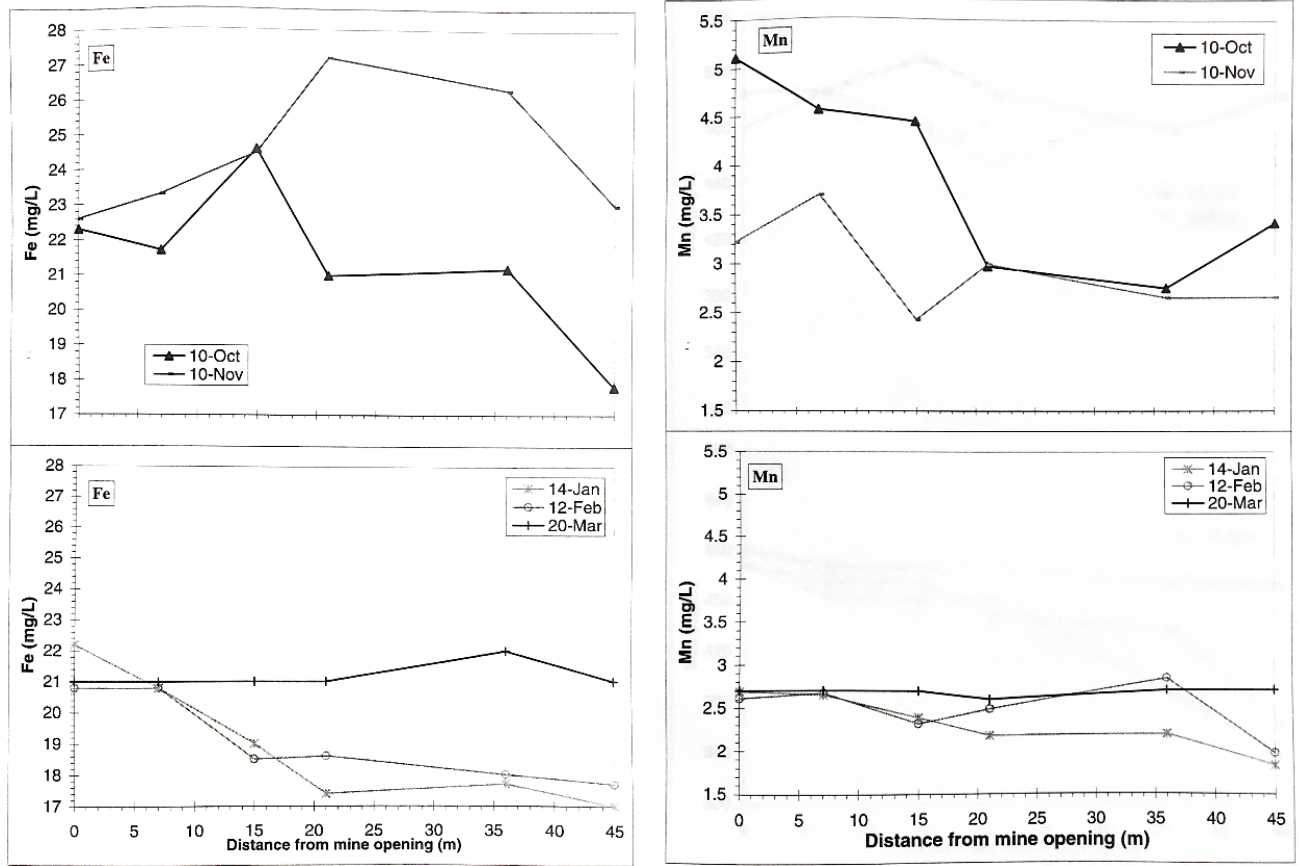


Figure 3 Concentrations of total Fe and Mn at varying distances from the Esco No. 40 mine exit from 10/10/96 to 03/20/97 adapted from Overly, 1997.

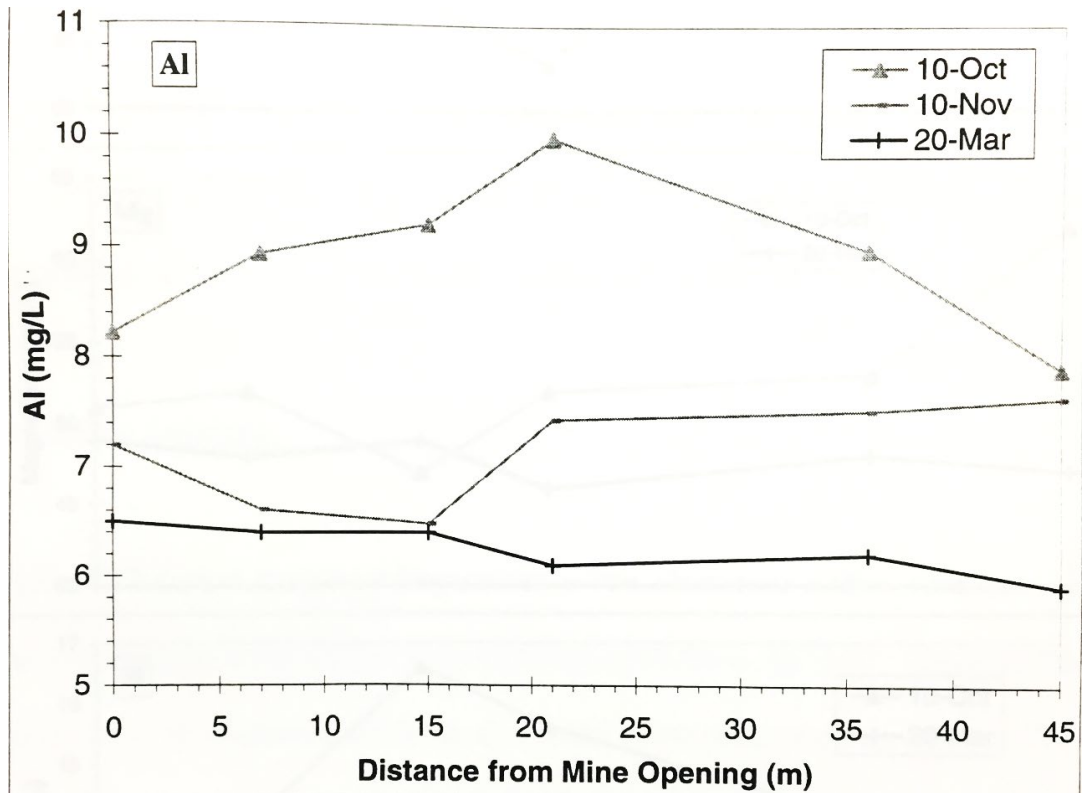


Figure 4 Concentrations of Al at varying distances from the Esco No. 40 mine exit from 10/10/96 to 03/20/97 adapted from Overly, 1997.

Clinton (2005) examined three different sites located in southeastern Ohio:

Sulphur Run, Rock Run, and Buffer Run. Sulphur Run exhibited a more alkaline pH for a system with AMD inputs, and Clinton (2005) noted that the surrounding carbonate lithology was responsible for the neutralization of the added acidity.

2.2 Microbiological Processes

The predecessor to this study was completed by Lopez et al. (1999) where microbial taxa at Esco #40 mine, particularly genera *Thiobacillus* and *Thiothrix*, and species *Leptothrix discophora* were distributed in relation to the fluid velocity which was directly influenced by the flow path of the cross-sectional area and slope or gradients in the elevation of the flow path. These microbes are gram negative which indicates a thinner peptidoglycan layer within the cell wall than gram positive microbes. The presence of these taxa were noted and were associated primarily with the precipitation of manganese oxides, hydroxylated aluminum-sulfates, and ferric hydroxides according to chemical modeling results. The bacteria found required iron specific water chemistries as well as acidic waters to survive. The hypothesized relationship was that a mechanism existed by which these bacteria utilized the cations present as an energy source and then precipitated minerals from the solution. Lopez et al. (1999) found that the population and type of bacteria is related to the water chemistry and the fluid velocity (Figures 5 - 7). In areas of the stream where the velocity was low, *Thiobacillus ferrooxidans* prevailed but in areas with high velocity, the bacteria *Thiothrix sp.* was unusually abundant. This bacterium has filaments that allow it to attach to the substrate and can have a better survival than the bacillus bacteria that are dragged by the velocity of the water. *Thiothrix sp.* exists in the site because of the high Al of this water. *Thiothrix sp.* armor itself with hydroxylated aluminum sulfate probably as a protection mechanism from the acidic waters (Robbins et al., 1996). It was also found in this study that the saturation

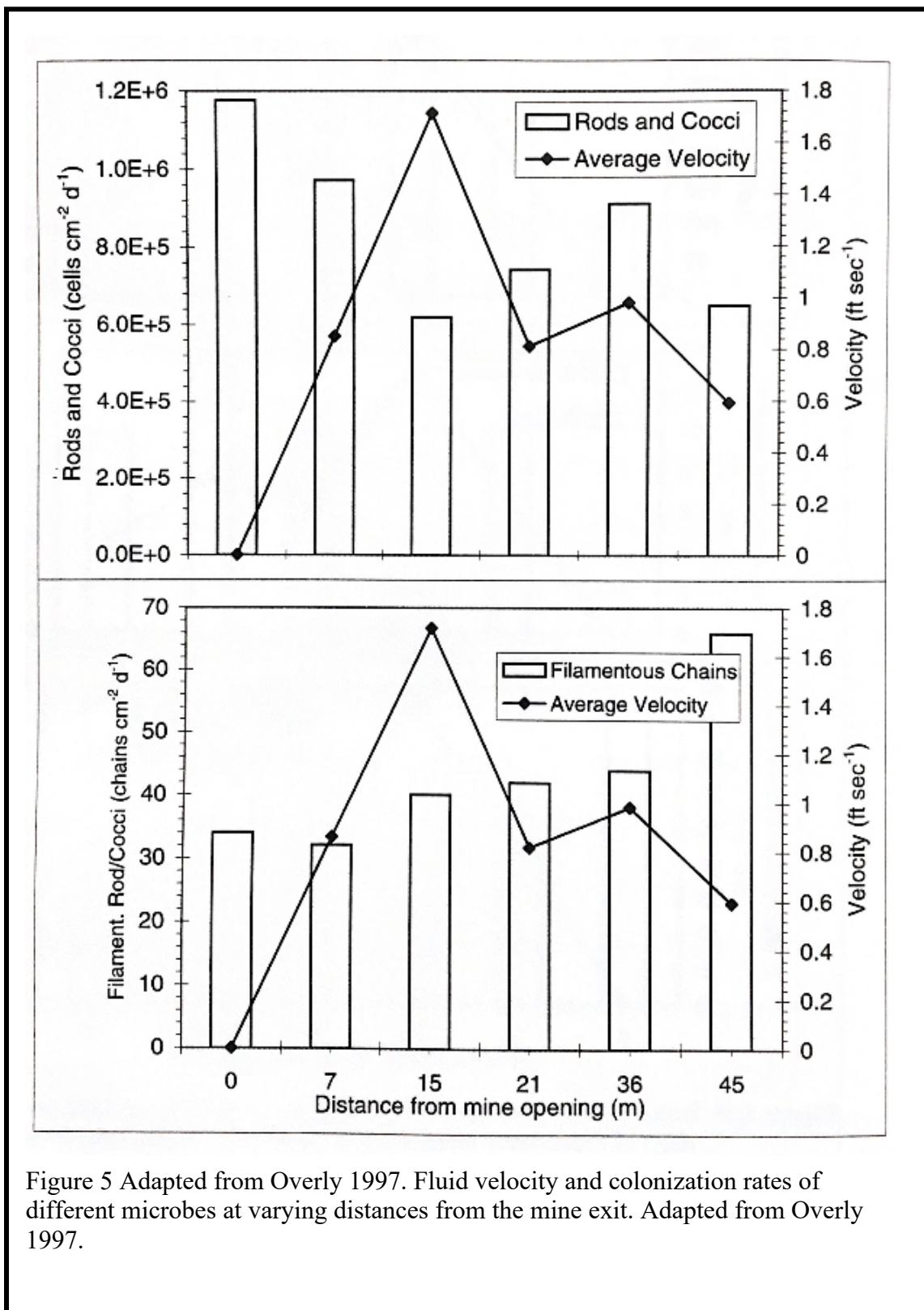


Figure 5 Adapted from Overly 1997. Fluid velocity and colonization rates of different microbes at varying distances from the mine exit. Adapted from Overly 1997.

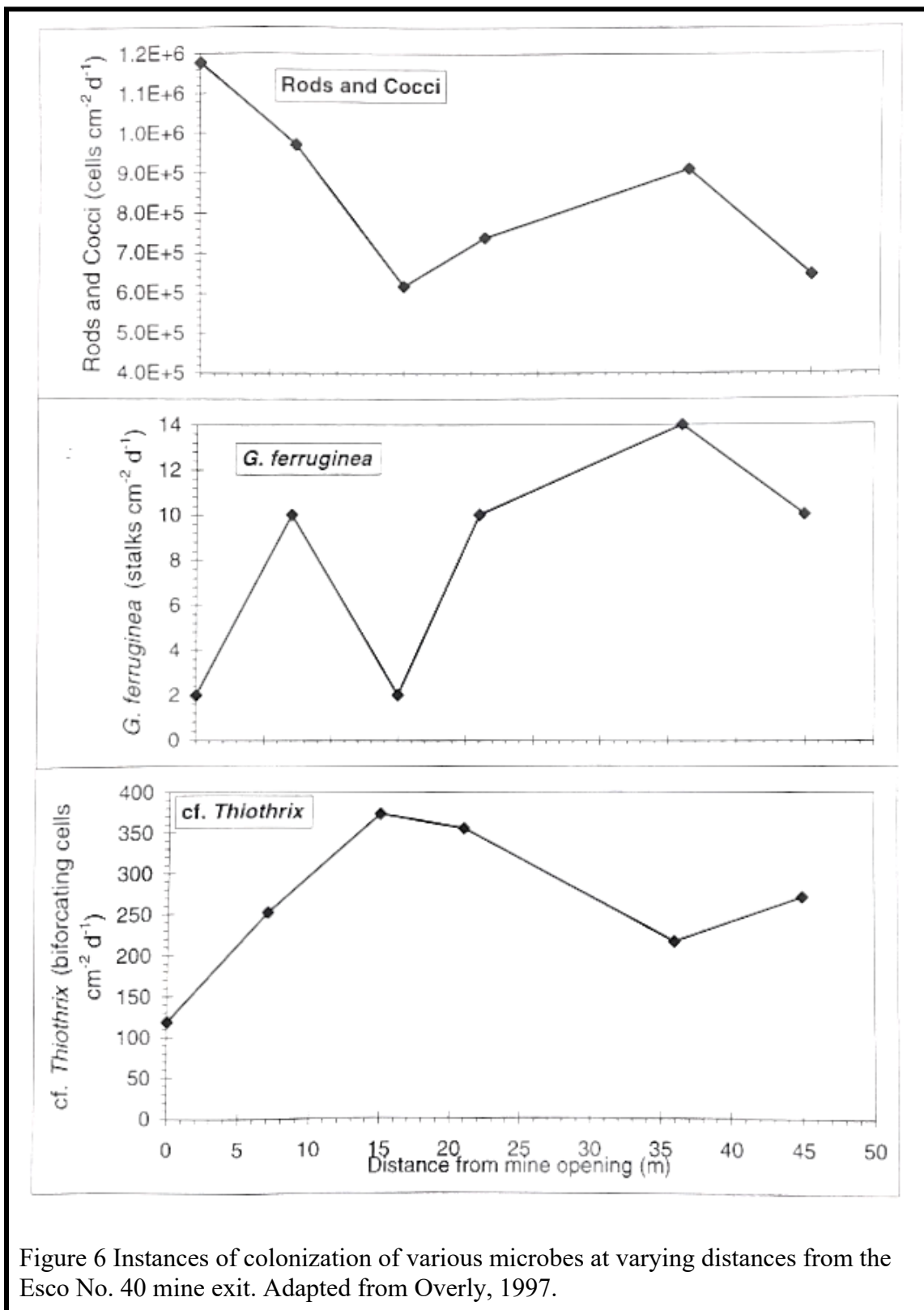


Figure 6 Instances of colonization of various microbes at varying distances from the Esco No. 40 mine exit. Adapted from Overly, 1997.

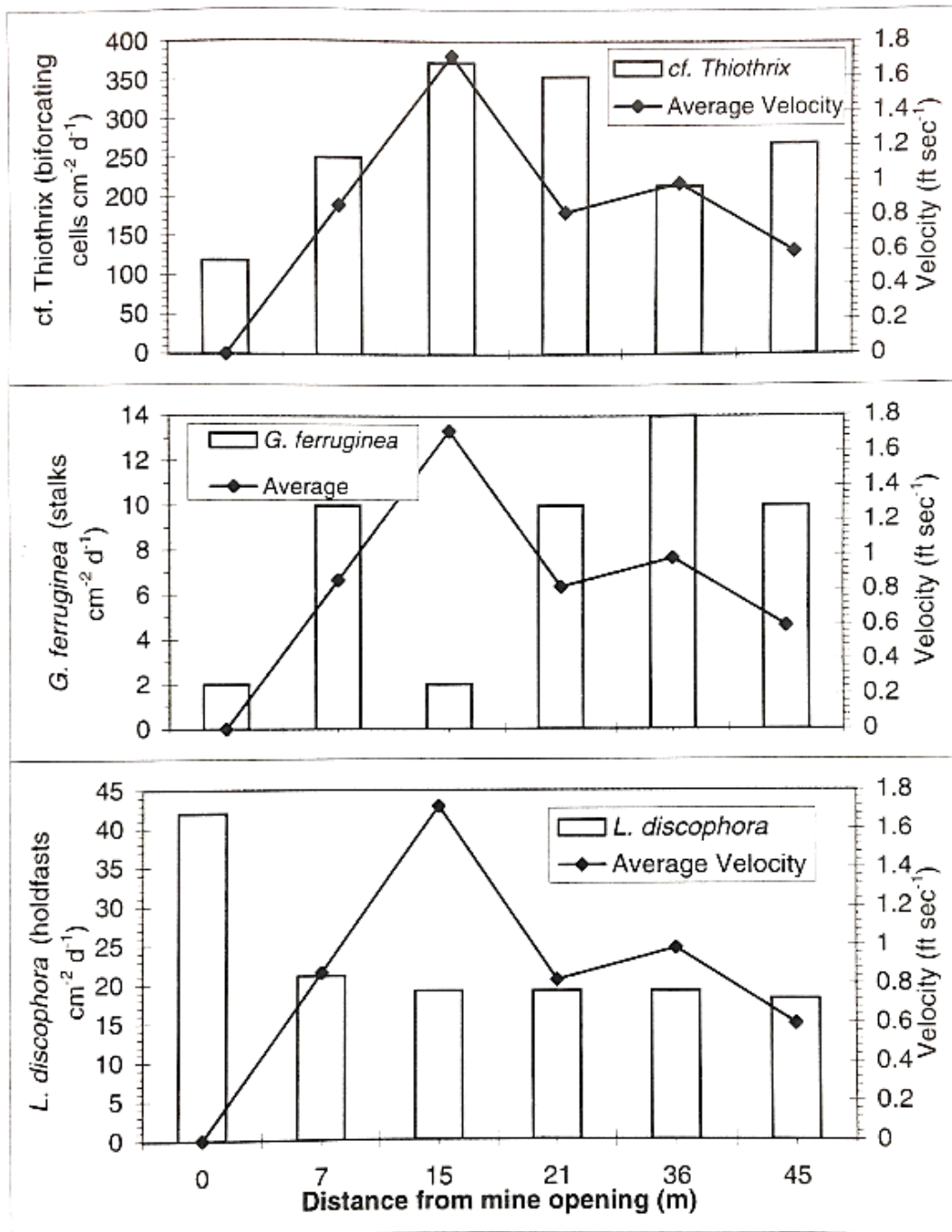


Figure 7 Fluid velocity and colonization rates of different microbes at varying distances from the mine exit. Adapted from Overly 1997.

indexes of the minerals also changed with the velocity of the fluid, and for hydroxylated aluminum sulfate was higher in the areas of higher velocity and more abundant *Thiothrix sp.* A similar study to that done by Overly (1997) and reported in Lopez et al. (1999) in waters of different chemistry could give important information about bacterial populations and their relationship with the physics of the flow.

Microbiology of acid mine drainage afflicted waterways also determine the rate at which acidity is produced. Only some particular organisms can tolerate and proliferate in the unique water chemistry of AMD and these microbes are commonly referred to as acidophiles or acidophilic microbes. The acidity generated from these reactions often eliminate a large percentage of organisms from the tributaries downstream of an abandoned mine site. Acidophilic bacteria have the ability to increase or decrease the rate of oxidation of sulfide minerals (Wichlacz, 1981).

Microorganisms normally found in AMD are gram-negative, mesophilic, acidophilic, chemoautotrophic (sources energy from oxidation of inorganic substances) bacteria (Nordstrom, 1977). These species are capable of fixing nitrogen and carbon dioxide and attain their main source of energy from ferrous iron and other reduced inorganic sulfur compounds during the oxidation process of sulfide minerals. The environments generated by these microbes often lead to conditions that promote sulfide mineral dissolution (Jia, Yan, et al., 2019). For these reasons microbes that utilize and thrive in AMD systems can be categorized as bioleaching microorganisms.

Sulfate reducing bacteria also known as SRBs tend to both be chemolithotrophic or chemoorganotrophic (an organism that sources energy from oxidation of reduced

inorganic compounds) and utilize sulfate as their terminal electron acceptor. SRBs have also been known to join ATP synthesis with anaerobic electron transport (Barton and Fauque, 2009). The SRBs that are acidophilic bacteria inhabiting AMD and its sediments are often limited to the class *Deltaproteobacteria* and phylum *Firmicutes* (Baker and Banfield, 2003).

2.2.1 Acidophilic Microbial Taxa

Thiothrix

Thiothrix is a genus of mostly gram negative chemolithotroph filamentous motile bacteria that oxidize inorganic forms of sulfur to obtain energy. These filamentous bacteria contain rosettes or mesh-like interlocking strands that extend radially from their rod-shaped bodies creating a distinctly advantageous body shape for dominating high velocity regions of flowing water systems (Figure 8) (Larkin and Shinabarger, 1983). *Thiothrix* is most located in waters high in sulfides, low in dissolved oxygen, and colder temperatures usually around 10.8°C. *Thiothrix* has been shown to contain cytochrome “c” which has been associated with microbes that can synthesize organic molecules from inorganic materials (Larkin and Shinabarger, 1983).

This genus of bacteria is particularly relevant in acid mine drainage as these are environments of low dissolved oxygen, high sulfur concentrations, and groundwater temperature conditions which are particularly tailored to these sulfur oxidizing bacterial

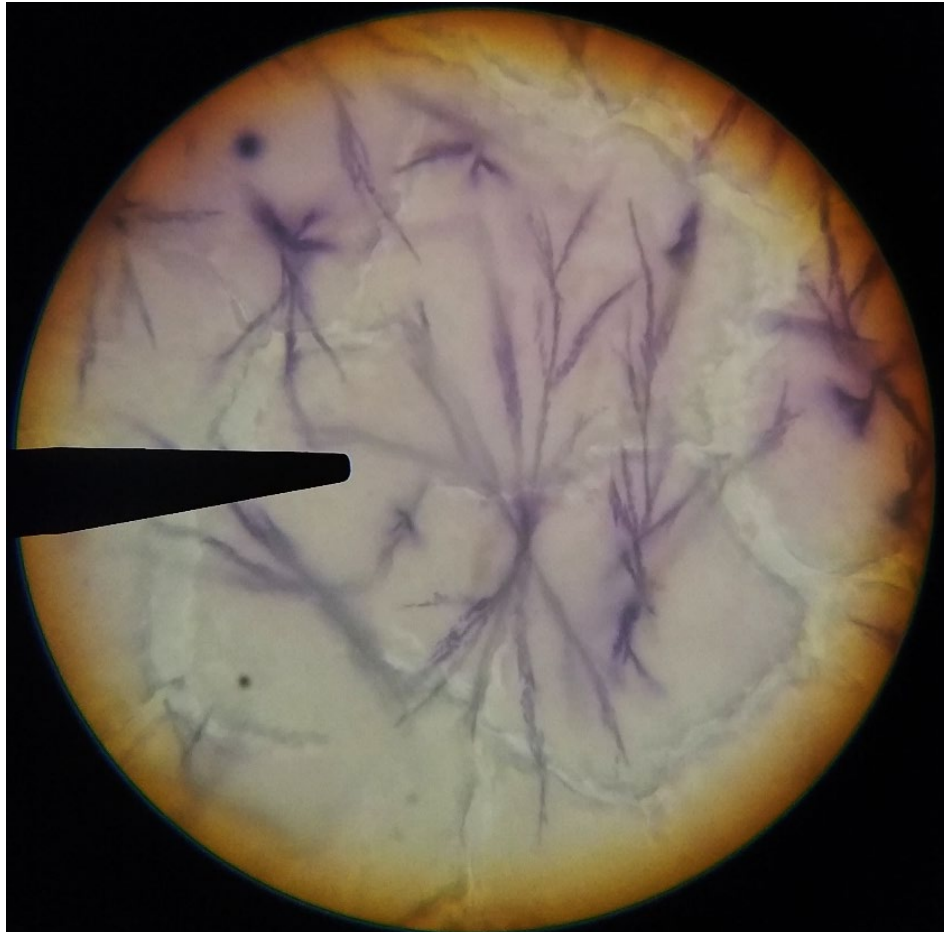


Figure 8 Filamentous rosettes of Thiobacillus thiooxidans shown as a gram positive (1000X) (gram-variable).

species. In addition, *Thiothrix* has rosettes which allow it to dominate the systems where AMD immediately exits a mine as this can be fast moving turbulent water allowing for filaments from the *Thiothrix* to latch onto the sediment or precipitates deposited thereafter. Lopez et al. (1999) described the most populous colonies identified along the mine exit of Esco No. 40 to be those morphometrically similar to that of *Thiothrix* with distinct rosettes of long colorless filaments which closely associated with hydroxylated alumino-sulfate minerals. It was also demonstrated that colonization rates of *Thiothrix* at the Esco No. 40 mine were most closely linked to fluid flow velocity. However, this result was only for the Esco No. 40 mine, in this thesis we explore other mine sites with more variable conditions.

Gallionella ferruginea

Gallionella ferruginea is a species of mostly gram negative chemolithotrophic bacteria that oxidize or “fixes” inorganic forms of iron to obtain energy. These microbes require environments with reduced forms of iron and a minimum amount of oxygen as well as sufficient levels of carbon, phosphorus, and nitrogen. *Gallionella ferruginea* is most located in waters high in iron, elevated dissolved oxygen, and generates ferric hydroxide products. These bacteria usually have reddish-brown coloration from the iron oxide precipitates that they produce (Hanert, 1981) (Figure 9).

G. ferruginea is relevant in acid mine drainage outflow as these are environments of reoxygenation, high inorganic iron concentrations, and high levels of ferric hydroxides. In addition, *G. ferruginea* can form biofilms at the air-water interface (Hallbeck and Pedersen, 1995).

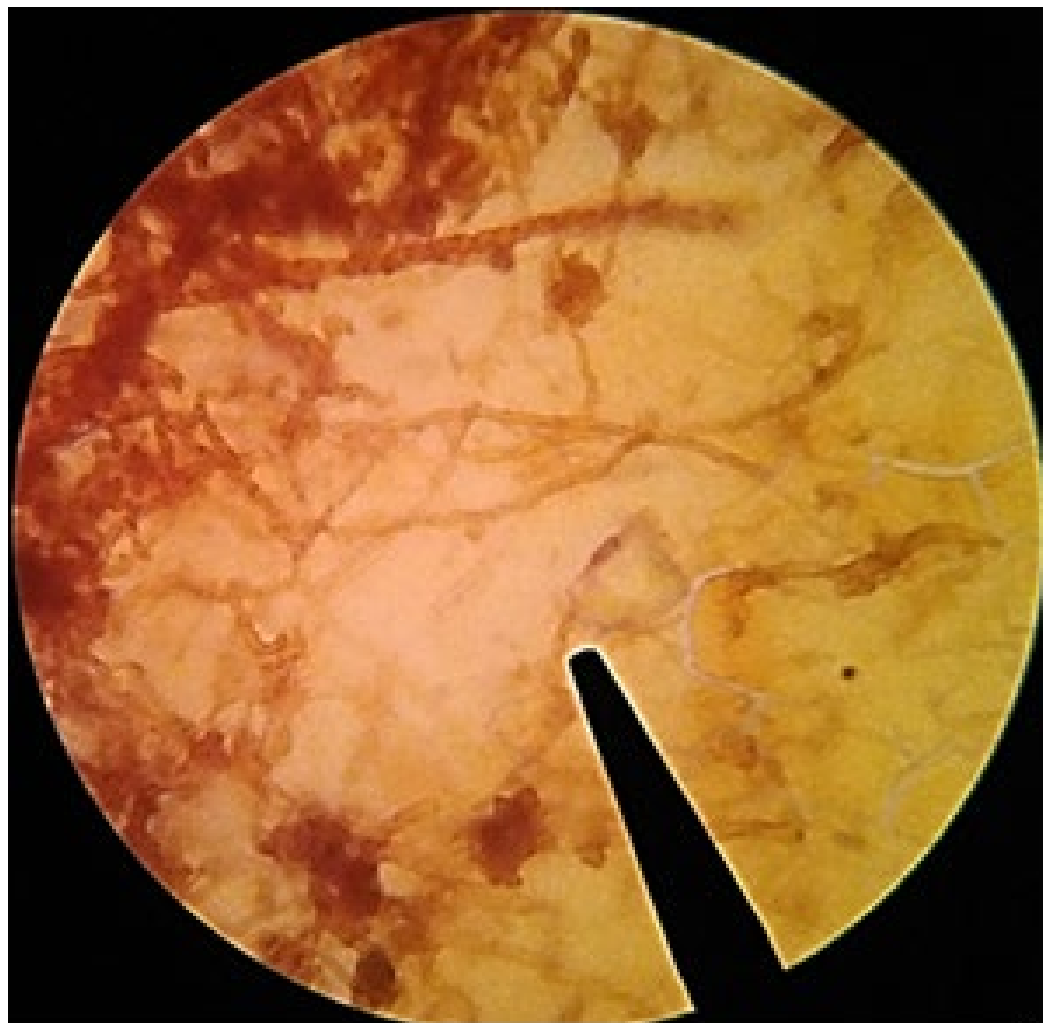


Figure 9 Ferric-hydroxide stained *Gallionella ferruginea* viewed at 1000X located in the Pine Run mine drainage.

Leptothrix

Leptothrix is a genus of gram negative aerobic oxidative organoheterotroph bacteria (Figure 10). These microbes require environments with absent to low flow velocities with neutral to slightly acidic fresh waters, low concentrations of organic matter. The forms of carbon utilized by Leptothrix can be either organic or inorganic. (Cloutier et al., 2017)

Leptothrix can be relevant in partially remediated acid mine drainage outflow as these are environments of reoxygenation, acidic to neutral pH, low organic matter, and oxidative conditions (Hallberg and Johnson, 2005). These bacteria are uniquely suited for latching onto the suspended slide contraptions with their lengthy chain conformations that can attach to the AMD substrate easier than other microbial conformations.



Figure 10 Rod shaped bacteria in chain conformation fitting the description of the *Leptothrix* genus found in the York Clay mine drainage (1000x).

Thiobacillus

Thiobacillus is a genus level classification that describes over 30 species of rod-shaped bacteria that share a similar morphology (Figure 11). Thiobacillus is a gram negative mostly obligate chemolithoautotrophy or weak heterotroph (*aquasulis* sp.) species of bacteria. These microbes derive energy from sources of sulfur, thiosulfate (an oxyanion of sulfur), and polythionates (oxidized forms of thiosulfates). (Schrenk et al., 1998)

Thiobacillus was largely the most common type of bacteria found on each slide and had exceedingly high counts for each slide. Thiobacillus is commonly found in AMD environments due to the abundance of sulfur, thiosulfates, and polythionates which are present in varying amounts based on the oxidizing conditions present.

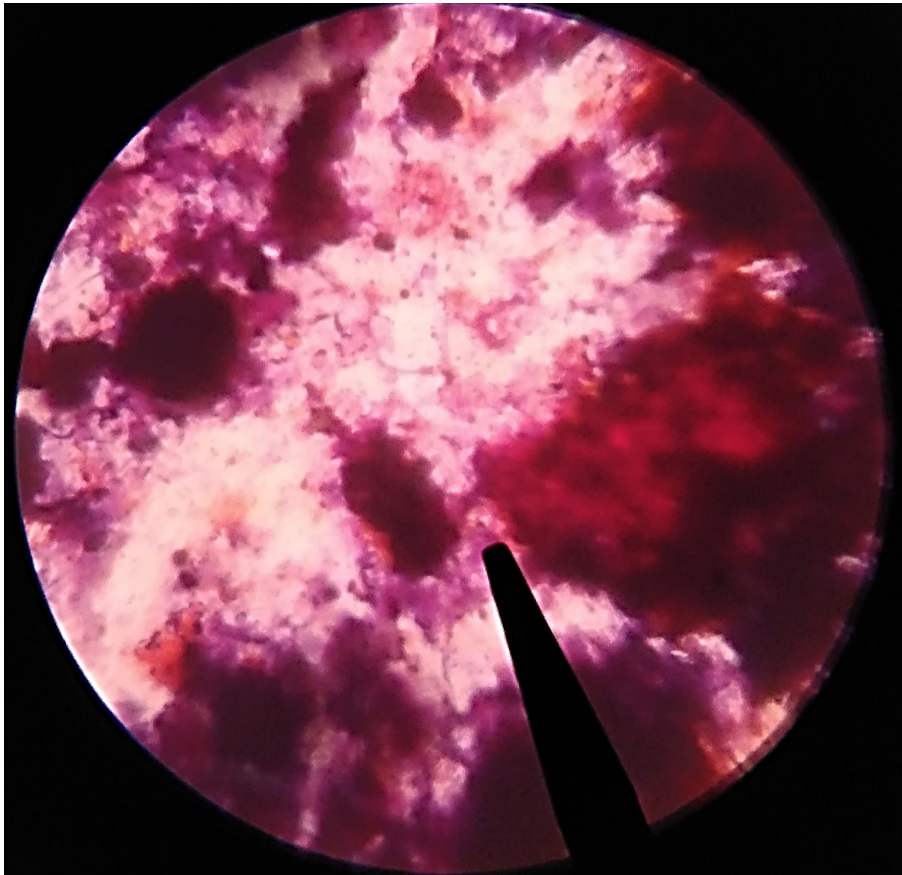


Figure 11 Rod-shaped gram-negative bacteria found in clusters of each slide fitting the description of Thiobacillus genus (1000x).

2.3 Physical Processes

Physical factors influence the generation of AMD in addition to chemical and biological processes. In particular, these include oxygen content of the water, properties of minerals, temperature, flow, and the hydrologic variables of the area. The importance of the physical characteristics of water and the air of the unsaturated zone weigh heavily into understanding chemical and mineralogical processes involved in AMD due to its involvement in the oxidation equation.

Oxygen can often be a limiting reactant and is responsible for determining stoichiometric amounts of sulfidic minerals that will effectively become oxidized. Johnson and Thornton (1987) found a direct correlation between trace element concentrations and the proportion of infiltrated surface drainage in mine waters. In underground mines, the source of inflow for mine water can also carry inorganic ions which can alter the properties of the water and influence the reactions of mine water with varying results (Johnson and Thornton, 1987). This differs widely from flooded mines that are sourced through ground water. Water can accumulate through underground mining complexes, which are gaps or cavities left behind in the bedrock from mining practices. It can reach these complexes through a number of methods, each with its own unique influence of the source chemistry for the mine water. The primary method of water reaching the mine is through fractures and faults located in the adjacent bedrock. This system of fractures and faults has little resistance to water movement which offers a larger volumetric contribution to the mine (Moebs and Clar, 1990). The second method is through inflow of water from water bearing strata including sandstone, limestone, coal,

and other unconsolidated materials which interact with the coal seam. Porosity of material and variability in the cross-sectional hydraulic conductivity come into play when determining the path by which this water reaches the mining complex (Moebs and Clar, 1990). The proportion of infiltrated surface drainage in mine waters has been strongly correlated with the trace elemental concentrations determined in mine waters (Johnson and Thornton, 1987). The third and final method by which water reaches the mining complexes through porous overlying material leading to infiltration from directly above the mine. Often noted in more shallow mine systems with decent air flow, this process can also contribute large quantities of acid mine drainage

Variations in temperature can also influence AMD reactions via kinetics and by influencing microbiological processes related to acid mine drainage. Kinetic influence of temperature essentially involves the lowering of the activation energy required to perform chemical reactions (Verb and Vis, 2005). This in turn makes chemical processes easier to undergo and increases the efficiency of the rate determining step (equation 2) of AMD. As a result of increased temperature, we see a direct proportionality to the solubility of metal ion concentrations of the mine waters. Fluctuations in temperature can increase or decrease the activity of microbiological life responsible for precipitating or utilizing the contaminants located in the mine waters. This directly affects biological interactions which in turn alters the water geochemistry as a whole (Morin et al., 1991).

Lopez et al. (1999) found dissolved oxygen (DO) levels were relatively low in the waters within the mine opening which was credited to the numerous oxidation reactions that took place within the mine depleting the dissolved oxygen content of the mine

waters. DO levels began to rise as the waters came in contact with the O₂ rich air which mixed at the air/water interface until the water reached its saturation level. Waters exiting the Esco #40 mine had reached saturation around 40-45 meters just prior to the first junction where the water mixes with a well oxygenated stream (see Figure 12).

Along the flow path after the water leaves the mine, there were variations of the elevation of the water. Elevation drops followed by catch basins were located 12-14 meters and 17-19 meters from the exit of the mine. At 15 and 21 meters the water reaches its highest rate of increasing dissolved oxygen content which is located in the catch basins. DO levels have been found to be inversely proportional to the volumetric flow rate (Pigati, 1997). In a study of the Majestic mine, Pigati noted that the water levels of the mine dropped in spring and summer which allowed more atmospheric gas to enter the mine. The range of dissolved oxygen content at Majestic was recorded as 0.7-1.8 mg/L. Lopez et al. (1999) observed that air temperature influences dissolution rate of O₂ which directly affects the rate of microbial activity of *Thiobacilli*.

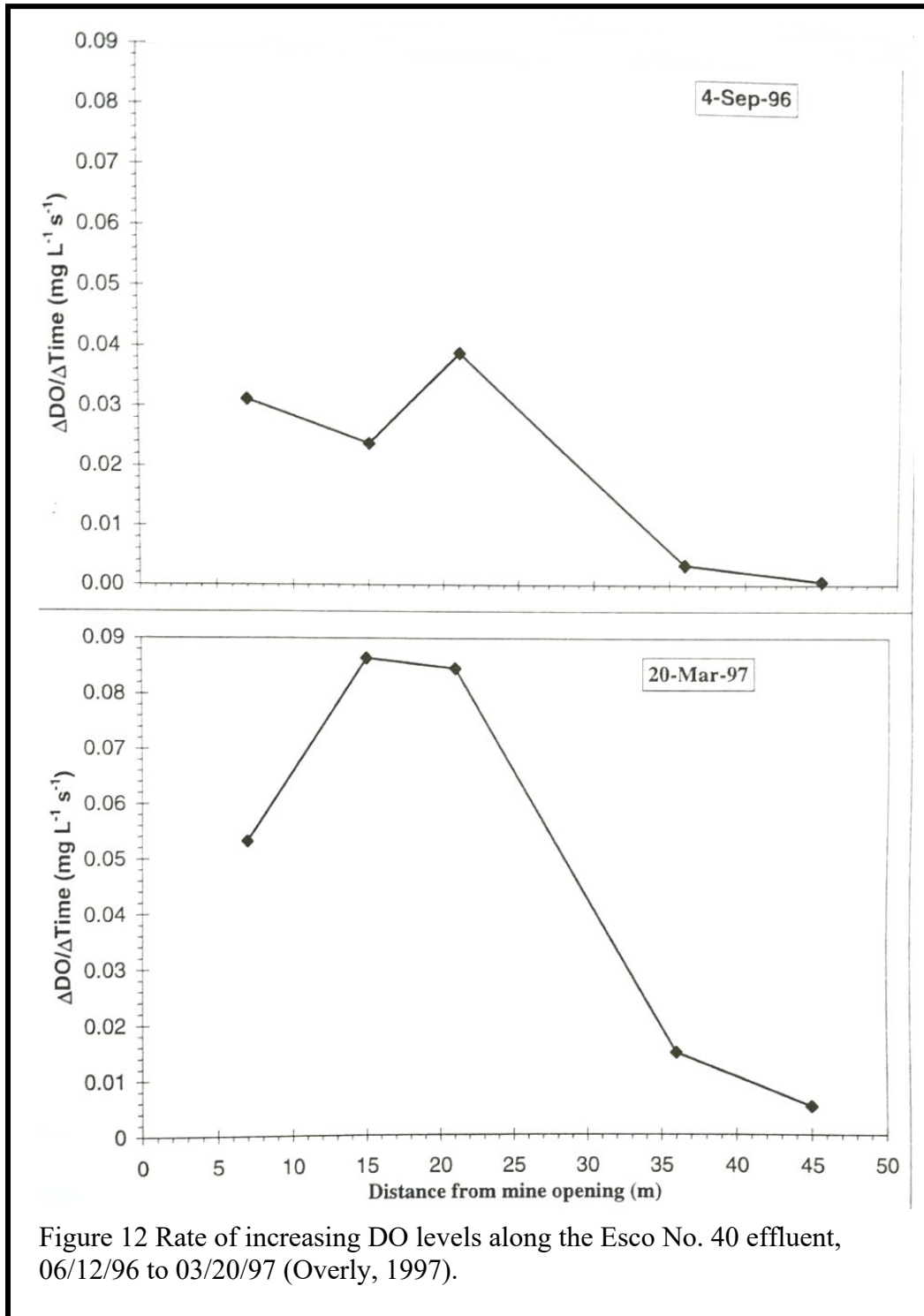


Figure 12 Rate of increasing DO levels along the Esco No. 40 effluent, 06/12/96 to 03/20/97 (Overly, 1997).

Pigati and Lopez (1999) report that water discharge from the Majestic Mine in SE Ohio presented lower discharge during summer months due to an increased evapotranspiration with the higher summer temperatures instead of a decrease in rainfall. Precipitation was not significantly lower during the summer to explain the lower flows. Higher evapotranspiration resulted in lower infiltration rate and lower discharge from the mine.

2.4 Acid Mine Drainage Sedimentological Processes

Primary outflow of mine drainage usually occurs at a former mine air shaft, drift entry, and slope entry which carves a stream channel and transports metals in the particulate phase of which is mostly dissolved and gets deposited further downstream (Johnson and Thornton, 1987). After reactions with sulfide minerals liberate sulfate, free acidity, and metals, these products are carried out of the mine into the drainage channel and into a nearby stream or river. Depending on the redox reactions of the products in the drainage, metals can remain suspended and transported downstream until they achieve the redox conditions to precipitate or they are sorbed onto the surface of sediment and deposited. Products can precipitate into colloidal form and aggregated into larger particles until sufficient accumulation has occurred downstream to allow precipitation into the channel.

2.4.1 Sediment Transport

The correlation between pH and sediment precipitation was examined by Boulton (1996) who looked at fluvial metal transport in the Afon Goch, a highly contaminated acid mine drainage (AMD) tributary in the United Kingdom. Boulton highlighted

variations in the composition of the headwaters of the Afon Goch. He also found lower concentrations of the soluble intermediary product Fe^{3+} with respect to colloidal iron hydroxide sediments that had already precipitated. For this reason, it is suggested that the concentration of the total iron load was not solely related to the pH of the stream but was more intricate. If more colloidal sediment were suspended in the headwaters, it would suggest that aggregation of these colloids into larger particles would be a more influential mechanism on metal load concentrations in highly contaminated environments similar to that of the Afon Goch. From this it is suggested that concentration of total iron load is influenced not only through pH, but through coagulations of iron hydroxide colloids. Boulton also indicated that the colloidal iron hydroxides present are extremely fine, and often incorporate into biofilm complexes found at the air/water interface.

2.4.2 Mineralogy of AMD Sediments

Various mineralogical assessments of AMD have been performed on AMD sediments. The dominant mineral phases found in AMD are likely a mix of schwertmannite, goethite, and jarosite mostly depending on the pH of the system and the primary environment in which the sediments are deposited.

In Bigham et al. (a)(1996) a bioreactor utilizing a strain of *Thiobacillus ferrooxidans* at the pH levels 2.3, 2.6, 3, 3.3, 3.6 was used to simulate conditions for precipitation of minerals. Schwertmannite was found to be the most abundant mineral around a pH of 3.0. In higher pH waters ~3.3-3.6 goethite prevailed over schwertmannite. Goethite was shown to also have higher affinities for surface adsorption of sulfate in lower pHs. However, in conditions with pH below 3.0 goethite was replaced with

jarosite with relation to schwertmannite. Bigham's findings indicate that ferrihydrite is not a major precipitate product of Fe oxidation under acidic conditions of pH around 2-4.

In Gagliano et al. (2004), researchers examined the geochemical stability and mineralogy of ochreous sediments deposited in a passive remediation wetland with an AMD input. The upper 6-9 cm of sediments were composed primarily of schwertmannite. There was also some presence of quartz and goethite in these upper regions at much lower abundances. Chemical analyses confirmed the ratio of Fe/sulfate was around 5. Middle regions of these sediments indicated transitions from schwertmannite in the superficial to goethite in the deep. It was then determined that the schwertmannite was a precursor to goethite, and the rate of transformation was determined to be 10-30 mol/m³/year which indicates a variable system. As for the deeper sediments, goethite was more dominant at around 33 cm and gypsum was also precipitated. Likely induced through carbonate dissolution of the limestone base of the remediation wetland. Calcium released from this limestone could react with the pore water of the sediments and precipitate gypsum. Samples collected nearly a half decade later indicate that gypsum was absent from sediments at these depths. One model proposed is that carbonate depletion lowered the calcium available in solution leading to conditions that favored gypsum dissolution. Jarosite [(K, Na) Fe₃(SO₄)₂(OH)₆] nodules roughly 5 mm in diameter were also noted next to yellow pigmentation in the deeper sediment (Gagliano et al., 2004).

Sediment precipitation has formerly been shown to associate with conditions of the stream such as that of pH, and depending on the presence or absence of microbes or

sufficient reactants, remaining ferrous iron can be oxidized into ferric iron as the stream geochemically develops (Bigham et al., 1996 (b)).

Bigham et al. (b)(1996) examined twenty-eight different mine drainage sites containing elevated levels of sulfate. Bigham wanted to evaluate the mineral schwertmannite for its solubility and paragenetic relationships with other minerals of acid sulfate waters (ASW). He found that the mineralogy of the ASW precipitates varies with pH of the source waters. More alkaline environments exhibiting pH greater than 6.5 are composed of more ferrihydrite $\text{Fe}_5\text{HO}_8 \cdot 4\text{H}_2\text{O}$, possibly mixed with goethite. ASW with pH ranging from 2.8 to 4.5 contain mostly schwertmannite with goethite and jarosite. Mixing of ferrihydrite and schwertmannite occurs mostly at pH conditions in between (e.g. 4.5 to 6.5). When the pH of a solution drops below 3, goethite and jarosite are the most common precipitates as ferrihydrite and schwertmannite both dissolve in solution. The average ratio of S/Fe was exactly 5.4 in Bigham et al. (b)(1996). This ratio can be used to describe sediments below or above this average of 5.4. The mineral goethite was determined to be the most stable as it persisted through the widest range of ASW sediments, even those dominated by other mineral phases. Each of these mineral phase interactions were largely mirrored in naturally occurring acidic waters of the Zillertaler Alps in Austria by other mineral phases. Each of these mineral phase interactions were largely mirrored in naturally occurring acidic waters of the Zillertaler Alps in Austria. Relevant mineral precipitates pH ranges for commonly present AMD minerals can be found in Figure 13. In addition to precipitation pH ranges, chemical formulas, geologic settings, and color are listed in Table 1.

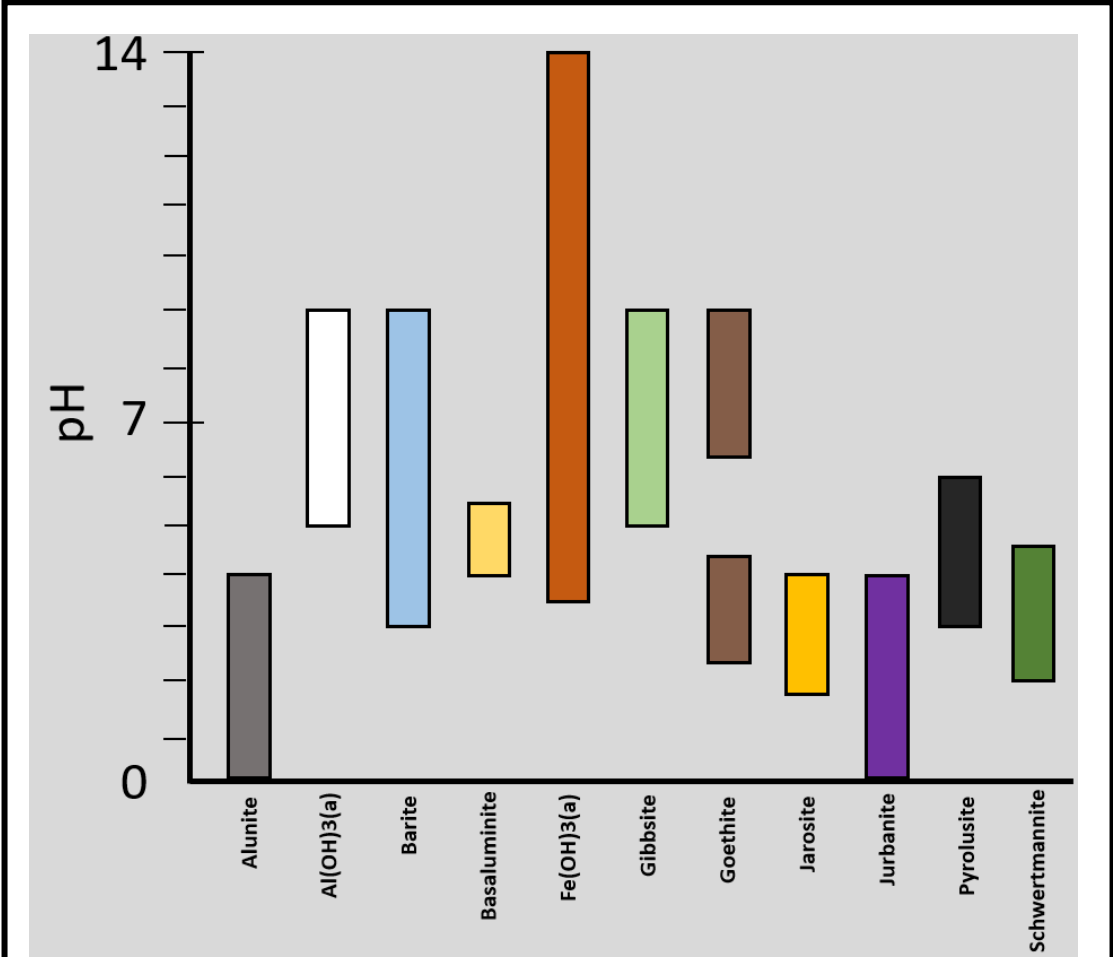


Figure 13 Popular AMD mineral precipitates represented by the ranges in which they precipitate (Potter-McIntyre et al., 2018; Ruiz-Agudo et al., 2015; Lozano et al. 2018; Bénézech et al., 2008; Yue et al., 2016; Lükewille et al., 1992; Mayanna et al., 2015; Bigham et al., 1996(a)).

Table 1. Table containing minerals names and accompanying information found in acid mine drainage sediments that are relevant to the mineralogy of the selected study sites (Potter-McIntyre et al., 2018; Ruiz-Agudo et al., 2015; Lozano et al. 2018; Bénézeth et al., 2008; Yue et al., 2016; Lükewille et al., 1992; Mayanna et al., 2015; Bigham et al., 1996(a)).

Mineral	Chemical Formula	Color	Geologic Environment	Precipitation pH Range
Alunite	$KAl_3(SO_4)_2(OH)_6$	white, pale shades of gray, yellow, red, to reddish brown	"Formed between 15 C and 400 C by the action of sulfate, which may be generated from pyrite or solfataric action, on aluminous rocks, commonly accompanied by kaolinitization and silicification."	<1-4
Aluminum Hydroxide (amorphous)	$Al(OH)_3(a)$	White		5-9
Barite	$BaSO_4$	Colourless, white, yellow, brown, grey, blue, etc.	"found as a gangue mineral in metallic ore deposits of epithermal or mesothermal origin"	3-9
Basaluminite	$Al_4(SO_4)(OH)_{10} \cdot 4H_2O$	Colourless, yellow, white	"Oxide zone in marcasitic ores."	4-5.5
Iron Hydroxide (amorphous)	$Fe(OH)_3(a)$	Orange, dark brown, yellow-brown	"Cold-water springs, Mine workings, warm subsea springs, warm water seabed, thermal springs, thermal water in brooks, rivers and lakes."	>3.5
Gibbsite	$Al(OH)_3$	White, light gray, light green, reddish white; reddish yellow (impure)	"Bog iron deposit."	5-9
Goethite	$\alpha-Fe^{3+}O(OH)$	brownish black, yellow-brown, reddish brown	"Common weathering product, primary hydrothermal mineral, bog and marine environments."	2.4-4.3
Jarosite	$KFe^{3+}_3(SO_4)_2(OH)_6$	Amber-yellow, yellow-brown, to brown or light yellow	"found in the oxidized zones of sulfide deposits, forming by the reaction of dilute sulfuric acid in groundwater, derived from the oxidation of pyrite, with gangue minerals and wall rock in the deposits."	2-4
Jurbanite	$Al(SO_4)(OH) \cdot 5H_2O$	colourless	"post-mine stalactite."	<4
Pyrolusite	$Mn^{4+}O_2$	Black or very dark grey	"forms under oxidizing conditions and high pH (oxidized zones of manganese ore deposits). Both colloidal processes and bacterial action are important in its formation."	3-6

CHAPTER 3: SITE SELECTION AND GEOLOGICAL SETTING

Southeastern Ohio has many different abandoned mine discharges with different concentrations of Fe, Mn, and Al. Preliminary data collection took place from May to June of 2019. This involved analyzing and confirming the contaminant concentrations and locations for potential study sites. Selection of the sites was limited to discharges from abandoned underground mines (Figure 14). The site selection was done looking for sites with contrasting water chemistry in terms of Fe, Al, and Mn. For that purpose, a triangular diagram depicting the composition of these three ions was done. Four sites located in southeastern Ohio (Figure 15) were selected: Pine Run Mine (Sunday Creek No. 9 and 12) and Esco Coal Mine (Essex No. 40) for iron, York Clay Coal Mine (York Clay & Mining NO. 4) for manganese, and Sines Coal Mine (Sines No. 2) for aluminum. A representative site with balanced concentrations was difficult to find as most locations were rich in Fe or Al, so the ratios used for plotting Fe:Al:Mn in Figure 15 were 2:1.5:15.

In searching for potential mine discharges, it was difficult to find contrasting chemistries with similar flow regimes. For the scope of this research limiting the search to four sites proved difficult, and the above listed had differing flow regimes. Esco mine seemingly had the largest velocity, Pine Run mine had an intermediate flow velocity, and York Clay or Sines both contained a low flow velocity. For the sake of simplicity, flow velocity ranges for each mine will serve as a basis in reference to each of these flow velocities. Demarcating “high”, “medium”, or both “low” flow velocity refer to Esco, Pine, or York Clay/Sines coal mines, respectively.

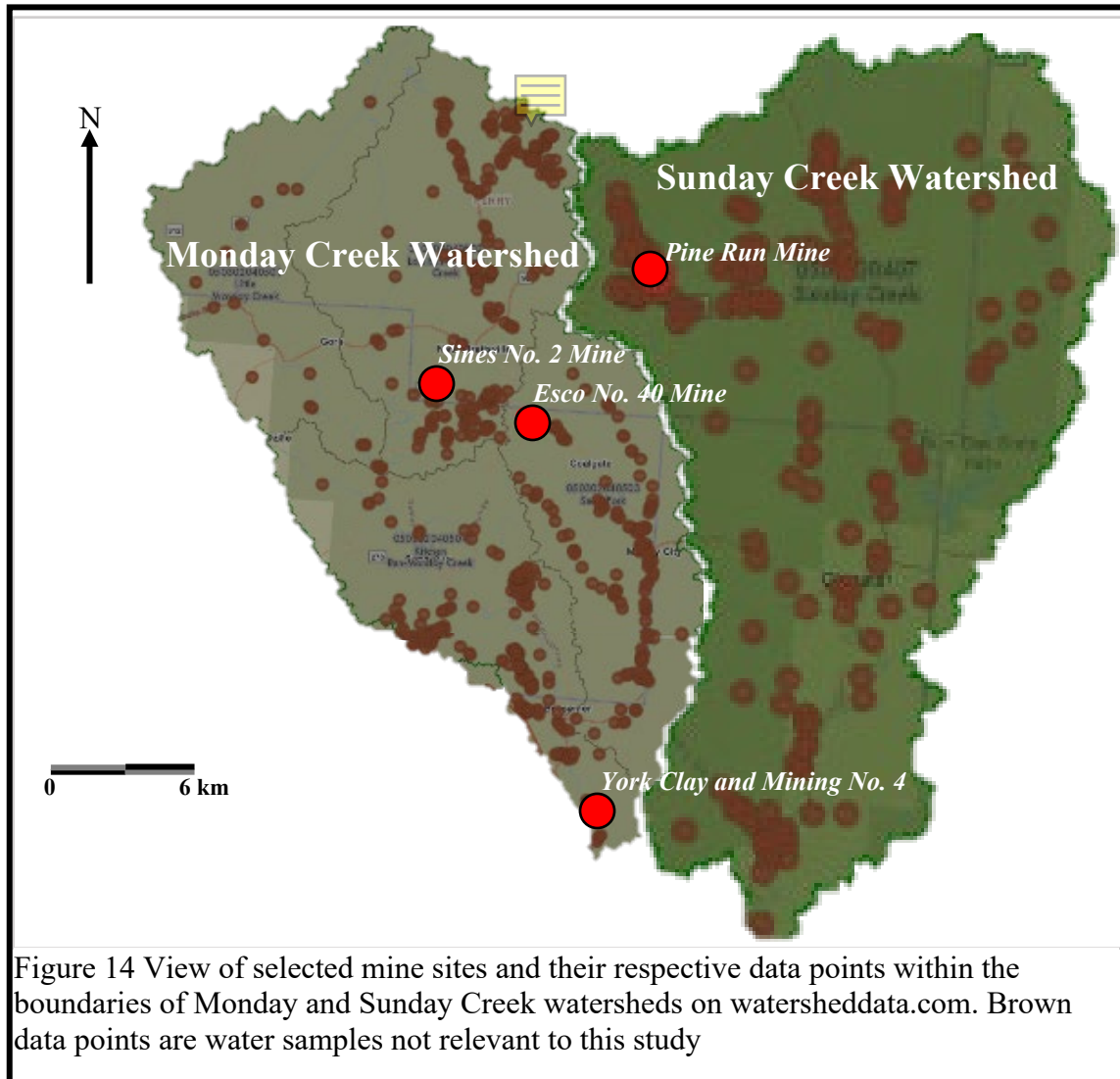
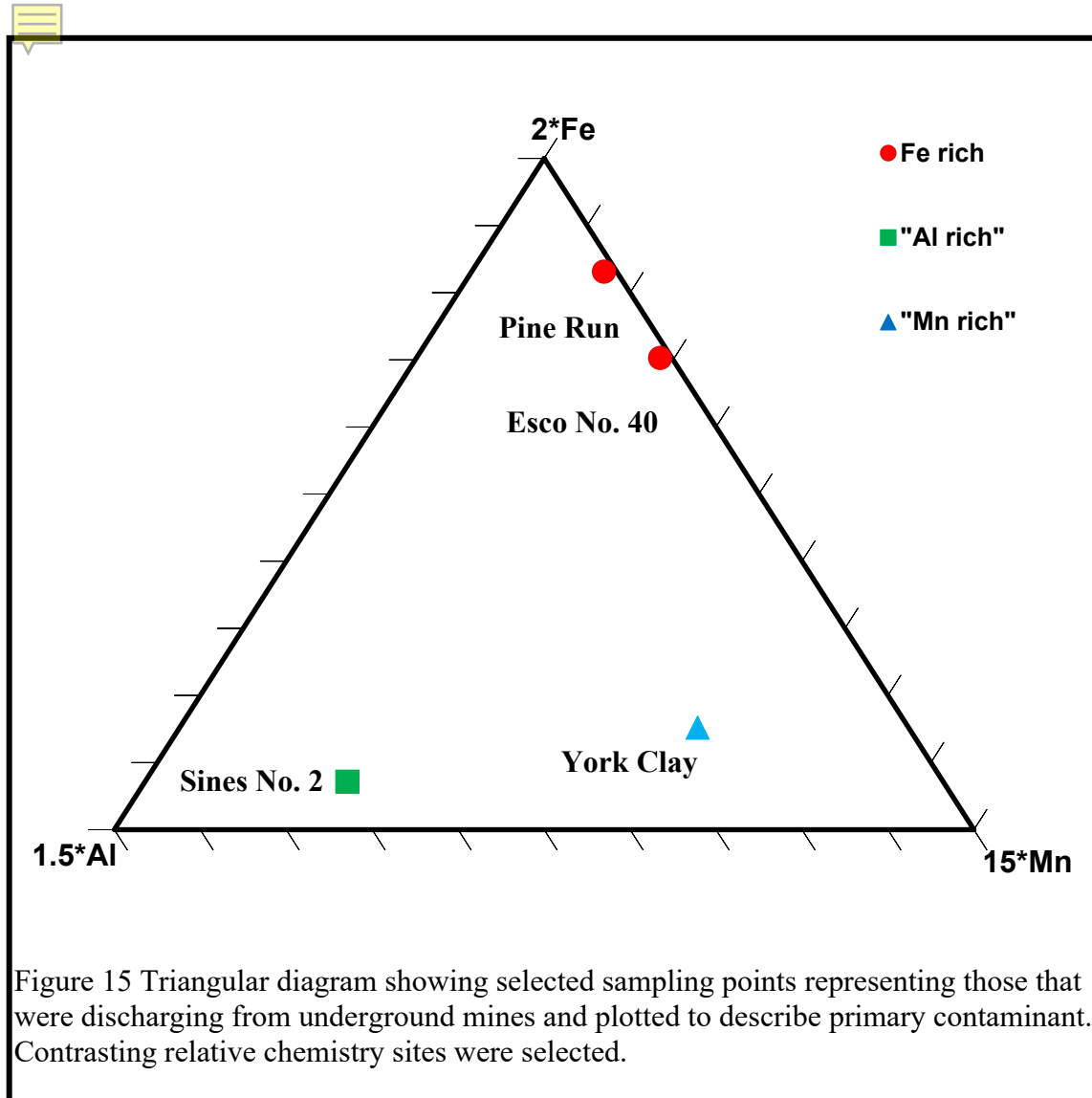


Figure 14 View of selected mine sites and their respective data points within the boundaries of Monday and Sunday Creek watersheds on watersheddata.com. Brown data points are water samples not relevant to this study



3.1 Climate

Southeastern Ohio exhibits climatic variations both daily and seasonally due to its geographic location. These can range from -33.3°C (-27.94°F) in the winter months to 40°C (104°F) in the summer but tends to average in a much more modest range of -5°C (23°F) to 29.4°C (84.92°F). Annual precipitation is on average 99.1 cm (39.02 inches) which mostly occurs during the months of spring and summer (ODNR, 2019).

3.2 Geology

Essex No. 40 coal mine (Essex coal mine), Sines No. 2 coal mine, York Clay and Mining No. 4 coal mine (York Clay mine No. 4), and Sunday Creek No. 9 and 12 coal mine (Pine Run coal mine) are all located within Hocking, Athens, and Perry Counties in Ohio (Figures 16 and 17) along the eastern boundary of the Appalachian Plateau. Each of the mine discharges are south of the Wisconsin glacial advance in regions that are characterized by narrow, steep-sided hills and narrow V-shaped valleys (Sturgeon, 1958). Fluvial and deltaic originating Pennsylvanian aged rocks dominate the area to the east. The rock types that are prevalent in southeastern Ohio are sandstones, fine-grained shales, limestones, clays, and coals.

Each of the discharges examined were the result of abandoned mines that were exploited within the Middle Kittanning (No. 6 seam) coal member as it has been the most economically feasible (Figure 18).

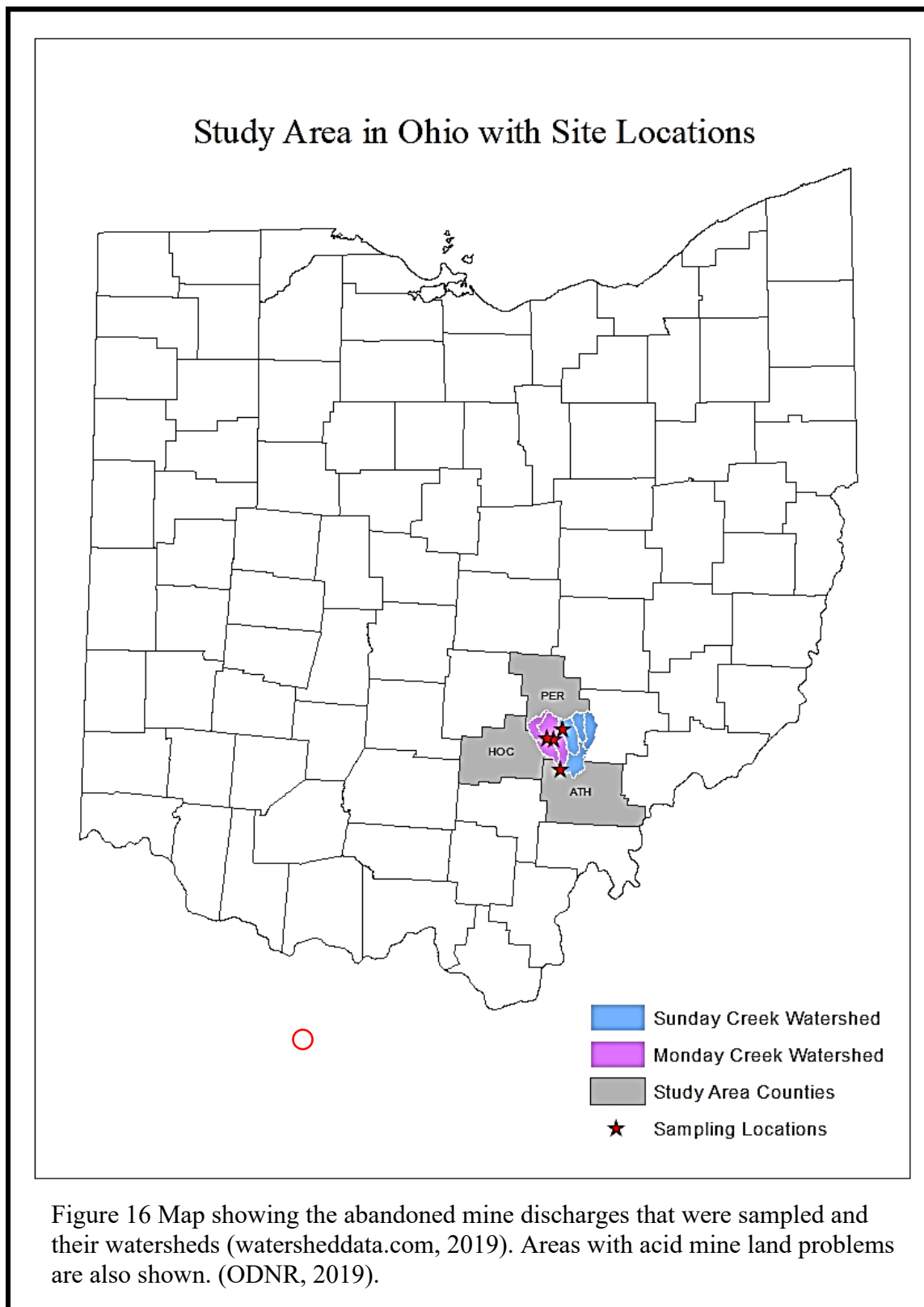
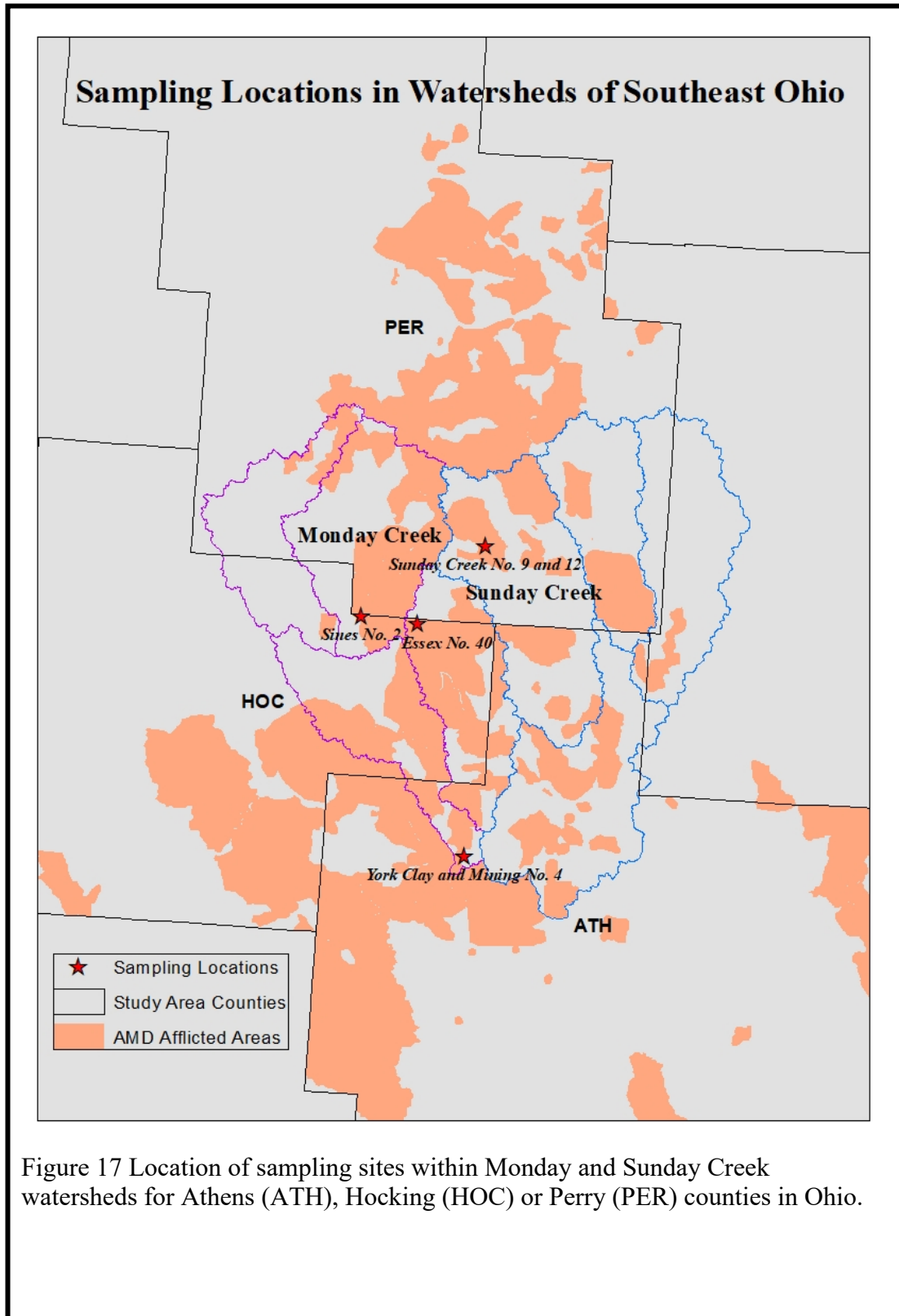


Figure 16 Map showing the abandoned mine discharges that were sampled and their watersheds (watersheddata.com, 2019). Areas with acid mine land problems are also shown. (ODNR, 2019).



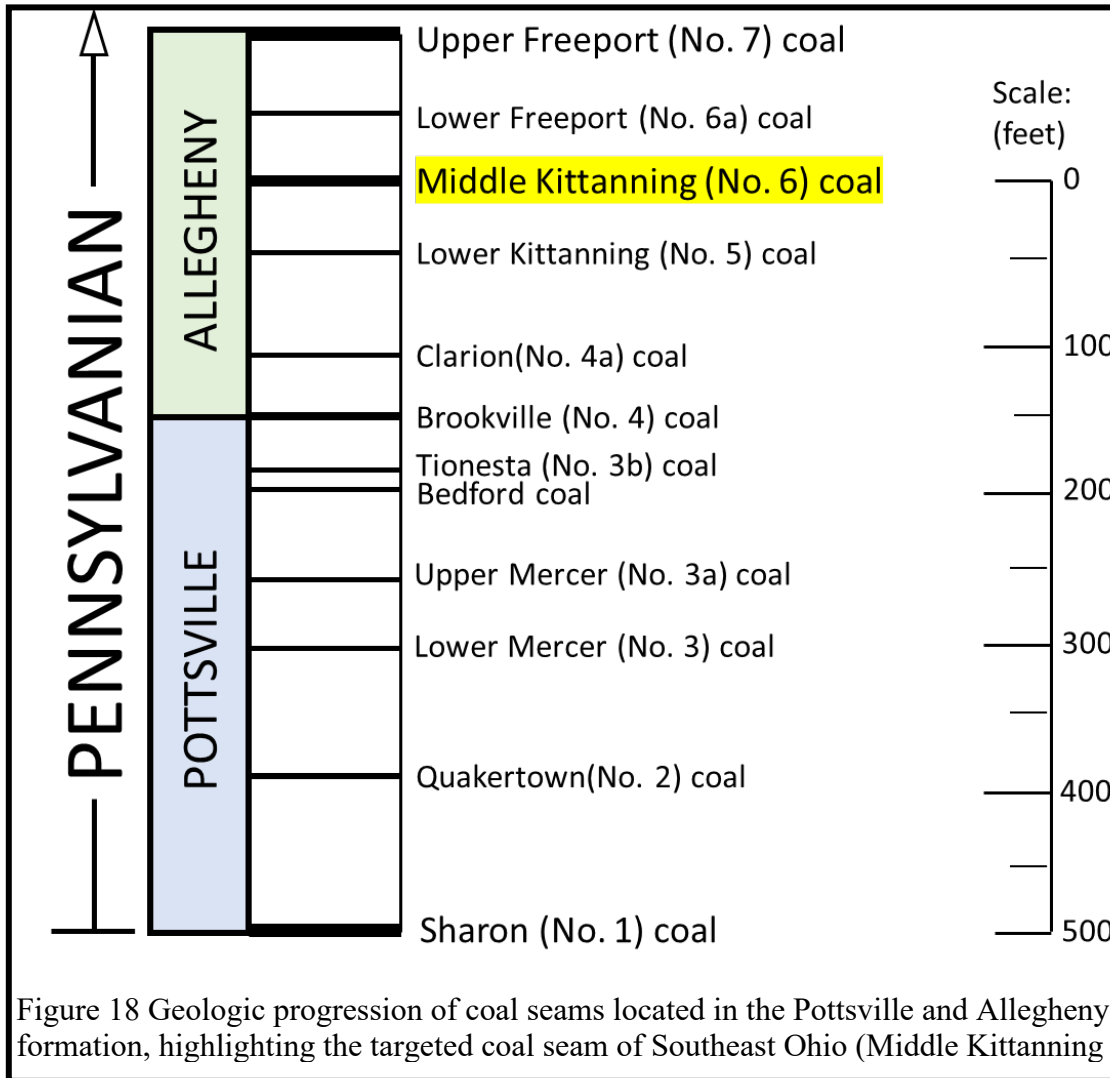


Figure 18 Geologic progression of coal seams located in the Pottsville and Allegheny formation, highlighting the targeted coal seam of Southeast Ohio (Middle Kittanning

The Middle Kittanning cyclothem is of the larger Allegheny Group which contains a number of valuable coal deposits: Upper Freeport, Lower Freeport, Middle Kittanning, and others (Merril, 1948). The Middle Kittanning coal seam was reported by Merrill to be 66” thick on average and contains pyrite as nodules or dissipated particles.

Permeability tends to be low and the rocks tend to be brittle in the Pennsylvanian sandstones which leads to extensive fractures in the rocks. The Monday and Sunday Creek watersheds both exhibit a rapid upper flow regime, that is very responsive to precipitation events, and a steady deep flow regime. This in conjunction with the high overland runoff in the region lead to rapid responses of streams to rainfall (Sturgeon, 1958).

The Middle Kittanning coal (No.6) was named in 1876 by J.P. Lesley and I.C. White from an exposure in Kittanning, Pennsylvania (Figure 19). The Middle Kittanning coal member ranks second in tonnage mined to the Pittsburgh coal and is widely considered the best stratigraphic marker in the Allegheny series (Stout, 1927). The No. 6 coal appears as a banded, bright coal separated into benches from two clay, shale partings that are consistent regardless of thickness. Bright, blocky coal comprises the lower and middle benches of coal, and the upper bench is bright and blocky at the base and gradates into a more shaly coal. Pyrite occurs as disseminated particles and nodules in the upper bench and is less abundant in the lower bench. The Middle Kittanning coal member ranges from 0.61 to 1.5 meters with an average of 0.91 meters thickness (Hall, 1951).

The Middle Kittanning coal lies above the Middle Kittanning clay which contains mica minerals, nodules of pyrite, siderite, a high percentage of carbonaceous material, plant impressions and woody fragments. The Middle Kittanning clays usually are soft and plastic with a dark gray appearance, and when weathered turn porcelain white and greasy and slippery. Overlying the Middle Kittanning coal is a carbonaceous shale which is thinly bedded and contains mica minerals with small bits of enclosed pyrite and is

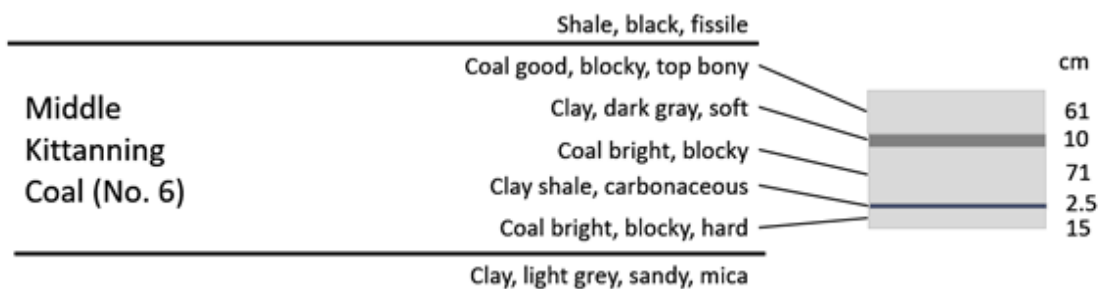


Figure 19 Descriptions of the lithologies found in and directly above and below the Middle Kittanning No. 6 coal seam.

considered continental in origin. This carbonaceous shale is dubbed a “roof shale” and like other roof shales of the Allegheny Formation, this shale grades upward into sandstones or shales of the next cyclothem (Hall, 1951).

CHAPTER 4: METHODOLOGY

4.1 Site Descriptions

Pine Run mine, formally known as Sunday Creek No. 9 and 12 coal mines, is located at 39.60135 latitude, and -82.16651 longitude. Pine Run mine is located roughly 3 miles East of Shawnee in New Lexington, Ohio (Figure 20) and was abandoned in 1910. The opening of the mine is an abandoned drift entry at the coordinates listed (Figure 21). The drainage of Pine Run flows southeast into the west branch of Sunday Creek. The discharge at Pine Run is relatively large in comparison to York Clay coal mine and Sines coal mine. The Pine Run discharge also exhibits a false bottom where iron hydroxide precipitate accumulates in the streambed.

Esco No. 40 coal mine, also referred to in as Essex coal mine, is located at 39.55652 latitude and -82.21528 longitude. The Esco No. 40 mine discharge is located 2.3 miles southeast of New Straitsville via OH-216 (Figure 22) and was abandoned in 1921. The opening is described as an abandoned slope entry at the coordinates listed (Figure 23). Esco No. 40 coal mine extracted the No. 6 coal seam. The drainage from Esco coal mine continues roughly 15 meters into a culvert and reemerges on the southern side of the road for another 15 meters until it mixes with a tributary of the Snow Fork stream, a tributary of Monday Creek. The flow velocity at Esco is relatively large in comparison to York Clay and Sines coal mines. Attempts have been made at remediation at Esco using a doser which has since been uninstalled as well as a limestone channel which has been since armored with Fe mineral precipitates.



Figure 20 Location of Pine Run coal mine with relation to Shawnee, OH.

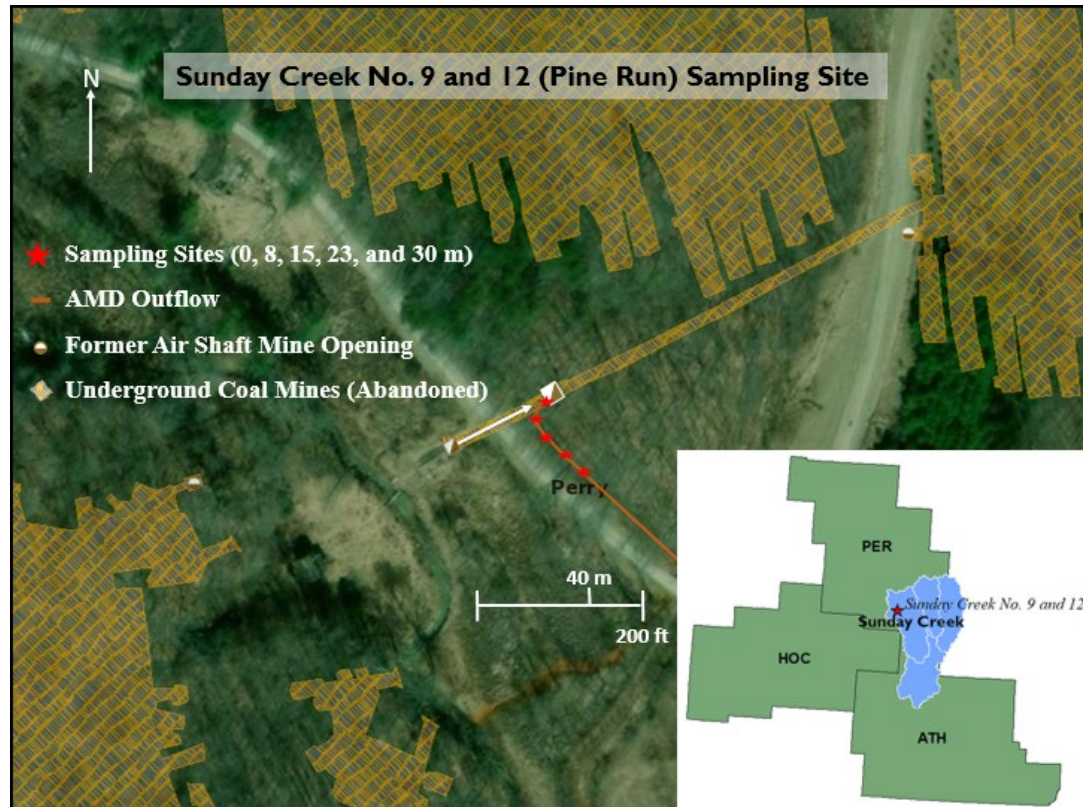
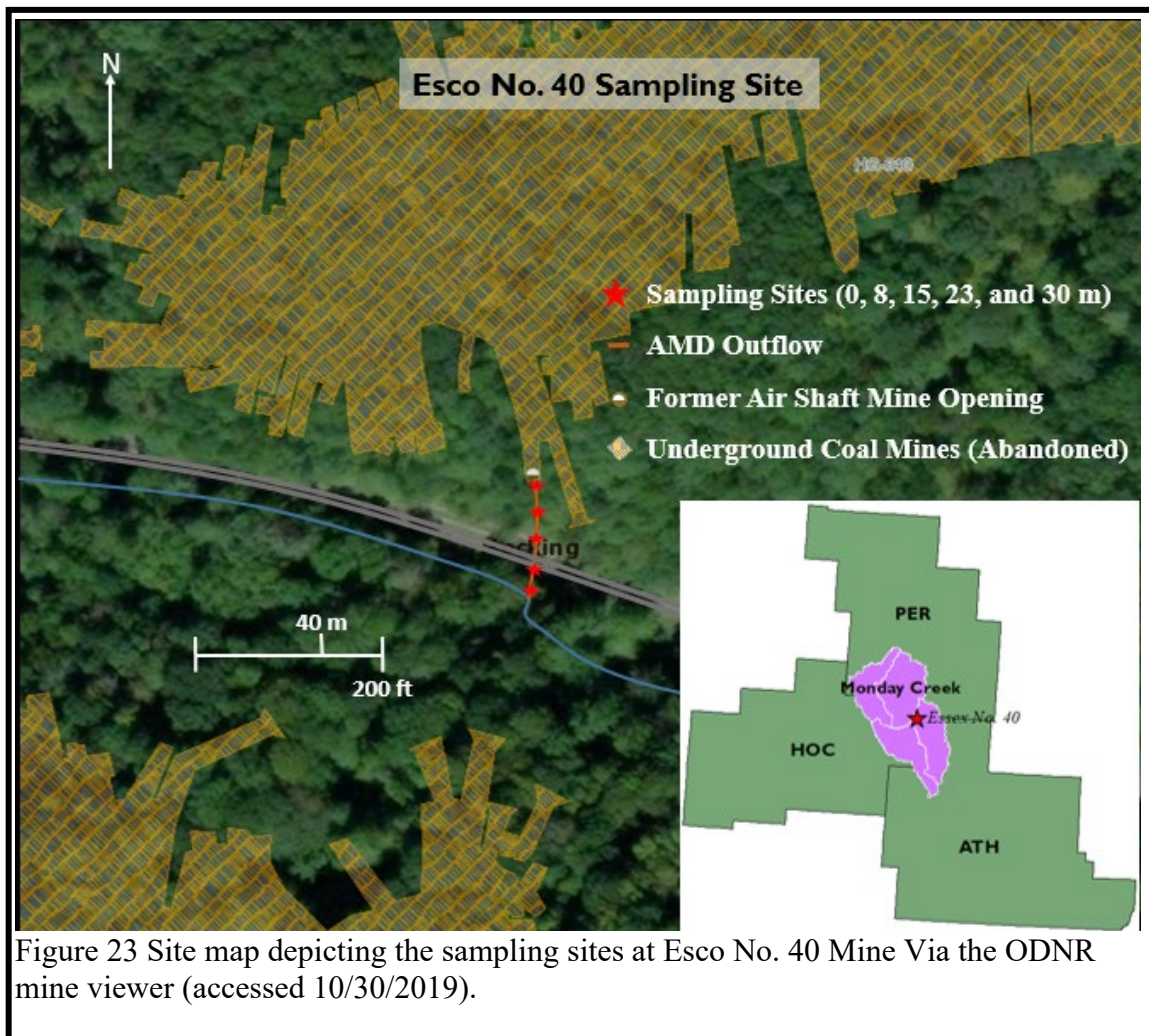


Figure 21 Site map depicting sampling sites at Sunday Creek No. 9 and 12 Mine (Pine Run). This figure was obtained using the ODNR mine viewer (accessed 10/30/2019).





Figure 22 Location of Esco mine in relation to New Straitsville, OH.

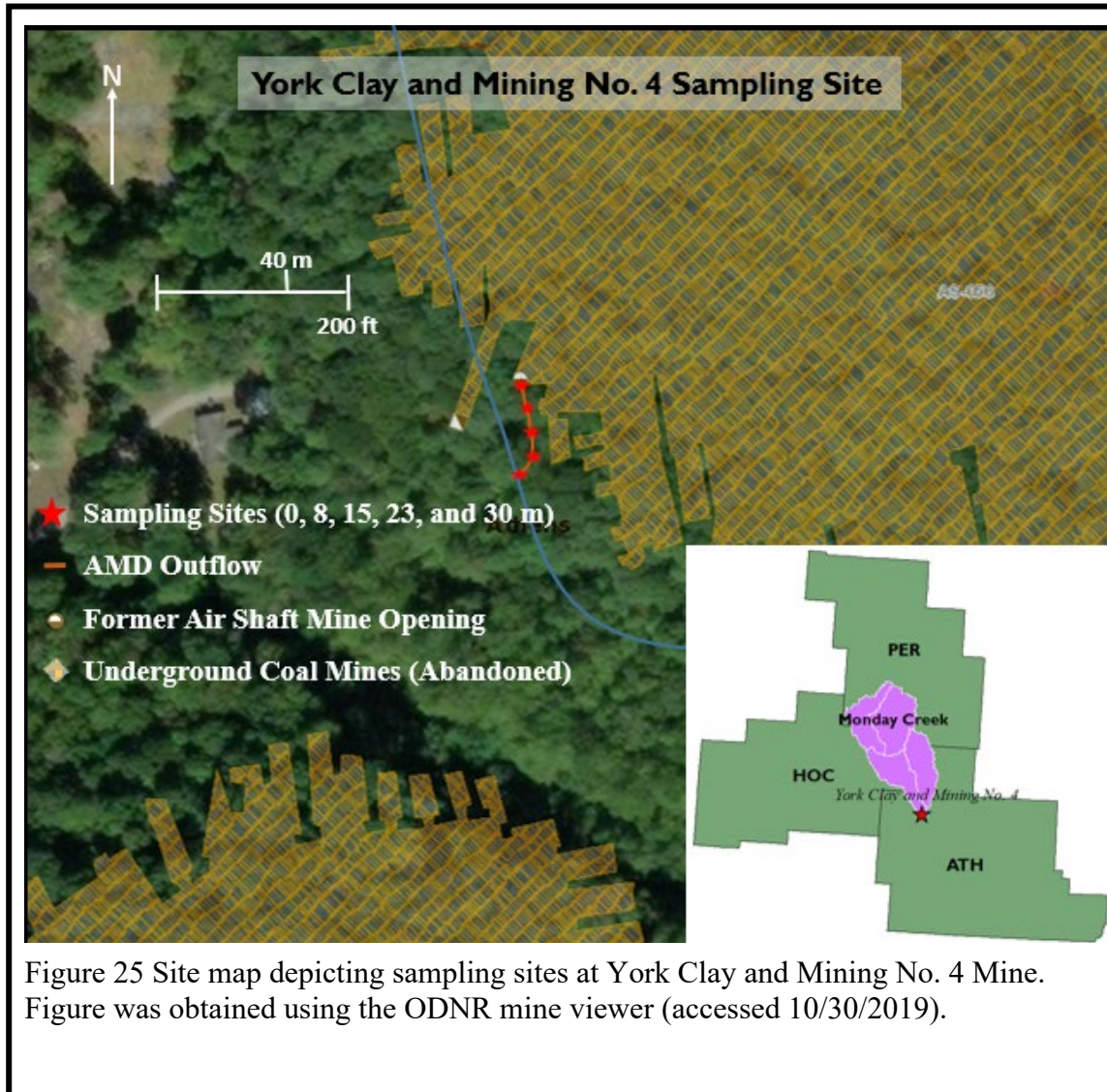


York Clay coal mine, known formally as York Clay and Mining No. 4 coal mine, is located at 39.42430 latitude and -82.18546 longitude. York Clay mine is located in York Township, 3.5 miles southeast of Nelsonville via Old U.S.33 (Figure 24) and was abandoned in 1921. The opening is described as an abandoned mine air shaft opening at the coordinates listed (Figure 25). The York Clay discharge flows roughly 30 meters southerly into a tributary of Monday Creek. Discharge from York Clay is consistently low-flow through each season.

Sines No. 2 coal mine is located at 39.56166 latitude and -82.25397 longitude. Sines coal mine is roughly 2.3 miles Southwest of New Straitsville on OH-595 in Coal Township of Perry County (Figure 26) and was abandoned in 1925. The opening of the mine is marked as an abandoned air shaft located at the coordinates listed (Figure 27). According to the Chief Inspector of Mines to the Governor of the state of Ohio (West Virginia, Public Documents. Vol. 2, 1906) Sines Bros & Co. operated the abandoned coal mine out of New Straitsville. Sines Bros extracted the No. 6 coal seam which was 6 feet in thickness. The Sines discharge continues hundreds of meters southeast into a tributary of Lost Run. Discharge at this site varies widely depending on the mine influx. At the time of sampling the Sines No. 2 discharge experienced extremely low-flow conditions.



Figure 24 Location of York Clay coal mine in relation to Nelsonville, OH.



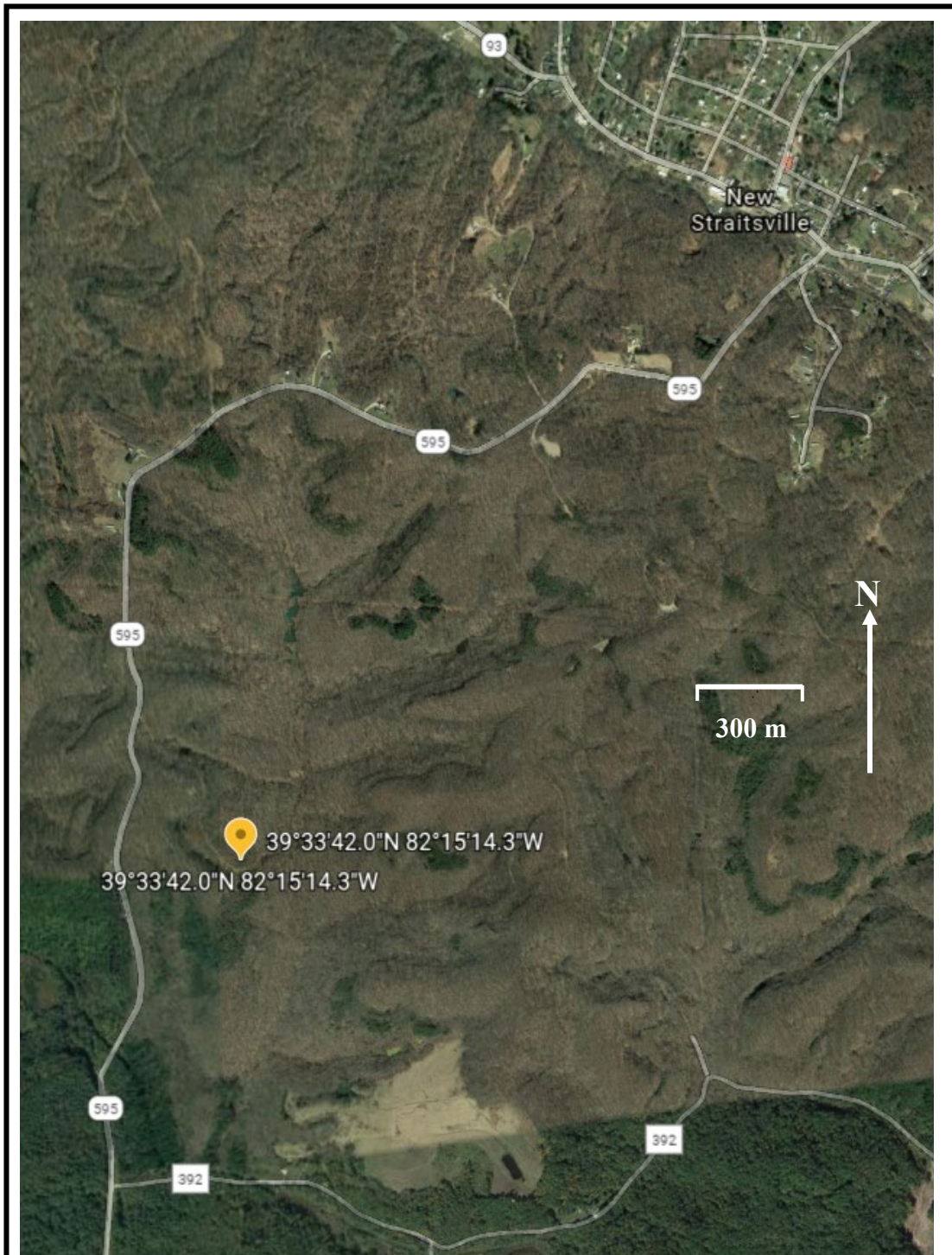
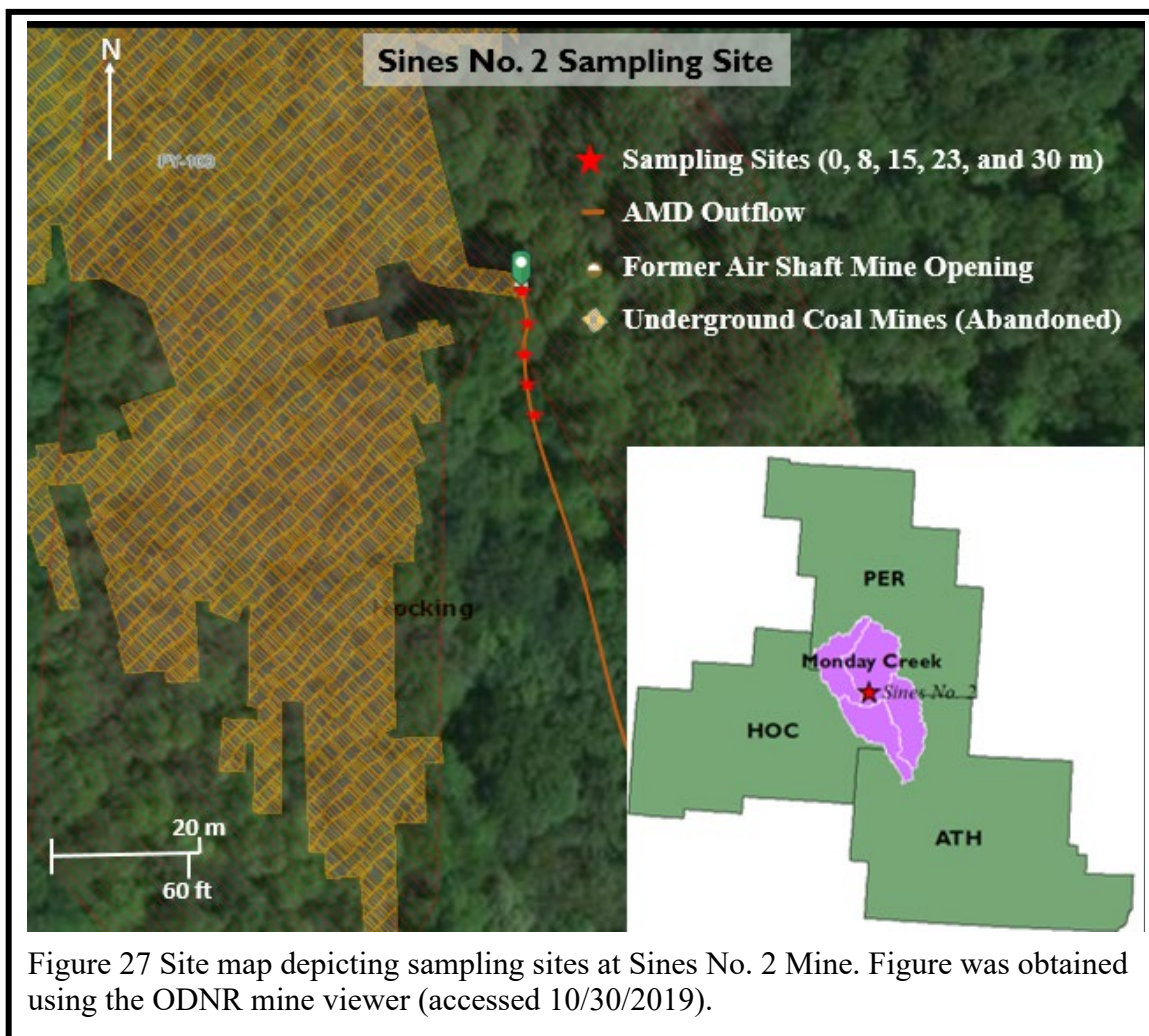


Figure 26 Location of Sines coal mine in relation to New Straitsville, OH.



4.2 Field Work


4.2.1 Field Parameters

Physical factors were recorded utilizing a Myron Ultrameter 6P for determination of temperature, redox potential, total dissolved solids, conductivity, and pH.

Additionally, dissolved oxygen and subsurface temperature was recorded via a YSI 55 dissolved oxygen meter. Stream discharge was calculated through velocity measurements and depth of water at 0.1-meter increments with a wading rod at each site.

Ferrous iron was determined for each site at a location utilizing the 1,10-phenanthroline method (Hach method 8146; HACH Company, 1997) using a battery powered HACH model DR2000 spectrophotometer and 25 mL sample cuvettes. Dilution factors and ferrous iron readings were recorded with ferrous readouts in mg/L. This was done to prevent any conversion of ferrous to ferric iron within the samples as it could happen when they are transported to the laboratory. Preliminary tests were completed in the first sampling event to confirm ferrous iron concentration was too sensitive, and results were more accurate if the tests were performed immediately after sampling at the field site.

Surveying of each stream site took place at the same time as sampling to determine discharge from each mine location. A Marsh McBriney Flo-Mate Model 2000 mounted on a stream depth pole was used to collect water velocities in feet per second and stream depth in centimeters at 0.1-meter increments. Data was then compiled for each site of all four locations and the the area for each cross section of each segment of

the stream was multiplied by the average water velocity, the sum of all the cross sectional areas time velocity was used to determine discharge. 

4.2.2 Water Sampling

Sampling of each location took place between September and October 2019 during low flow to get the most accurate depiction of the influences of AMD. At each location, five predetermined locations were sampled at 25-foot intervals from the mine opening to evaluate changes that occur within the water and sediment. (Figures 4.1-4.4) Acid-washed polypropylene wide-neck 125 mL Nalgene wide neck bottles were utilized for collection of filtered water samples. Water was passed through a 0.45 μm membrane, formerly described by Batley and Gardner (1977) as the soluble fraction of any solution. 0.45 μm filters also retain most phytoplankton and bacteria which is beneficial for preserving the soluble fraction of metals. Samples were preserved for cation analysis through acidifying the water sample with 4 N nitric acid. Another unpreserved sample was collected as is for anions. Bottles were filled to the neck and sealed with a filled cap to minimize the oxygen present within the bottle which might alter the chemistry of the sample. Bottles were placed on ice and transported to the lab immediately.

4.2.3 Sediment Sampling

Sediments were collected with a long corer and stored inside plastic wrap and sterile Ziploc bags. The upper 3-5 cm of sediments were collected at the middle of the channel to account for vertical stratification. Sediment sampling only targeted deposited sediments and ochreous precipitates. In order to reduce the number of samples to analyze, suspended sediments were not analyzed, which was a limitation of

the methodology chosen and will influence any conclusions regarding metal transport. Fixed sediment site collection was chosen to remain consistent with the water and biological analysis. Representative samples were often coincidental as the distance from site to site was short enough to include resolution of the stream profile. This usually included features like stream meanders, culverts, or pool type features. Finer sediments and precipitates were targeted in the bends and channels as these usually were more representative in terms of chemistry with higher metal loads (Herr and Gray, 1997). Sampling distances also accounted for any horizontal stratification that may exist within the sediments or ochreous precipitate. All sediment samples were placed on ice and transported back to the lab immediately.

4.2.4 Biological Sampling

Three biological sampling procedures were used. The autoclaved (sterilized) slide contraptions were placed in the flow of each location and removed at separate intervals (7, 19, and 28 days) which were placed at each site as illustrated in Figure 28. The second procedure involved the same autoclaved wide neck 125 mL Nalgene sampling bottles which contained anion samples for the first sampling event. Any bacteria that may have been suspended in solution were living within the mine waters and could be isolated for colony forming unit analysis and morphological assessment. The final procedure involved the standard sediment sampling procedure utilizing sterile equipment which was later pulverized and washed to remove any microbes that were latched onto the sediments or precipitates. Any samples collected for bacterial analysis were placed on ice immediately, and isolation procedures were performed on return to the



Figure 28 Slide contraptions implemented for collection of selected acidophilic microbial colonization rates at each site for all four mine locations.

lab and bacteria were preserved in 50 mL sterile Falcon Tubes and frozen at -4°C until transported to the sequencing lab.

Out of the three sampling procedures biological sequencing and the plating of microbes on acidic media for cfu analysis were unable to be completed due to the COVID-19 pandemic. Laboratories were not active, and the equipment required for sequencing analysis could not be operated to determine microbial abundance and speciation for water and sediment samples. For this reason, the primary method of biological assessment was through bacterial counts of the bacteria gram stained on the bacterial slide contraptions at 1000x. From the three intervals collected, 7 and 19 days yielded useful bacterial counts that were used primarily for statistical comparison. The 28-day bacterial slides appear to have been accumulated bacteria on the slide, but erosional processes acted on the slides leading to erroneous colonization rate counts.

4.3 Laboratory Work

4.3.1 Cations and Anions Analysis in Water Samples

Water samples were collected and digested per EPA Method 3005A for inductively coupled plasma mass spectrometry (ICP) and cation analysis. These samples were then analyzed by ICP completed by the Instituto Tecnológico y de Energías Renovables, in Tenerife, Canary Islands, Spain. Ion chromatography was used to determine the concentration of the ions F, Br, PO_4 , and SO_4 . Spectrophotometric methods were used in the determination of Cl in water (mercuric thiocyanate method HACH method 8113), NO_3 in water (NitraVer 6 cadmium reduction method HACH method 8192).

4.3.2 Sediment Analysis

Sediments were digested according to EPA method 3050B for ICP analysis.

Organic matter was determined by a modified Loss on Ignition (LOI) procedure 44.3.3 (ASTM D2974 1988) from the Handbook on Reference Methods for Soil Analysis (Carter, 1993) to ash all organic matter. The LOI procedure was modified to 600°C for 16 hours rather than the 400°C at 4 hours as there was still evidence of organics at the claimed temperature at the 4-hour and 16-hour mark. Some of the LOI values were artificially high due to oxidation of sulfur artificially increasing percent mass loss of the sample. This was mitigated through determination of sulfate in the air-dried soils.

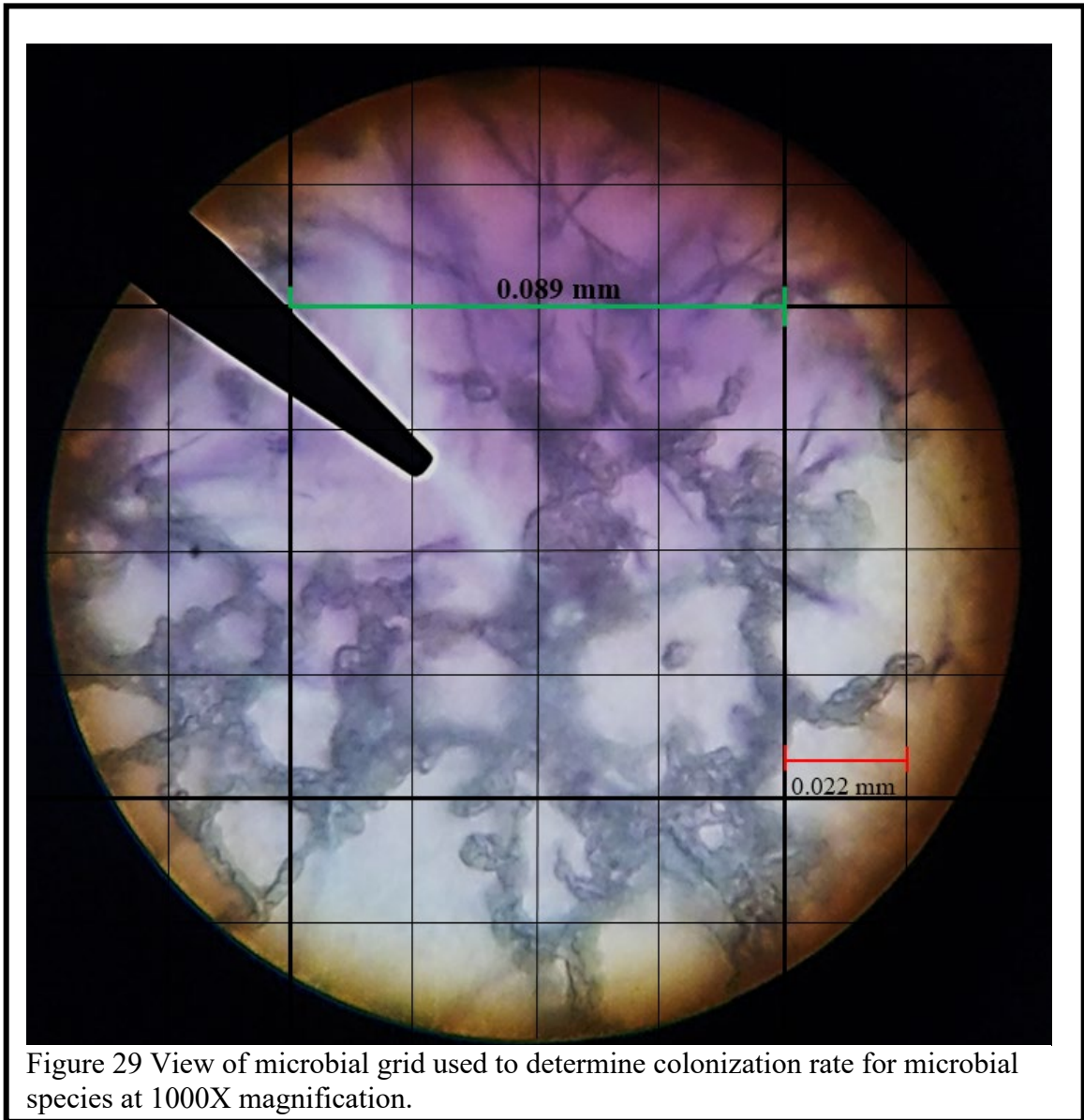
Sulfate content was determined for sediments via a monocalcium phosphate extraction method described by Singh et al. 1997, this requires digesting the sample with an extraction reagent (0.5 M ammonium acetate, 0.25 M acetic acid) and powdered charcoal, then placed on a shaker for approximately 30 - 33 minutes. Grain size analysis was also completed for each site and average grain size was calculated. Loss on ignition analysis was performed on each of the samples three times and percentage lost was recorded indicating a combination of organic matter combustion and oxidation of reduced forms of sulfur in the sediment. Nitrate content was also determined using US EPA Lachat Method 602. Extraction solution ($K_2S_2O_8$ and 3.75 M NaOH) was produced and equipment used was washed with 10% sulfuric acid for removal of residual nitrogen. 50 grams of sample was oven dried for each site at 105°C and subsequently cooled to room temperature. 0.4 grams of oven dried sample is placed in a 60 mL test tube with 1.0 gram of $K_2S_2O_8$, 1.0 mL of 3.75 M NaOH, and 40 mL Di H_2O and the tubes were capped loosely. This

solution was placed in the digester for 45 minutes at 121°C. When the solution was removed and cooled to room temperature, 1.0 mL of 3.75 M NaOH was added and leachate was collected using filter paper. This solution was then analyzed using the USEPA Cadmium Reduction Method which yielded our nitrate content for all of our sediment samples.

4.3.3 Microbial Ecology

Two techniques were used to assess and describe the different types of microbes found in each location. The first methodology used involved collecting three acidophilic target bacterial phyla (section 3.2.1) from substrates accumulated on suspended microscope slides and removed at specified time intervals (7, 19, and 28 days).

Thiobacillus Ferrooxidans was not determined because of the highly populated content in each of the slides, as it was present in all the slides. These microbes were then gram stained and examined under a Bausch and Lomb microscope for classification. Once the species were identified, a grid-counting approach (Figure 29) was used at 1000X oil immersion lens in representative locations on the slide to determine the colonization rates ($1/\text{cm}^2\text{d}$) for *Thiothrix*, *G. ferruginea*, and *L. discophora* (section 2.2.1). It was later determined that the 28 day suspended slide counts would be removed as the data was erroneous, so for the purposes of this study, days 7 and 19 were used in the determination of colonization rate for our acidophilic microbial taxa. Reasoning as to why the data for the 28-day colonization had errors was due to scouring processes occurring on the slides



leading to the substrate disintegrating sometime after the 19-day collection. This likely caused the peripheral and less attached layers of bacteria to become removed along with the substrate. In most cases the 28-day slides yielded decreased colonization which is less indicative of chemical or biological forces and more so an indicator of how flow velocity influences the ability of the observed taxa to occupy substrates suspended in the flow.

The other parameter for examining microbes was a colony forming unit analysis on nutrient agar (Figure 30). Count of bacterial colonies and colony morphology were recorded for each location. It was initially planned to only complete the colony counts on LB nutrient agar however this agar has a neutral pH which is not ideal for acidophilic microbe propagation.

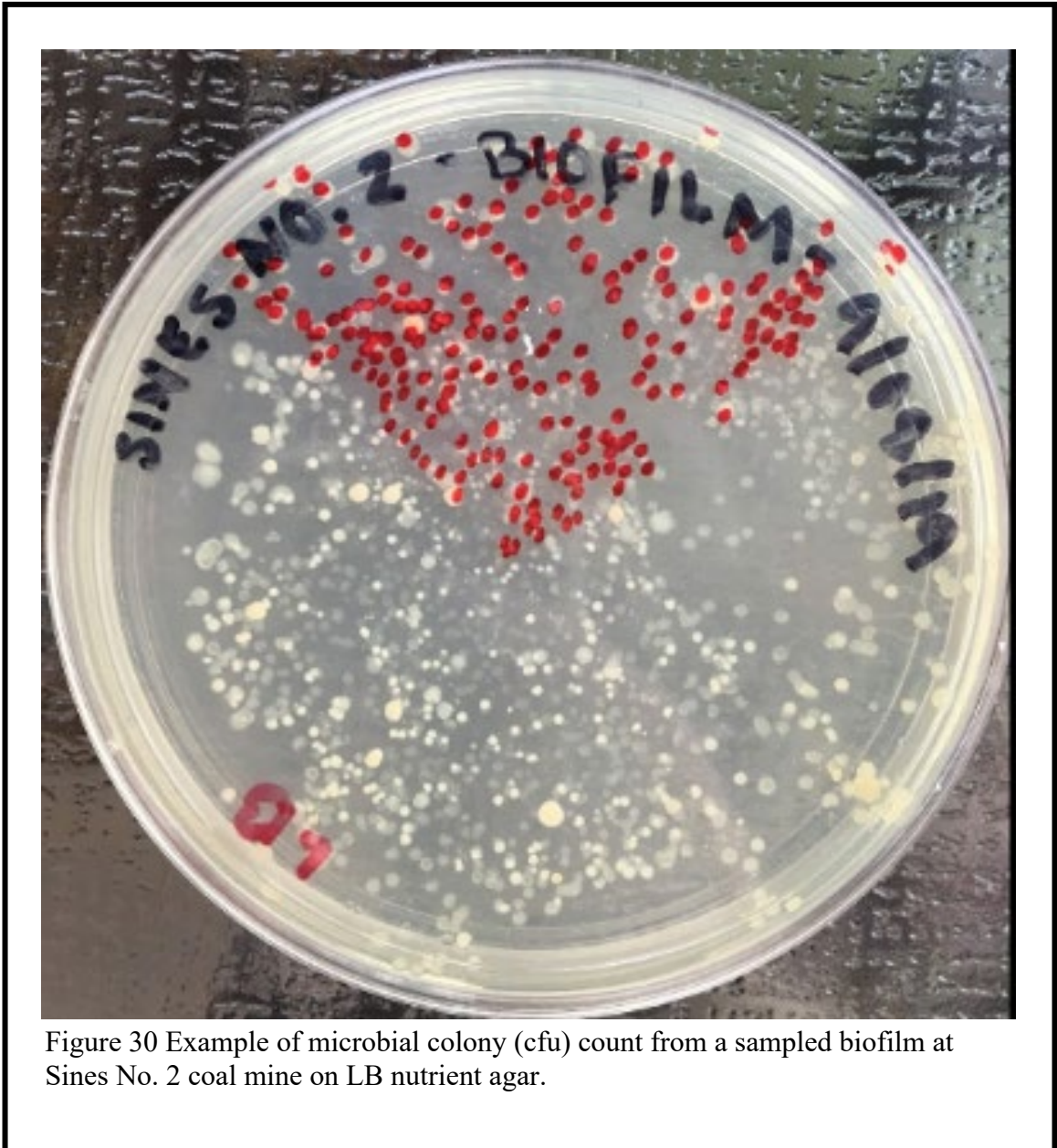



Figure 30 Example of microbial colony (cfu) count from a sampled biofilm at Sines No. 2 coal mine on LB nutrient agar.

4.4 Geochemical Modeling and Statistical Analysis

4.4.1 Simulations in PHREEQCI

Once result of ICP analysis were received, concentrations of major cations and anions were combined with physical conditions for each sample site and a WATEQ4F analysis was completed in PHREEQC. The resulting minerals that existed in saturated and supersaturated states were noted and their saturation indexes were recorded. After confirming said minerals could form under the conditions of AMD waters, a final list of minerals, compounds, and saturation indexes were compiled and compared across sites and mine discharges to determine relationships with chemistry, physics, and microbial presence.

4.4.2 Statistical Analysis

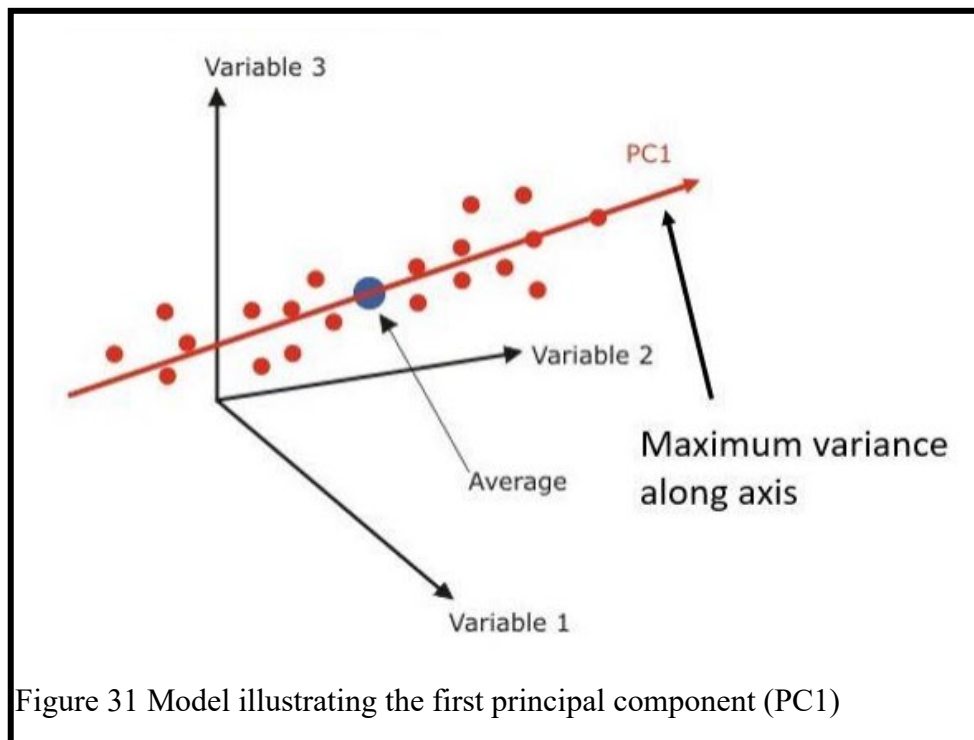
The vast amount of data collected from the combined field work and lab work requires an application of statistics to interpret any hidden patterns and unveil meaningful correlations taking place within the data. For this study we used a combined statistical approach using the Spearman rank correlation matrix (non-parametric statistics) analysis that was done using the program PAST (Hammer and Harper, 2001) and a Principal Component Analysis (PCA) using the program Unscramble (Esbensen et al., 2009). 

Principal Component Analysis

Principal Component Analysis (PCA) simplifies intricate data sets and retains the trends contained within those data sets. This high dimensional data is reduced and summarizes the connections contained within the data. Bilinear modeling is used giving an outline of the information in a multidimensional table. The initial variables are

reduced into a smaller number of latent variables denoted as principal components (PC). This procedure is illustrated in Figure 31. When plotted, these principal components can illustrate similarities, differences, or trends from the initial dataset. PCA reduces surrounding noise of cluttered datasets and strips the larger compilation of data into a more digestible set of principal components. (CAMO Software). In this study the Unscrambler X version 10.5 was used which computes the principal component based on the equation given (Martens and Ni, 1992):

$$X = TP^T + E$$



where T represents the scores matrix, P represents the loadings matrix and E represents the error matrix or residual. Spearman rank correlation (non-parametric statistics) was chosen over Pearson's as it looks for correlations between variables in data sets and is ideal for data sets such as ours with $n < 30$ ($n = 20$). Correlations were restricted to groups as the data set was too large to run as a whole.

CHAPTER 5: RESULTS AND DISCUSSION

5.1 General Presentation of Data

This section lists tables of the general data for all relevant collected data used in the main body of this thesis document. Descriptive statistics for each parameter are presented in each table (average, maximum, minimum, and standard deviation). Empty cells within the table represent samples or values that were unable to be determined. In the ionic concentration tables for both sediment and water and the saturation index table, these absent values are the result of samples that were damaged in transport to the lab where IC and ICPMS analyses were performed (Instituto Tecnológico y de Energías Renovables, in Tenerife, Canary Islands, Spain). Values missing from the colony forming unit (cfu) analysis were a result of cancelled lab procedures due to the SARS-CoV-2 pandemic. Cfu data was to be completed for all sites, however, only three of the data sets were collected prior to quarantine closures of our lab spaces.

In terms of field parameters, the data in Table 2 indicates our four distinct flow regimes. Esco (Essex) represents a high flow velocity site with velocity values ranging from $3.05E^{-2}$ to $3.66E^{-1}$ m/s, Pine represents an intermediate flow velocity with velocities ranging from $3.35E^{-2}$ to $7.01E^{-2}$ m/s, and York Clay and Sines represent low flow velocity systems with velocities ranging from $3.05E^{-3}$ to $9.14E^{-3}$ m/s). In terms of pH, Sines was our most acidic system with pH ranging from 2.3 to 2.35, Pine Rum had pH values ranging from 4.86 to 4.97, Esco had pH values ranging from 5.15 to 5.83, and York Clay was our most non-acidic system with pH values ranging from 6.97 to 7.12.

Table 2 Field parameters for all mine sites on 10/20/2019 (York Clay, Sines, Essex coal mines) and 10/23/2019 (Pine Run coal mine).

	meters	Velocity (m/s)	Conductivity (μ S)	TDS (ppm)	ORP (mV)	pH	Temp ($^{\circ}$ C)	DO (mg/L)
<i>York Clay</i>	0	3.05E-03	310.2	210.0	25.0	7.04	13.2	2.59
<i>York Clay</i>	8	3.05E-03	280.2	181.4	50.0	6.99	13.0	2.34
<i>York Clay</i>	15	6.10E-03	279.6	181.6	81.0	6.97	12.9	2.00
<i>York Clay</i>	23	9.14E-03	270.0	179.9	89.0	6.99	13.0	1.89
<i>York Clay</i>	30	6.10E-03	281.8	184.9	31.0	7.12	13.1	2.76
<i>Sines</i>	0	3.05E-03	2184.0	1609.0	488.0	2.30	15.8	1.08
<i>Sines</i>	8	6.10E-03	1756.0	1269.0	498.0	2.30	15.8	1.28
<i>Sines</i>	15	6.10E-03	1751.0	1266.0	499.0	2.30	15.9	1.30
<i>Sines</i>	23	6.10E-03	1740.0	1258.0	499.0	2.30	16.1	1.36
<i>Sines</i>	30	9.14E-03	1703.0	1229.0	502.0	2.35	16.8	1.29
<i>Essex</i>	0	3.66E-01	830.9	583.7	182.0	5.15	11.8	1.41
<i>Essex</i>	8	2.44E-01	807.7	563.6	174.0	5.37	11.8	1.80
<i>Essex</i>	15	2.13E-01	802.5	563.1	166.0	5.73	11.9	1.90
<i>Essex</i>	23	3.05E-02	805.9	562.2	154.0	5.58	11.9	1.63
<i>Essex</i>	30	2.44E-01	805.4	563.0	147.0	5.83	11.9	1.73
<i>Pine</i>	0	3.35E-02	1214.0	869.5	212.0	4.88	12.0	0.25
<i>Pine</i>	8	3.66E-02	1215.0	870.8	182.0	4.86	12.1	0.33
<i>Pine</i>	15	5.79E-02	1222.0	873.9	184.0	4.87	12.1	0.37
<i>Pine</i>	23	7.01E-02	1219.0	875.5	179.0	4.97	12.1	0.44
<i>Pine</i>	30	5.49E-02	1221.0	872.6	176.0	4.95	12.1	0.65
	MIN	3.05E-03	270.0	179.9	25.0	2.30	11.8	0.25
	MAX	3.66E-01	2184.0	1609.0	502.0	7.12	16.8	2.76
	MEAN	7.04E-02	1035.0	738.3	225.9	4.94	13.3	1.42
	SD	1.06E-01	586.5	434.3	169.4	1.75	1.7	0.74

The two most acidic systems Sines and Pine Run exhibited the largest conductivity and total dissolved solid (TDS) values. Temperature values for each site indicate Esco and Pine Run contain the coldest discharges, and York Clay and Sines discharges have slightly more equilibrated temperatures. In terms of dissolved oxygen (DO), Pine Run, Esco, and Sines all exhibited increases in DO after exiting the mine opening with Pine Run containing the most oxygen depleted waters.

Water ion concentration data and procedures used are outlined in Table 3. One of the most notable takeaways from this data is the concentrations of primary contaminants. Ionic concentration can often be an indication of which ions are leaching into the water column from the adjacent lithologies within the mine, and this table demonstrates that Fe, Al, Mn, and SO₄ are abundant in the discharge for each of our sites. The only thing changing for each mine is the proportion of these primary contaminants in the dissolved phase. From this we can confirm that Pine Run and Esco are dominated by Fe, Sines contains a large proportion of Al, and York Clay contains a proportionally large amount of Mn content. Presence of other ionic species such as Mg and Si could indicate that the clay minerals or shales from adjacent lithologies containing Al, Mg, and Si are leaching into our mine discharge and are present in elevated concentrations within the initial 30 meters.

Sediment ionic concentrations and procedures used are presented in Table 4. This data suggests Sines, our most acidic mine, contains the largest concentrations of Fe, Esco sediments contained the most consistently high concentrations of Al, and York Clay contained the largest values for Mn in the sediment. All of our selected mines contained

Table 3 Chemical composition for analyzed waters (mg/L) using ion chromatography (IC) and inductively coupled plasma mass spectrometry (ICPMS), and UV-VIS spectrophotometry for all mine sites on 10/20/2019 (York Clay, Sines, Essex coal mines) and 10/23/2019 (Pine Run). *= ICPMS. **= ion chromatography, ***=UV-VIS

		*Fe in water	***Fe2+ in water	*Al in water	*Mn in water	**SO4 in	**NO3 in	*Ca in water	*Mg in water	*Si in water	*Na in water	**K in water	*Ni in water	*Zn in water	*Cu in water	*Co in water	*Li in water	*NH4 in
	meters	mg/L	mg/L	mg/L	mg/L	mg/L	mg/L	mg/L	mg/L	mg/L	mg/L	mg/L	mg/L	mg/L	mg/L	mg/L	mg/L	mg/L
York Clay	0	6.22	0.04	3.99	0.80	502.27	0.29	81.65	29.09	12.77	39.51	9.65	0.031	0.084	0.010	0.014	0.050	1.240
York Clay	8	5.59	0.09	10.35	2.00	496.76	0.15	90.71	30.16	13.53	42.00	8.75	0.036	0.100	0.007	0.017	0.053	1.625
York Clay	15	2.32	0.04	7.19	2.60	498.51	0.17	85.35	29.83	13.65	42.09	9.62	0.043	0.132	0.018	0.022	0.059	1.450
York Clay	23	1.21	0.04	8.38	1.00	495.30	0.18	95.29	31.56	16.43	64.51	12.17	0.053	0.178	0.018	0.032	0.064	1.751
York Clay	30	1.85	0.01	7.16	2.70	493.57	0.15	87.23	29.53	13.98	39.72	13.57	0.036	0.161	0.002	0.024	0.060	1.720
Sines	0	5.10	0.03	50.80	4.20	762.78	0.76	61.14	70.45	71.83	59.87	7.27	0.388	0.702	0.038	0.248	0.217	1.175
Sines	8	3.84	0.01	50.41	1.50	760.60	0.36	62.62	66.44	70.57	54.85	5.98	0.389	0.619	0.024	0.250	0.221	0.988
Sines	15	3.55	0.03	48.92	1.40	757.73	0.60	61.70	67.75	72.63	57.14	5.21	0.385	0.606	0.028	0.249	0.224	0.631
Sines	23	3.41	0.01	48.78	0.60	758.96	0.70	61.48	66.16	81.85	54.06	6.95	0.386	0.637	0.028	0.249	0.223	0.550
Sines	30	3.16	0.04	48.12	0.70	752.68	0.72	66.33	68.38	81.00	59.65	5.47	0.397	0.198	0.029	0.254	0.234	1.009
Essex	0		21.25	0.51	0.40	280.00	0.03											
Essex	8	21.60	15.00	0.41	2.20	363.45	0.04	69.35	40.03	9.75	29.00	6.00	0.053	0.158	0.007	0.026	0.081	0.487
Essex	15	22.00	20.75	1.08	0.60	389.54	0.08	70.47	41.01	12.37	29.10	6.50	0.051	0.143	0.007	0.026	0.079	0.838
Essex	23	34.40	0.75	0.51	2.60	372.69	0.18	67.31	39.13	12.00	29.67	5.46	0.052	0.185	0.007	0.026	0.077	0.766
Essex	30	29.40	12.25	0.47	0.40	315.04	0.24	68.88	40.13	11.09	27.86	5.07	0.052	0.153	0.001	0.026	0.079	0.615
Pine	0	59.40	22.50	0.69	1.00	518.40	0.04	96.81	48.16		96.51	10.85					<0.01	2.288
Pine	8	30.60	31.50	0.48	0.90	441.04	0.03	78.70	41.37		87.33	5.94					<0.01	3.588
Pine	15	34.62	23.25	0.21	1.20	682.18	0.01	109.43	28.85	10.18	151.16	7.21	0.100	2.605	0.114	0.046	0.029	2.061
Pine	23	18.06	25.75	0.80	0.60	682.85	0.01	89.91	40.86	7.67	106.96	7.51	0.060	0.118	0.007	0.041	0.022	1.209
Pine	30	35.56	31.25	2.00	0.70	644.67	0.02	92.26	41.50	16.37	162.46	9.42	0.067	0.150	0.029	0.042	0.023	1.148
	MIN	1.21	0.01	0.21	0.40	280.00	0.01	61.14	28.85	7.67	27.86	5.07	0.031	0.084	0.001	0.014	0.022	0.487
	MAX	59.40	31.50	50.80	4.20	762.78	0.76	109.43	70.45	81.85	162.46	13.57	0.397	2.605	0.114	0.254	0.234	3.588
	MEAN	16.94	10.23	14.56	1.41	548.45	0.24	78.77	44.76	31.04	64.92	7.82	0.152	0.408	0.022	0.094	0.106	1.323
	SD	16.59	12.23	20.87	1.01	163.59	0.25	14.56	15.19	29.83	39.49	2.47	0.159	0.606	0.026	0.104	0.081	0.751

Table 3 cont.

		**F in water	**Br in water	*Be in water	*B in water	*Ti in water	*Ga in water	*Ge in water	*As in water	*Rb in water	*Sr in water	*Cd in water	*Cs in water	*Ba in water	*Pb in water
	meters	mg/L	mg/L	mg/L	mg/L	mg/L	mg/L	mg/L	mg/L	mg/L	mg/L	mg/L	mg/L	mg/L	mg/L
York Clay	0	0.118	<0.06	0.003	1.470	0.169		1.50E-03		1.70E-02	3.99E-01	7.63E-03		2.91E-02	1.78E-03
York Clay	8	0.139	<0.06	0.004	1.355	0.193	1.40E-03	2.51E-03		1.77E-02	4.17E-01	4.60E-03		3.27E-02	3.72E-03
York Clay	15	0.146	0.064	0.005	1.440	0.182	2.26E-03	4.18E-03	1.12E-03	1.83E-02	4.17E-01	3.04E-03	1.01E-03	4.36E-02	5.64E-03
York Clay	23	0.165	<0.06	0.006	1.420	0.188	2.86E-03	5.21E-03	1.20E-03	1.88E-02	4.18E-01	2.78E-01	1.80E-03	5.01E-02	6.25E-03
York Clay	30	0.146	<0.06	0.005	1.329	0.192	2.16E-03	3.96E-03	1.06E-03	1.81E-02	4.24E-01	2.42E-03		4.87E-02	4.87E-03
Sines	0	0.865	<0.06	0.022	1.240	0.132	6.97E-03	1.25E-02	3.15E-03	1.08E-02	2.26E-01	1.23E-02	1.03E-03	2.51E-02	5.28E-03
Sines	8	0.880	<0.06	0.021	1.270	0.133	7.20E-03	1.33E-02	3.19E-03	1.08E-02	2.27E-01	1.84E-02		2.62E-02	4.81E-03
Sines	15	0.862	<0.06	0.020	1.283	0.133	7.21E-03	1.33E-02	3.22E-03	1.05E-02	2.25E-01	9.06E-02	1.78E-03	2.69E-02	4.94E-03
Sines	23	0.892	<0.06	0.022	1.253	0.133	7.29E-03	1.33E-02	3.26E-03	1.05E-02	2.27E-01	1.17E-02		3.00E-02	4.30E-03
Sines	30	0.869	<0.06	0.022	1.072	0.146	7.43E-03	1.35E-02	3.31E-03	1.07E-02	2.37E-01	6.37E-03	1.55E-03	2.78E-02	5.25E-03
Essex	0														
Essex	8	0.181	<0.06	0.002	1.211	0.148				7.98E-03	5.02E-01	5.40E-03		1.45E-02	
Essex	15	0.171	<0.06	0.003	1.529	0.224	1.73E-03	2.18E-03	4.01E-03	8.65E-03	5.09E-01	4.61E-03		2.62E-02	
Essex	23	0.175	<0.06	0.002	1.174	0.145				7.73E-03	4.90E-01	9.59E-03		1.36E-02	
Essex	30	0.168	<0.06		1.120	0.148				7.61E-03	4.94E-01	2.14E-02		1.25E-02	
Pine	0	0.054	0.195												
Pine	8	0.049	0.201												
Pine	15	1.606	1.264		2.008	0.357	2.32E-02	9.36E-02	3.19E-01	2.46E-02	5.59E-01	4.34E-02	5.01E-02	1.06E-01	5.89E-01
Pine	23	0.059	0.200		1.744	0.173				1.69E-02	6.65E-01	2.28E-03	1.74E-03	1.13E-02	
Pine	30	0.093	0.157		1.675	0.182		1.12E-03		1.81E-02	6.82E-01	4.08E-03	1.21E-02	1.71E-02	4.30E-03
	MIN	0.049	0.064	0.002	1.072	0.132	1.40E-03	1.12E-03	1.06E-03	7.61E-03	2.25E-01	2.28E-03	1.01E-03	1.13E-02	1.78E-03
	MAX	1.606	1.264	0.022	2.008	0.357	2.32E-02	9.36E-02	3.19E-01	2.46E-02	6.82E-01	2.78E-01	5.01E-02	1.06E-01	5.89E-01
	MEAN	0.402	0.347	0.010	1.388	0.175	6.34E-03	1.39E-02	3.43E-02	1.38E-02	4.19E-01	3.09E-02	8.89E-03	3.18E-02	5.33E-02
	SD	0.445	0.452	0.009	0.243	0.054	6.16E-03	2.45E-02	1.00E-01	5.12E-03	1.49E-01	6.73E-02	1.71E-02	2.23E-02	1.69E-01

Table 4 Sediment chemistry data (mg/L) via ion chromatography (IC), inductively coupled plasma mass spectrometry (ICPMS) and UV-VIS spectrophotometry for all mine sites on 10/20/2019 (York Clay, Sines, Essex coal mines) and 10/23/2019 (Pine Run coal mine). *= ICPMS. **= ion chromatography, ***=UV-VIS spectrophotometry.

		*Fe in sed	*Al in sed	*Mn in sed	***SO4 in sed	***NO3 in sed	*Ca in sed	*Mg in sed	*Si in sed	*Na in sed	*K in sed	*Ni in sed	*Zn in sed	*Cu in sed	*Li in sed	*Be in sed	*B in sed
	meters	mg/kg	mg/kg	mg/kg	mg/kg	mg/kg	mg/kg	mg/kg	mg/kg	mg/kg	mg/kg	mg/kg	mg/kg	mg/kg	mg/kg	mg/kg	mg/kg
York Clay	0	4271.93	2220.71	143.60	1500.00	2.50	55.86	297.34	80.54	384.43	256.22	4.96	20.75	9.75	3.50	0.21	16.16
York Clay	8	4435.16	1732.90	132.98	1520.00	2.30	48.67	319.88	101.21	186.07	246.77	4.85	12.24	2.83	3.45	0.19	15.89
York Clay	15	4732.69	1645.65	115.04	580.00	2.30	50.63	285.75	71.40	141.82	246.77	4.75	11.15	2.86	3.06	0.23	16.10
York Clay	23	3901.06	2182.97	99.81	270.00	2.00	58.63	301.29	68.70	100.85	242.26	5.69	13.11	4.11	9.43	0.29	16.55
York Clay	30	5551.05	2649.32	68.01	370.00	2.10	59.63	423.55	108.79	384.43	343.26	5.70	13.98	3.77	5.57	0.26	15.54
Sines	0	8279.98	1763.56	47.58	2010.00	1.70	25.37	199.75	102.78	262.71	296.74	3.08	23.39	7.00	3.42	0.18	16.08
Sines	8	11085.20	1297.33	57.23	3590.00	3.20	7.81	197.64	93.61	112.57	217.29	3.27	11.92	3.18	2.45	0.12	14.91
Sines	15	7650.34	1101.74	52.64	570.00	2.10	9.07	194.43	72.87	142.17	180.04	3.09	12.03	3.37	2.21	0.13	16.15
Sines	23	11684.90	1268.22	62.73	4220.00	3.10	13.45	227.44	68.42	309.38	212.40	3.52	13.63	5.01	2.91	0.22	15.06
Sines	30	7366.38	1133.40	50.73	1540.00	2.70	10.42	176.03	57.18	176.65	182.84	3.24	10.03	3.24	2.11	0.11	14.05
Essex	0	38517.98	9089.70	1.50	33520.00	4.70	102.52	21.36	89.42	214.66	31.07	0.37	50.06	0.41	0.12	3.89	17.06
Essex	8				29200.00	3.10											
Essex	15	22576.67	6280.40	77.90	31990.00	2.60	139.65	96.28	54.14	2252.98	116.00	1.67	44.19	2.12	0.52	3.14	16.95
Essex	23	53041.00	6661.76	64.00	37080.00	3.90	111.65	37.96	97.34	1701.47	40.20	0.86	95.07	0.39	0.24	3.88	16.62
Essex	30	27769.10	6930.34	196.05	25050.00	3.10	95.40	85.75	188.69	690.77	82.14	2.40	65.47	0.97	1.94	3.49	16.18
Pine	0		260.51	20.08	5582.00	2.70	134.17	366.75	104.37	53.99	212.10	7.17	100.83	4.15	4.24	0.47	16.75
Pine	8	70293.49	3823.62	15.95	50690.00	4.00	147.95	117.19	95.10	134.74	102.08	3.49	113.26	4.02	1.64	1.01	17.89
Pine	15	60801.50	15898.77	15.21	59510.00	3.30	136.31	136.38	193.62	90.10	143.78	2.86	8.05	3.66	1.68	0.62	16.05
Pine	23	81864.46	1227.57	17.35	70210.00	2.90	226.10	105.97	85.47	158.68	145.39	2.28	102.30	1.41	1.04	0.35	18.13
Pine	30	81396.12	1059.11	14.50	77350.00	3.70	154.54	112.26	170.32	136.80	197.47	1.88	98.63	2.31	1.48	0.11	16.38
	MIN	3901.06	260.51	1.50	270.00	1.700	7.806	21.356	54.143	53.988	31.066	0.371	8.053	0.390	0.123	0.110	14.055
	MAX	81864.46	15898.77	196.05	77350.00	4.700	226.100	423.552	193.619	2252.975	343.255	7.171	113.257	9.747	9.425	3.894	18.132
	MEAN	28067.72	3590.93	65.94	21817.60	2.900	83.569	194.894	100.210	401.855	183.938	3.428	43.163	3.398	2.685	0.995	16.237
	SD	28604.50	3879.36	51.82	25730.33	0.762	61.682	112.923	40.771	581.581	83.782	1.745	39.320	2.223	2.145	1.406	0.962

Table 4 cont.

		*Ti in sed	*V in sed	*Cr in sed	*Ga in sed	*Ge in sed	*As in sed	*Rb in sed	*Sr in sed	*Zr in sed	*Mo in sed	*Ag in sed	*Cd in sed	*Cs in sed	*Ba in sed	*Pb in sed	*Bi in sed
	meters	mg/kg	mg/kg	mg/kg	mg/kg	mg/kg	mg/kg	mg/kg	mg/kg	mg/kg	mg/kg	mg/kg	mg/kg	mg/kg	mg/kg	mg/kg	mg/kg
York Clay	0	3.89	4.75	3.60	1.19	0.69	1.68	3.20	7.50	1.53	0.12	0.04	0.21	0.27	22.69	3.16	0.03
York Clay	8	3.20	4.55	3.36	1.04	0.57	1.90	2.90	4.47	1.45	0.15	0.04	0.18	0.25	18.64	2.35	0.02
York Clay	15	3.92	4.51	3.32	1.14	0.71	2.51	2.95	6.28	1.53	0.17	0.03	0.08	0.26	17.44	2.86	0.03
York Clay	23	4.71	4.33	3.35	1.26	0.97	1.67	3.29	7.14	1.20	0.13	0.02	0.08	0.31	17.34	2.88	0.03
York Clay	30	4.29	5.26	3.85	1.45	0.87	1.83	4.35	6.49	1.82	0.15	0.03	0.10	0.40	24.32	3.10	0.03
Sines	0	1.89	4.40	3.69	1.24	0.67	2.45	3.31	2.48	2.03	0.23	0.04	0.22	0.58	7.63	2.15	0.03
Sines	8	2.87	4.10	3.31	1.09	0.55	1.81	2.50	2.27	1.89	0.21	0.14	0.06	0.27	6.09	1.66	0.03
Sines	15	4.62	3.71	3.12	1.04	0.52	1.74	2.38	2.13	1.78	0.22	0.03	0.08	0.26	6.63	1.69	0.02
Sines	23	3.20	4.76	3.72	1.34	0.67	3.17	3.10	2.24	2.10	0.28	0.02	0.11	0.37	5.84	1.84	0.03
Sines	30	3.37	3.15	3.60	0.98	0.46	1.44	2.28	2.13	1.56	0.17	0.09	0.19	0.29	6.05	1.75	0.03
Essex	0	2.47	4.04	2.05	0.36	2.73	8.29	0.06	1.66	0.10	0.44		0.25	0.17	0.55	14.58	
Essex	8																
Essex	15	3.96	1.72	2.14	0.32	1.77	7.08	0.19	2.35	0.09	0.27	0.05	0.42	1.32	3.16	9.06	
Essex	23	4.46	2.30	2.09	0.37	3.61	11.19	0.19	2.25	0.13	0.29		0.45	0.09	26.31	18.36	
Essex	30	3.82	2.95	2.19	0.69	2.01	7.50	1.34	2.21	0.58	0.28		0.18	0.19	3.39	14.92	
Pine	0	9.28	3.40	3.35	1.19	1.15	1.95	3.55	3.70	1.56	0.29	0.02	0.38	0.52	9.31	21.63	0.03
Pine	8	6.75	2.33	3.66	0.56	3.83	2.15	1.91	4.19	0.67	0.13	0.01	0.21	0.32	8.76	23.48	0.01
Pine	15	8.16	2.82	3.64	0.71	2.49	1.45	2.55	3.87	0.87	0.16	0.02	0.24	0.45	12.00	20.75	0.01
Pine	23	4.36	2.04	2.17	0.37	4.28	1.58	1.50	2.45	0.67	0.13	0.01	0.18	0.26	33.15	21.59	
Pine	30	9.69	2.26	2.35	0.83	2.36	1.19	3.66	3.86	1.00	0.19	0.02	0.20	0.54	24.34	25.69	0.02
	MIN	1.893	1.717	2.051	3.23E-01	4.65E-01	1.19E+00	6.20E-02	1.66E+00	8.97E-02	1.21E-01	1.45E-02	5.83E-02	8.98E-02	5.46E-01	1.66E+00	1.07E-02
	MAX	9.686	5.261	3.854	1.45E+00	4.28E+00	1.12E+01	4.35E+00	7.50E+00	2.10E+00	4.36E-01	1.37E-01	4.46E-01	1.32E+00	3.32E+01	2.57E+01	3.37E-02
	MEAN	4.678	3.548	3.082	9.04E-01	1.63E+00	3.29E+00	2.38E+00	3.67E+00	1.19E+00	2.11E-01	3.73E-02	2.01E-01	3.74E-01	1.33E+01	1.02E+01	2.61E-02
	SD	2.204	1.083	0.666	3.69E-01	1.25E+00	2.91E+00	1.24E+00	1.89E+00	6.63E-01	8.08E-02	3.28E-02	1.13E-01	2.61E-01	9.42E+00	9.18E+00	6.74E-03

SO₄ contamination with a wide range across our sites of roughly 270 – 77350 mg/kg. Similarly to Table 3, Table 4 demonstrates consistently elevated concentrations of other ions such as Mg, Si, and K in the sediment which are likely sourced similarly from the mine lithologies. These ions could be in the form of common AMD mineral precipitates in the initial 30 meters, however potential mineral precipitates could be identified through evaluating conditions as they relate to precipitation of specific mineral species. This is most commonly achieved through geochemical modeling of the mine discharge and determination of supersaturated conditions for said minerals. This analysis will be presented later in section 5.1.

Values for the various analyses performed in determination microbial presence are presented in Table 5. Colony forming unit (cfu) analysis is presented as numerical values representing all colony morphologies present on pH neutral agar. These counts were not able to be performed for Pine Run due to the limitations of the SARS-CoV-2 pandemic. However, York Clay exhibited the largest values for cfu. This is consistent with the pH ranges for the three mines evaluated. York Clay discharge contained nearly perfectly neutral pH conditions and this data suggests the discharge at York Clay contained the largest number of cfu that could tolerate and utilize a neutral nutrient LB agar. Cfu values for Esco and Sines contain drastically reduced values as fewer species in these acidic waters can both exist in acidic waters and utilize pH neutral agar. In terms of colonization rate (CR), *Thiothrix* was most elevated in Esco, York Clay, and Pine. *Gallionella ferruginea* CR values were highest in the Pine Run discharge, and *Leptothrix discophora* CR values were largest for Sines and York Clay mines.

Table 9 Microbial data (pH nutrient agar colony forming units (cfu) and slide colonization rates (1/cm²d)) for all mine sites on 10/20/2019 (York Clay, Sines, Essex coal mines) and 10/23/2019 (Pine Run coal mine).

	meters	cfu (colonies)	cf.Thio7 (CR)	cfThio19 (CR)	cfThioAve (CR)	Gferr7 (CR)	Gferr19 (CR)	GferrAve (CR)	Ldisc7 (CR)	Ldisc19 (CR)	LdiscAve (CR)
York Clay	0	188	22	30	26	10	16	13	28	16	22
York Clay	8	36	32		32	7		7	60		60
York Clay	15	126	1	5	3	1	4	3	6	4	5
York Clay	23	36	1		1	0		0	4		4
York Clay	30	17		0	0		5	5		5	5
Sines	0	3	0	1	1	42	0	21	1	5	3
Sines	8	0	0	0	0	0	0	0	0	1	1
Sines	15	0	0	0	0	1	0	1	2	16	9
Sines	23	4	0	0	0	1	0	1	1	23	12
Sines	30	1		0	0		0	0		35	35
Essex	0	25	202	185	194	2	69	36	2	2	2
Essex	8	9	160	120	140	1	98	50	0	0	0
Essex	15	2	126		126	0		0	0		0
Essex	23	79	88	54	71	1	96	49	1	1	1
Essex	30	50	124	120	122	1	30	16	3	2	3
Pine	0		15	2	9	148	180	164	0	1	1
Pine	8		6	8	7	188	228	208	2	2	2
Pine	15		4		4	72		72	1		1
Pine	23		1	44	23	31	245	138	6	6	6
Pine	30		2	56	29	35	120	78	1	0	1
	MIN	0	0	0	0	0	0	0	0	0	0
	MAX	188	202	185	194	188	245	208	60	35	60
	MEAN	38	44	39	39	30	68	43	7	7	9
	SD	54	66	56	59	54	85	61	15	10	15

Saturation index (SI) values determined for each mine discharge are listed in Table 6. Positive values for SI indicate supersaturated conditions for the minerals listed. From this we can determine that Pine Run contains supersaturated values for Alunite, Barite, Basaluminite, $\text{Fe}(\text{OH})_3(\text{a})$, Gibbsite, Goethite, Jarosite, Jurbanite, and Pyrolusite; Esco contains supersaturated values for Alunite, $\text{Al}(\text{OH})_3(\text{a})$, Barite, Basaluminite, $\text{Fe}(\text{OH})_3(\text{a})$, Goethite, Jarosite, and Pyrolusite; York Clay contains supersaturated values for Alunite, $\text{Al}(\text{OH})_3(\text{a})$, Barite, Basaluminite, $\text{Fe}(\text{OH})_3(\text{a})$, Gibbsite, Goethite, Jarosite, Jurbanite, and Pyrolusite; and Sines contains supersaturated values for Barite and Goethite.

In Table 7 are the values for average grain size diameter in millimeters as well as percentage lost on ignition. While grain sizes ranging from medium silt to coarse sand were present in the sieve analysis, these average grain size values indicate that average fraction of grains for each site was medium to coarse sand. The largest grain size average values were found in the sediments of Sines mine and the lowest grain size average values were found within the Pine Run sediment. Loss on ignition (LoI) values were initially an attempt to determine organic matter content of the sediment for each sub-site. Due to elevated values for LoI, we realized determining organic matter through this method would be difficult as the mass of the sediment was reduced further due to oxidation of S content. The largest values for LoI were found in the sediments of Pine Run and the lowest values for LoI were found in the sediments of York Clay and Sines.

Sediment mass for each mine sub-site is listed in Table 8. These values indicate

Table 11 Saturation indexes for minerals at all mine sites on 10/20/2019 (York Clay, Sines, Essex coal mines) and 10/23/2019 (Pine Run coal mine). Values were found using the program PHREEQCI.

	meters	Alunite	Al(OH)3(a)	Barite	Basaluminite	Fe(OH)3(a)	Gibbsite	Goethite	Jarosite (ss)	Jarosite (K)	Jarosite (Na)	Jarosite (H)	Jurbanite	Pyrolusite
York Clay	0	8.88	1.37	0.47	12.53	4.09	4.17	9.54	6.22	5.31	2.08	-2.61	-0.44	8.94
York Clay	8	10.35	1.83	0.52	14.51	4.03	4.63	9.47	6.13	5.18	2.01	-2.65	0.12	8.87
York Clay	15	10.10	1.69	0.65	14.07	3.63	4.50	9.07	9.32	4.13	0.92	-3.72	0.06	8.81
York Clay	23	18.43	4.67	0.33	25.62	3.32	7.47	8.77	3.56	2.62	-0.49	-5.28	2.71	8.74
York Clay	30	9.35	1.56	0.69	13.16	3.61	4.36	9.06	4.62	3.75	0.37	-4.40	-0.41	9.23
Sines	0	-6.41	-8.32	0.29	-17.51	-3.53	-5.54	2.03	-1.68	-3.37	-6.26	-6.24	-0.89	-0.05
Sines	8	-6.50	-8.32	0.32	-17.52	-3.65	-5.54	1.90	-2.11	-3.81	-6.66	-6.60	-0.89	-0.01
Sines	15	-6.58	-8.33	0.33	-17.58	-3.69	-5.55	1.87	-2.26	-3.97	-6.74	-6.70	-0.90	-0.02
Sines	23	-6.44	-8.32	0.37	-17.59	-3.71	-5.54	1.86	-2.23	-3.89	-6.81	-6.73	-0.90	-0.01
Sines	30	-6.18	-8.13	0.33	-17.13	-3.60	-5.36	1.99	-2.14	-3.76	-6.52	-6.50	-0.86	0.06
Essex	0													
Essex	8	4.22	-1.73	0.13	3.73	3.25	1.08	8.65	8.61	7.20	4.02	1.07	-0.24	5.57
Essex	15	7.86	-0.19	0.40	9.19	3.61	2.63	9.02	8.62	7.30	4.09	0.78	0.61	6.32
Essex	23	4.57	-1.40	0.10	4.63	3.66	1.42	9.06	9.16	7.79	4.67	1.49	0.32	5.95
Essex	30	5.66	-0.73	0.03	6.74	3.84	2.09	9.24	8.73	7.40	4.28	0.89	-0.22	6.48
Pine	0	3.09	-2.75		0.69	3.15	0.06	8.56	10.31	8.86	5.95	2.99	-0.18	4.41
Pine	8	6.23	0.54		9.53	4.82	3.35	10.23	8.23	7.16	4.46	-0.58	-1.19	8.27
Pine	15	6.89	-1.49	1.07	5.82	2.90	1.32	8.31	9.62	8.13	5.59	2.45	1.18	4.33
Pine	23	3.57	-2.52	0.11	1.52	2.73	0.29	8.14	8.86	7.39	4.69	1.60	-0.02	4.49
Pine	30	4.76	-2.14	0.25	3.02	2.99	0.67	8.40	9.69	8.24	5.62	2.37	0.35	4.53
	MIN	-6.58	-8.33	0.03	-17.59	-3.71	-5.55	1.86	-2.26	-3.97	-6.81	-6.73	-1.19	-0.05
	MAX	18.43	4.67	1.07	25.62	4.82	7.47	10.23	10.31	8.86	5.95	2.99	2.71	9.23
	MEAN	3.78	-2.25	0.38	1.97	1.66	0.55	7.11	5.33	3.77	0.80	-2.02	-0.09	5.00
	SD	7.12	4.12	0.26	13.23	3.28	4.13	3.22	4.87	4.90	4.88	3.66	0.91	3.49



Table 13. Average sediment size and organic matter content for all mine sites on 10/20/2019 (York Clay, Sines, Essex coal mines) and 10/23/2019 (Pine Run coal mine).

	meters	Average Diameter (mm)	Loss on Ignition
<i>York Clay</i>	0	0.64	7.36%
<i>York Clay</i>	8	0.61	6.74%
<i>York Clay</i>	15	0.60	7.12%
<i>York Clay</i>	23	0.54	9.91%
<i>York Clay</i>	30	0.62	6.93%
<i>Sines</i>	0	1.36	6.29%
<i>Sines</i>	8	0.79	7.41%
<i>Sines</i>	15	1.02	8.46%
<i>Sines</i>	23	1.16	6.17%
<i>Sines</i>	30	0.89	3.88%
<i>Essex</i>	0	0.54	26.62%
<i>Essex</i>	8	0.78	29.22%
<i>Essex</i>	15	0.58	24.19%
<i>Essex</i>	23	0.67	25.87%
<i>Essex</i>	30	0.64	5.68%
<i>Pine</i>	0	0.54	10.81%
<i>Pine</i>	8	0.56	13.53%
<i>Pine</i>	15	0.53	10.75%
<i>Pine</i>	23	0.55	10.54%
<i>Pine</i>	30	0.54	12.43%
	MIN	0.53	3.88%
	MAX	1.36	29.22%
	MEAN	0.71	12.00%
	SD	0.23	7.84%

Table 15 Mass of sediment in each sieve for all mine sites on 10/20/2019 (York Clay, Sines, Essex coal mines) and 10/23/2019 (Pine Run coal mine).

Sieve #	18	35	60	140	270	635
mm	1	0.5	0.25	0.105	0.053	0.008
	(g)	(g)	(g)	(g)	(g)	(g)
YC1	6.840	150.450	62.430	42.730	18.990	4.700
YC2	44.460	141.800	23.030	19.610	9.090	1.240
YC3	4.460	147.250	50.300	26.030	11.450	6.580
YC4	5.170	77.830	12.840	10.240	3.190	0.460
YC5	2.650	86.530	12.450	9.550	4.680	1.460
S1	0.930	60.730	33.530	16.090	3.660	0.120
S2	0.400	55.190	29.240	9.970	3.760	0.450
S3	0.000	100.000	71.970	18.970	7.200	0.510
S4	0.530	94.800	54.430	16.910	5.770	0.320
S5	1.550	75.570	48.690	15.400	7.040	0.640
E1	9.980	6.220	2.710	1.360	0.210	0.020
E2	3.920	5.010	3.830	1.610	0.090	0.010
E3	23.270	16.590	6.840	2.820	0.140	0.010
E4	28.650	18.890	1.970	0.510	0.010	0.010
E5	46.910	63.800	16.190	12.010	3.980	0.060
P1	10.166	11.712	11.303	12.073	2.559	0.112
P2	12.525	30.363	26.883	15.540	3.613	0.129
P3	12.374	33.549	33.245	16.059	2.425	0.707
P4	9.307	25.931	33.418	19.332	4.089	0.161
P5	10.464	75.818	22.176	24.426	5.346	0.165

the variable amounts of sediment recovered for each site that consisted of the grain size fraction $< 2\text{mm}$ (#10 sieve). From this table we can note the largest fraction of sediment is located in the coarser grain sizes (#18 and #35 sieves).

5.2 Statistical Analysis of Data

Statistical analysis of data involved a principle component analysis (PCA) paired with a Spearman's rank correlation matrix to highlight any important relationships present within the dataset. Due to the large size of the data, each PCA and Spearman's matrix is presented in sections rather than as one complete output. From the PCA analysis, only relevant outputs will be presented and explained. Similarly, each Spearman's correlation matrix is divided by section and only relationships with p-values below 0.01 are presented and further classified by the R coefficient based on the positive or negative value, and values above $|0.8|$ and $|0.95|$ are highlighted to indicate the strongest correlations in the matrices.

5.2.1 Principle Component Analysis

PCA analysis for ions in water are presented in Figures 32 and 33. Scores Plot Figure (upper left) shows a two-dimensional scatter plot of scores for water ions from the PCA conducted, the first component explains 92% of the variation, and the second component 7%. It shows the scores grouped according to the sampling site with only Pine Run mine exhibiting more disperse scores.

Influence plot (lower left) showing the plot of F-residuals vs. Hotelling's T^2 statistics. Sines No. 1 sampling point (0 meters) is the only exceedingly high F-residual in the PCA model as all other points plot below the F limit and Hotelling's T^2 for the two

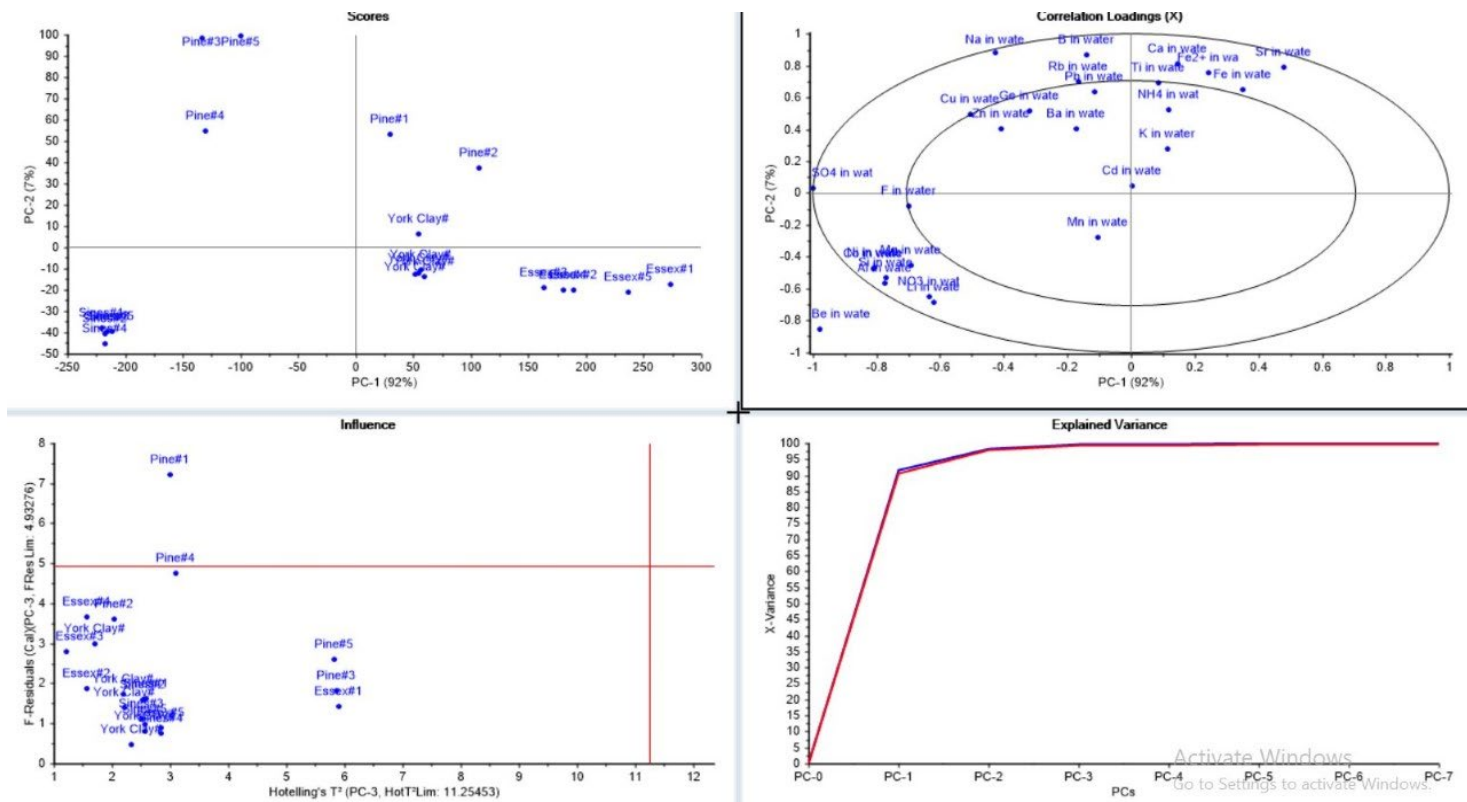
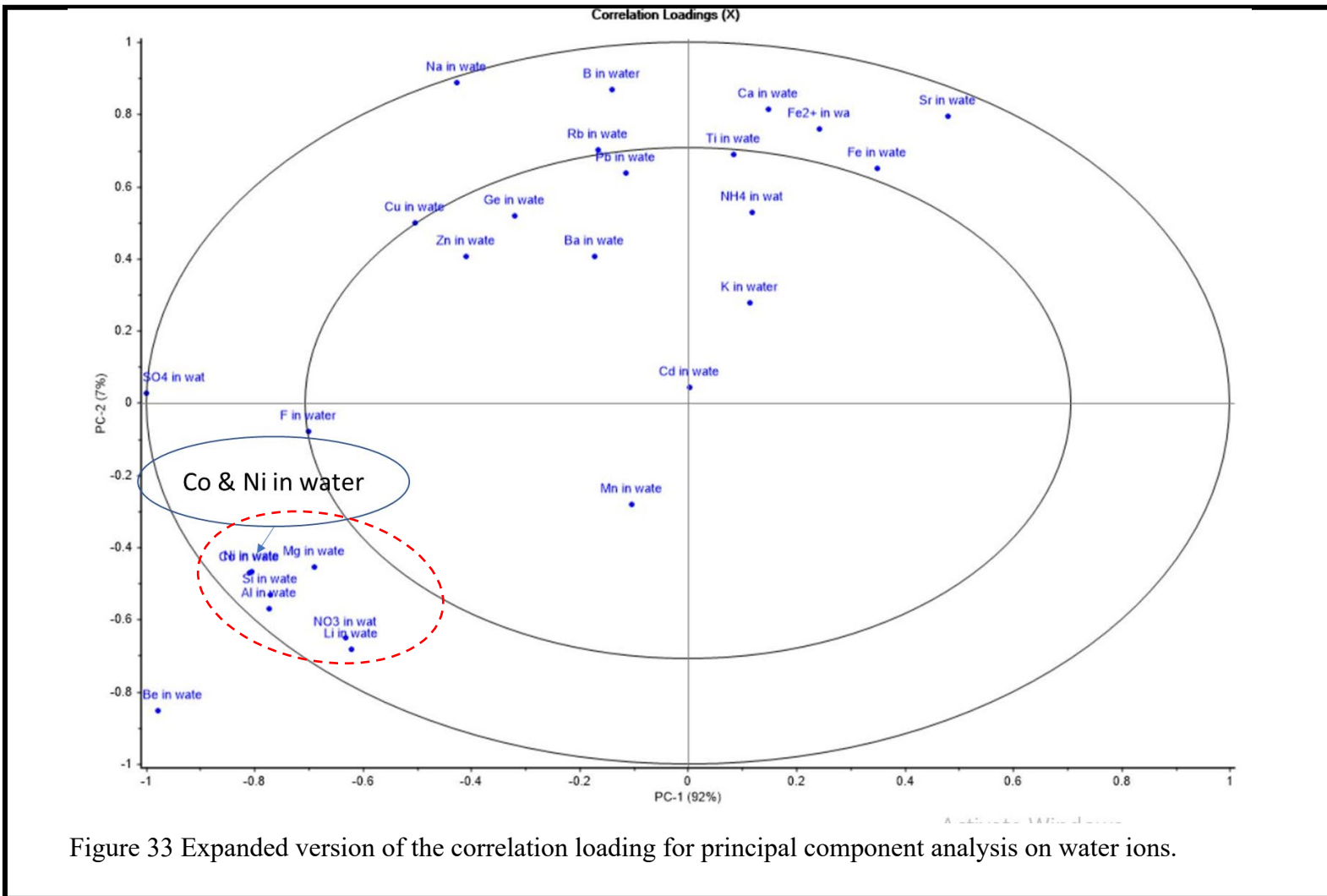


Figure 32 Overview of the result of PCA conducted on the water ions using the Unscramble x software, A) Scores plot, B) Correlation Loading, C) Influence plot, D) Explained Variance.



axis. This display suggests that Sines (0 meters) sample site may be the only one poorly described by the model.

Explained variance plot (lower right) indicates that two principal component axis seem to explain close to 99% of the variance. The principal component analysis was able to explain 100% of the variance at 3-PC. There is no significant difference between the calibration curve (blue line) and validation curve (red line).

Correlation loading plot (upper right) shows the correlation loading plot generated for the concentration of the water ions in the PCA performed. The principal component analysis explained 92% of the variance in the first principal component (Figure 32). The correlation loading plot shows that the only parameters to explain less than 50% variance were: Ba, Cd, F, Ge, K, Mn, NH₄, Pb, Ti, Zn in water (Figure 33). While those clustered together are highly correlated such as Co, Ni, Mg, Si and Al. Lithium and NO₃ are also clustered. Mg, Al, Si may be closely linked due to the high amount of mica mineral and carbonate Mg geology in the surrounding rocks.

PCA analysis for ions in water and sediments are presented in Figures 34 and 35. Scores Plot Figure (upper left) shows a two-dimensional scatter plot of scores for sediment ions and water ions from the PCA conducted, the first component explains 98% of the variation, and the second component 1%.

Influence plot (lower left) showing the plot of F-residuals vs. Hotelling's T² statistics. Pine #3 sampling point (15 meters) is the only exceedingly high F-residual in the PCA model as all other points plot below the F limit and Hotelling's T² for the two

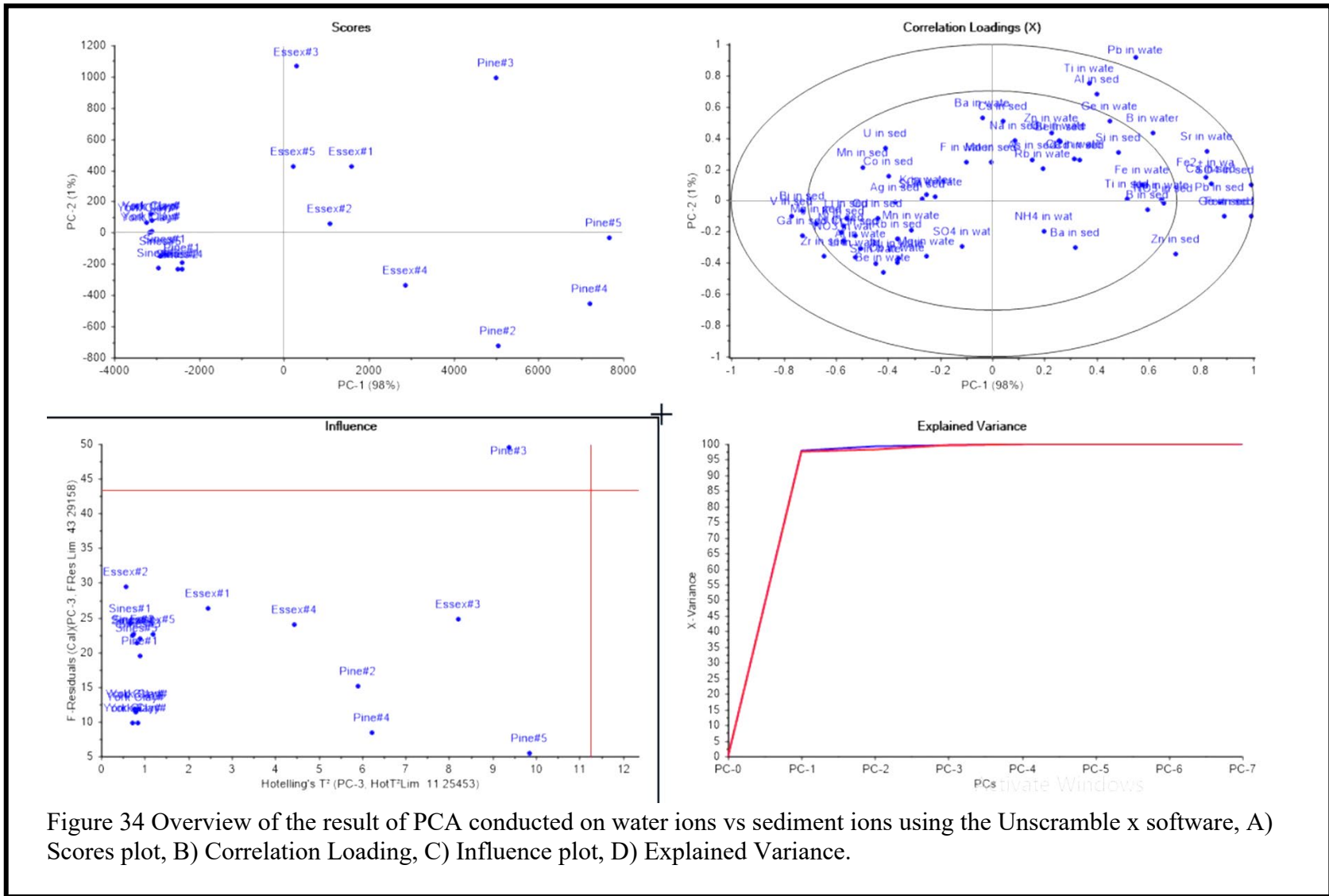


Figure 34 Overview of the result of PCA conducted on water ions vs sediment ions using the Unscramble x software, A) Scores plot, B) Correlation Loading, C) Influence plot, D) Explained Variance.

axis. This display suggests that the Pine #3 (15 meters) sample site may be poorly described by the model.

Explained variance plot (lower right) indicates that two principal component axis seem to explain close to 99% of the variance. The principal component analysis was able to explain 100% of the variance at 3-PC. There is no significant difference between the validation and calibration curves (red and blue lines in lower right of Figure 34).

Correlation loading plot (upper right) shows the correlation loading plot generated from the concentrations of ions in water and sediments in the PCA performed. The principal component analysis explained 98% of the variance in the first principal component (Figure 35). The correlation loading plot shows that the only parameters to explain less than 50% variance were: Al, Ba, Be, Ca, Cd, Co, Cr, F, Ge, K, Li, Mg, Mn, Na, NH₄, Ni, NO₃, Rb, SO₄, and Si in water, and Ag, As, B, Ba, Cd, Co, Cr, Cs, Cu, K, Li, Mg, Mn, Mo, Na, Ni, NO₃, Rb, Si, Sr, Ti, and U in sed. While those clustered together are highly correlated. Al, Be, Bi, Co, Cr, Cu, Ga, K, Li, Mg, Mn, Ni, NO₃, Rb, Si, V, and Zr are grouped on the negative end of PC1,

PCA for the field parameters and microbial data is presented in Figures 36 and 37. Scores Plot Figure (upper left) shows a two-dimensional scatter plot of scores for field parameters vs bacteria from the PCA conducted, the first component explains 95% of the variation, and the second component 3%. The scores are clearly divided in groups according to the sampling site, showing the similarity for the samples of each site.

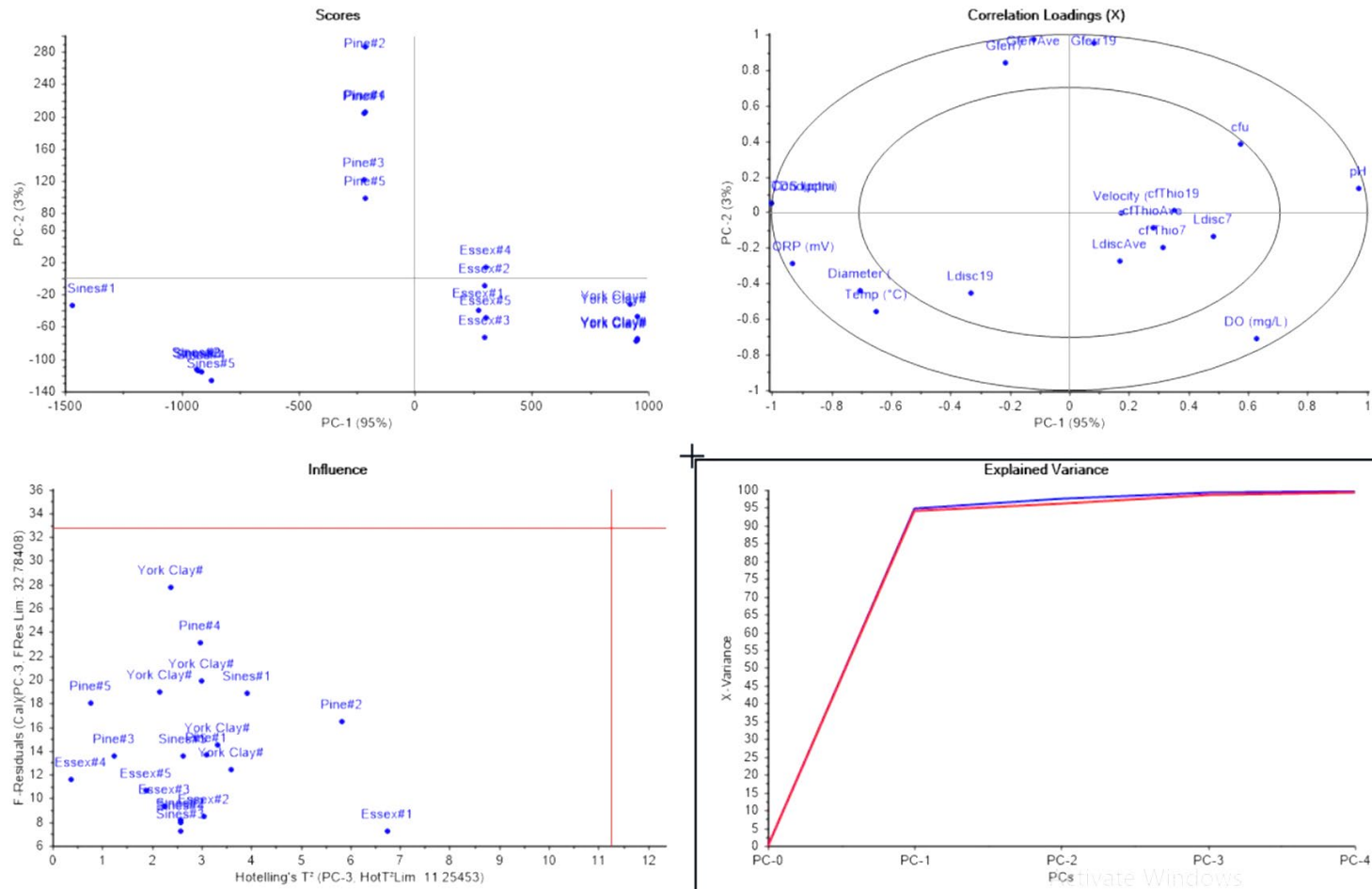


Figure 36 Overview of the result of PCA conducted on field parameters vs microbes using the Unscramble x software, A) Scores plot, B) Correlation Loading, C) Influence plot, D) Explained Variance.

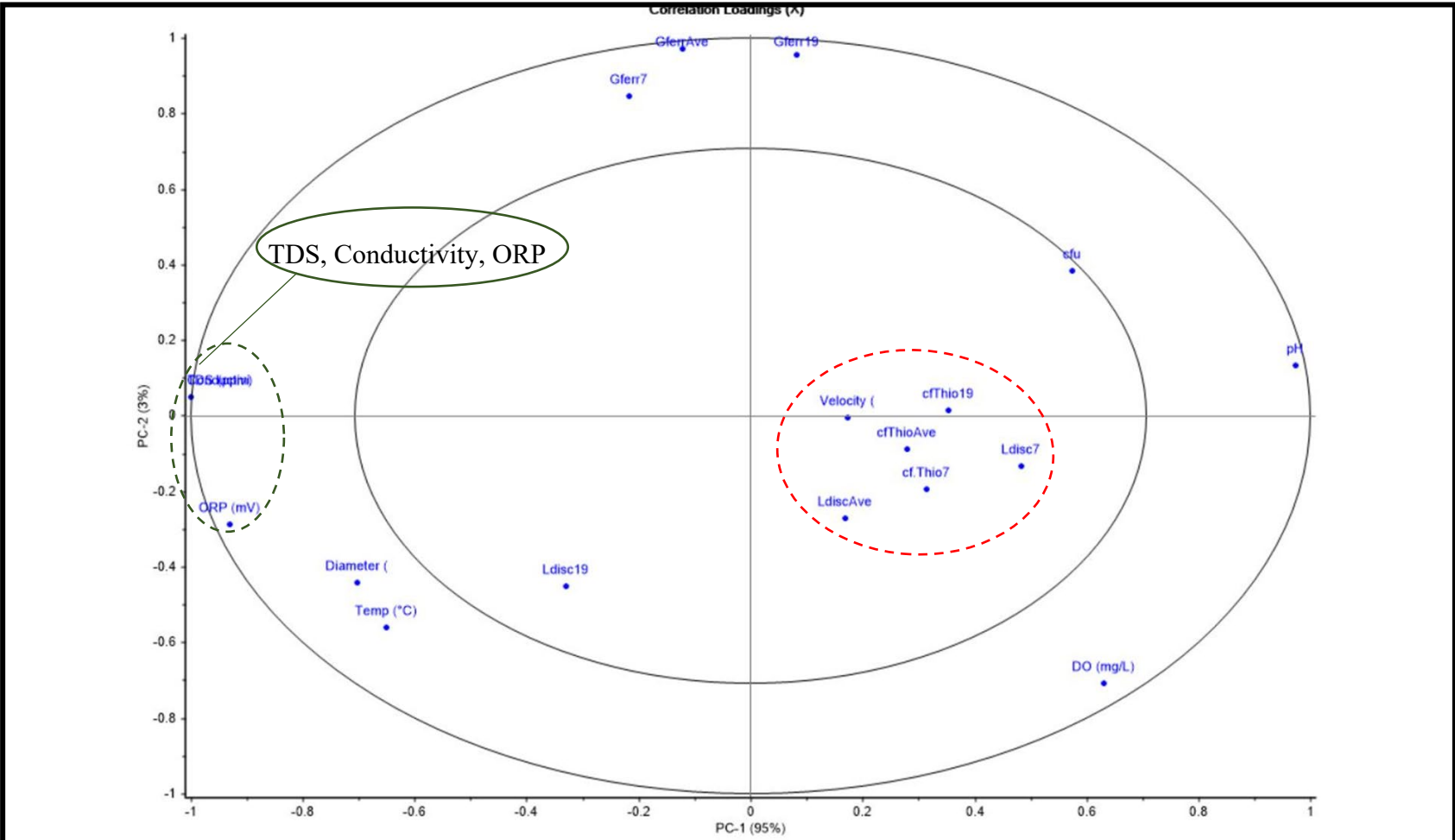


Figure 37 Expanded version of the correlation loading for principal component analysis of field parameters vs microbes.

Influence plot (lower left) showing the plot of F-residuals vs. Hotelling's T^2 statistics. There are no exceedingly high Hotelling's T^2 and F-residuals in the PCA model as all points plot below the F limit and Hotelling's T^2 for the two axis. This display suggests that there are no influential sample points that can be poorly described by the model.

Explained variance plot (lower right) indicates that two principal component axis seem to explain close to 99% of the variance. The principal component analysis was able to explain 100% of the variance at 3-PC. There is no significant difference between the validation (red line) and calibration (blue line) curves.

Correlation loading plot (upper right) shows the correlation loading plot generated from the field parameters and microbial counts with the PCA performed. The principal component analysis explained 95% of the variance in the first principal component (Figure 36). The correlation loading plot shows that the only parameters to explain less than 50% variance were: velocity, *L. discophora* day 7, 19, and average; and *Thiothrix* day 7, 19, and average cfu of *L. discophora* bacteria; and colony forming units (cfu) (Figure 37). While those clustered together are highly correlated. Note that the variables *Thiothrix* day-7, *Thiothrix* day-19, *Thiothrix* average, *L. discophora* average, *L. discophora* day-7, and velocity fall in a cluster which indicates they are closely correlated. This suggested relationship is a valid one as relationships outlined later in this chapter indicate that these species are related in some way with flow regime. TDS, conductivity and ORP fall in opposite sides of the diagram with respect to pH, suggesting a negative correlation between them. This relationship is relevant as discharges with more charge carrying ions and increased ORP values also have the lowest pH values.

PCA for the concentration of ions in the water and microbial data are presented in Figures 38 and 39. Scores Plot Figure (upper left) shows a two-dimensional scatter plot of scores for water ions and bacteria counts from the PCA conducted, the first component explains 61% of the variation, and the second component 23%. In terms of water ions and bacteria, variables grouped together along the PC-1 axis with the exception of Pine Run.

Influence plot (lower left) showing the plot of F-residuals vs. Hotelling's T^2 statistics. There are no exceedingly high Hotelling's T^2 and F-residuals in the PCA model as all points plot below the F limit and Hotelling's T^2 for the two axis. This display suggests that there are no sample points that can poorly described by the model.

Explained variance plot (lower right) indicates that two principal component axis seem to explain about roughly 84% of the variance. The principal component analysis was able to explain 100% of the variance at 4-PC. There is some offset between the calibration and the validation curves, however this correlation between water ions and bacteria is the only variance plot that cannot be explained completely by PC-3. This indicates that more data is needed to make better predictions regarding the correlation of water ions and microbes.

Correlation loading plot (upper right) shows the correlation loading plot generated from the water ions and microbial counts PCA performed. The principal component analysis explained 61% of the variance in the first principal component and 23% in the

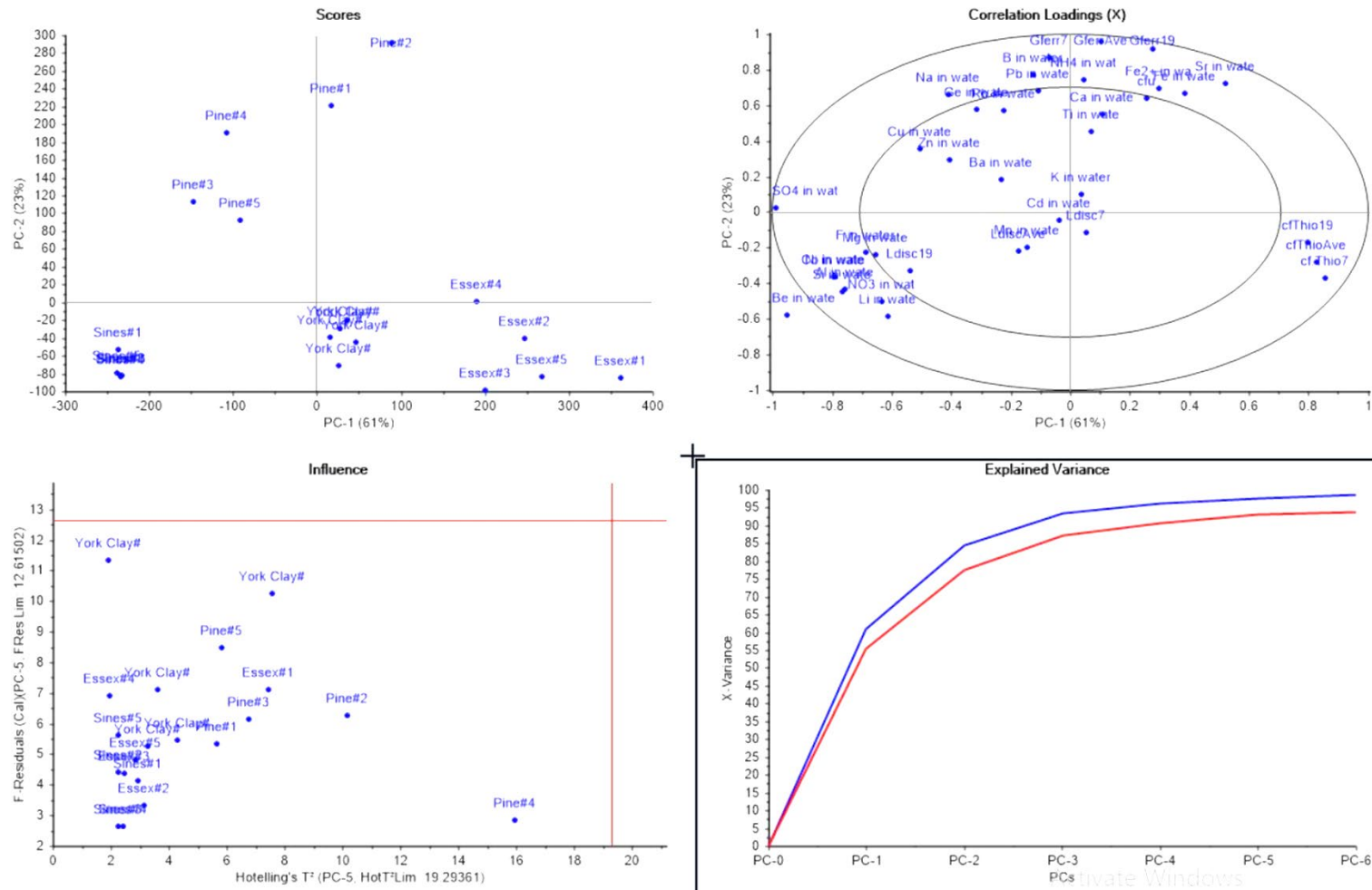


Figure 38 Overview of the result of PCA conducted on water ions vs microbes using the Unscramble x software, A) Scores plot, B) Correlation Loading, C) Influence plot, D) Explained Variance.

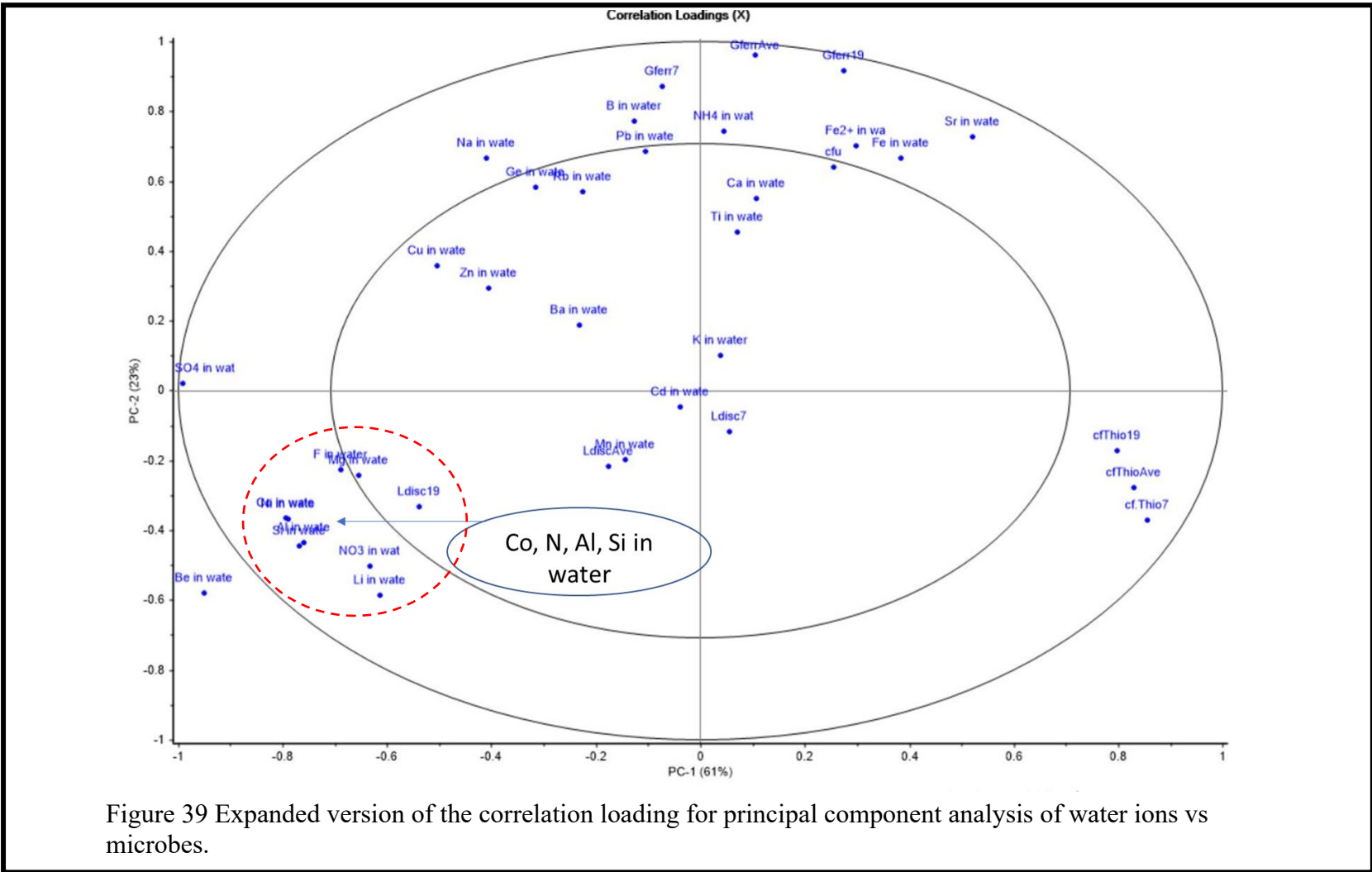


Figure 39 Expanded version of the correlation loading for principal component analysis of water ions vs microbes.

second principle component (Figure 38). The correlation loading plot shows that the only parameters to explain less than 50% variance were: Ba, Ca, Cd, Cu, Ge, K, Mg, Mn, Pb, Rb, Ti, Zn, and *L. discophora* day 7, 19 and average (Figure 39). While those clustered together are highly correlated. *Thiothrix* and SO₄ in water lie on opposite ends of the PC1 line indicating they have a negative relationship. The explanation of a negative correlation involves *Thiothrix* requiring a utilizable form of Sulfur. Most likely found in the precipitate forms. For this reason, SO₄ in its dissolved form may not attract the presence of *Thiothrix* species as they will likely reside in regions where inorganic S is to be oxidized.

PCA for the sediment ions and microbial data is presented in Figures 40 and 41. Scores Plot Figure (upper left) shows a two-dimensional scatter plot of scores for sediment ions and bacterial counts from the PCA conducted, the first component explains 98% of the variation, and the second component 1%.

Influence plot (lower left) showing the plot of F-residuals vs. Hotelling's T² statistics. Esco #2 sampling point (8 meters) is the only exceedingly high F-residual in the PCA model as all other points plot below the F limit and Hotelling's T² for the two axis. This display suggests that the Esco #2 (8 meters) sample site may be poorly described by the model.

Explained variance plot (lower right) indicates that two principal component axis seem to explain close to 99% of the variance. The principal component analysis was able to explain 100% of the variance at 3-PC. There is no significant difference between the calibration validation curves.

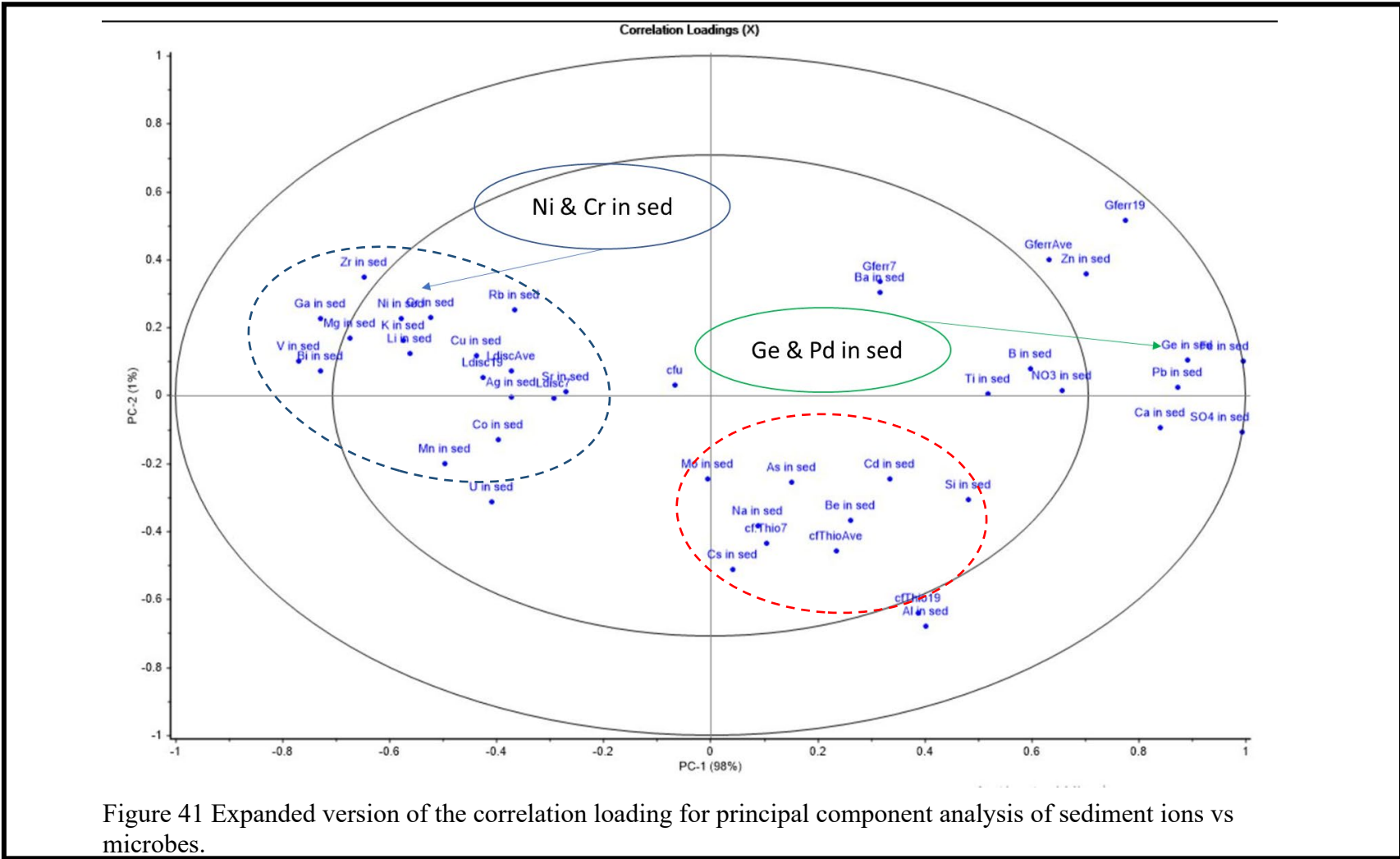


Figure 41 Expanded version of the correlation loading for principal component analysis of sediment ions vs microbes.

Correlation loading plot (upper right) shows the correlation loading plot generated from the sediment ions and microbial counts PCA performed. The principal component analysis explained 98% of the variance in the first principal component. The correlation loading plot shows that the only parameters to explain less than 50% variance were: Ag, As, B, Ba, Be, Cd, Co, Cr, Cs, Cu, K, Li, Mg, Mn, Mo, Na, Ni, NO₃, Rb, Si, Sr, Ti, U, colony forming units (cfu), *Thiothrix* day 7, and average; *G. ferruginea* day 7, and *L. discophora* day 7, 19, and average. While those clustered together are highly correlated. Al in the sediment grouped closely with *Thiothrix*. This grouping is expected as Lopez et al. (1999) previously described a relationship between velocity and hydroxylated-alumino-sulfates. *Thiothrix* has been shown to group closely in prior PCA analysis with velocity and likewise should group near these co-precipitated forms of Al in the sediment.

5.2.2 Spearman Correlation Analysis

As stated previously, this study utilizes a Spearman correlation analysis as well as a principle component analysis (PCA) to analyze the quality and relationships present in the geochemical and microbial data collected. This will serve to shine light on any important relationships or correlations present in the dataset as a whole.

Significant Correlations in Water ($p < 0.01$; $|R| \geq 0.80$)

Field parameters vs. field parameters. In this section a Spearman's univariate test was used to examine the quality of the data collected for the following parameters at all four mine sites: mean velocity at each site, conductivity, total dissolved solids (TDS), oxidative-reductive potential (ORP), pH, temperature, and dissolved oxygen (DO). These relationships can be noted in Table 10 where significant relationships with $p < 0.01$ are

shown as cells with their correlation coefficient (r) values indicating how well they fit a correlation between the pair of parameters.

Among those relationships shown, the significant relationships are as follows: mean velocity vs temperature, conductivity vs TDS, conductivity vs ORP, conductivity vs pH, conductivity vs DO, TDS vs ORP, TDS vs pH, TDS vs DO, ORP vs pH, ORP vs DO, pH vs DO, and Temp vs DO.

In terms of notable positive relationships, conductivity and ORP shared a positive relationship. This indicated that elevated conductivity values were present in regions where ORP was high. Values for pH and DO also shared a positive relationship which was an expected correlation as the oxygen depleted mine waters reoxygenate, precipitation takes place and pH becomes more alkaline. While acidity is released within the first 30 meters from our AMD reaction, some neutralization could be taking place due to the carbonate lithologies. In some regions these lithologies are armored and acidity prevails dropping the pH as the waters become oxygenated stressing that these environments are non-equilibrated.

In terms of negative relationships, conductivity and pH share a negative correlation as increases in charge carrier ions cause decreases in pH. Conductivity and DO also have a negative relationship as oxygenation decrease the number of charge carrier ions in solution from precipitation. Finally, DO and ORP have a negative

Table 10 Results of Spearman's correlation matrix for field parameters with R values displayed for all significant relationships ($p < 0.01$).

All p-values < 0.01 : Blue = +R Red = -R Yellow Fill = R > 0.8 Green Fill = R > 0.95	Velocity	Conductivity	TDS	ORP	pH	Temp	DO
Conductivity							
TDS		0.99					
ORP		0.90	0.91				
pH		-0.95	-0.95	-0.96			
Temp	-0.81						
DO		-0.74	-0.73	-0.74	0.78	0.02	

correlation which is not expected due to some irregularities in oxygenation trends of sub sites within the data set.

Water ions vs field parameters. A Spearman's correlation analysis was used to compare the following parameters: mean velocity, conductivity, total dissolved solids, oxidative/reductive potential, pH, temperature, dissolved oxygen, Fe in water, Al in water, SO₄ in water, NO₃ in water, Mg in water, Si in water, Na in water, Ni in water, Zn in water, Cu in water, Co in water, Br in water, Be in water, Ti in water, Ga in water, Ge in water, Pb in water, and Fe²⁺ in water. These results are presented in Table 11.

Correlations between the water ions and field parameters yielded significant relationships with p-values less than 0.01 in the relationships displayed (Table 11). Some of the most relevant significant relationships involving Fe, Al, Mn, or SO₄, as well as high Spearman's R relationships are represented in cross-plots on the following pages (Figure 42 and 43).

In terms of positive relationships, conductivity and SO₄ or Mg shared a positive relationship. This correlation is expected as conductivity and SO₄ is a charge carrier ion in large abundance in AMD. Mg also shares this positive relationship. Velocity and Fe also shared a positive relationship which is expected. As velocity increases there is more suspended matter within the water column, leading to more suspended Fe content. ORP and Mg or SO₄ share a positive correlation as well. Higher ORP indicates greater oxidation and SO₄ is an oxidized species. Liberation of Mg from clay minerals with Mg also occurs.

Table 11 Results of Spearman's correlation matrix for water ions and field parameters with R values displayed for all significant relationships ($p < 0.01$).

All p-values < 0.01 : Blue = +R Red = -R Yellow Fill = R > 0.8 Green Fill = R > 0.95	Velocity	Conductivity	Total Dissolved Solids	ORP	pH	Temp	DO
Fe in water	0.57					-0.70	
Al in water	-0.79					0.85	
SO4 in water	-0.57	0.70	0.71	0.61	-0.66	0.79	
NO3 in water	-0.64					0.69	
Mg in water		0.76	0.78	0.82	-0.81		
Si in water	-0.60					0.86	
Na in water							-0.76
Ni in water		0.87	0.86	0.95	-0.92		-0.81
Zn in water		0.70	0.63	0.70	-0.71		
Cu in water		0.62		0.64	-0.68		-0.61
Co in water		0.84	0.84	0.95	-0.90		-0.77
Br in water							-0.66
Be in water	-0.72					0.80	
Ti in water				-0.58	0.60		
Ga in water						0.71	
Ge in water						0.78	
Pb in water						0.67	
Fe2+	0.72					-0.72	

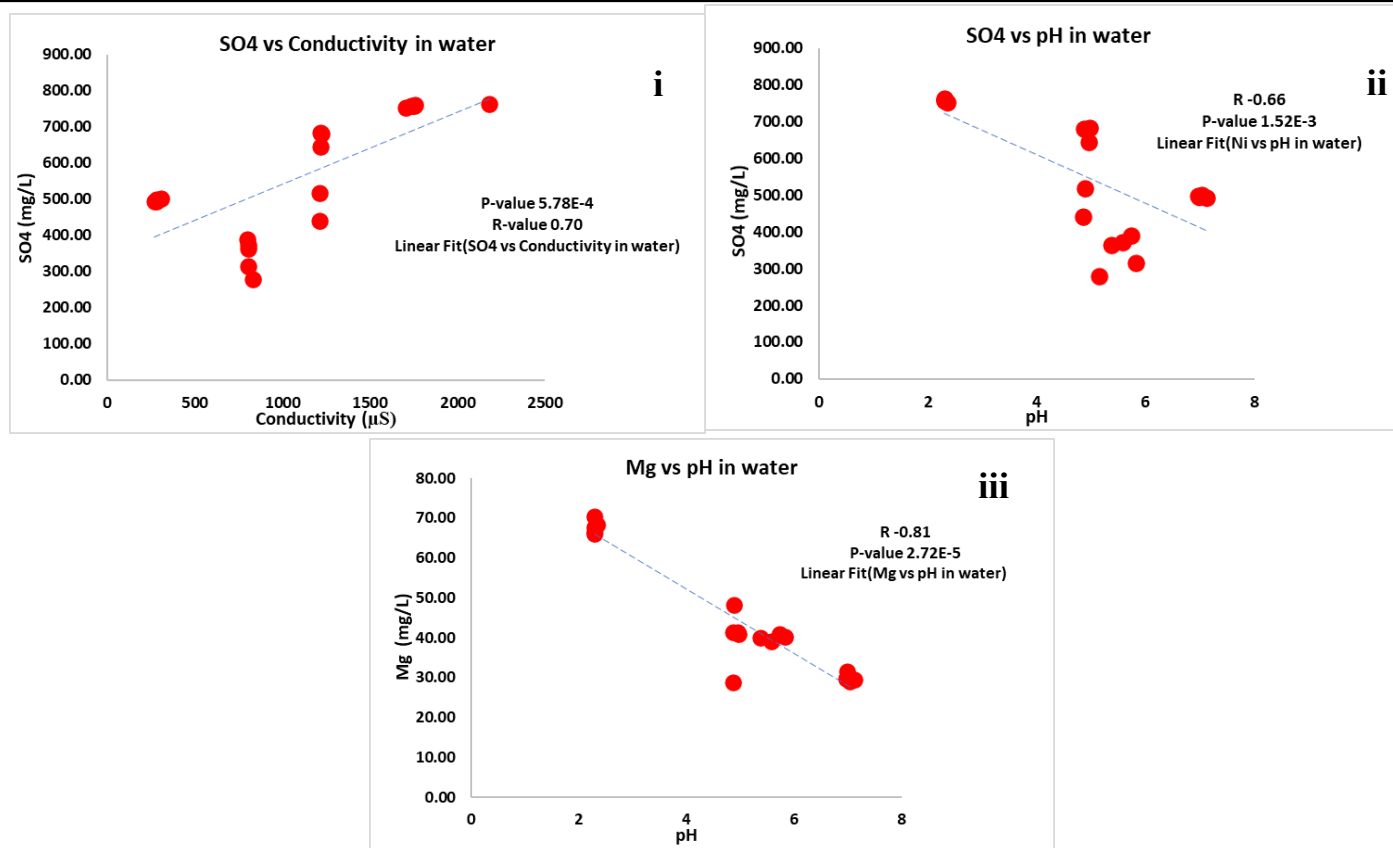
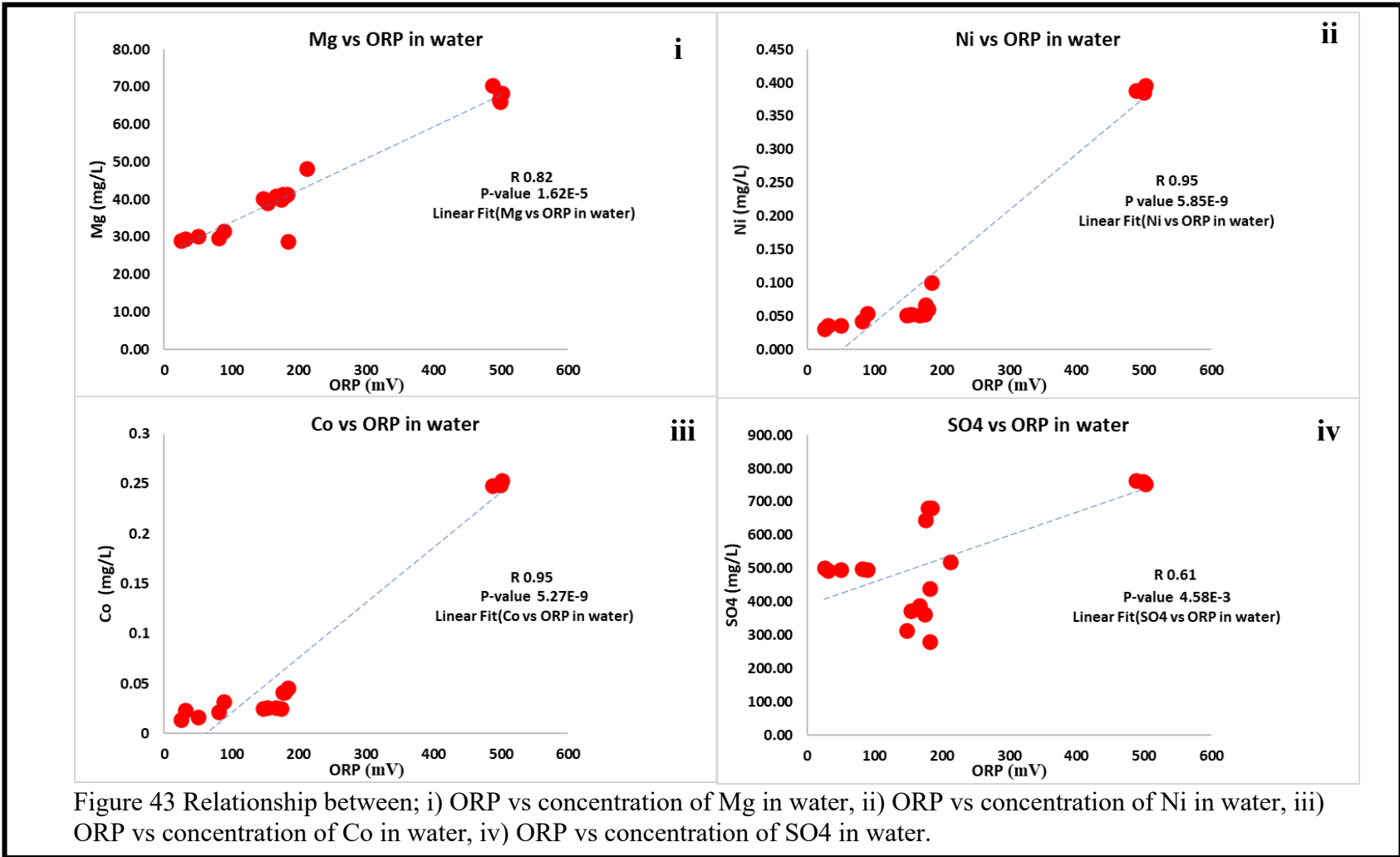


Figure 42 Relationship between; i) correlation of conductivity vs concentration of SO4 in water, ii) correlation of pH vs concentration of Mg in water, iii) correlation of pH vs SO4 in water.



In terms of negative relationships, pH and SO₄ or Mg share negative correlations as the presence of Mg ions can be associated with increased Conductivity or decreased pH based on the prior relationship outlined in the field parameters. Velocity shares a negative correlation with Al, SO₄, and NO₃ in water as these are more likely to be precipitated out into the sediments as water reoxygenates in these higher velocity regions.

SO₄ can be speculated to correlate strongly with conductivity (Figure 42i) due to increases in the concentrations of other ions accompanying a rise in SO₄. Sulfate is coming from the oxidation of pyrite and production of hydrogen ions that attack rock minerals and produce high conductivity. Increases in SO₄ concentrations also liberate more H⁺ ions which lowers the pH of the solution as shown on the cross plot (Figure 42ii). Mg content is largely sourced from clay minerals and possible carbonate minerals dissolution from inside the mine which correlates with a drop in pH as more H⁺ is released. In the case of Mg, Co, and Ni which are sourced from minerals within the mine sites, we note strong correlations with increased oxidation or ORP values, meaning as more dissolution of minerals take place, oxidation increases and pH values become more acidic. For SO₄ a positive relationship with ORP is noted which means increased oxidation translates to increased conversion of sulfide to SO₄ which is the primary form of sulfur in the mine waters.

Sulfate content of the samples correlated significantly with most of the field parameters albeit with no R coefficients larger than 0.8 or -0.8. In these AMD environments we can note increased oxidation from sulfide to sulfate which is reflected in the positive relationship of SO₄ in water vs ORP (p-value = 0.00458, R-value = 0.61).

Positive correlations between oxidizing conditions and some of the heavy metals drew significant relationships such as the case of Zn, Cu, Ti, and most strongly in Ni and Co. Mg in water correlated in a similar manner to the heavy metals to ORP, pH, and conductivity, and is likely sourced from the clay minerals present within the mine.

Mean velocity correlated significantly with Fe (total) in water, Fe^{2+} , Al, SO_4 , and NO_3 . Positive correlations were present for Fe total and Fe^{2+} in water and negative correlations were found in the other ions listed. Generally, these results show that increases in flow velocity may lead to decreased concentrations in those samples. Fe and Fe^{2+} may hold a positive correlation due to the two Fe heavy sites (Esco and Pine Run coal mines) existing as the highest mean flow velocity per site. The Mn and Al contaminated sites are low or extremely low flow sites with these ions coming from alteration of minerals in the surrounding environment. For Al, SO_4 , and NO_3 we see a negative correlation with flow velocity as these species are transported further down the channel as suspended load or precipitate as oxygen is introduced at high turbidity regions. In pooling environment such as site 4 of Esco mine and site 1 of York Clay mine we can note elevated levels of Fe in water and in the case of Esco it can be noted in the sediments of site 4.

Correlations of concentrations of ions in waters. In this section a Spearman's rank correlation matrix was used to examine the relationships of the data collected for the following parameters at all four mine sites: Fe, Al, Mn, SO_4 , NO_3 , Ca, Mg, Si, Na, K, Ni, Zn, Cu, Co, Li, NH_4 , F, Br, Be, B, Ti, Ga, Ge, As, Rb, Sr, Cd, Cs, Ba, Pb and all other water ions not listed here which yielded non-significant results. These

relationships can be noted in Table 12 where significant relationships with $p < 0.01$ are shown as cells with their correlation coefficient (r) values indicating how well they describe a correlation between the parameters.

There were significant correlations for Fe, Al, and SO_4 with other ions in the water samples as it should be expected from the oxidation of pyrite, liberation of SO_4 , Fe and H^+ ions and attack of the acidic waters to the aluminum silicates. However, there is too much scatter in the data to represent strong trendlines on a cross-plot.

Significant Correlations in Sediments ($p < 0.01$; $|R| \geq 0.80$)

Field parameters vs concentrations of ions in sediments. In this section a Spearman's correlation matrix was used to examine the significant correlations of the data collected for the following parameters at all four mine sites: mean velocity, conductivity, TDS, ORP, pH, Temp, DO, and Fe, Mn, SO_4 in sed, NO_3 , Ca, Mg, Na, K, Ni, Zn, Cu, Li, Be, V, Cr, Ga, Ge, Rb, Sr, Zr, Mo, Ag, Bi, U, Co and all other sed ions not listed here which yielded non-significant results. These relationships are displayed in Table 13.

In terms of positive correlations, velocity and Fe, SO_4 or NO_3 in the sediment shared a positive relationship as these are more likely to be precipitated out into the sediments as water reoxygenates in these higher velocity regions. Mn in the sed and DO or pH also shared a positive relationship. In more alkaline and oxygenated regions of our sites, Mn is likely to precipitate out into the sediments. This positive relationship is shown in the cross-plot Figure 44(iii).

Table 12 Results of Spearman's correlation for water ions with R values displayed for all significant relationships (p<0.01).

All p-values < 0.01 : Blue = +R Red = -R Yellow Fill = R > 0.8 Green Fill = R > 0.95	Al in water	SO4 in water	NO3 in water	Ca in water	Mg in water	Si in water	K in water	Ni in water	Zn in water	Cu in water	Co in water	Li in water	NH4 in water	F in water
Fe in water	-0.71		-0.58			-0.63								
Al in water		0.70	0.73			0.88								
Mn in water														
SO4 in water						0.63		0.72		0.76	0.72			
NO3 in water				-0.77		0.75						0.81		
Ca in water					-0.62	-0.50	0.66					-0.83	0.69	
Mg in water								0.76			0.76			
Si in water														
Na in water										0.74				
K in water													0.62	
Ni in water									0.76	0.71	0.96			0.68
Zn in water											0.75			0.88
Cu in water											0.66			
Co in water														0.66
Li in water													-0.72	0.79

Table 13 Results of Spearman's correlation matrix for sediment ions and field parameters with R values displayed for all significant relationships (p<0.01).

All p-values < 0.01 : Blue = +R Red = -R Yellow Fill = R > 0.8	Velocity	Conductivity	TDS	ORP	pH	Temp	DO
Fe in sed	0.71						-0.72
Mn in sed		-0.60	-0.59	-0.60	0.59		0.80
SO4 in sed	0.70					-0.61	-0.59
NO3 in sed	0.62						
Ca in sed	0.72					-0.78	
Mg in sed	-0.74						
Na in sed							0.61
K in sed	-0.83					0.66	
Ni in sed	-0.62						
Zn in sed						-0.60	
Cu in sed	-0.60					0.62	
Li in sed	-0.71						
Be in sed						-0.58	
V in sed	-0.77					0.63	
Cr in sed	-0.64					0.69	
Ga in sed	-0.79					0.73	
Ge in sed						-0.58	
Rb in sed	-0.63						
Sr in sed				-0.59			
Zr in sed	-0.80					0.89	
Mo in sed							
Ag in sed	-0.69					0.73	
Bi in sed	-0.72					0.67	
U in sed		-0.68	-0.70	-0.69	0.70		0.58
Co in sed		-0.61	-0.60				

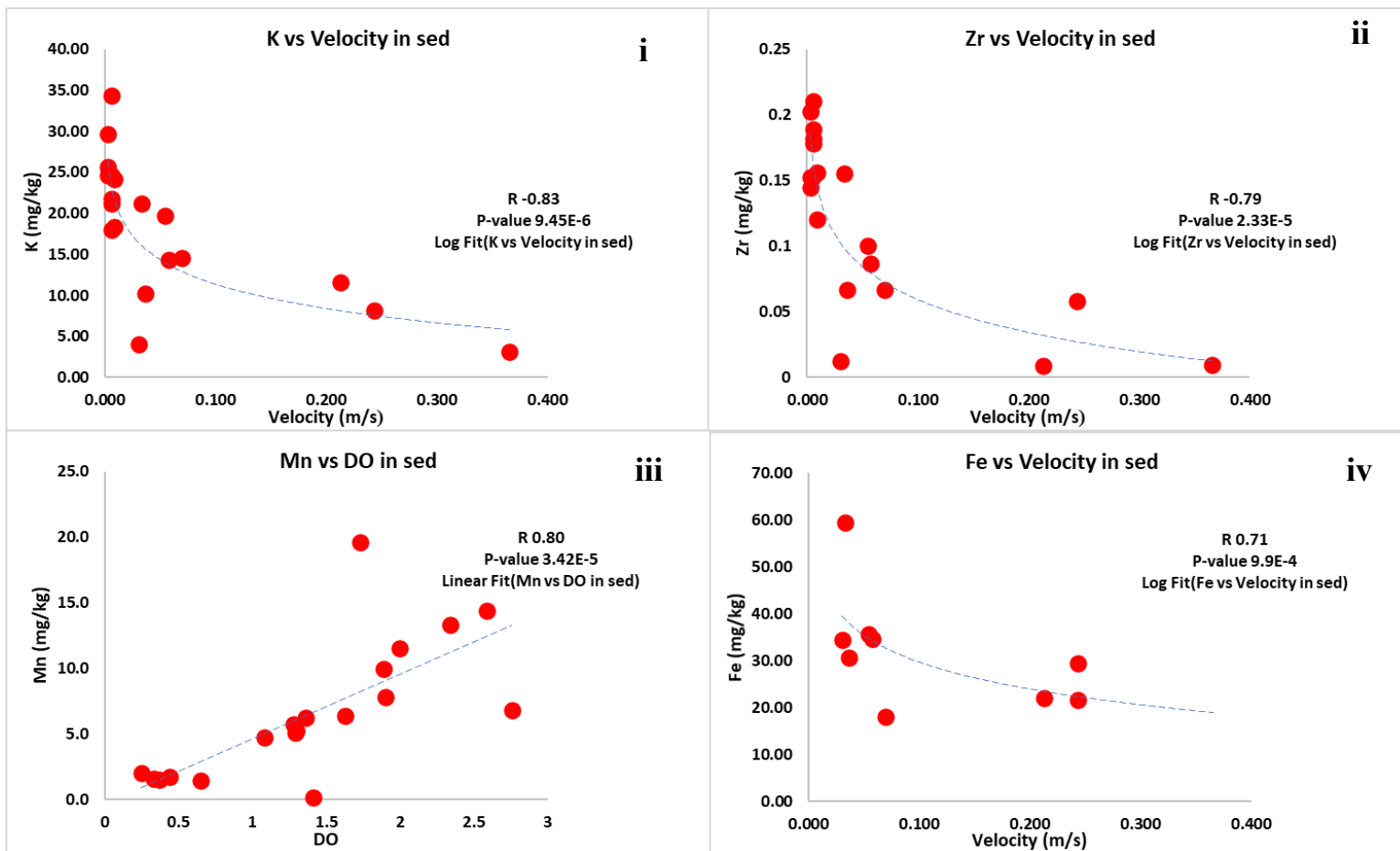


Figure 44 Relationship between variables; i) mean velocity vs K in sed, ii) mean velocity vs Zn in sed, iii) DO vs Mn in sed, iv) mean velocity vs Fe in sed

In terms of negative relationships, velocity and Mg or K in the sediment share a negative correlation. Higher velocity discharges in this study seemed to contain less Mg and K content than that of our lower flow environment. DO and Fe or SO₄ in the sediment also shared a negative relationship. Environments with higher DO are likely the site where precipitate may be formed, however precipitation into the streambed is more likely in lower velocity regions where DO may be not fully saturated yet. A number of the negative relationships with large R coefficients are represented in Figure 45.

Correlations between concentrations of ions in sediments. In this section a Spearman's rank correlation matrix was used to examine the correlations between collected for the following parameters at all four mine sites: Fe, Al, Mn, SO₄, NO₃, Ca, Mg, K, Ni, Zn, Cu, Li, Be, B, Ti, V, Cr, Ga, Ge, Rb, Sr, Zr, Cd, U, Ag, Cs, Ba, Pb, Bi, Co in sediments and all other sed ions which yielded non-significant results. Table 14 and Figures 45 and 46 illustrate some of the more important correlations.

In terms of positive relationships, Fe and SO₄ in the sediment shared a positive relationship as Fe and SO₄ are very likely to co precipitate according to the AMD reaction. NO₃ and Fe or SO₄ also share a positive correlation as NO₃ content was more prevalent in the precipitates of our Fe contaminated mine sites.

In terms of negative correlations, Mn and Fe or SO₄ in the sediment share a negative correlation as Mn oxides prefer more neutral environments and precipitated into the sediments at our Mn-dominated low-flow sites, naturally forming this negative correlation. Mg and Fe, SO₄, and NO₃ in the sediment also shared a negative

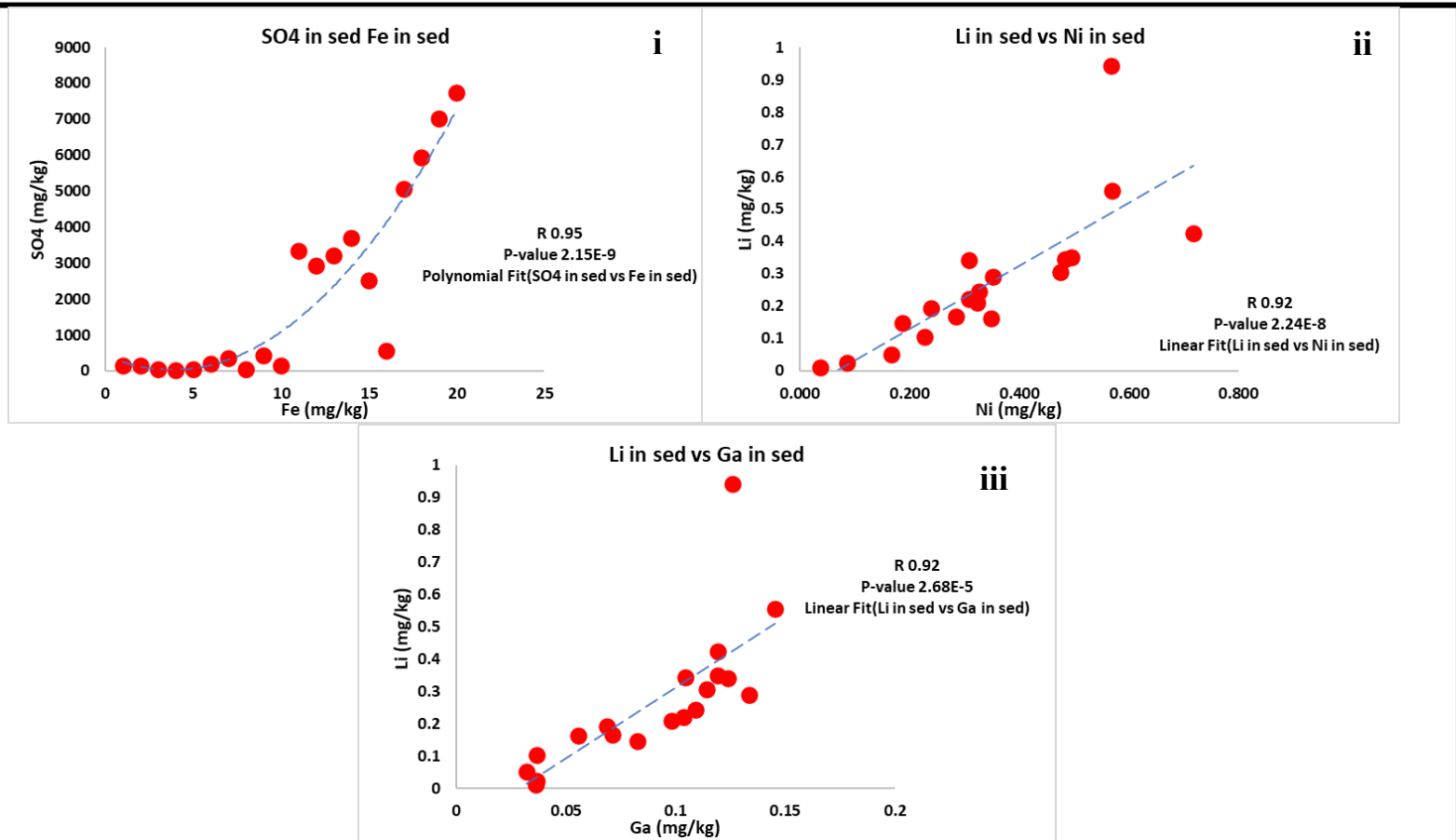
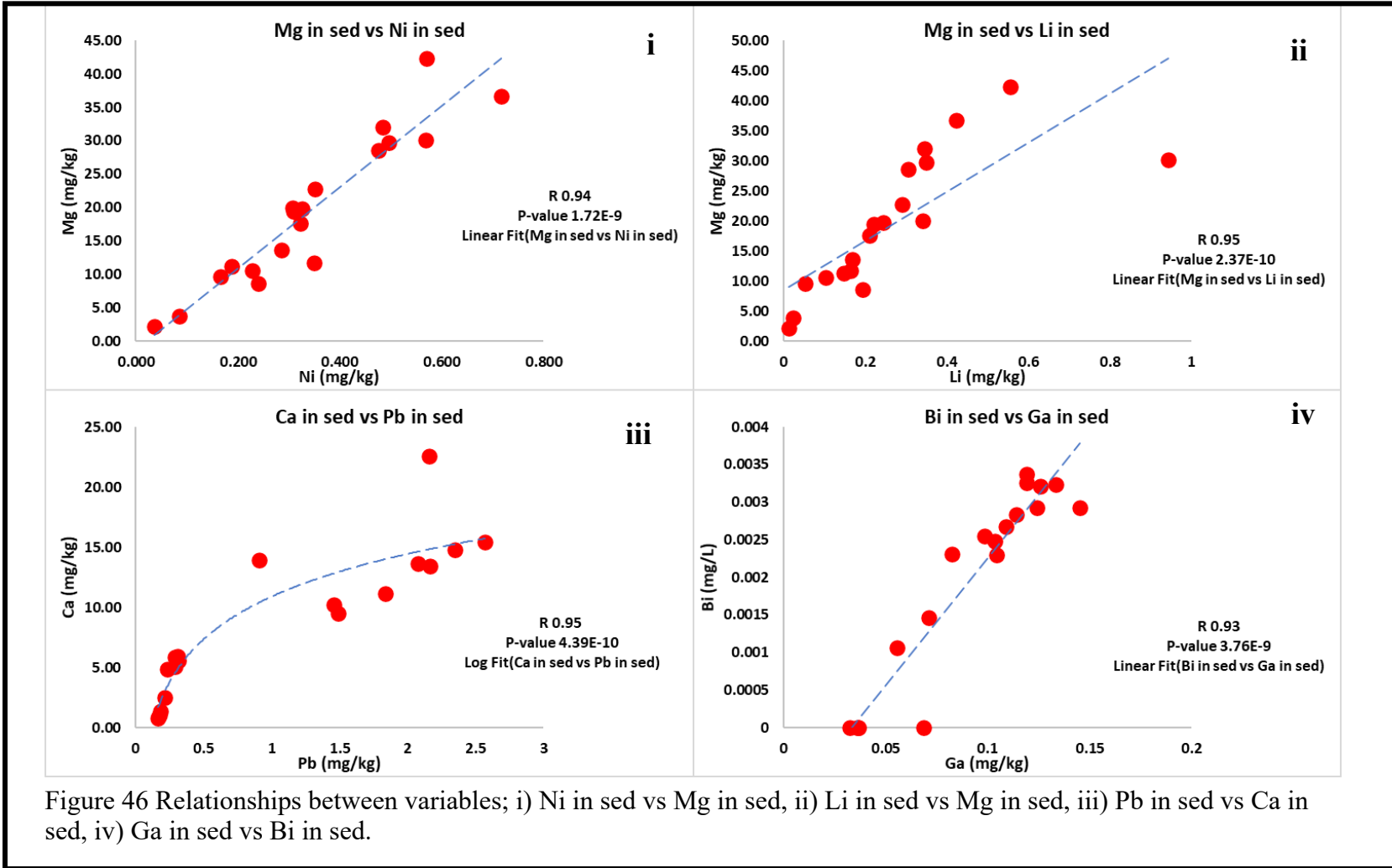


Figure 45 Relationship between variables; i) Fe in sed vs SO4 in sed, ii) Ni in sed vs Li in sed, iii) Ga in sed vs Li in sed.



relationship as regions where Mg was deposited into the sediments were in environments where Fe, SO₄, and NO₃ do not dominate the streambed.

Significant Correlations of Water Ions vs Sediment Ions ($p < 0.01$; $|R| \geq 0.80$)

In this section a Spearman's correlation matrix was used to examine the correlations of the data collected for all tested ions in the sediments and water at all four mine sites. Some of the more important relationships are displayed in Table 15 and Figures 47 and 48. NO₃ in water and Ca in the sediment shared a negative relationship where NO₃ is sourced from the organic matter content and Ca is largely from the dissolution of carbonate or clay minerals which has settled in the sediment through precipitation. Regions where NO₃ is elevated in the water means that there may be larger contributions from the organic matter to the water column. On the contrary, if Ca in sediments is larger, contributions from the carbonates or clay minerals in the mine are largely contributing to the chemical precipitates in the sediments. Mn in sediments and Na in water also shared a similar negative relationship. Mn in the sediments is mostly from co-precipitated manganese with iron minerals or precipitation of Mn oxides and Na in the water is largely from the dissolution of clay minerals in the mine.

Table 15 Results of Spearman's correlation for water ions and sediment ions with R values displayed for all significant relationships ($p < 0.01$).

All p-values < 0.01 : Blue = +R Red = -R Yellow Fill = R > 0.8	Fe in sed	Al in sed	Mn in sed	SO4 in sed	NO3 in sed	Ca in sed	Mg in sed	Na in sed	K in sed	Ni in sed	Zn in sed	Li in sed	Be in sed	B in sed	Ti in sed	V in sed
Fe in water	0.76			0.82	0.66	0.67										-0.65
Al in water	-0.60			-0.65	-0.60	-0.81			0.68				-0.57			0.61
SO4 in water		-0.65														
NO3 in water				-0.65		-0.86										
Ca in water						0.61									0.62	
Mg in water																
Si in water						-0.78										
Na in water			-0.85					-0.81								
K in water							0.73		0.72	0.64		0.66				
Ni in water			-0.71													
Cu in water			-0.67					-0.64								
Co in water			-0.73													
Li in water						-0.76								-0.62	-0.67	
NH4 in water								-0.59								
F in water											-0.68			-0.65		
Br in water			-0.67			0.67		-0.62							0.65	
Be in water	-0.63			-0.71	-0.59	-0.85					-0.61			-0.61		0.58
Ga in water						-0.63					-0.85			-0.59		
Ge in water						-0.67					-0.89			-0.63		
As in water											-0.71					
Rb in water									0.58							
Cs in water																
Ba in water	-0.66			-0.59							-0.80					
Pb in water											-0.80					
Fe 2+	0.69			0.80	0.57	0.87			-0.62		0.59			0.64		-0.73

Table 15 cont.

All p-values < 0.01 : Blue = +R Red = -R Yellow Fill = R > 0.8	Ga in sed	Ge in sed	As in sed	Rb in sed	Sr in sed	Zr in sed	Ag in sed	Cd in sed	Ba in sed	Pb in sed	Bi in sed	U in sed	Co in sed
	Fe in water	-0.60							0.65		0.68		
Al in water	0.66	-0.62				0.82	0.78			-0.61	0.59		
SO4 in water						0.80	0.57						
NO3 in water		-0.66				0.63				-0.68			
Ca in water					0.65					0.61			
Mg in water					-0.60								
Si in water	0.67					0.83					0.69		
Na in water													-0.63
K in water	0.60			0.76	0.80						0.61	0.64	
Ni in water												-0.68	-0.65
Cu in water													-0.65
Co in water												-0.63	-0.67
Li in water		-0.70			-0.64				-0.62	-0.83			
NH4 in water					0.81								
F in water										-0.64			
Br in water		0.64								0.70			
Be in water	0.60	-0.73				0.72	0.70			-0.80			
Ga in water						0.62	0.57						
Ge in water						0.67	0.67						
As in water													
Rb in water					0.63								
Cs in water			-0.56										
Ba in water													
Pb in water	0.61					0.61							
Fe 2+	-0.68	0.69				-0.73	-0.59			0.78			

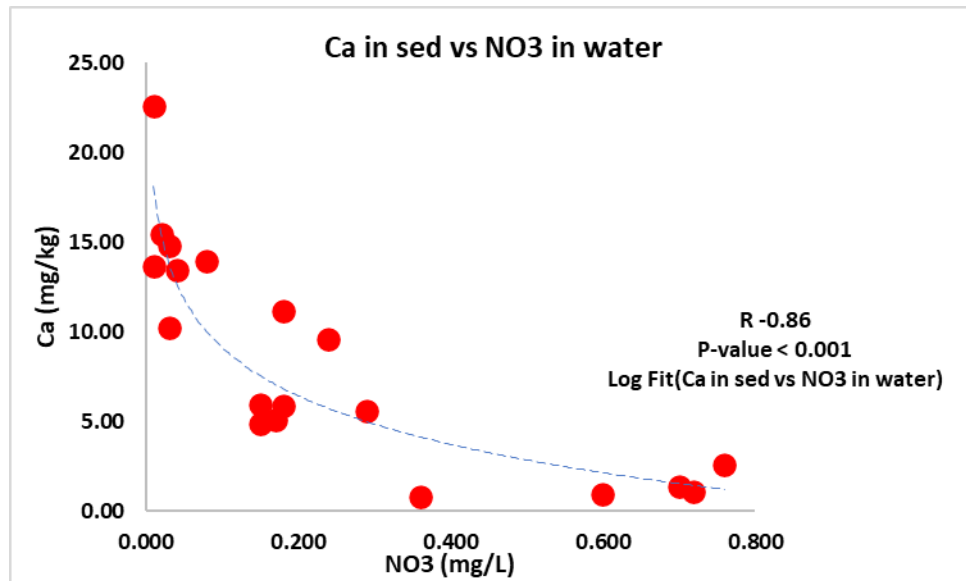


Figure 47 Negative correlation between Ca in sed and NO3 in water

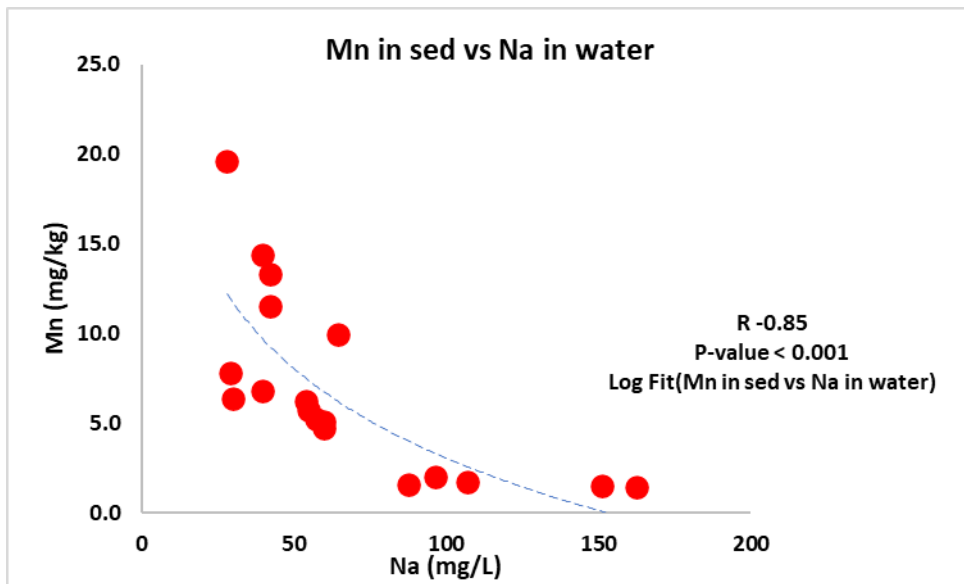


Figure 48 Negative correlation between Mn in sed and Na in water

Significant Correlations for Microbial Counts ($p < 0.01$; $|R| \geq 0.80$)

Field parameters vs microbes. In this section a Spearman's correlation matrix was used to examine the quality of the data collected for all of the listed field parameters and the following at all four mine sites: *Thiothrix* day 7, *Thiothrix* day 19, *Thiothrix* average count, *G. ferruginea* day 7, *G. ferruginea* day 19, *G. ferruginea* average count, *L. discophora* day 7, *L. discophora* day 19, *L. discophora* average count, and colony forming unit on pH 7 nutrient agar.

In terms of positive relationships, velocity and *Thiothrix* (Figure 49) or *G. ferruginea* shared a positive relationship. This is an expected relationship as these microbes dominated the colonization at our high (Esco) and medium (Pine Run) flow sites. *L. discophora* and Temperature also share a positive correlation as our more temperature equilibrated flow paths exhibited *L. discophora* as the dominant microbial species.

In terms of negative correlations, *Thiothrix* and temperature (Figure 50) share a negative correlation as *Thiothrix* can live in a wide range of temperatures and often prefers slightly colder temperatures. *G. ferruginea* and DO also shared a negative relationship, and *L. discophora* and velocity share a negative relationship which can be explained as *L. discophora* dominated the low flow environments of our Mn (York Clay) and Al (Sines) contaminated sites.

Table 16 Results of Spearman's correlation for field parameters and bacterial counts with R values displayed for all significant relationships ($p < 0.01$).

All p-values < 0.01 : Blue = +R Red = -R Yellow Fill = R > 0.8	cf.Thio7	cfThio19	cfThioAve	Gferr7	Gferr19	GferrAve	Ldisc7	Ldisc19	LdiscAve
	Velocity	0.60	0.74	0.62		0.69			
Temp	-0.86	-0.88	-0.87		-0.76			0.73	0.68
DO				-0.61					

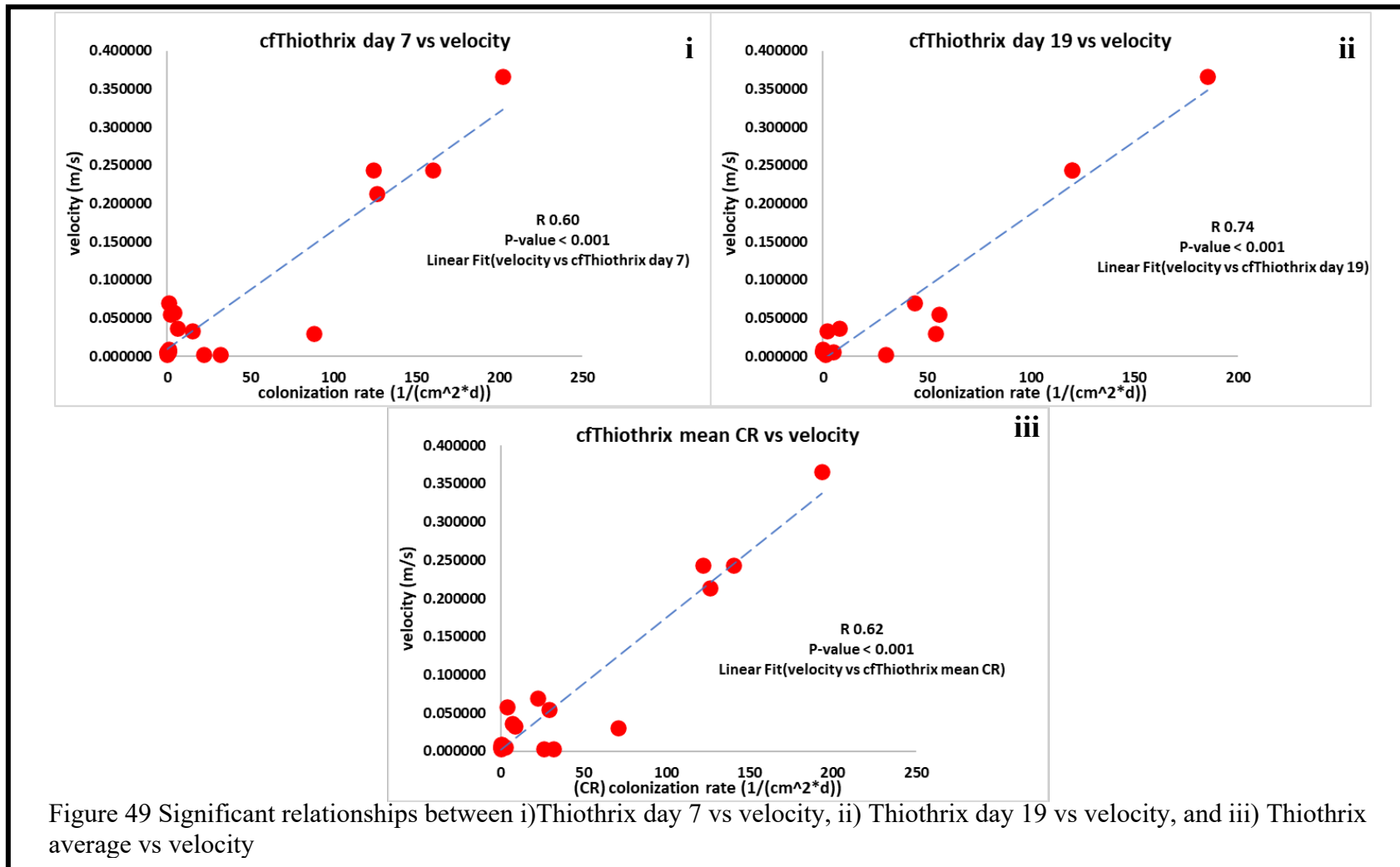


Figure 49 Significant relationships between i) Thiothrix day 7 vs velocity, ii) Thiothrix day 19 vs velocity, and iii) Thiothrix average vs velocity

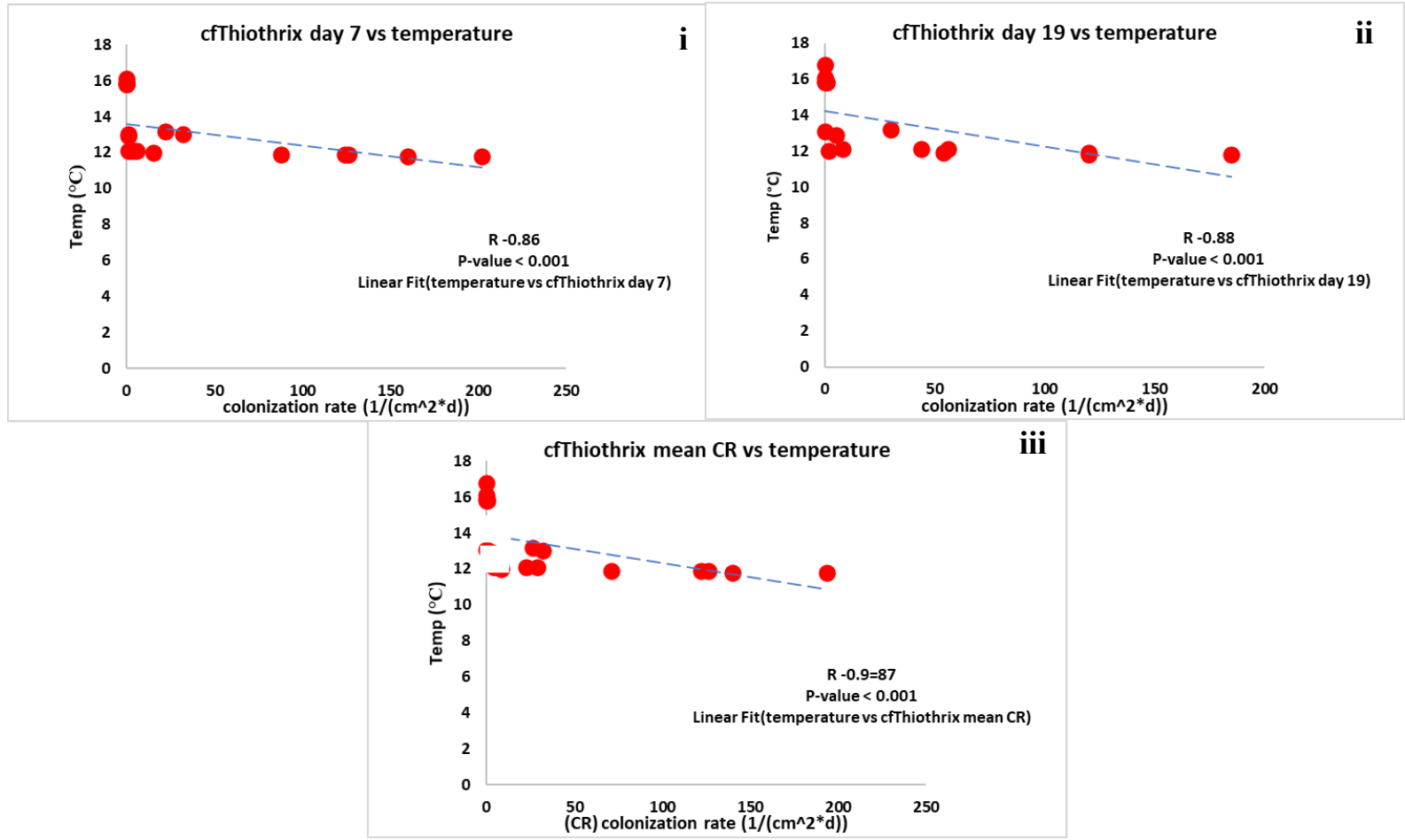


Figure 50 Significant relationships between i)Thiothrix day 7 vs temperature, ii) Thiothrix day 19 vs temperature, and iii) Thiothrix average vs teperature

Correlations between concentrations of ions in water and microbial counts. In this section a Spearman's univariate correlation matrix was used to examine the quality of the data collected for all tested water ions and all microbial counts (colony forming units and slide counts) at all four mine sites. Some of the more important relationships are presented in Table 17 and Figure 51.

In terms of positive relationships, Fe in water and *Thiothrix* or *G. ferruginea* shared a positive relationship. *G. Ferruginea* utilizes Fe in its energy generating pathway and *Thiothrix* utilizes inorganic forms of S which when oxidized co precipitates with Fe.

In terms of negative relationships, *Thiothrix* and Al or SO₄ in water share a negative correlation. *Thiothrix* correlates with velocity and hydroxylated alumino sulfates has formerly shared a relationship with velocity (Lopez et al., 1999). Al and SO₄ in the water are the precursors. *G. ferruginea* and Al or NO₃ in water also shared a negative relationship as *G. ferruginea* prefers Fe dominated settings and Al and NO₃ are decidedly low in concentration where *G. ferruginea* prevails. *L. discophora* and Fe in water share a negative correlation as *L. discophora* thrives in low flow systems dominated by Al (Sines) or Mn (York Clay) with plenty of carbon sources for energy generating reactions.

Table 17 Results of Spearman's correlation for water ions and bacterial counts with R values displayed for all significant relationships ($p < 0.01$).

All p-values < 0.01 : Blue = +R Red = -R Yellow Fill = R > 0.8	cf.Thio7	cfThio19	cfThioAve	Gferr7	Gferr19	GferrAve	Ldisc7	Ldisc19	LdiscAve
Fe in water		0.69	0.66		0.74	0.75		-0.66	-0.60
Al in water	-0.71	-0.81	-0.69		-0.80	-0.67			
SO4 in water	-0.89	-0.74	-0.74						
NO3 in water					-0.90	-0.67			
Si in water	-0.75	-0.79	-0.78		-0.84	-0.63			
Ni in water	-0.69								
Zn in water					-0.75				
Cu in water	-0.67								
Co in water	-0.71								
Li in water				-0.66	-0.87	-0.71			
F in water					-0.86				
Be in water	-0.59	-0.78	-0.70		-0.91	-0.79			
Ga in water	-0.66	-0.85	-0.76		-0.89	-0.63			
Ge in water	-0.68	-0.82	-0.76		-0.89	-0.65			
As in water		-0.85	-0.60		-0.89	-0.64			
Cd in water					-0.68				
Ba in water					-0.72	-0.59			
Pb in water		-0.69	-0.72		-0.79				

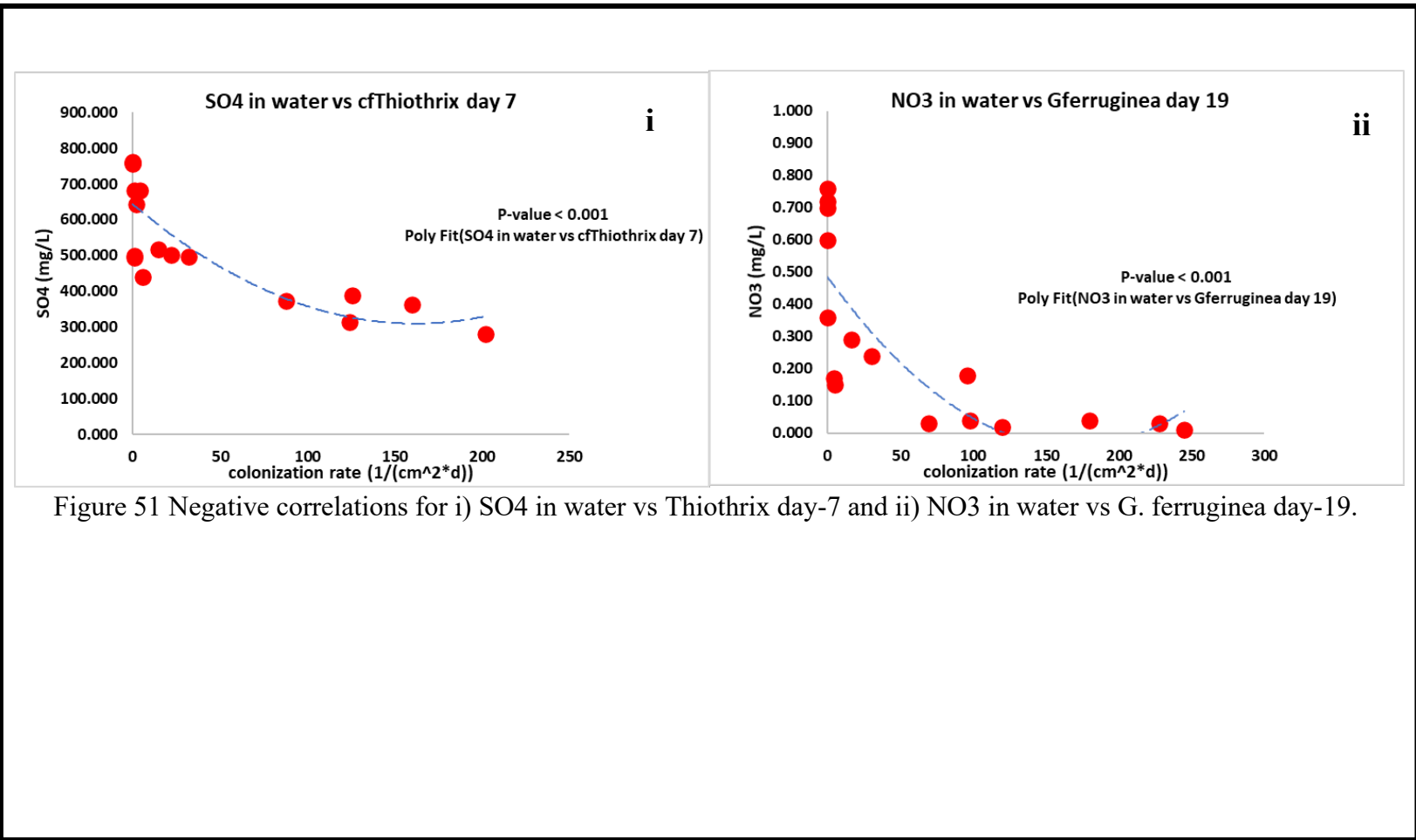


Figure 51 Negative correlations for i) SO4 in water vs Thiothrix day-7 and ii) NO3 in water vs G. ferruginea day-19.

Correlations between concentrations of ions in sediment and microbial counts. In this section a Spearman's correlation matrix was used to examine the quality of the data collected for all sediment ions and bacterial counts (cfu and slide) at all four mine sites. Some of the more important relationships are outlined in Table 18 and Figure 52.

Thiothrix and *Gallionella ferruginea* share positive correlations with SO₄ likely due to the utilization of inorganic forms of sulfur by *Thiothrix* which often accompanies reduced iron forms utilized by *Gallionella*. *Thiothrix* was largely correlated to the precipitation of hydroxylated alumino-sulfate minerals that constitute the white precipitates found at Esco No. 40 mine (Lopez et al., 1999). In this study of the Esco mine effluent, *Thiothrix* was identified as the most dominant species and the characteristic white precipitate of hydroxylated alumino-sulfates was found coating the bedload most prominently here (section 5.3.3). The strong positive relationship between *Thiothrix* and SO₄ indicates at the very least that *Thiothrix* is involved in the precipitation of hydroxylated sulfate precipitates. At Pine Run we noted more ferric iron mineral precipitates constituting a large portion of the stream bed forming a false bottom. Accompanying these precipitates is *G. ferruginea* which was shown to be encrusted in iron oxides in both the research completed in Lopez et al. 1999 and this study. This is confirmed through the positive correlation between colonization rates of *G. ferruginea* and Fe concentrations in the sediments.

Table 18 Results of Spearman's correlation for sediment ions and bacterial counts with R values displayed for all significant relationships ($p < 0.01$).

All p-values < 0.01 : Blue = +R Red = -R Yellow Fill = R > 0.8	cf.Thio7	cfThio19	cfThioAve	Gferr7	Gferr19	GferrAve	Ldisc7	Ldisc19	LdiscAve
Fe in sed					0.11	0.10			
SO4 in sed		0.55			0.48	0.49			-0.48
Ca in sed		-0.66			-0.36	-0.25			
Mg in sed		0.41							
Si in sed						-0.21		0.32	
Zn in sed					-0.34	-0.09			
Cu in sed			-0.53						
B in sed					0.49				
V in sed					-0.44				0.47
Cr in sed		-0.74	-0.72						
Ga in sed	0.29	0.50	0.41						
Ge in sed					-0.11	-0.07			
Zr in sed	0.11	0.06	0.13		-0.16				
Ag in sed		0.30			0.39	0.42			
Pb in sed				0.13	-0.43	-0.29			
Bi in sed	0.13	0.00	0.04						

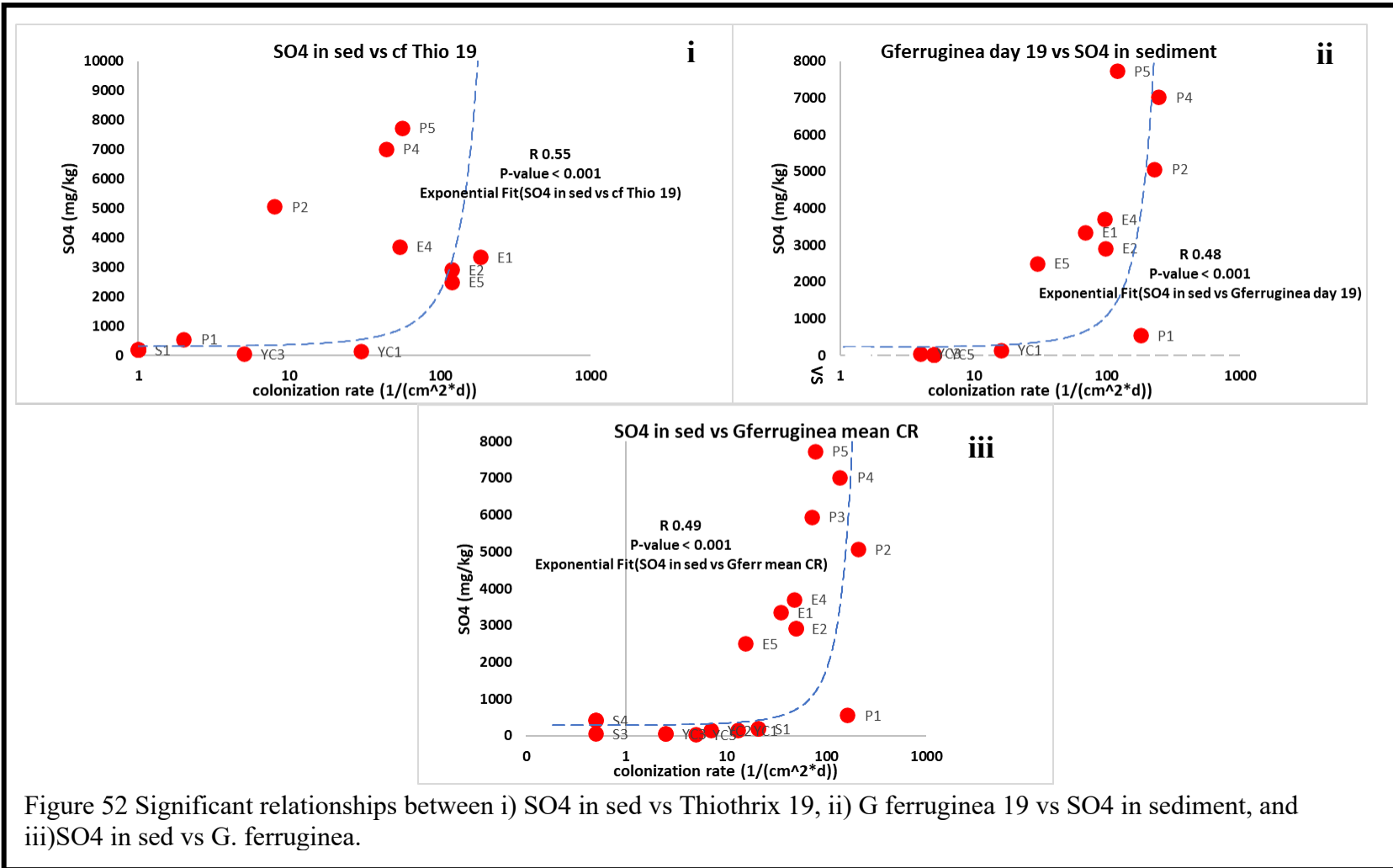


Figure 52 Significant relationships between i) SO₄ in sed vs Thiothrix 19, ii) G ferruginea 19 vs SO₄ in sediment, and iii) SO₄ in sed vs G. ferruginea.

5.3 Analysis of Sediments and Geochemical Modeling

5.3.1 Sediment Grain Size

Grain sizes were determined using a mesh sieve and a scale for sediment cores at each site. These values were averaged to determine the mean (Table 19) the following equation was used:

$$X = \sum_{x_i f_i} x_i$$

where X is the average grain size, and x_i can be determined by the following:

$$x_i = \frac{\text{Grain size A} + \text{Grain size B}}{2}$$

Average grain sizes were then plotted on a Hjulström curve (Figure 53). This plot indicated the state of the sediment based on either deposition, transportation, or fully entrained environments. The depositional environments we noted were closer to that of York Clay or Sines, transportation environments were like that of Pine Run, and a fully entrained system was closest to that of Esco mine discharge.

Table 19 Mean sediment size for samples collected at 0, 8, 15, 23, and 30 meters at each coal mine.

	York Clay	Sines	Essex 1	Pine 1
meters	Diameter (mm)	Diameter (mm)	Diameter (mm)	Diameter (mm)
0	0.544	0.545	1.360	0.639
8	0.777	0.556	0.785	0.614
15	0.575	0.533	1.015	0.602
23	0.666	0.554	1.159	0.539
30	0.645	0.541	0.887	0.619

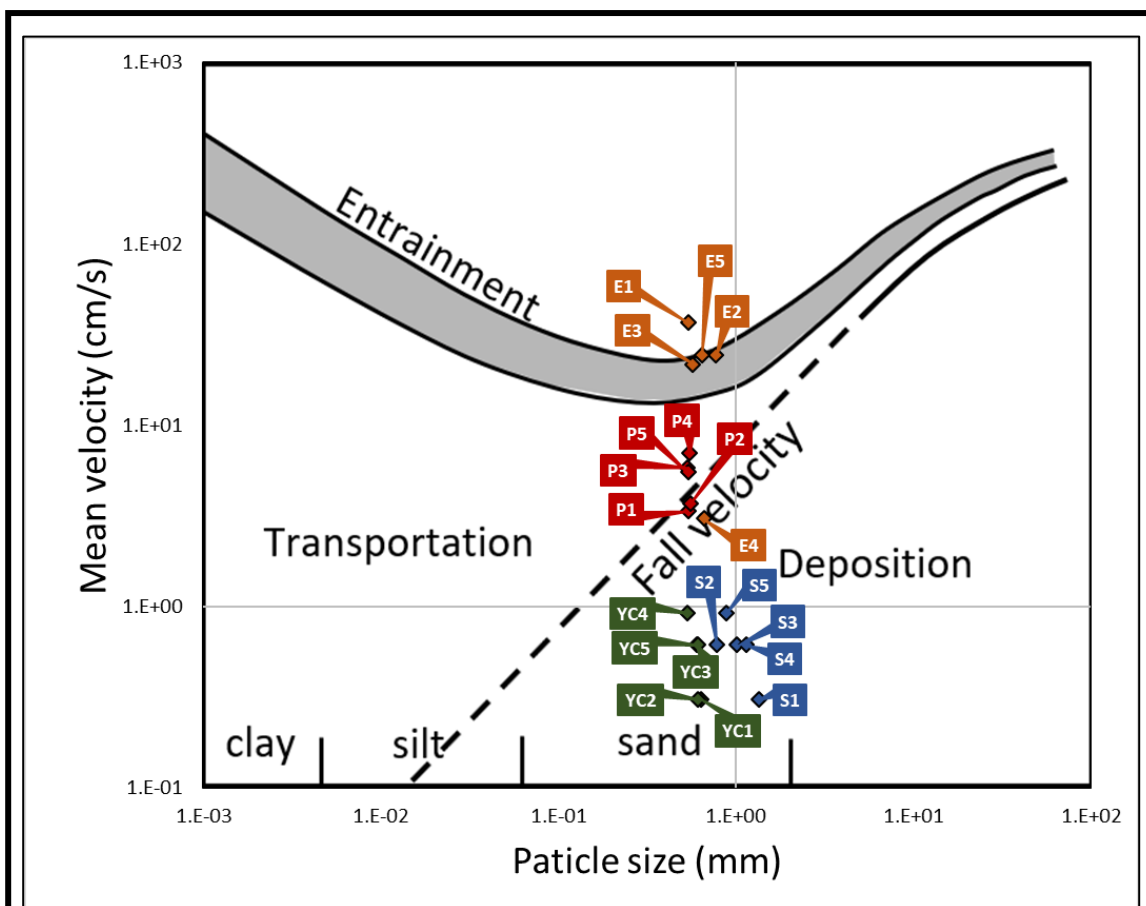


Figure 53 Plot of average grain size for all sites on a Hjulström curve adapted from Grabowski et al. (2011).

5.3.2 Sediment Grain Size vs All Parameters

In this section a Spearman's correlation matrix was used to examine the correlations of the data collected for all of the listed field parameters and the following parameters at all four mine sites: bacterial counts for Thiobacillus sp. day 7, Thiobacillus day 19, Thiobacillus average count, *G. ferruginea* day 7, *G. ferruginea* day 19, *G. ferruginea* average count, *L. discophora* day 7, *L. discophora* day 19, *L. discophora* average count, and colony forming unit (cfu) on pH 7 nutrient agar. Some of the important relationships are represented in Table 20, Table 21, and Figure 54. Thiobacillus shares a positive linear correlation with velocity as these microbes are favored at the higher velocity regions of the mine effluent. On day 7, 19, and average we consistently see Thiobacillus share a positive correlation to flow velocity as the unique morphology of Thiobacillus allows it to latch onto sediment in high velocity regions (Lopez et al., 1999). Thiobacillus also shares a negative correlation with temperature as *Thiobacillus* prefers colder temperatures similar to that of the groundwater (Koch et al., 2006).

Specific grain sizes recovered which were: (#18 (1 mm-coarse sand), #35 (0.5 mm-coarse/medium sand), #60 (0.25 mm-medium sand), #140 (0.105 mm-very fine sand), #270 (0.053 mm-coarse silt), and #635 sieves (0.008 mm-medium silt)). From the comparison of the weights recovered from each sieve at each site, significant positive correlations were present between SO₄ in water and sediment fraction lower than 0.25 mm, NO₃ in water and sediment fraction lower than 0.25 mm, *L. discophora* day-7 and sediment fraction lower than 0.5 mm, *L. discophora* day-7 and sediment fraction lower than 0.053 mm, *L. discophora* day-19 and sediment fraction lower than 0.25 mm,

Table 20 Results of Spearman's correlation for all measured grain sizes or mean min and max grain size with all other items (ions, field parameters, and bacterial counts) with R values displayed for all significant relationships ($p < 0.01$).

All p-values < 0.01 : Blue = +R Red = -R Yellow Fill = R > 0.8	Fe in water	SO4 in water	NO3 in water	Ca in water	Na in water	Cu in water	K in water	Li in water	NH4 in water	Br in water	Be in water	Ge in water	Rb in water	Ba in water	Pb in water	Fe2+	Vel	Cond	TDS	pH	DO
Diameter (mm)			0.82	-0.93				0.84	-0.66	-0.69	0.69					-0.29	-0.47				
Minimum Diameter (mm)	-0.50		0.10	0.34			0.52	-0.14				0.55	0.66	0.68	0.63		-0.59				
Maximum Diameter (mm)		-0.55			-0.67	-0.62				-0.61								-0.52	-0.54	0.51	0.67

Table 21 Cont.

All p-values < 0.01 : Blue = +R Red = -R Yellow Fill = R > 0.8	.25 mm	.105 mm	.053 mm	.008 mm	*Fe in water	**SO4 in water	**NO3 in water	*Be in water	Velocity (m/s)	pH	Fe in sed	Mn in sed	Ca in sed	K in sed	Zn in sed	Cu in sed	Be in sed	V in sed	Ge in sed	As in sed	Sr in sed	Zr in sed	Mo in sed	Cd in sed	Pb in sed
1 mm						-0.54		-0.68		0.44															
.5 mm	0.66	0.75	0.88	0.72	-0.65				-0.55		-0.61	0.61	-0.58	0.63	-0.58		-0.54	0.65	-0.65			0.59		-0.63	-0.64
.25 mm		0.75	0.73			0.67	0.61		-0.54								-0.62					0.61		-0.58	
.105 mm			0.92	0.65					-0.53							0.67				-0.62				-0.60	
.053 mm				0.78												0.64									
.008 mm																					0.66				

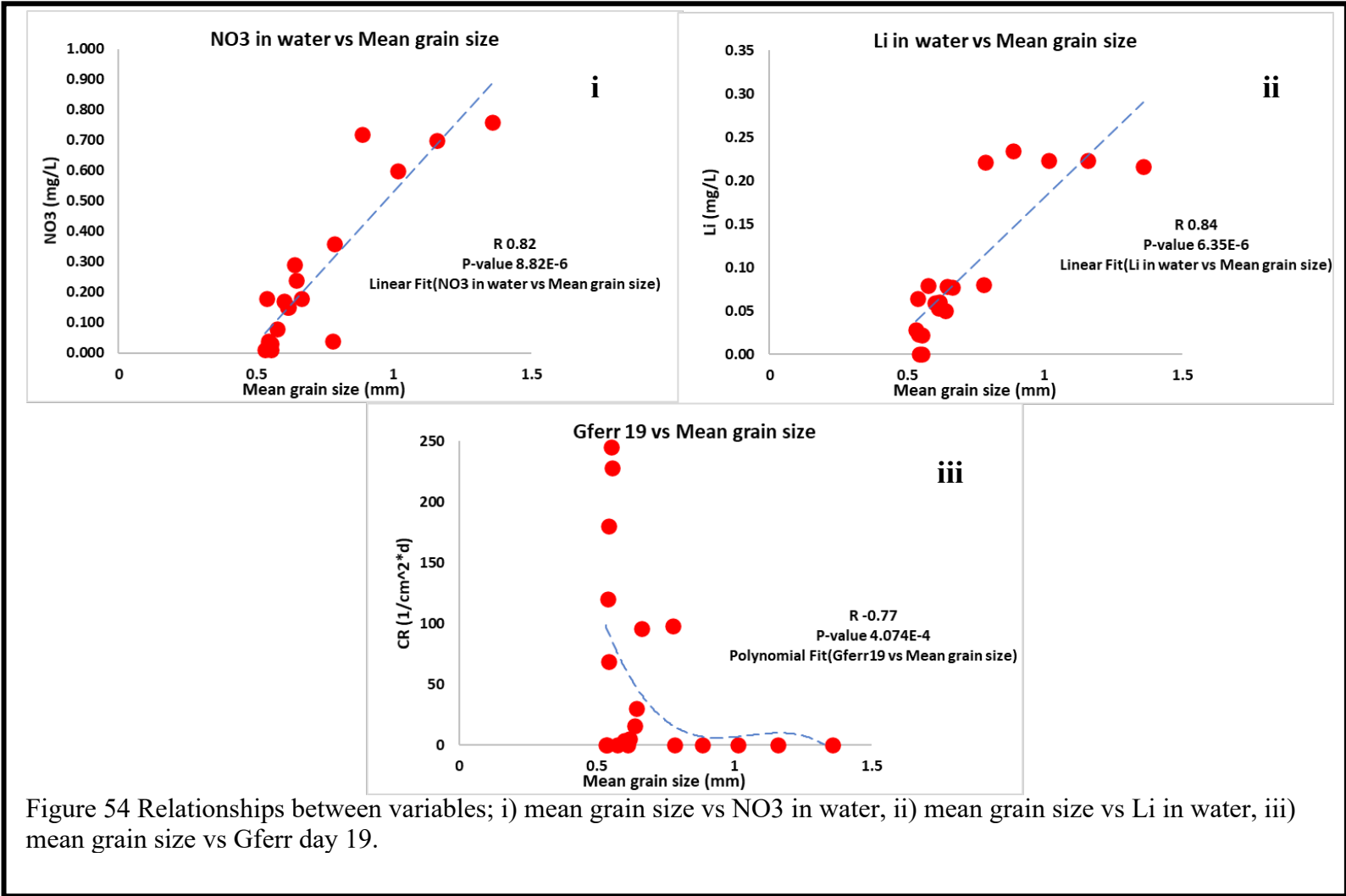


Figure 54 Relationships between variables; i) mean grain size vs NO3 in water, ii) mean grain size vs Li in water, iii) mean grain size vs Gferr day 19.

L. discophora average and sediment fraction lower than 0.5 mm, cfu counts and grain sizes lower than 0.105, 0.053, and 0.008 mm, and finally saturation indexes for amorphous $\text{Fe}(\text{OH})_3$ and sediment fraction lower than 1 mm. Significant negative correlations could be found for Fe in water and sediment fraction lower than 0.5 mm, SO_4 in water and sediment fraction lower than 1 mm, Fe in sed and sediment fraction lower than 0.5 mm, Velocity and the 0.5, 0.25, and 0.105 mm sediment fractions, As in sed and sediment fraction lower than 0.105 mm, *Thiothrix* day-7 and the sediment fraction lower than 0.25 and 0.105 mm, *Thiothrix* average and sediment fraction lower than 0.25 mm.

Notably the bedload collected in the first 30 meters of outflow is most likely to be more coarse in nature as velocity keeps colloidal forms of $\text{Fe}(\text{OH})_3$ entrained within the flow. Precipitation of Fe, and SO_4 in water at sediment fractions lower than 0.5 and 1 mm respectively is indicated by negative correlations suggesting at those grain sizes there is less of those specific ions in the water as they are most likely in the form of amorphous $\text{Fe}(\text{OH})_3$ and oxidized alumino-sulfates. Fe in sediment shows a negative relationship with the sediment fraction lower than 0.5 mm size which suggests reintroduction of Fe into the water column. The 0.5 mm fraction is technically coarse and medium sands and could likely show that this fraction is where Fe commonly switches between transport or saltation and full deposition into the bedload.

In terms of the microbial data *Thiothrix* has negative correlations with medium and very fine sand grain sizes which indicates that as more *Thiothrix* occupy these sediments, they utilize the inorganic forms of S from these compounds and promote

precipitation oxidized forms such as SO_4 in the sediments. *L. discophora* seems to share positive correlations with the 0.5, 0.25, and 0.53 mm grain sizes. This could suggest *L. discophora* favors sediments in the coarse silt to medium/coarse sand grain sizes.

Positive correlations shown for the smallest sized fractions (0.105, 0.053, and 0.008 mm) could suggest greater microbial diversity in the smaller grain size fractions but these only reflect acidophilic microbes that are capable of utilizing agar with circumneutral pH which may be selecting against species more limited to acidic ranges of mine drainage.

5.3.3 PHREEQCI Simulations and Different Precipitates

The main result generated using the program PHREEQCI with the WATEQ4F thermodynamic data base generated the mineral saturation index (SI) values for different minerals that could be forming in AMD conditions. SI values follow the equations:

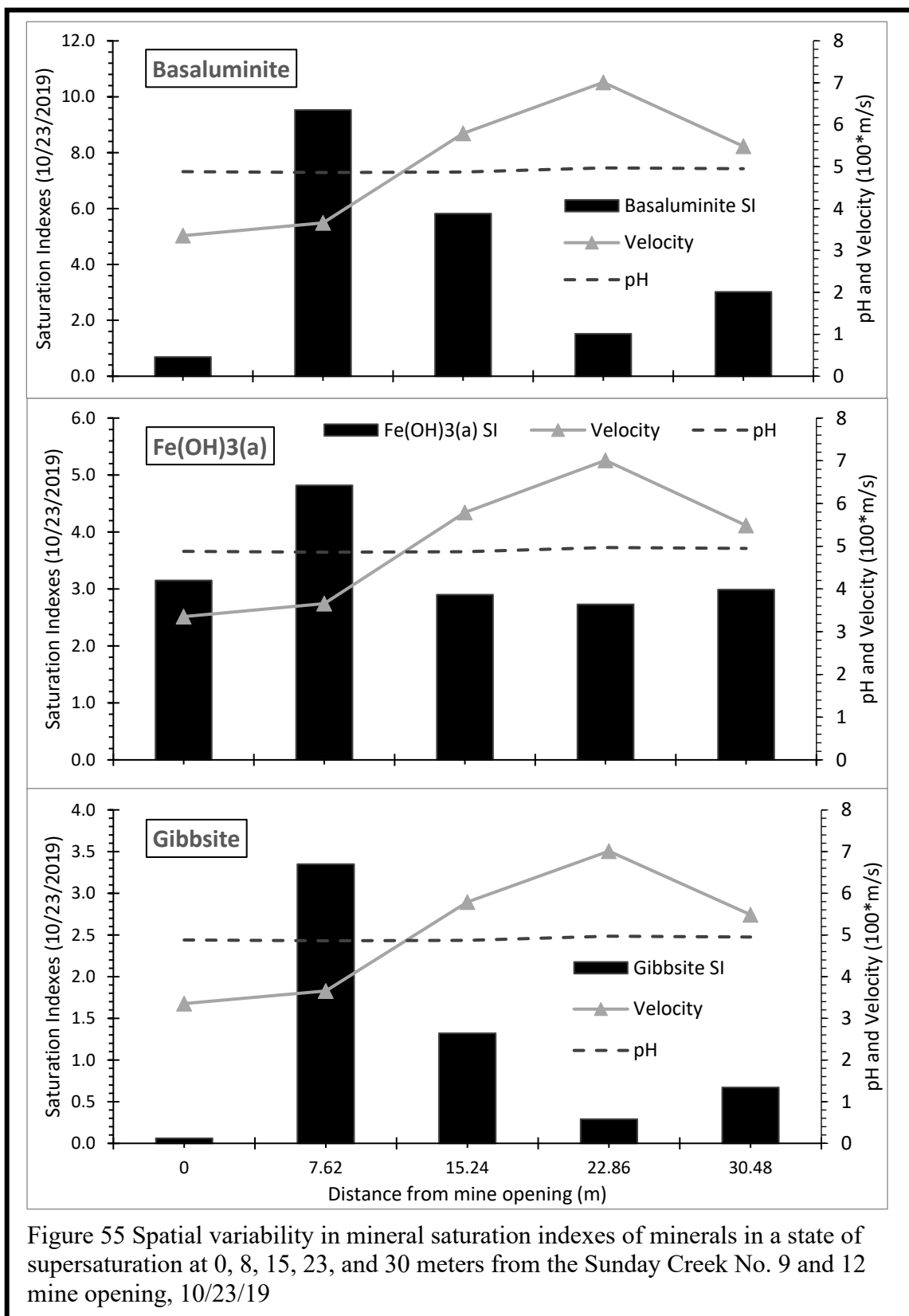
$$SI = \text{Log} \left(\frac{IAP}{KT} \right)$$

With ion activity product (IAP) and the equilibrium constant (K) for a specific temperature (T). This SI value generated can predict the extent to which a solution may be supersaturated or unsaturated for a particular mineral. This indicator is useful in determining a minerals precipitation or dissolution from solution (Drever, 1988).

WATEQ4F simulations were performed on the waters of each location and the resulting saturation index values are plotted against pH and velocity the following figures. Only minerals with instances of positive saturation index values were considered. These saturation index values provide insight into the precipitation or dissolution of the plotted minerals in the mine drainage along the flow path.

Pine Run Mine PHREEQCI Simulations

Effluent from the Pine Run coal mine was supersaturated with ten minerals were as follows: Alunite, $\text{Al}(\text{OH})_3(\text{a})$, Barite, Basaluminite, $\text{Fe}(\text{OH})_3(\text{a})$, Gibbsite, Goethite, Jarosite, Jurbanite, and Pyrolusite (Figure 56). Despite the supersaturated value, this does not always indicate the minerals presence in the precipitate as kinetics are not accounted for in PHREEQCI. The most abundant precipitate formed at Pine Run was Ferrihydrite or “yellow boy” which was found along the whole flow path forming a false bottom in the streambed. Based on the average pH (~ 5) of the waters at Pine Run, the most likely mineral precipitates to occur are Barite, Basaluminite, $\text{Fe}(\text{OH})_3(\text{a})$, Gibbsite, and Pyrolusite.



Esco No. 40 PHREEQCI Simulations

Effluent from the Esco mine was shown to be supersaturated with eight minerals which were as follows: Alunite, Barite, Basaluminite, $\text{Fe}(\text{OH})_3(\text{a})$, Gibbsite, Goethite, Jarosite, and Pyrolusite (Figure 56). Saturation values were absent from site one due to missing information needed to run the simulation. Trends of each mineral tended to vary in a similar fashion with overall increases in precipitation at site 5 from site 2 for Alunite, Barite, Basaluminite, $\text{Fe}(\text{OH})_3(\text{a})$, Gibbsite, Goethite, and Pyrolusite. The only variation from this trend was consistent levels of Jarosite saturation values. The most abundant precipitate formed at Esco was Ferrihydrite or “yellow boy” which was found along the whole flow path forming a false bottom in the streambed. There was also a white precipitate which in similar settings has been shown to be an alumino-sulfate hydroxide mineral by Robbins et al (1996) and could have a composition such as basaluminite. Based on the average pH (~5.7) of the waters at Esco, the most likely mineral precipitates to occur are $\text{Al}(\text{OH})_3(\text{a})$, Barite, Basaluminite, $\text{Fe}(\text{OH})_3(\text{a})$, Gibbsite, and Pyrolusite.

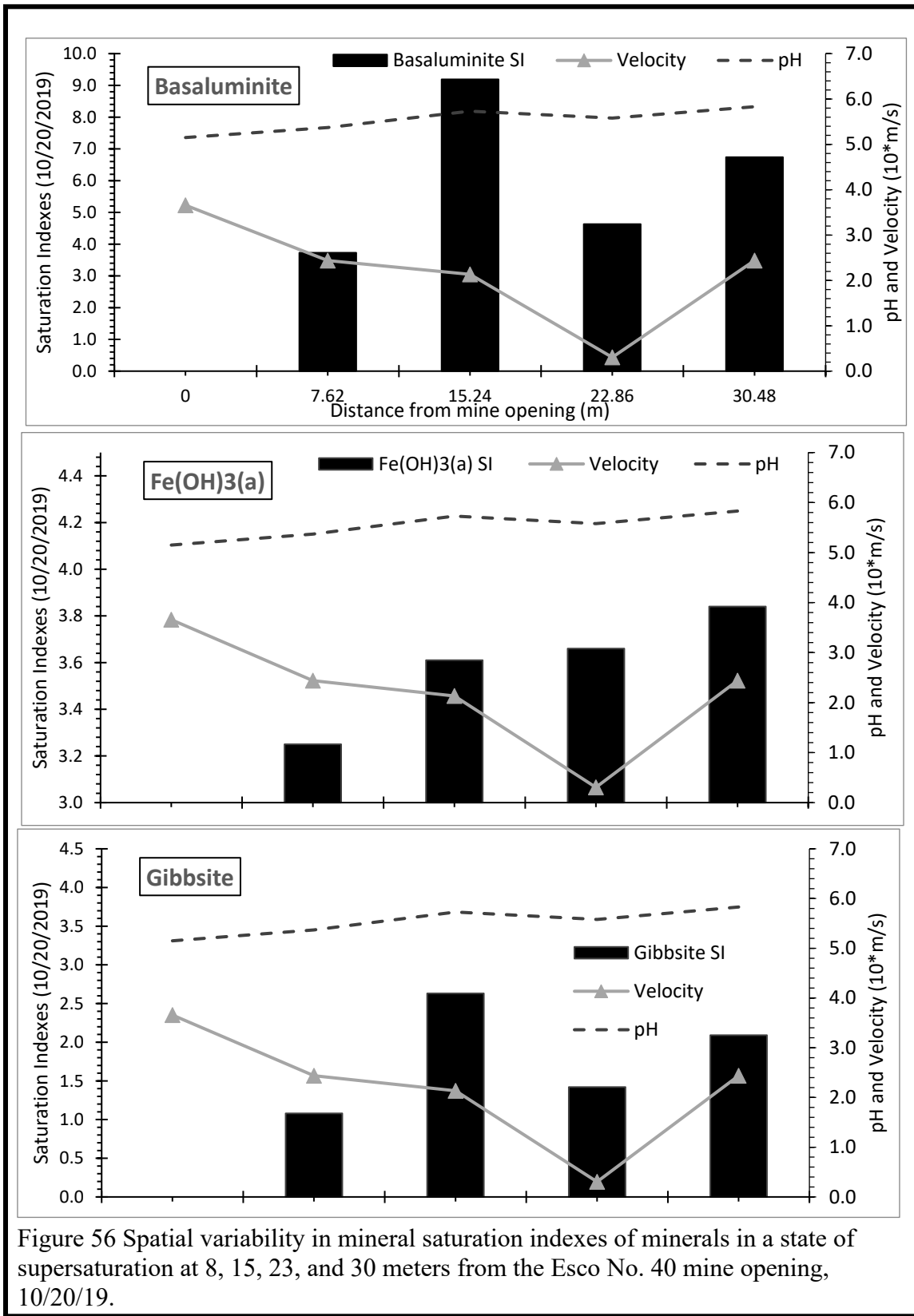
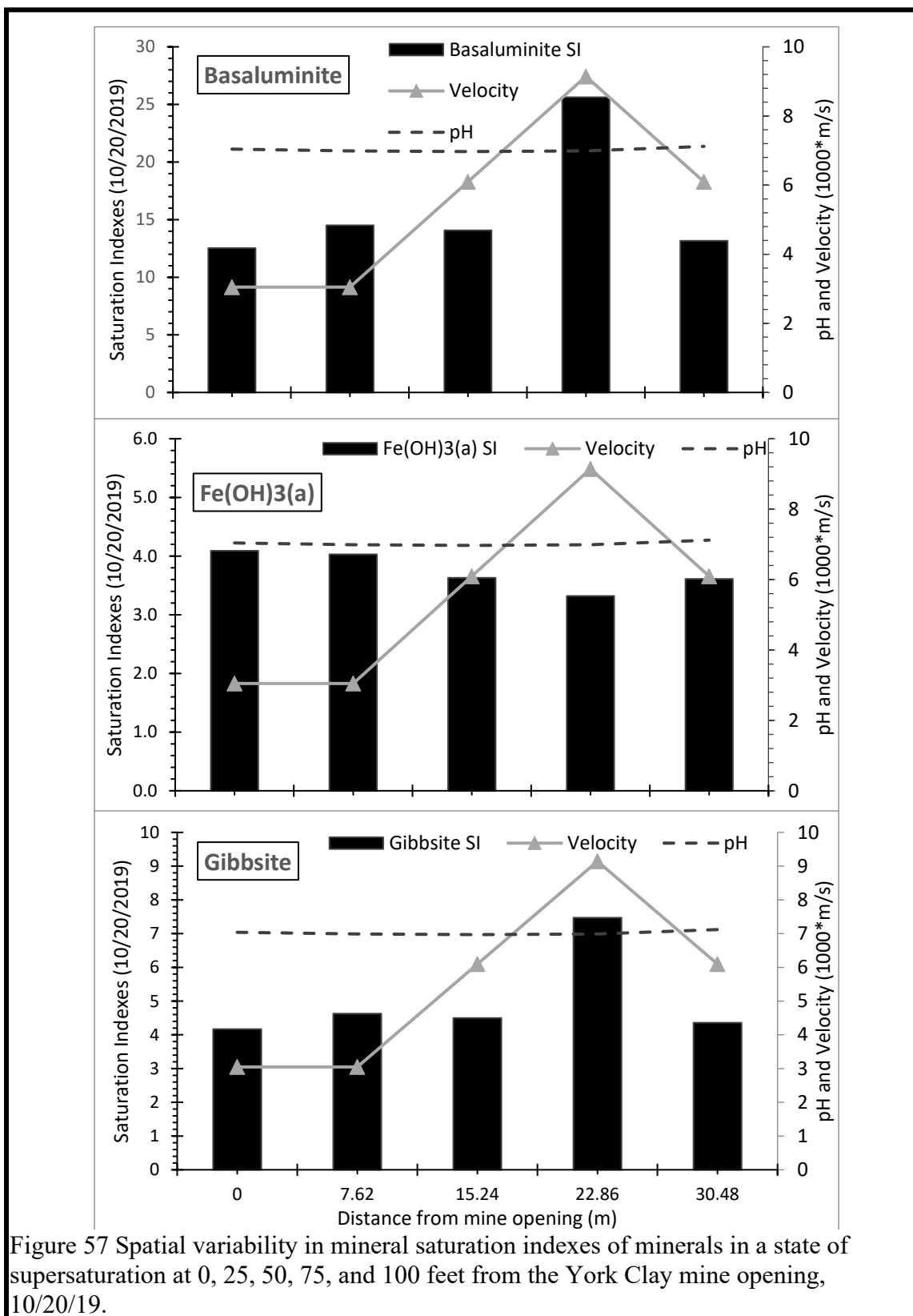


Figure 56 Spatial variability in mineral saturation indexes of minerals in a state of supersaturation at 8, 15, 23, and 30 meters from the Escro No. 40 mine opening, 10/20/19.

York Clay and Mining No. 4 PHREEQCI Simulations

Effluent from the York Clay coal mine was shown to be supersaturated with eleven minerals which were as follows: Alunite, $\text{Al}(\text{OH})_3(\text{a})$, Barite, Basaluminite, $\text{Fe}(\text{OH})_3(\text{a})$, Gibbsite, Goethite, Hausmannite, Jarosite, Jurbanite, and Pyrolusite (Figure 57). York Clay discharge showed almost no red minerals as ferrihydrite and only small amounts of white precipitate present similar to that shown at Esco mine. Based on the average pH (~ 7) of the waters at York Clay, the most likely mineral precipitates to occur are $\text{Al}(\text{OH})_3(\text{a})$, Barite, $\text{Fe}(\text{OH})_3(\text{a})$, Gibbsite, and Goethite.



Sines No. 2 PHREEQCI Simulations

Effluent from the Sines No. 2 coal mine was shown to be supersaturated with two minerals which were as follows: Barite and Goethite (Figure 58). Barite and Goethite showed some variation along the flow path however, remained relatively similar to the initial SI values at the mine opening. The most abundant precipitate formed at Sines was iron hydroxide which could occur as either Goethite or Ferrihydrite which was found at points along the flow path coating hard surfaces in the streambed. There was also a white precipitate present similar to that shown at Esco mine, just in a much smaller abundance. The saturation index for barite was probably too low to cause precipitation of this mineral, normally the saturation index has to be considerable higher than 0 to precipitate the mineral because the solution should produce initial mineral grains larger than some critical grain size that depends on the saturation index. Low saturation index would need a larger critical size crystal. The saturation index for barite was probably too low to cause precipitation of this mineral, normally the saturation index has to be considerable higher than 0 to precipitate the mineral because the solution should produce initial mineral grains larger than some critical grain size that depends on the saturation index. Low saturation index would need a larger critical size crystal. Based on the average pH (~2.3) of the waters at Sines, the most likely mineral precipitate to occur is Goethite.

Mineral Precipitates

Figure 59 through Figure 62 illustrate the various mineral precipitates found within the discharge for each site.

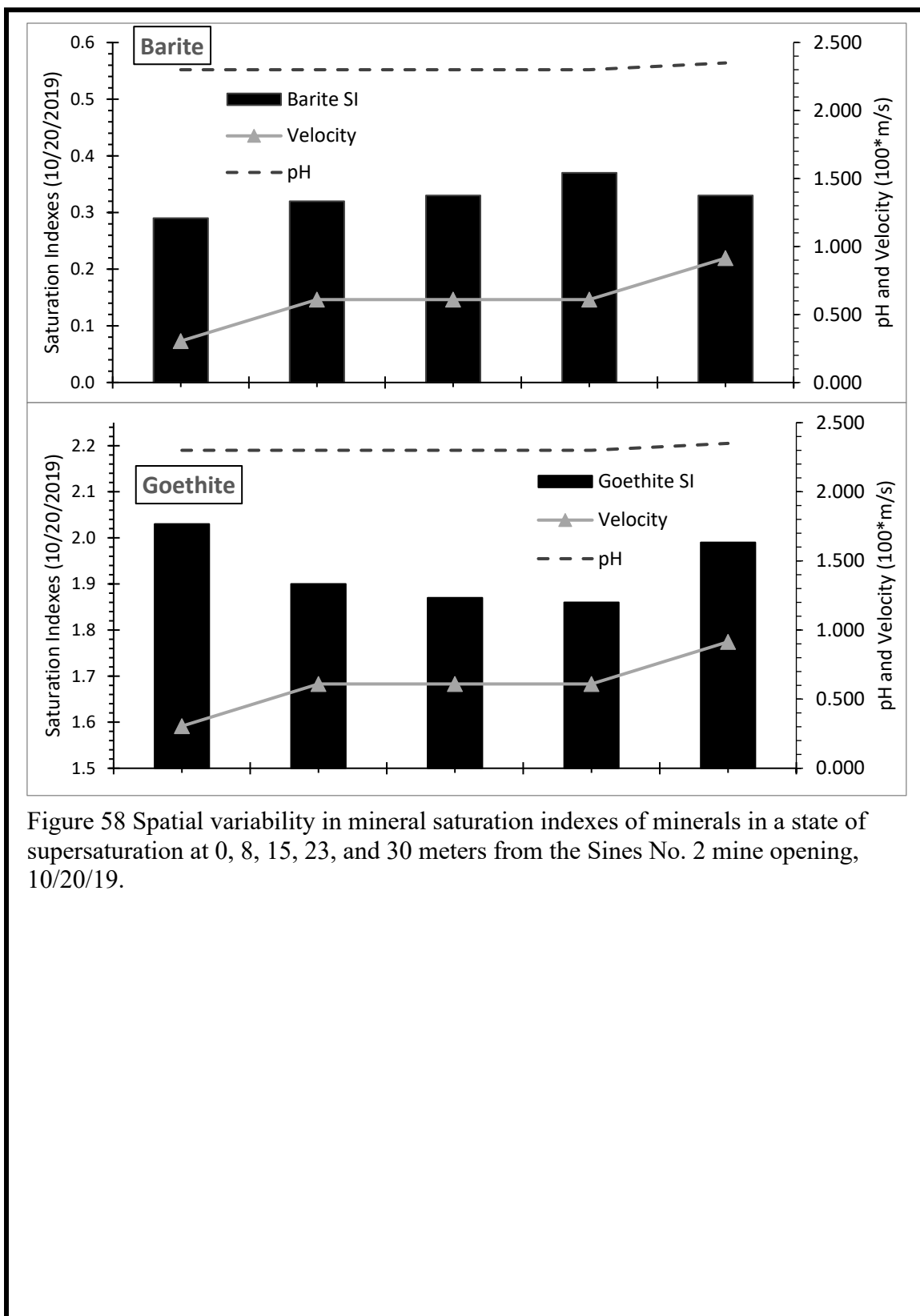


Figure 58 Spatial variability in mineral saturation indexes of minerals in a state of supersaturation at 0, 8, 15, 23, and 30 meters from the Sines No. 2 mine opening, 10/20/19.



Figure 59 Orange colored precipitates covering stream bed of the Esco No. 40 discharge, likely a form of iron III hydroxide precipitate. White mineral precipitate can also be noted likely precipitated hydroxylates aluminosulfates.



Figure 60 Orange colored precipitate of stream bed at Sines No. 2 discharge. This is likely precipitated iron hydroxide (yellowboy).



Figure 61 Yellow and orange colored mineral precipitate thickly coating stream bed of the Pine Run (Sunday Creek No. 9 and 12) mine effluent creating a false bottom. This is likely a large portion of iron hydroxide (yellowboy) deposition from accumulated forms of iron hydroxide.



Figure 61 (Continued)



Figure 62 White precipitate visible on the York Clay and Mining No. 4 effluent.

5.4 Microbial Ecology

5.4.1 Descriptive Analysis

This section of the thesis is reserved for findings from the microbial analyses performed at each mine site. While the correlations and data have already been presented in earlier sections, this section will display some of the key findings. Microbes were collected via suspended slides in the mine effluent at each site. Figure 63 shows the total yield of usable slides from each location. While not all of the slides were recovered, this data proved useful in determining colonization rates for the three target microbes.

Analysis of these slides was documented at 1000x magnification through bacterial counts for three groups of bacteria and documented as present or absent for other morphologic species fitting into two groups (gram \pm rods or cocci) Figures 64 through 75. Tables 22 through 26 were compiled for each site that indicate colonization rate of the microbes:

Thiothrix sp., *Gallionella ferruginea*, and *Leptothrix* sp. in $\frac{1}{(cm^2 day)}$ and presented in

sections that include imaging of the most relevant microbes.

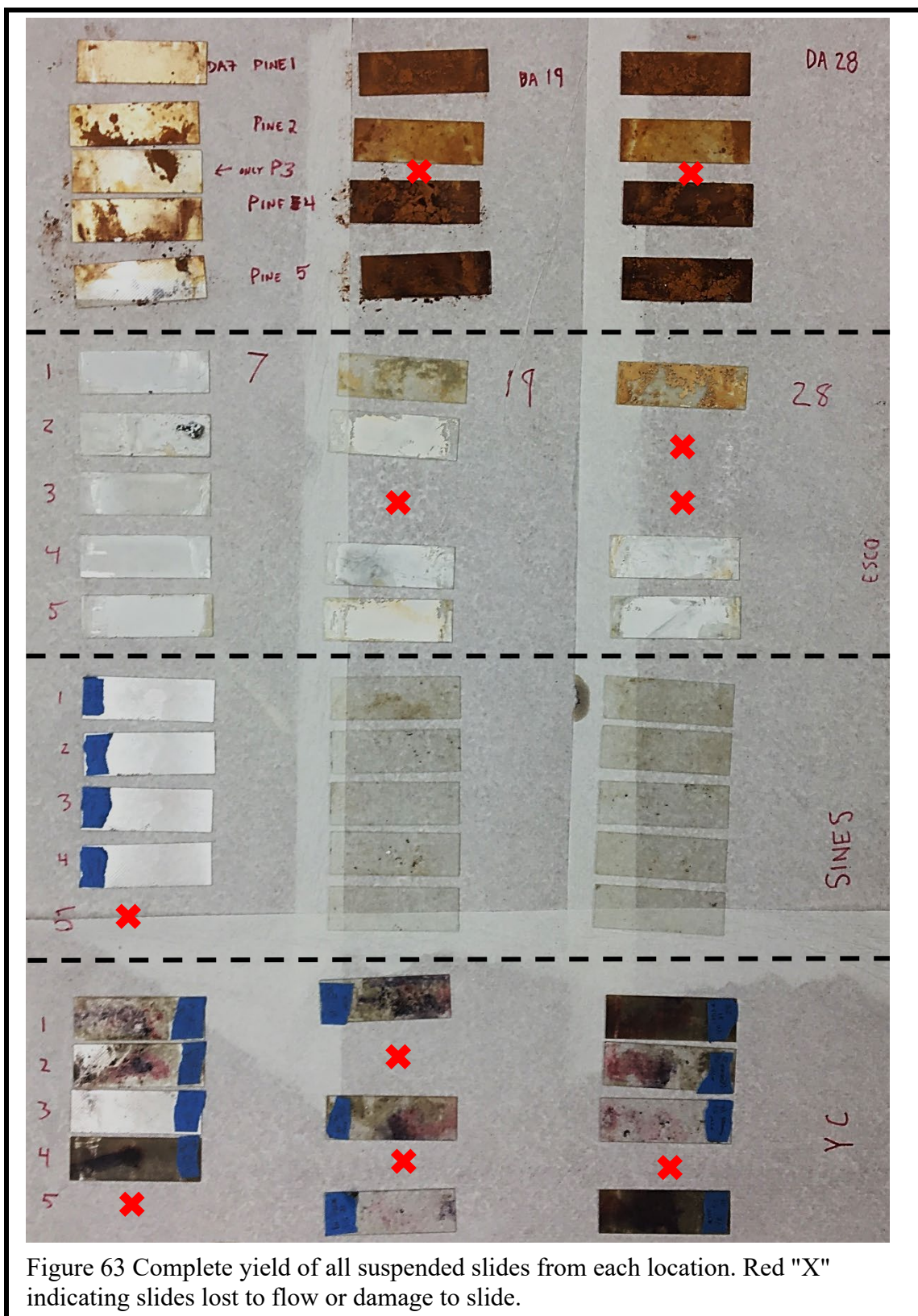


Figure 63 Complete yield of all suspended slides from each location. Red "X" indicating slides lost to flow or damage to slide.

Pine Run Mines Bacterial Slide Morphology

Table 22 Bacterial that settled on the glass slide contraptions located at 0, 8, 15, 23, and 30 meters in the Pine Run coal mine effluent from 10/23/2019-11/17/2019. Colonization rate averages (1/cm²d) are provided for the three major species evaluated.

Pine Run Coal Mine	Distance from Mine Opening				
Parameters	0 meters	7.62 meters	15.24 meters	22.86 meters	30.48 meters
pH	4.88	4.86	4.87	4.97	4.95
DO (mg/L)	0.25	0.33	0.37	0.44	0.65
Conductivity (µS)	1214	1215	1222	1219	1221
Temperature (°C)	12	12.1	12.1	12.1	12.1
stalks of <i>G. ferruginea</i> (colonization rate: CR)	144	179	72	135	65
holdfasts of <i>L. discophora</i> (CR)	1	5	1	6	1
cf. <i>Thiothrix</i> (CR)	6	6	4	18	20
Gram + rods	+	+	+	+	+
Gram - rods	+	+	+	+	+
Gram + cocci	+	+	+	+	+
Gram - cocci	-	-	-	-	-

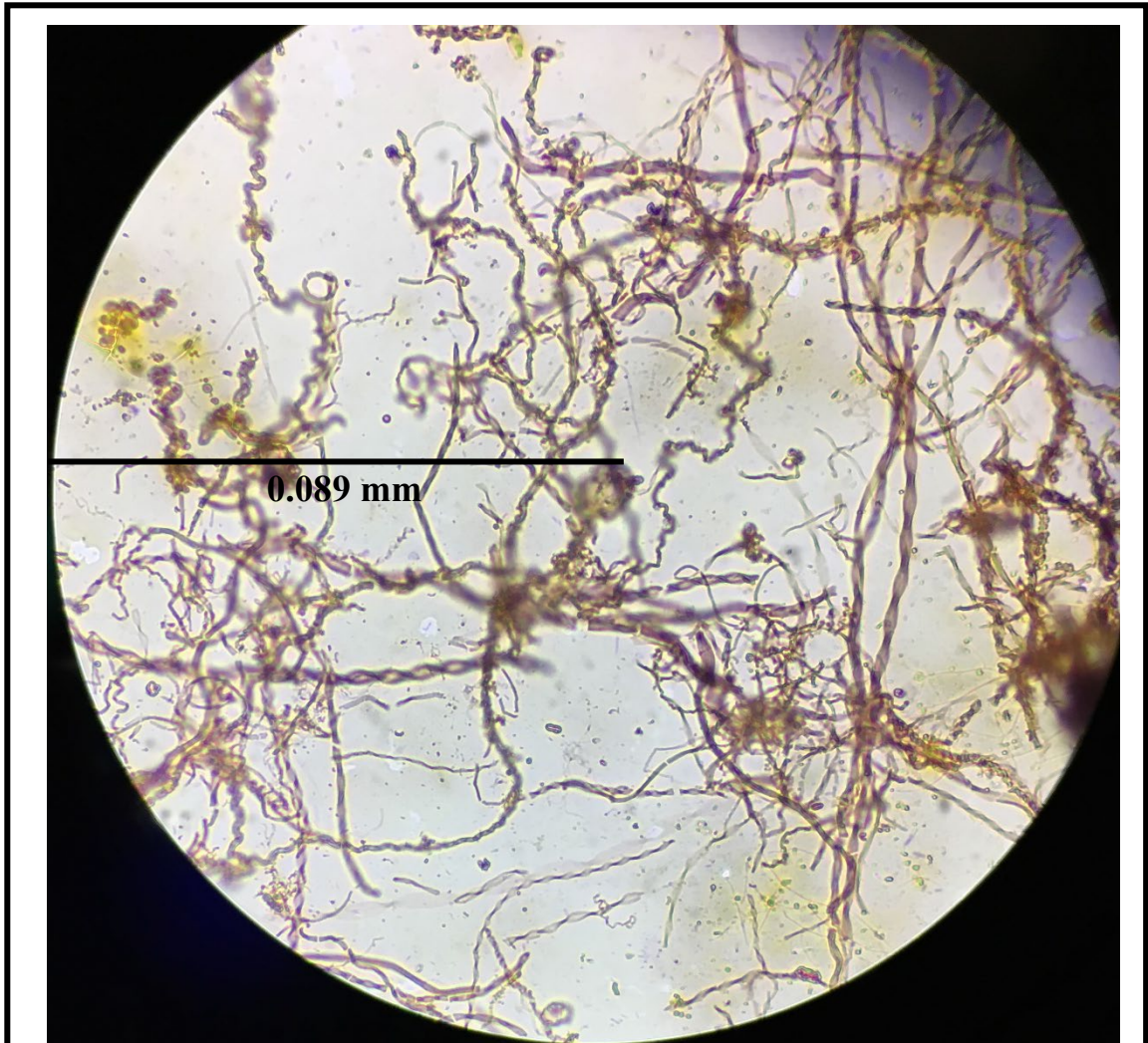


Figure 64 *Gallionella ferruginea*, single gram + cocci, and single gram + rods from the outflow of Sunday Creek No. 9 and 12 at Pine Run (1000x).

Esco No. 40 Mine Bacterial Slide Morphology

Table 23 Bacterial that settled on the glass slide contraptions located at 0, 8, 15, 23, and 30 meters in the Esco No. 40 coal mine effluent from 10/23/2019-11/17/2019. Colonization rate averages (1/cm²d) are provided for the three major species evaluated.

Esco No. 40 Coal Mine Parameters	Distance from Mine Opening				
	0 meters	7.62 meters	15.24 meters	22.86 meters	30.48 meters
pH	5.15	5.37	5.73	5.58	5.83
DO (mg/L)	1.41	1.80	1.90	1.63	1.73
Conductivity (μS)	830.90	807.70	802.50	805.90	805.40
Temperature (°C)	11.8	11.8	11.9	11.9	11.9
stalks of <i>G. ferruginea</i> (colonization rate: CR)	36	50	0	49	16
holdfasts of <i>L.</i> <i>discophora</i> (CR)	2	0	0	1	3
cf. <i>Thiothrix</i> (CR)	193.5	140	126	71	122
Gram + rods	+	+	+	+	+
Gram - rods	+	+	+	+	+
Gram + cocci	+	+	+	+	+
Gram - cocci	-	-	-	-	-

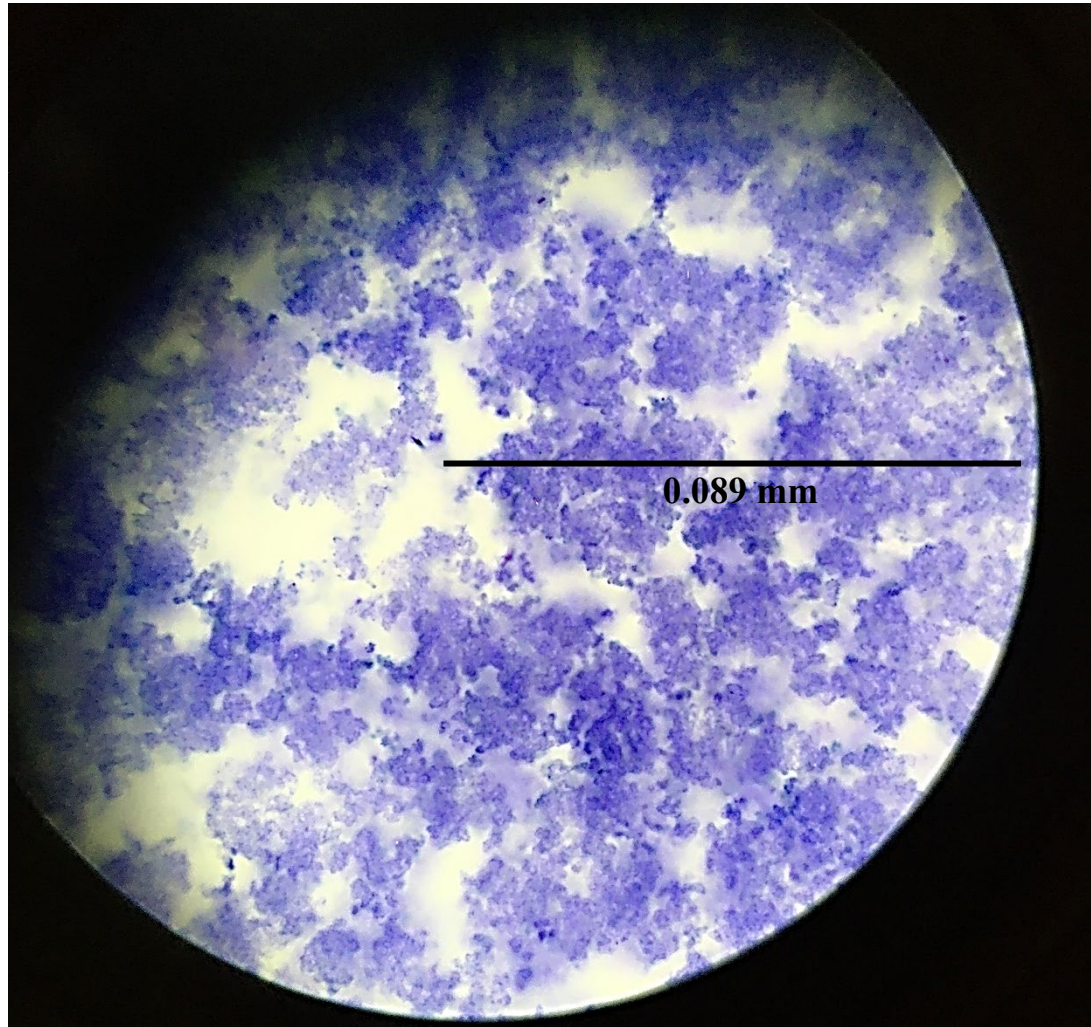


Figure 65 Thiobacillus Gram + rods (single) and cocci (clusters and single) isolated from Esco No. 40 outflow (1000x).

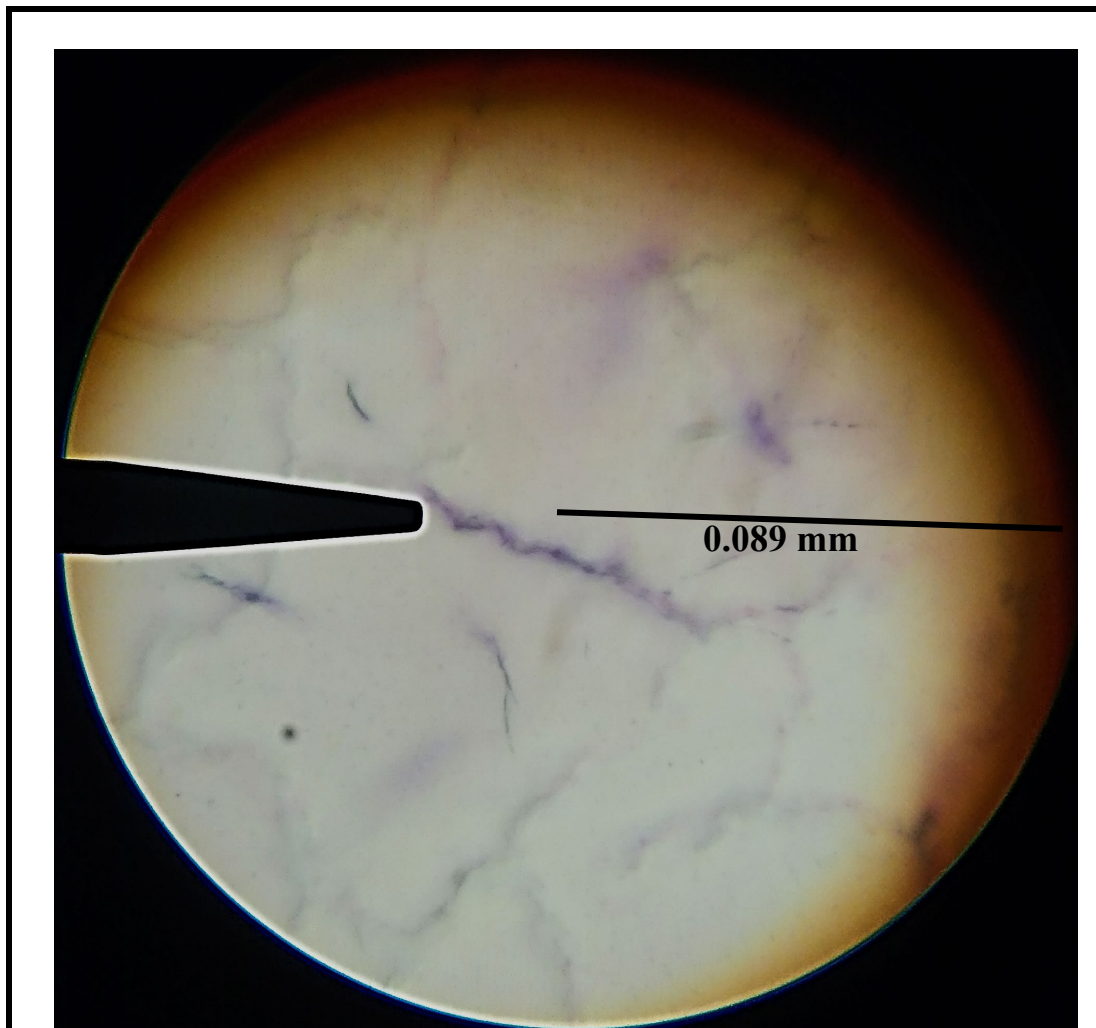


Figure 66 *Gallionella ferruginea* gram - isolated from Esco No. 40 (1000x).

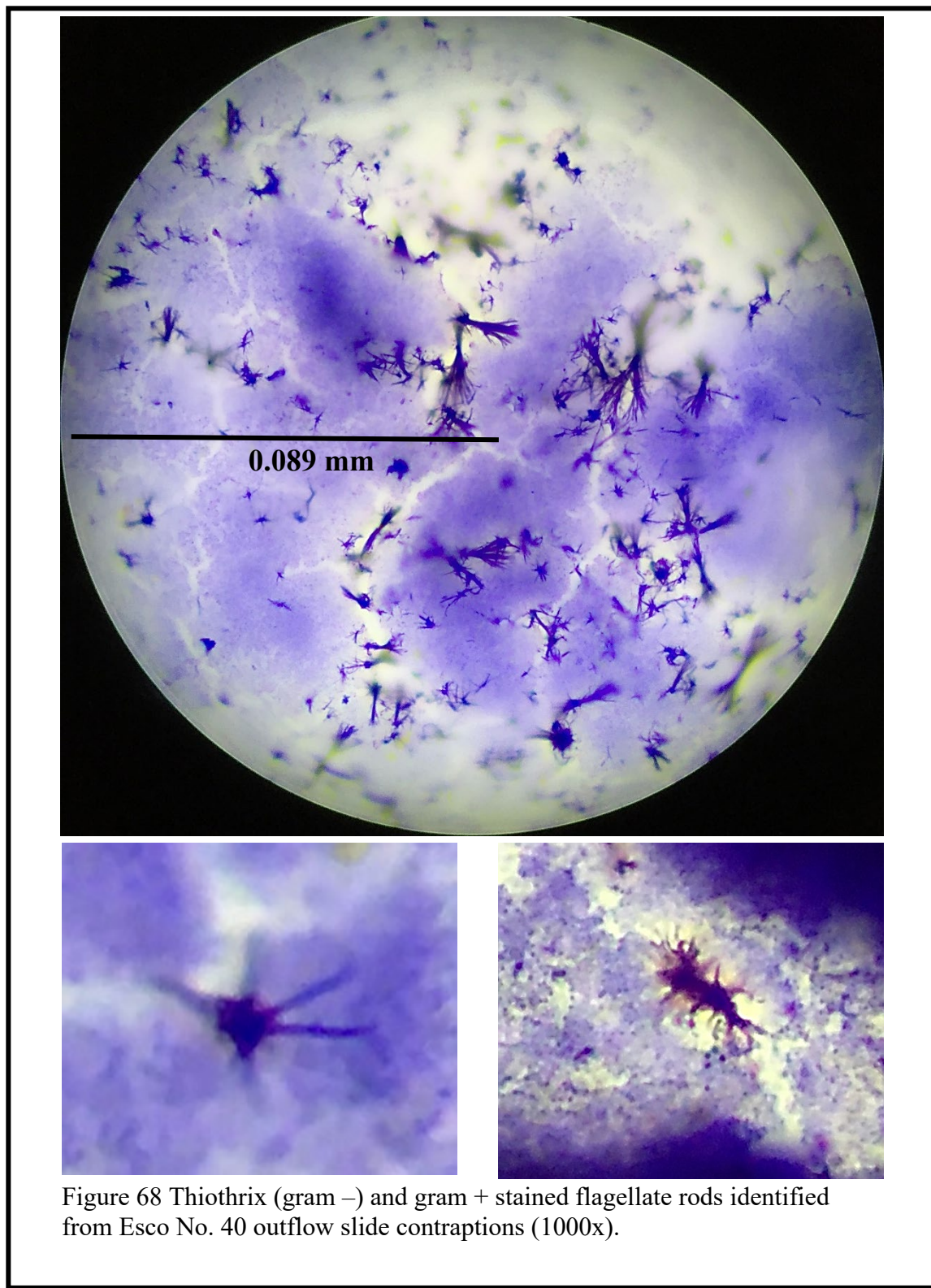


Figure 68 Thiobacillus (gram -) and gram + stained flagellate rods identified from Esco No. 40 outflow slide contraptions (1000x).

York Clay and Mining No. 4 Bacterial Slide Morphology

Table 24 Bacterial that settled on the glass slide contraptions located at 0, 8, 15, 23, and 30 meters in the York Clay Mine coal mine effluent from 10/23/2019-11/17/2019. Colonization rate averages (1/cm²d) are provided for the three major species evaluated.

York Clay Coal Mine	Distance from Mine Opening				
Parameters	0 meters	7.62 meters	15.24 meters	22.86 meters	30.48 meters
pH	7.04	6.99	6.97	6.99	7.12
DO (mg/L)	2.59	2.34	2.00	1.89	2.76
Conductivity (µS)	310.20	280.20	279.60	270.00	281.80
Temperature (°C)	13.2	13.0	12.9	13.0	13.1
stalks of <i>G. ferruginea</i> (colonization rate: CR)	13	7	3	0	5
holdfasts of <i>L. discophora</i> (CR)	22	60	5	4	5
cf. <i>Thiothrix</i> (CR)	26	32	3	1	0
Gram + rods	+	+	+	+	+
Gram - rods	+	+	+	+	+
Gram + cocci	+	+	+	+	+
Gram - cocci	-	-	+	-	+

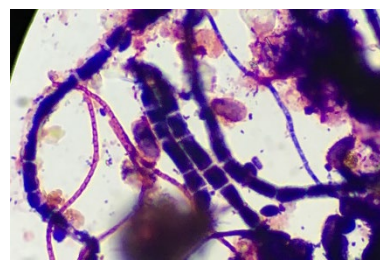
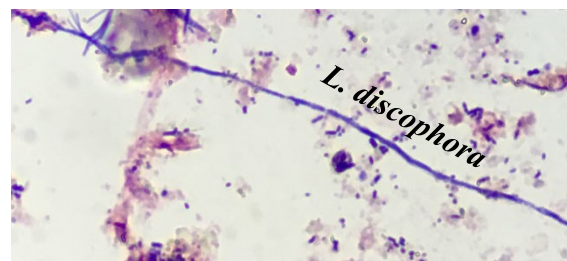
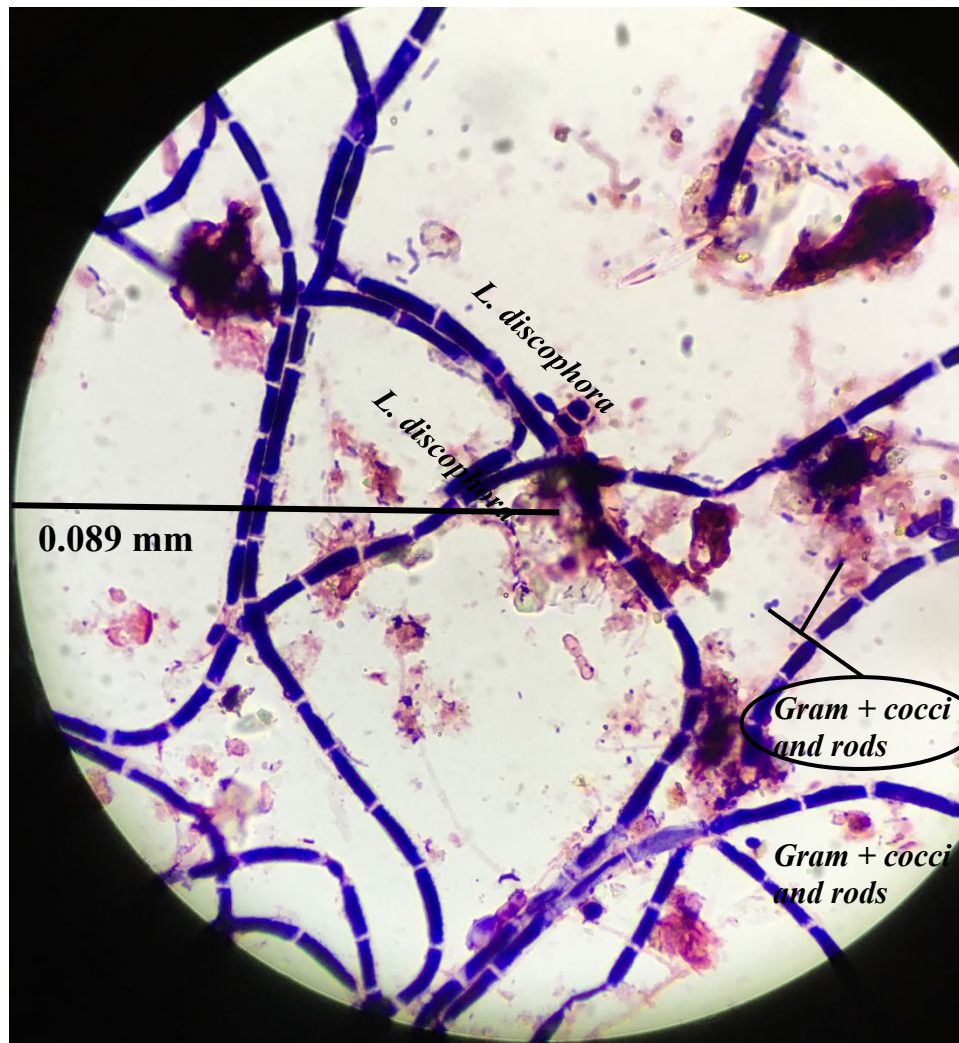


Figure 69 *L. discophora* and (gram +) located in the effluent of York Clay and Mining No. 4 coal mine (1000x).

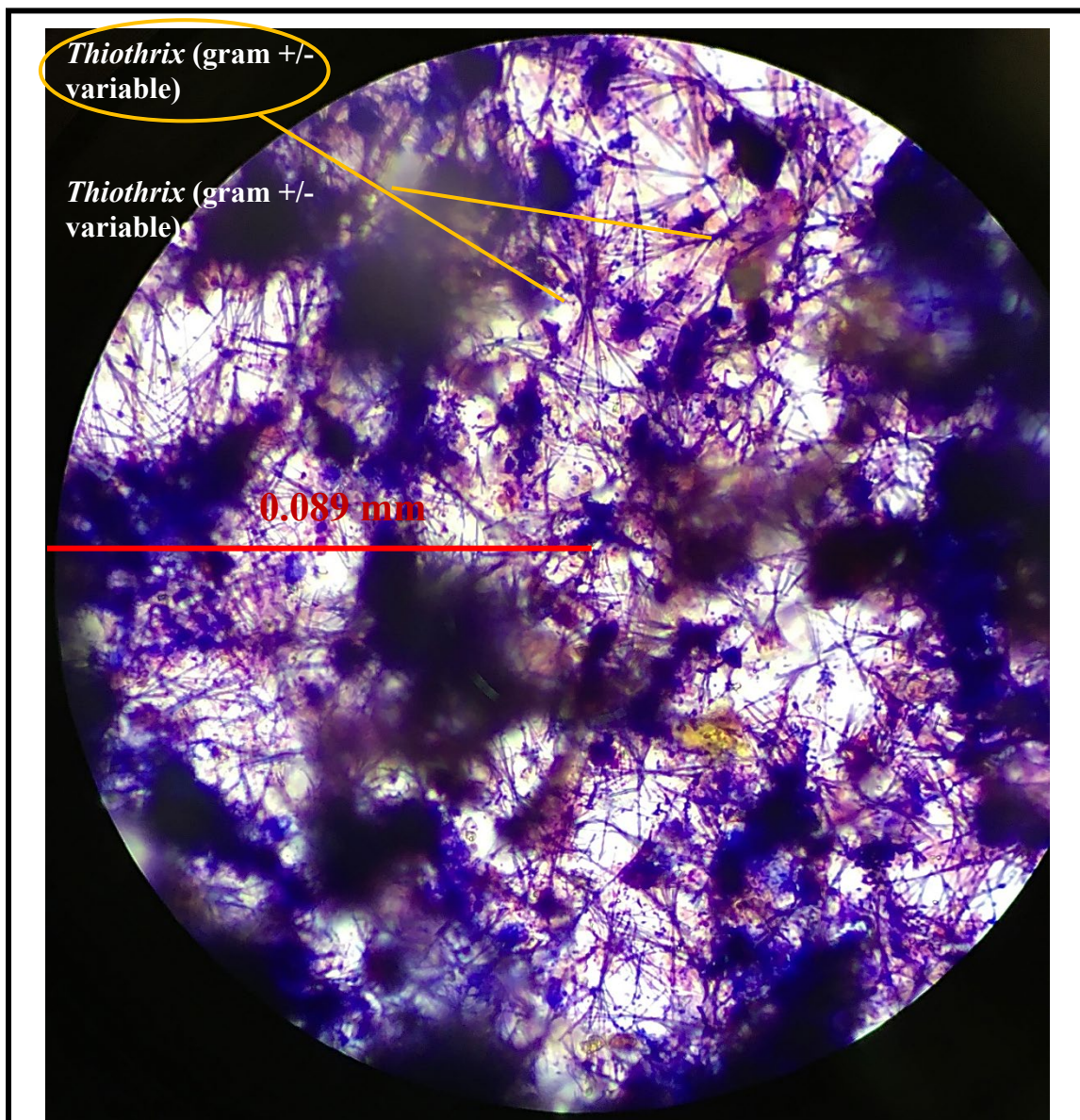


Figure 70 Thiothrix (gram -) and gram + flagellated rods located in the effluent of York Clay and Mining No. 4 coal mine (1000x).

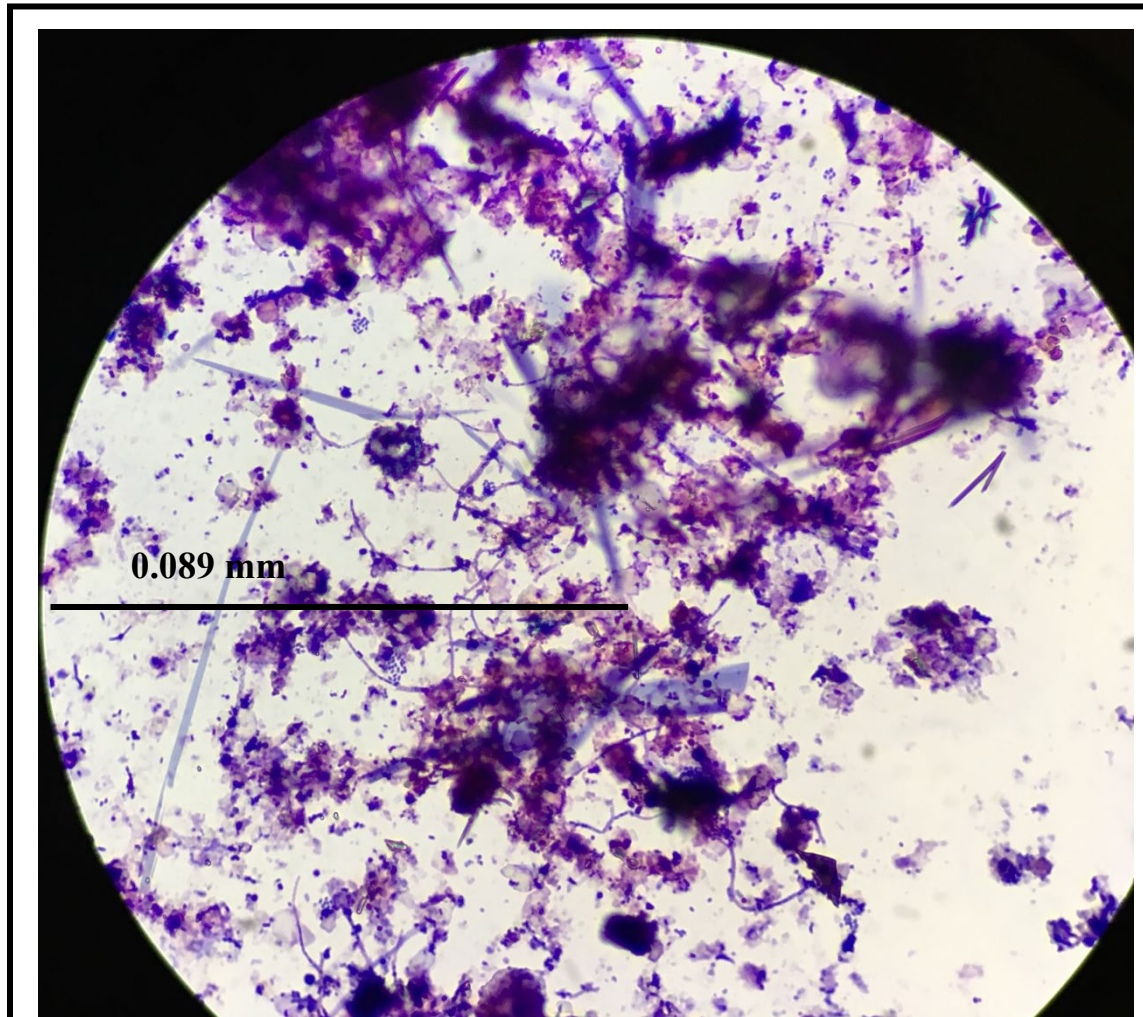


Figure 71 Thiobacillus (gram variable) and Gram + cocci single, clustered, and chain conformation located in the mine effluent of York Clay and Mining No. 4 (1000x).

Sines No. 2 Bacterial Slide Morphology

Table 25 Bacterial that settled on the glass slide contraptions located at 0, 8, 15, 23, and 30 meters in the Sines No 2 coal mine effluent from 10/23/2019-11/17/2019. Colonization rate averages (1/cm²d) are provided for the three major species evaluated.

Sines No. 2 Coal Mine Parameters	Distance from Mine Opening				
	0 meters	7.62 meters	15.24 meters	22.86 meters	30.48 meters
pH	2.30	2.30	2.30	2.30	2.35
DO (mg/L)	1.08	1.28	1.30	1.36	1.29
Conductivity (μS)	2184	1756	1751	1740	1703
Temperature (°C)	15.8	15.8	15.9	16.1	16.8
stalks of <i>G. ferruginea</i> (colonization rate: CR)	21	0	1	1	0
holdfasts of <i>L. discophora</i> (CR)	3	0.5	9	12	35
cf. <i>Thiothrix</i> (CR)	1	0	0	0	0
Gram + rods	+	+	+	+	+
Gram - rods	+	+	+	+	+
Gram + cocci	+	+	+	+	+
Gram - cocci	+	+	+	+	+

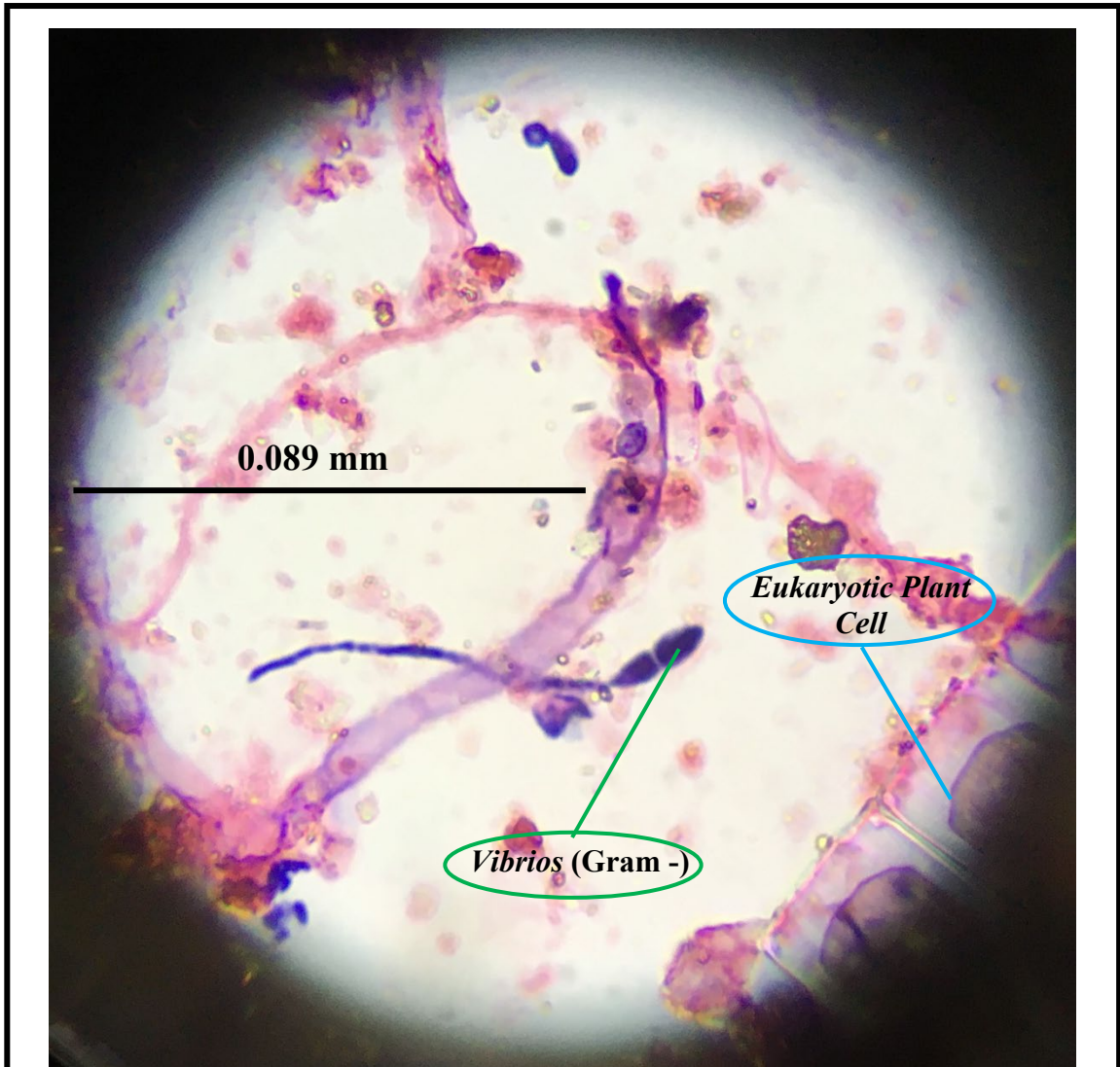
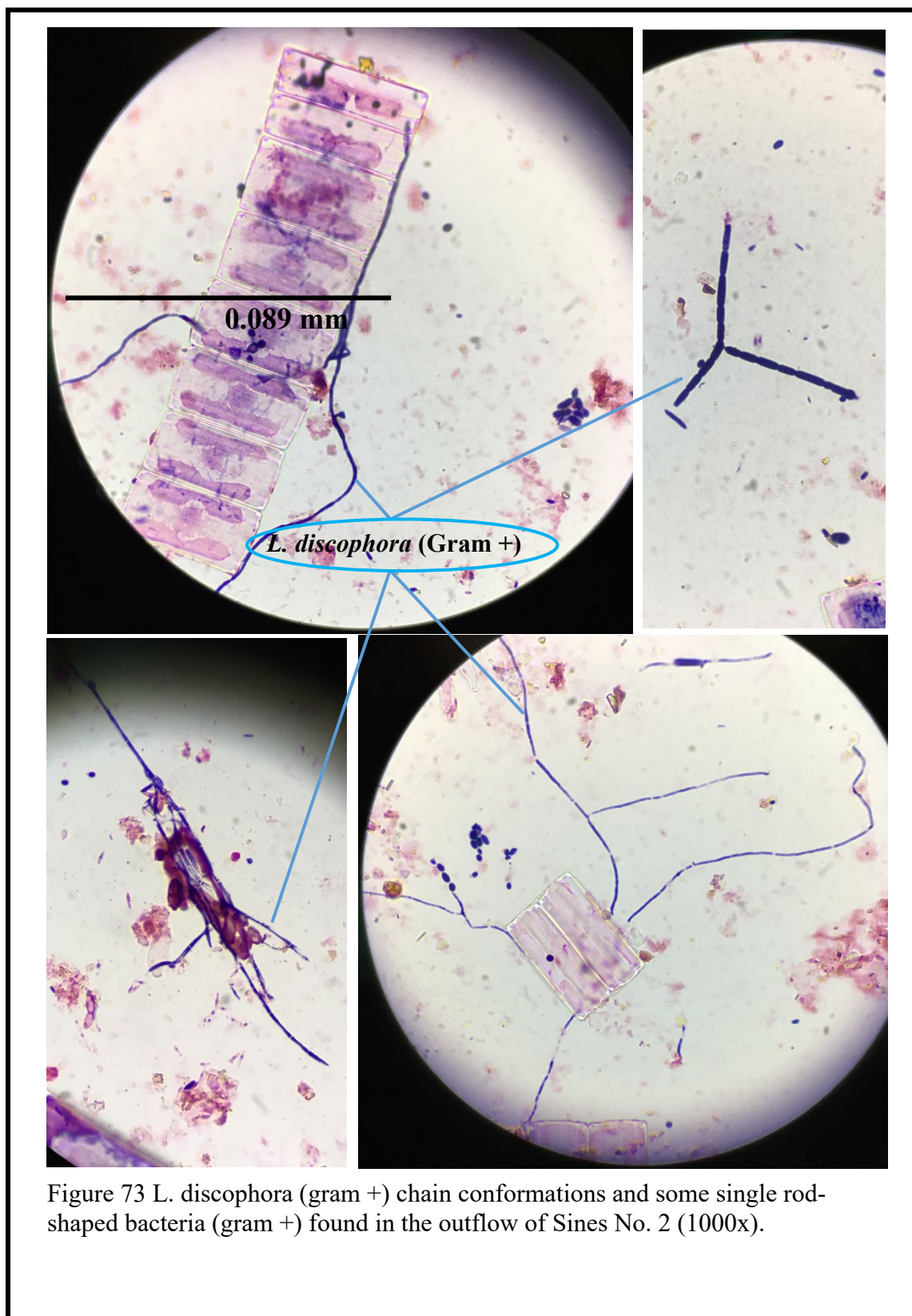
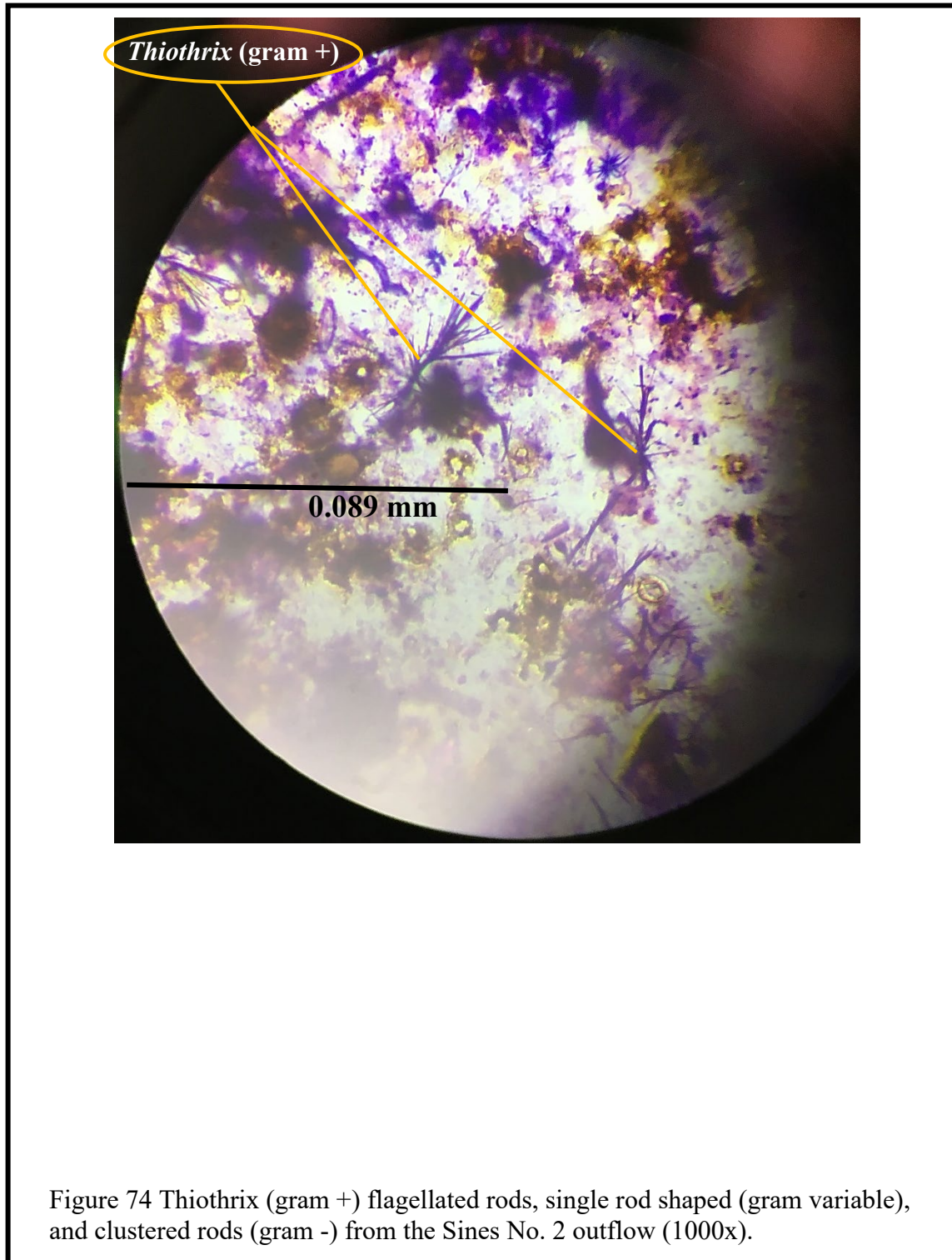


Figure 72 *Vibrios* (failed decolorization appearing gram +) found in the outflow of Sines No. 2 (1000x).





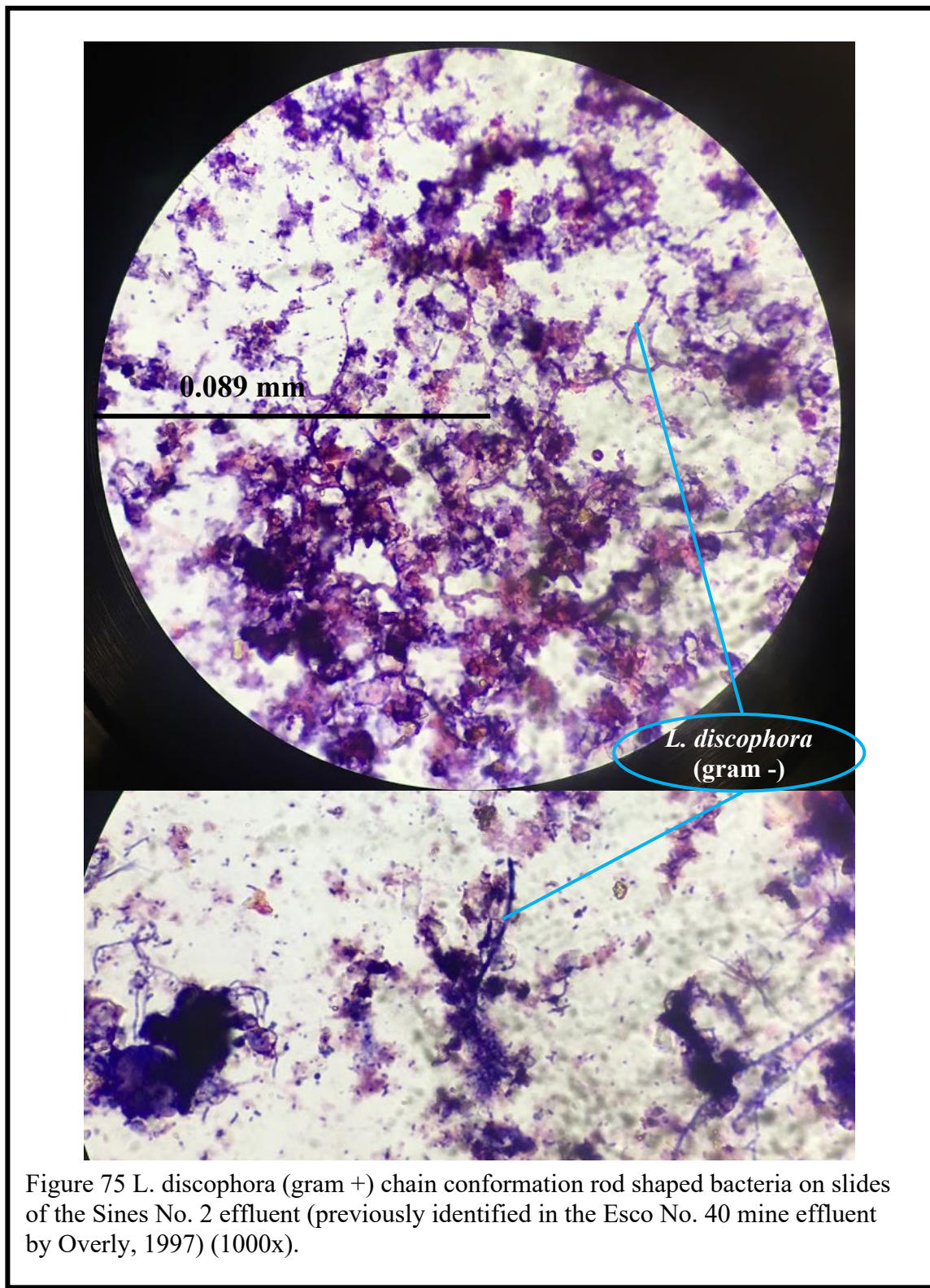


Figure 75 *L. discophora* (gram +) chain conformation rod shaped bacteria on slides of the Sines No. 2 effluent (previously identified in the Esco No. 40 mine effluent by Overly, 1997) (1000x).

CHAPTER 6: DISCUSSION

In an attempt to bring all of the significant results of this study together, a comprehensive thesis model is suggested based on the relationships outlined in Chapter 5. This model will be presented in three sections: 1) a section on spatial variability, 2) a compilation of statistically relevant findings to this model, and 3) interactions of flow, sediment composition, and microbial presence. It is important to stress that this was a study that encompassed the first 30 meters of four mine sites with chemically different waters, sediment composition, and flow regimes. In a survey such as this, any findings of our model must stand against vigorous scientific scrutiny and should yield repeatable findings in future research, completed in a similar vein, to remain relevant. This model is based entirely on the relationships identified from the data presented in Chapter 5.1.

In terms of spatial variability, the drainage exhibits colder temperatures and lower DO content in samples closer to the mine opening. Velocity trends varied widely amongst all four sites, with Esco having the largest flow velocity, Pine Run exhibiting and intermediate velocity, and York Clay and Sines mines containing low flow velocities. General concentration trends for concentrations of water ions Fe, Al, and Mn decreased as flow velocity was larger. Supersaturated conditions for the precipitation of mineral Basaluminite, $\text{Fe}(\text{OH})_3(\text{a})$, and Gibbsite varied from site to site with no particular trend based on flow regime. Microbial colonization of *G. ferruginea* dominated Pine Run mine, the intermediate-flow designated Fe-contaminated mine. *Thiothrix* seemingly colonized the substrates of Esco, the high-flow velocity SO_4 -contaminated mine. In the case of both

low-flow Mn and Al contaminated mines (York Clay and Sines), *L. discophora* generally was the most prevalent.

The significant relationships with relevance to our suggested model have been presented and discussed in long form in Chapter 5.2. To reiterate these findings, the following are relationships with the greatest significance to this model:

Positive Correlations (Spearman's R coefficient): conductivity vs ORP (0.9), pH vs DO (0.78), conductivity vs SO₄ (0.7), ORP vs SO₄ (0.61), velocity vs Fe in sed (0.71), velocity vs SO₄ in sed (0.7), DO vs Mn in sed (0.8), pH vs Mn in sed (0.59), Fe in sed vs SO₄ in sed (0.95), *Thiothrix* vs velocity (0.62), *G. ferruginea* day 19 vs velocity (0.69), *L. discophora* vs temperature (0.68), Fe in water vs *G. ferruginea* (0.75), *Thiothrix* vs Fe in water (0.66), *Thiothrix* vs SO₄ in sed (0.55), *G. ferruginea* vs Fe in sed (0.10), *G. ferruginea* vs SO₄ in sed (0.49), coarse sand (1-1.99 mm) vs Fe(OH)₃(a) (0.52), coarse sand (1-1.99 mm) vs pH (0.44), medium/coarse sand (0.5-0.99 mm) vs Mn in sed (0.61), and medium/coarse sand (0.5-0.99 mm) vs *L. discophora* (0.59).

Negative Correlations (Spearman's R coefficient): conductivity vs pH (-0.95), pH and SO₄ in water (-0.66), velocity and SO₄ in water (-0.57), velocity and Al in water (-0.79), Fe in sed vs Mn in sed (-0.67), SO₄ in sed vs Mn in sed (-0.62), *Thiothrix* vs Temp (-0.87), *L. discophora* vs velocity (-0.61), *L. discophora* vs Fe in water (-0.60), *L. discophora* vs SO₄ in sed (-0.48), medium/coarse sand (0.5-0.99 mm) vs Fe in sed (-0.61), coarse sand (1-1.99 mm) vs SO₄ in water (-0.54), velocity vs medium/coarse sand (0.5-0.99 mm) (-0.55), velocity vs medium sand (0.25-0.49 mm) (-0.54), velocity vs fine sand (0.105-0.24 mm) (-0.53), and *Thiothrix* vs medium sand (0.25-0.49 mm) (-0.59).

Finally, to fully describe interactions of sediment composition, flow regime, and microbial presence within this model, we can look toward significant correlations found between these three domains. Figure 76 illustrates the trends of fine, medium, and medium/coarse sand with relation to velocity and DO. From this we can see velocity negatively correlates with all of the finer grain size fractions presented and DO correlates negatively with the medium grain size fractions.

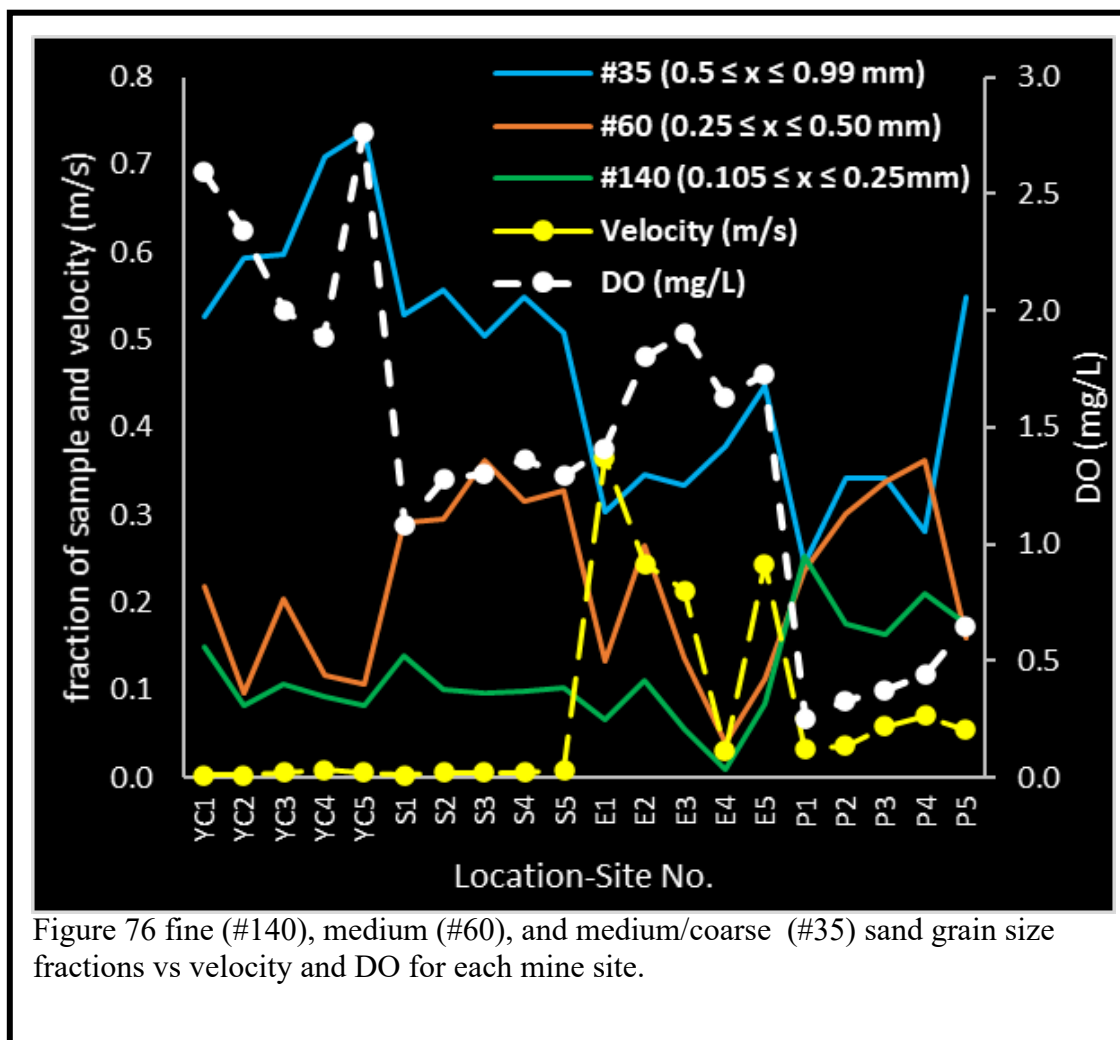


Figure 76 fine (#140), medium (#60), and medium/coarse (#35) sand grain size fractions vs velocity and DO for each mine site.

Figure 76 demonstrates how the finer sand grain size fraction (0.105-0.25 mm) correlates negatively with *Thiothrix* and positively with *G. ferruginea*. The coarse sand (1-1.99mm) grain size fraction correlated positively with *Thiothrix*. In the case of both *Thiothrix* and *G. ferruginea* these correlations may suggest that these bacteria are associated with grain sizes fractions for the respective inorganic sources they utilize in their energy generating pathways. When we plot the average grain sizes and velocities for each sub-site, the resulting Hjulström plot could potentially indicate the environments we might expect to find our target microbial taxa. These hypothesized zones are outlined in Figures 77 through 79.

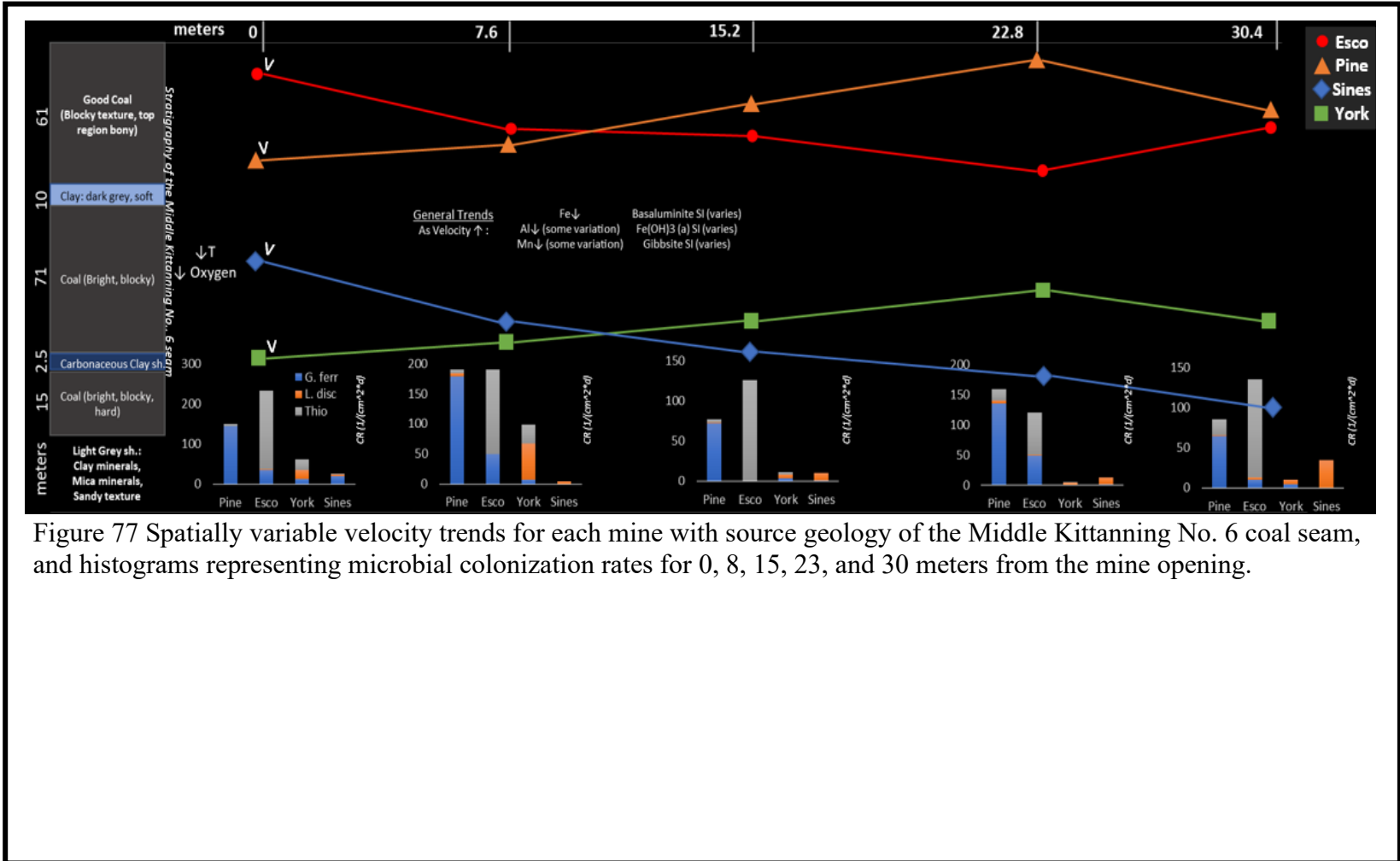


Figure 77 Spatially variable velocity trends for each mine with source geology of the Middle Kittanning No. 6 coal seam, and histograms representing microbial colonization rates for 0, 8, 15, 23, and 30 meters from the mine opening.

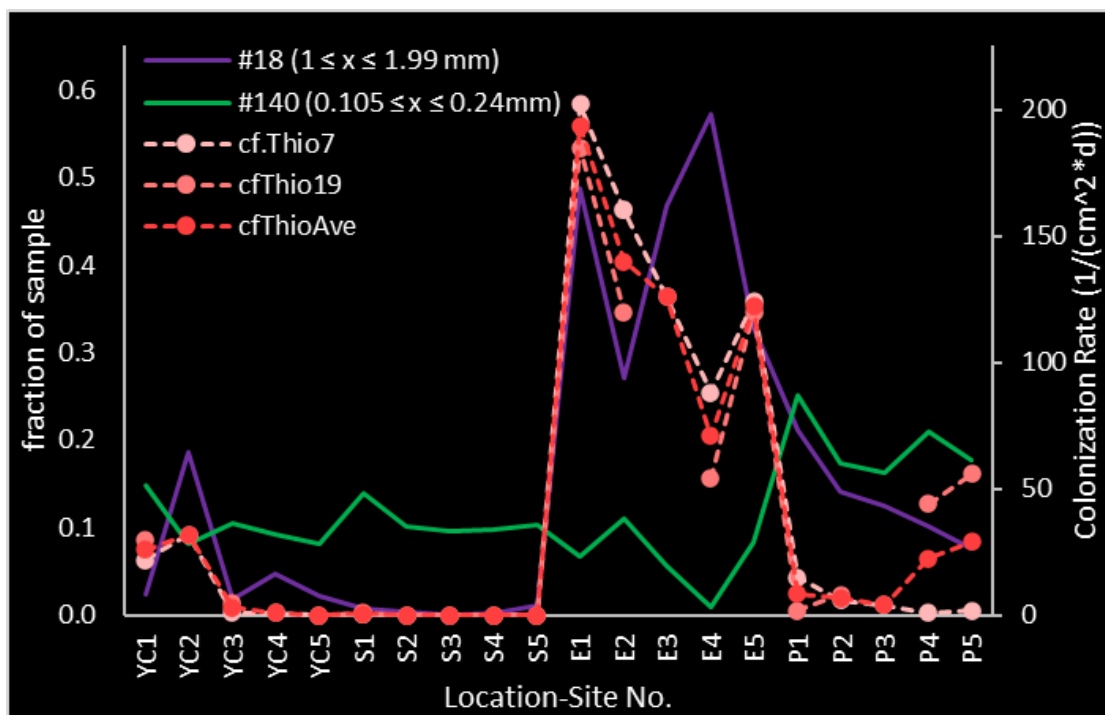
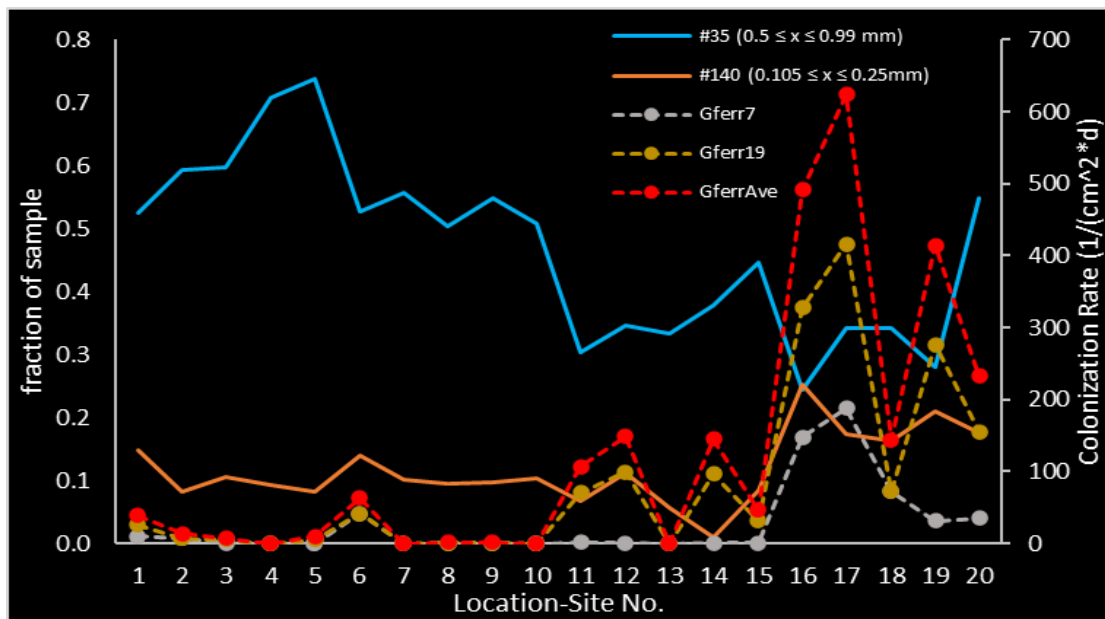


Figure 78 Coarse (1-1.99 mm), coarse/medium (0.5-0.99 mm), and fine (0.105-0.24 mm) sand grain size fractions with correlation to Thiothrix and *G. ferruginea* taxa.

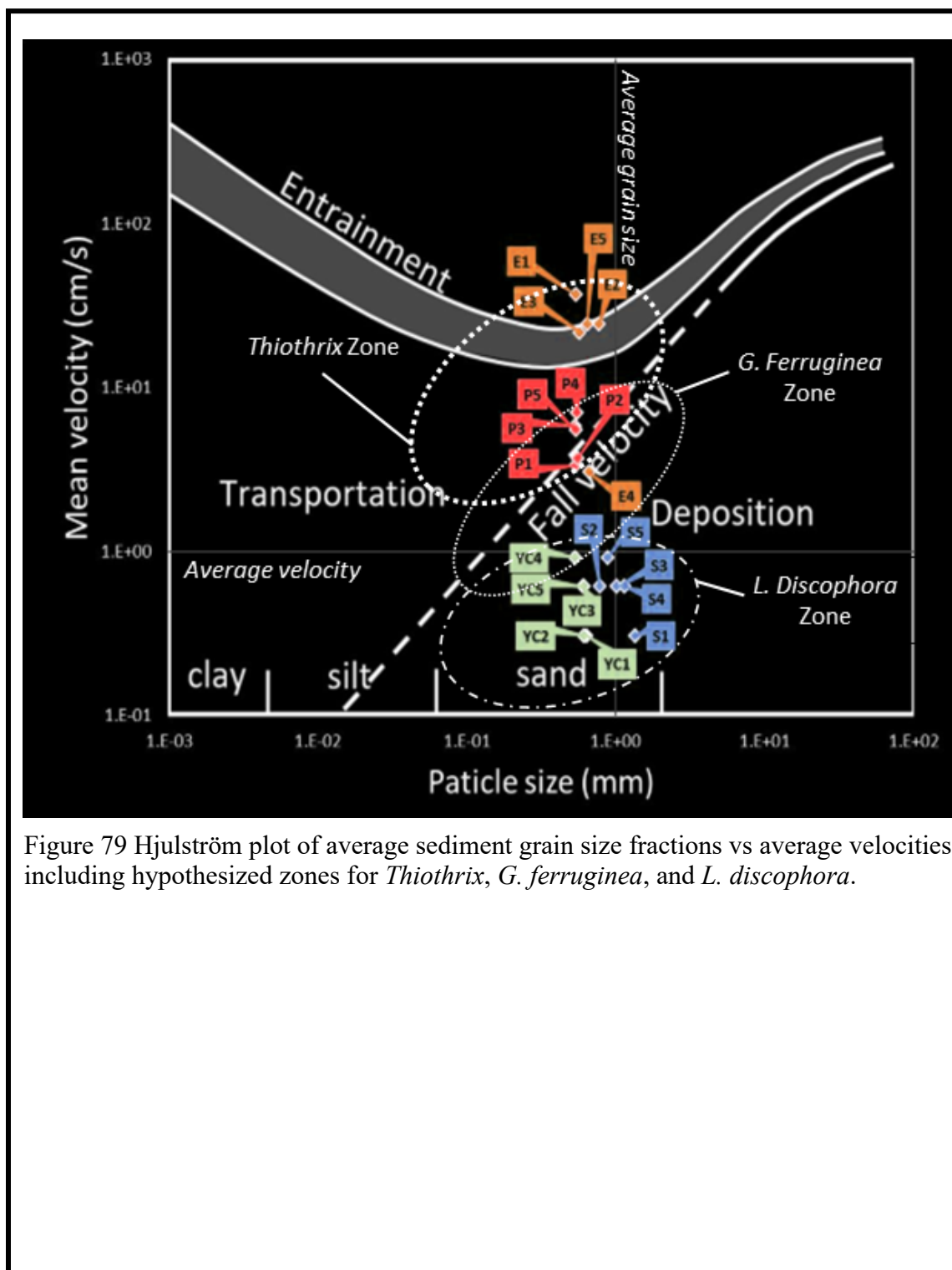


Figure 79 Hjulström plot of average sediment grain size fractions vs average velocities including hypothesized zones for *Thiothrix*, *G. ferruginea*, and *L. discophora*.

CHAPTER 7: CONCLUSIONS

This study focused on highlighting the connection between the physical, chemical, sedimentary, and microbial aspects of various acid mine drainage settings of contrasting chemistry and developing a comprehensive descriptive model of these interconnected properties. The selection of the study sites was based on the concentration of the main contaminant cations generated during acid mine drainage: Fe, Al, and Mn. Four contrasting systems were chosen to best represent AMD settings. Pine Run and Esco mines served as primary Fe, York Clay mine as a primary Mn, and Sines mine as a primarily Al contaminated study site. Testing for each abandoned mine included field and laboratory elements. Field and laboratory testing aimed to fully describe the multifaceted systems of chemically different environments and quantify these differences to determine statistically significant comparisons across each site. All collected data including drainage parameters, chemistry, sediments, and microbial data were then used to determine relationships that could describe a comprehensive model.

Overall, we set out to answer three questions:

- 1. How does physics of flow affect the distribution of metal contaminants in water and sediments as well as the presence of bacteria that utilize these contaminants?*

Physics of flow along the first 30 meters of a mine drainage can vary widely. If turbulence is high, then oxygen can immediately reoxygenate the waters and precipitation of contaminants from the mine can accompany a rise in pH. This distributes the precipitates either through entrainment, transportation, or deposition. Of the primary metal contaminants, total Fe in the sediments shared a strong positive correlation with

velocity. Total Fe content of the sediments increased with velocity which indicates that as velocity is increasing more Fe is precipitated out into various mineral forms likely due to the generally increasing velocity as the waters exit the mine and consequent higher oxygenation rate and iron oxidation. In terms of both Al and Mn in water, when velocity increases there is a weakly correlated decrease in concentration of each however there was too much variation to say for certain.

2. *In addition to Thiobacillus ferrooxidans, which bacteria genera and species favor Fe, Al, or Mn concentrated AMD and how does the water and sediment chemistry influence the proliferation of these bacteria?*

Our model indicates that in Fe-contaminated settings, *G. ferruginea* could likely be favored. *G. ferruginea* has formerly been shown to utilize inorganic forms of Fe and fixes them to obtain energy. The PCA analysis confirms this finding as *G. Ferruginea* colonization, Fe²⁺, and total Fe content in water are grouped closely together. *G. ferruginea* shares a positive relationship with SO₄ in the sediment suggesting when *G. ferruginea* fixes inorganic forms of Fe, precipitation of minerals containing both Fe or SO₄ take place.

In systems proportionately contaminated by Al and Mn, our model suggests *L. discophora* could be the most ideal taxa. *L. discophora* shared stronger relationships to Mg, Si, and Al in water. *L. discophora* is likely more dependent on the clay minerals found within the adjacent shales leaching into the water as well as more neutral pH drainage. York Clay contained the largest amount of *L. discophora* as this system had lower levels of Fe, Al, and Mn overall and neutral pH. Most of the trace ions that

correlate closely with *L. discophora* are likely sourced from clay and mica minerals as well as impurities in the surrounding rock of the No. 6 seam.

In any mine drainage where water velocity is high SO_4 is largely present in the sediments, our analysis suggest *Thiothrix* is favored. *Thiothrix* correlated negatively with SO_4 in the water and positively with SO_4 in the sediment as it reduces inorganic forms of S to obtain energy and contributes to the precipitation of SO_4 in the sediment. *Thiothrix* colonization rates had an inverse relationship with temperature and a strong positive relationship with velocity confirming that *Thiothrix* flourishes in slightly colder and higher velocity waters. Bacterial morphology of the *Thiothrix* species includes rosettes or flagellated appendages that could allow them to cling on to the substrates in higher velocity regions of the water (Lopez, 1999).

3. *Is there a common model that can explain the presence and utilization of metal contaminants by specific taxa of bacteria in unique flow regimes and system chemistries?*

Of the relevant findings that can contribute to a comprehensive model, a comparison of water ion data across each mine site indicates that elements such as Mg, Si, and Al in water are closely grouped in the PCA diagrams and likely sourced from the adjacent rocks containing clay and mica minerals. These minerals are often located at the base and within the uppermost clay strata of the No. 6 coal seam. These species behave similarly when suspended in the mine drainage exiting the mine. Positive relationships were determined between ORP vs Mg and SO_4 in water suggesting these species oxidize

or attach to oxidized products and precipitate out of the water as ORP rises and oxidation of the system increases.

Comparisons of data found within the sediments, suggests that Mn in sediment and DO share a positive relationship. This indicates that as oxygen content of the water increases, so does Mn content in the sediment from Mn co-precipitation with Fe minerals or formation of Mn oxides if the pH is high enough. The positive relationship of Fe and SO₄ in sediment indicates that these species likely co-precipitate alongside one another.

The PHREEQCI simulations indicates that the supersaturated minerals were alunite, amorphous aluminum hydroxide, barite, basaluminite, amorphous iron hydroxide, gibbsite, goethite, jarosite, jurbanite, and pyrolusite. Some of these minerals could be present in the sediments. Mineral formulas from these, which are listed in section 2.4.2, show the primary elements of these precipitated minerals are Al, Fe, S, O, K, Mn, Ba, and H indicating that *Thiothrix* species colonization may be correlated in Al precipitates, *Thiothrix* and *G. ferruginea* are both found in the presence of SO₄, and Fe precipitates, and *L. discophora* may favor environments high in carbon content and low in all primary contaminants similar to remediated acid mine drainage systems. *L. discophora*'s grouping in the principle component analysis may indicate some tolerance of weaker metal concentrations that precipitate out of the discharge.

Although this study attempted to encompass each of the primary acid mine drainage systems and described a number of significant relationships between the physics of flow, water chemistry, sedimentology, and microbiology, this study only describes the specific AMD systems of Sunday and Monday Creek during the late summer and early

fall. Results of this study could be useful in an approach to surveying all aspects of mine drainages accounting for systems with varying parameters, chemistries, sedimentology, and microbial composition. The results of this study indicate a strong relationship between distribution of total Fe in the sediment due to physics of flow, which of the microbial taxa thrive in each particular environment, and attempts to highlight relevant relationships that contribute to a comprehensive model explaining the interactions of these systems.

The findings of our model are pure speculation based on the data we collected and application of these findings in current remediation technologies will require more further research. Speculative insights are provided into the complex relationships between geochemical makeup and microbial presence as well as correlations between specific taxa and sediment grain size fractions. Remediation systems often change the physics of flow, and water or sediment chemistry, so the effects of these changes on the microbiology should be considered when implementing remediation plans. This research does provide some new avenues of interest at the intersection of microbiology, geochemistry, and flow regime as current remediation technologies could stand to benefit from new interdisciplinary perspectives. Ultimately, microbial population and their domains should be considered as a relevant aspect of diverse chemical and physical systems when designing remediation systems for acid mine drainage sites.

REFERENCES

- Baker, B. J., and Banfield, J. F., 2003. Microbial communities in acid mine drainage. *FEMS Microbiol. Ecol.* 44, p. 139–152.
- Barton, L. L., and Fauque, G. D., 2009. Biochemistry, physiology, and biotechnology of sulfate-reducing bacteria. *Adv. Appl. Microbiol.* 68, 41–98.
- Batley, G. & Gardner, D., 1977. Sampling and storage of natural waters for trace metal analysis. *Wat. Res.*, 11 p., 745-56.
- Bénézech, P., Palmer, D. A., & Wesolowski, D. J., 2008. Dissolution/precipitation kinetics of boehmite and gibbsite: Application of a pH-relaxation technique to study near-equilibrium rates. *Geochimica et Cosmochimica Acta*, 72(10), p. 2429-2453.
- (a) Bigham, J. M., Schwertmann, U., & Pfab, G., 1996. Influence of pH on mineral speciation in a bioreactor simulating acid mine drainage. *Applied geochemistry*, 11(6), p. 845-849.
- (b) Bigham, J. M., Schwertmann, U., Traina, S. J., Winland, R. L., & Wolf, M., 1996. Schwertmannite and the chemical modeling of iron in acid sulfate waters. *Geochimica et Cosmochimica Acta*, 60(12), p. 2111-2121.
- Boult, S., 1996. Fluvial metal transport near sources of acid mine-drainage: relationships of soluble, suspended, and deposited metal. *Mineralogical Magazine*, 60(399), p. 325-335.
- Carter, M. R., 1993. *Soil Sampling and Methods of Analysis*, 815 p.
- Clinton, T. J., 2005. Natural versus antropogenic remediation of acid mine drainage in

- southeast Ohio: an assessment of water and sediment chemistry [Master's thesis], Ohio University, 151 p.
- Cloutier, M. L., Carmichael, S. K., Carson, M. A., Madritch, M. D., & Bräuer, S. L., 2017. Carbon quantity and quality drives variation in cave microbial communities and regulates Mn (II) oxidation. *Biogeochemistry*, 134(1-2), p. 77-94.
- Crowell, D. L., 1995. *History of the coal-mining industry in Ohio*. Ohio. Division of Geological Survey, 204 p.
- Drever, J. I., 1988. *The geochemistry of natural waters (Vol. 437)*. Englewood Cliffs: prentice Hall, 437 p.
- Earthworks, 2013. *Earthworks Annual Report, Vol 1*:
<https://earthworks.org/cms/assets/uploads/archive/files/publications/EWAnnualReport2013.pdf> (accessed January 2019), 4 p.
- Esbensen, K. H., Guyot, D., Westad, F., & Houmoller, L. P., 2002. Multivariate data analysis: in practice: an introduction to multivariate data analysis and experimental design. *Multivariate Data Analysis*, 574 p.
- Gagliano, W. B., Brill, M. R., Bigham, J. M., Jones, F. S., & Traina, S. J., 2004. Chemistry and mineralogy of ochreous sediments in a constructed mine drainage wetland. *Geochimica et Cosmochimica Acta*, 68(9), p. 2119-2128.
- Grabowski, R. C., Droppo, I. G., & Wharton, G., 2011. Erodibility of cohesive sediment: The importance of sediment properties. *Earth-Science Reviews*, 105(3-4), p. 101-120.
- Hach Company (Eds.), 1997. *Hach Water Analysis Handbook (4th ed.)*: Loveland, Co.,

- Hach Company. 1268 p.
- Hall, J. F., 1951. The geology of southern Hocking County, Ohio, Doctoral dissertation, The Ohio State University, 241 p.
- Hallbeck, L., & Pedersen, K., 1995. Benefits associated with the stalk of *Gallionella ferruginea*, evaluated by comparison of a stalk-forming and a non-stalk-forming strain and biofilm studies in situ. *Microbial ecology*, 30(3), p. 257-268.
- Hallberg, K. B., & Johnson, D. B., 2005. Biological manganese removal from acid mine drainage in constructed wetlands and prototype bioreactors. *Science of the Total Environment*, 338(1-2), p. 115-124.
- Hammer, Ø., Harper, D.A.T., Ryan, P.D, 2001. PAST: Paleontological statistics software package for education and data analysis. *Palaeontologia Electronica* 4(1): 9pp.
http://palaeo-electronica.org/2001_1/past/issue1_01.htm
- Hanert, H. H., 1981. The genus *Gallionella*. In *The prokaryotes*. Springer, Berlin, Heidelberg, p. 509-515
- Herr, C., & Gray, N. F., 1997. Sampling riverine sediments impacted by acid mine drainage: problems and solutions. *Environmental Geology*, 29(1-2), p. 37-45.
- Hoffert, J. R., 1947. Acid mine drainage. *Industrial & Engineering Chemistry*, 39(5), p. 642-646.
- Jia, Y., Tan, Q., Sun, H., Zhang, Y., Gao, H., & Ruan, R., 2019. Sulfide mineral dissolution microbes: Community structure and function in industrial bioleaching heaps. *Green Energy & Environment*, 4(1), p. 29-37.
- Johnson C. A. and Thornton I., 1987. Hydrological and chemical factors controlling the

- concentrations of Fe, Cu, Zn, and As in a river system contaminated by acid mine drainage. *Water Research* 21, p. 359-365
- Koch, M., Rudolph, C., Moissl, C., & Huber, R., 2006. A cold-loving crenarchaeon is a substantial part of a novel microbial community in cold sulphidic marsh water. *FEMS microbiology ecology*, 57(1), p. 55-66.
- Larkin, J. M., & Shinabarger, D. L., 1983. Characterization of *Thiothrix nivea*. *International Journal of Systematic and Evolutionary Microbiology*, 33(4), p. 841-846.
- López, D. L., Overly, B., Robbins, E. I., & Carroll, K., 1999. The role of flow regime on the chemical evolution of acidic waters discharged from an abandoned underground coal mine. *Proc. 'Sudbury '99, Mining in the Environ*, p. 89-98.
- Lozano, A., Fernández-Martínez, A., Ayora, C., & Poulain, A., 2018. Local structure and ageing of basaluminite at different pH values and sulphate concentrations. *Chemical Geology*, 496, p. 25-33.
- Lükewille, A., & Van Breemen, N., 1992. Aluminium precipitates from groundwater of an aquifer affected by acid atmospheric deposition in the Senne, Northern Germany. *Water, Air, and Soil Pollution*, 63(3-4), p. 411-416.
- Martens, H., & Nij, T., 1992. *Multivariate calibration*. John Wiley & Sons.
- Mayanna, S., Peacock, C. L., Schäffner, F., Grawunder, A., Merten, D., Kothe, E., & Büchel, G., 2015. Biogenic precipitation of manganese oxides and enrichment of heavy metals at acidic soil pH. *Chemical Geology*, 402, p. 6-17.
- Moebis, N. N. and Clar M. L., 1990. Feasibility of water diversion and overburden

dewatering. U.S. Bureau of Mines Information Circular 9024, 68 p.

Nordstrom D. K., 1977. Hydrogeochemical and microbiological factors affecting the heavy metal chemistry of an acid mine drainage system. Ph.D. Dissertation, Stanford University, California, 210 p.

Morin, K. A., & Hutt, N. M., 1994. An empirical technique for predicting the chemistry of water seeping from mine-rock piles. Proceedings of the Third International Conference on the Abatement of Acidic Drainage, Pittsburgh, Pennsylvania, p. 24-29.

ODNR, 2019. Ohio Department of Natural Resources:

<https://ohiodnr.gov/wps/portal/gov/odnr-core/documents/water-documents>
(accessed January 2019)

Otwinowski, M., 1994. Quantitative analysis of chemical and biological kinetics for the acid mine drainage problem, Synergetic Technology, Alberta, Canada, 150 p.

Overly, B. M., 1997. Variations in chemical and bacterial species of acid mine drainage affecting the Snow Fork basin, Ohio: the Esco# 40 underground mine (Doctoral dissertation, MS thesis, Ohio University), 240 p.

Parratt, R. L., & Kullerud, G., 1979. Sulfide minerals in coal bed V, Minnehaha mine, Sullivan County, Indiana. *Mineralium Deposita*, 14(2), p. 195-206.

Pigati, E. M., 1997. The hydrology and geochemistry of an abandoned underground coal mine: The Majestic Mine, Athens County, Ohio (Doctoral dissertation, Ohio University).

Pigati, E., & Lopez, D. L., 1999. Effect of subsidence on recharge at abandoned coal

mines generating acidic drainage: the Majestic Mine, Athens County, Ohio. *Mine Water and the Environment*, 18(1), p. 45-66.

Potter-McIntyre, S. L., & McCollom, T. M., 2018. Jarosite and Alunite in Ancient Terrestrial Sedimentary Rocks: Reinterpreting Martian Depositional and Diagenetic Environmental Conditions. *Life*, 8(3), p. 32.

Robbins, E. I., Nord Jr, G. L., Chou, I. M., Savelle, C. E., Eddy, J. I., Livi, K. J. T., ... & Briggs, K. M., 1996. Microbial and mineralogical analysis of aluminum-rich precipitates that occlude porosity in a failed anoxic limestone drain, Monongalia County, West Virginia. *Pittsburgh Coal Conference*, Pittsburgh, PA (United States).

Ruiz-Agudo, C., Putnis, C. V., Ruiz-Agudo, E., & Putnis, A., 2015. The influence of pH on barite nucleation and growth. *Chemical Geology*, 391, p. 7-18.

Schrenk, M. O., Edwards, K. J., Goodman, R. M., Hamers, R. J., & Banfield, J. F., 1998. Distribution of *Thiobacillus ferrooxidans* and *Leptospirillum ferrooxidans*: implications for generation of acid mine drainage. *Science*, 279(5356), 1519-1522.

Singer, P. C., & Stumm, W., 1970. Acidic mine drainage: the rate-determining step. *Science*, 167(3921), p. 1121-1123.

Singh, B., Harris, P. J., & Wilson, M. J., 1997. Geochemistry of acid mine waters and the role of micro-organisms in such environments. *Advances in GeoEcology*, 30, p. 159-192.

Stout, W., 1927. *Geology of Vinton County*. Bulletin 31 Columbus, OH: Ohio

Department of Natural Resources, Division of Geological Survey, 402 p.

Sturgeon, M. T., 1958. The geology and mineral resources of Athens County, Ohio. Ohio. Division of Geological Survey, 629 p.

Verb, Robert G., Vis, Morgan L., February 1, 2005. Periphyton Assemblages as Bioindicators of Mine-Drainage in Unglaciaded Western Allegheny Plateau Lotic Systems: Water Air Soil Pollution, Volume 161, Issue 1, p. 227-265.

Wichlacz P. L., and Unz R. F., 1981. Acidophilic, heterotrophic bacteria of acid mine water. Appl Environ Microbiol 41, p. 1254-1261

Yue, T., Han, H., Sun, W., Hu, Y., Chen, P., & Liu, R., 2016. Low-pH mediated goethite precipitation and nickel loss in nickel hydrometallurgy. Hydrometallurgy, 165, p. 238-243.

APPENDIX

Specific Conductance

Measures of conductivity (Figure 80) are simply an indication of the effluent's ability to pass electrical flow, or in other terms a measure of the total concentration of ions located in the water. Apart from Pine Run mine, decreasing trends in conductivity can be noted in the spatial variability of Esco No. 40, York Clay, and Sines. These decreases indicate a large amount of precipitation after the mine entrance. The largest decrease in conductivity can be noted at Sines No. 2 mine. Similarly, to TDS, this decrease is the largest over 0 to 8 meters ranging from 2184 to 1756 μS respectively. York Clay has the second largest decrease in conductivity spanning 310.2 to 280.2 μS over 0 to 8 meters. Esco No. 40 has a slight decrease from 830 to 803 μS at 0 and 15 meters, respectively. The same exception to the TDS trend can be noted in the conductivity measure of Pine Run mine where it rises from 1214 to 1222 over the first 15 meters and then levels off indicating that precipitation has already taken place of many of the ions located inside the effluent contained behind the bat gate.

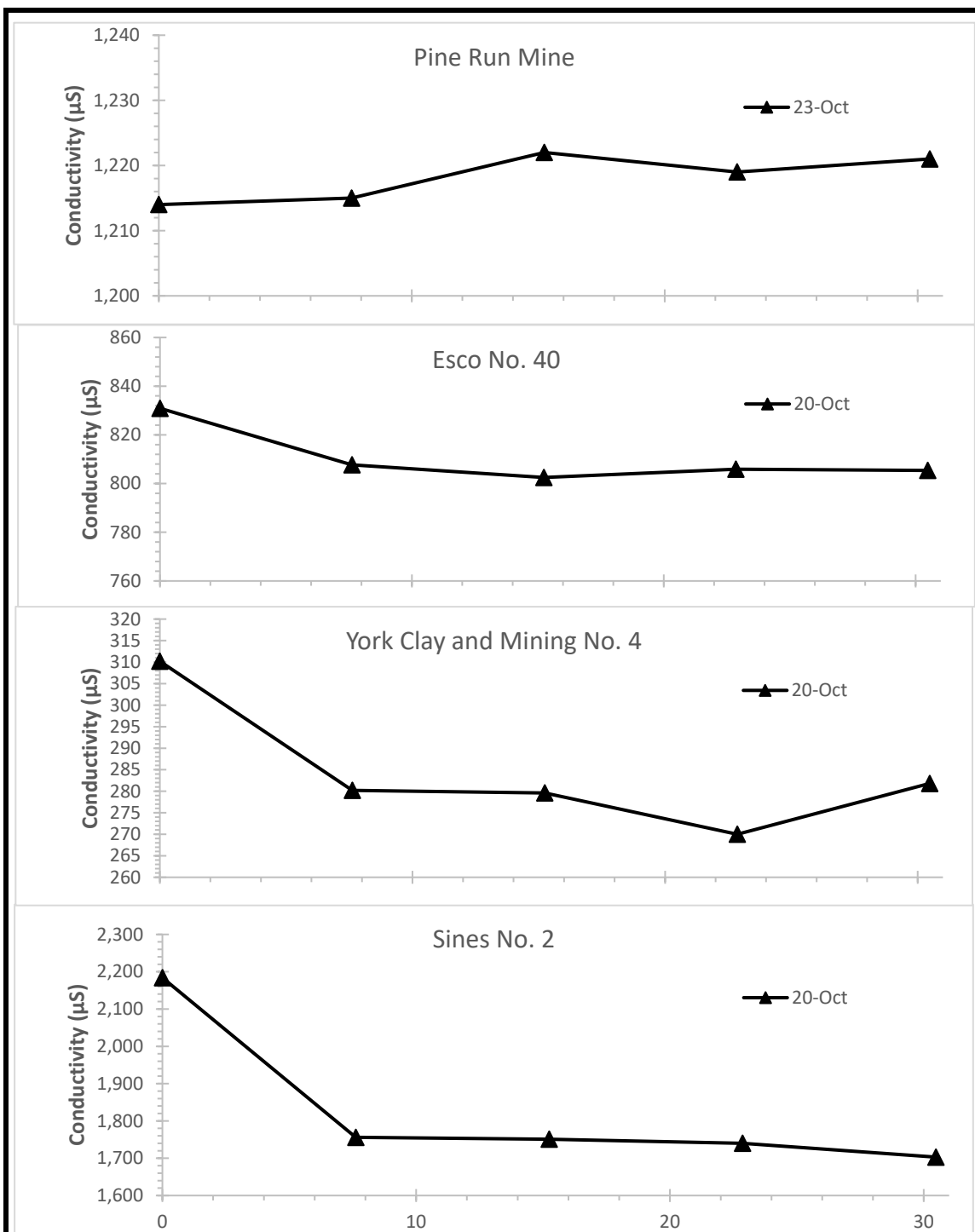


Figure 80 Variations in conductivity of water exiting each of the underground mine locations at 0, 8, 15, 23, and 30 meters from discharge point, 10/20/2019 to 10/23/2019

Total Dissolved Solids

Measures of total dissolved solids in the effluent from each of the four mine sites was plotted in Figure 81 and is shown for the dates 10/20/2019 or 10/23/2019. Total dissolved solids represent the measure of inorganics and organic matter that are dissolved in the mine effluent. Due to the reintroduction of oxygen into the system and the altering of ferrous and ferric iron concentrations, the general trend indicates a large measure of dissolved solids in the effluent located just outside the mine exit. These dissolved solids are then gradually precipitated out of solution and this is represented by a stark decrease in TDS concentrations.

The largest decrease in TDS can be noted from the 0 to 8-meter samples at Sines No. 2 mine which show a drop from 1609 to 1269 ppm. York Clay mine has TDS levels that drop from 210 to 180 ppm over the first 8 meters and then levels off. Esco No. 40 mine drops from 830.9 to 802.5 ppm over the first 15 meters and then levels off. The only notable variation to this decreasing trend is that of Pine Run mine which has the 0 meter sample located right outside of the bat gate where a large amount of precipitation has already taken place resulting in effluent that has low dissolved solids at the entrance and increases from 870 to ~876 ppm over the first 23 meters and then levels off.

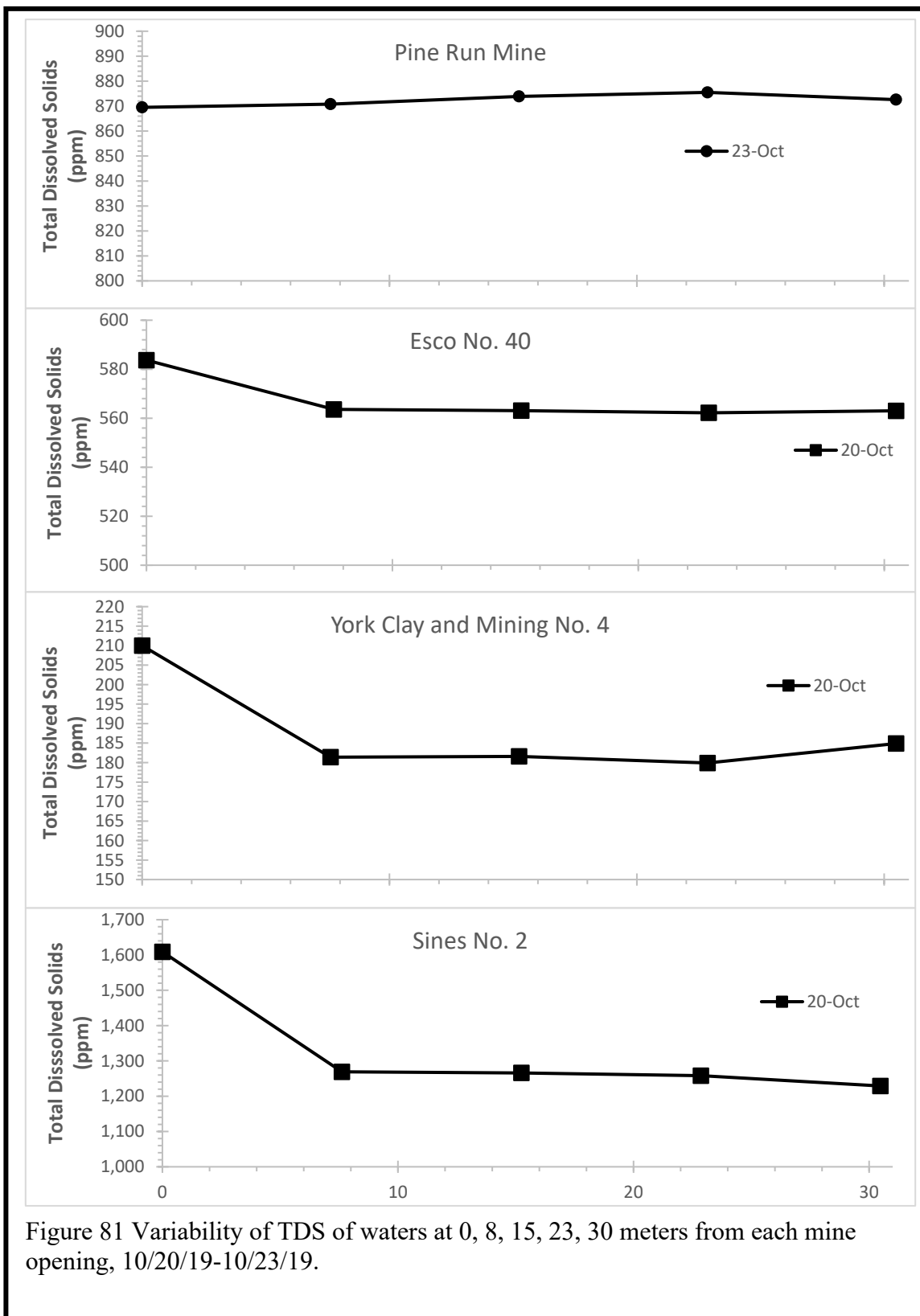


Figure 81 Variability of TDS of waters at 0, 8, 15, 23, 30 meters from each mine opening, 10/20/19-10/23/19.

Dissolved Oxygen

Spatial variations in dissolved oxygen at each of the mine sites (Pine Run, Esco, York Clay, and Sines) for 10/20/2019 or 10/23/2019 are displayed in Figure 82. The expected trend for dissolved oxygen was shown for Pine Run, Esco, and Sines.

Concentrations for dissolved oxygen were low as they exited the mine shaft which represented depleted levels representing a relatively high demand for oxygen in the system within the mine. This is attributed to 1) the utilization of oxygen in the oxidation reactions taking place within the mine as well as 2) the low exposure of gaseous molecules at the air water interface. When the water is expelled from the mine into the surrounding environment, more O₂ saturated air is introduced into the effluent. This oxygen is incorporated into the effluent at the air water interface through turbulence and dissolved oxygen concentrations rise. Dissolved oxygen in the system increases steadily until an equilibrium is reached and the water becomes saturated with oxygen with only two exceptions in this study.

These variations in response can be noted at Esco No. 40 and York Clay and Mining No. 4. Esco No. 40 mine exhibits a dip in DO at roughly 23 meters from the mine opening which is due to the sampling point exiting a culvert into a large pool. This varies from the traditional flow path as the water is depleted of oxygen once again within the culvert however from 23 to 30 meters the trend presents itself again as a rise in DO.

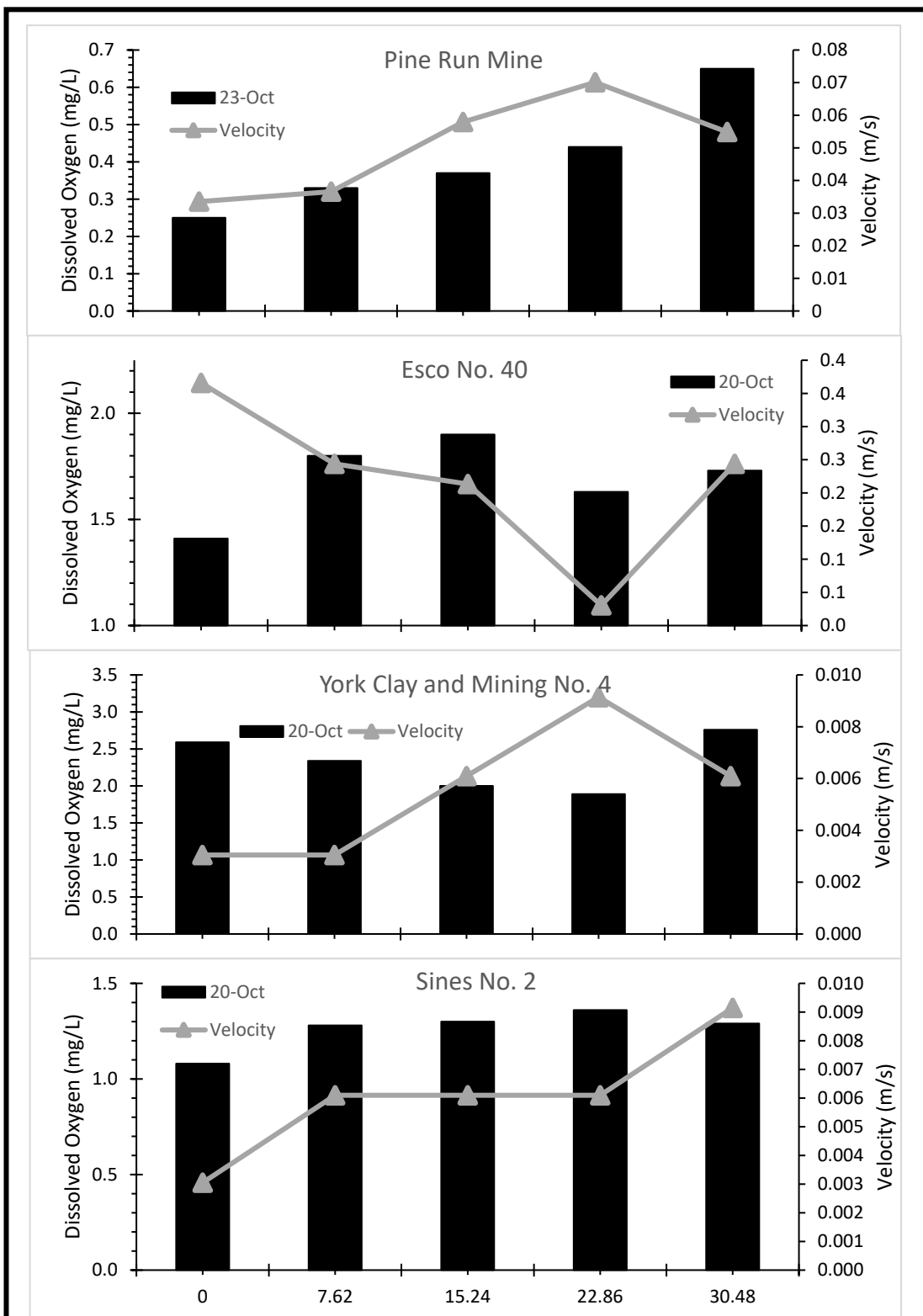


Figure 82 Variations in dissolved oxygen vs. velocity of waters exiting each abandoned underground coal mine location, 10/20/2019 to 10/23/2019.

In the effluent from York Clay, a steady drop in dissolved oxygen from 0 to 23 meters can be noted. This drop can be attributed to the effluent being exposed to the O₂ saturated air for a longer period, possibly already being saturated fully with O₂, and exhibits a minimal rise in velocity with little turbidity. For this reason, if oxygen demand in the water was exceeding the amount introduced from full saturation, we might see a decline in dissolved oxygen as represented in Figure 6-1. However, from 23 to 30 meters a rise in DO can be noted where a meander in the stream and a spike in drop in velocity are noted where oxygen is once again saturating the system.

Dissolved oxygen concentrations along the flow path were greatest at York Clay ranging from 1.89 mg/L to 2.59 mg/L (10/20/2019). Esco No. 40 mine had the second largest dissolved oxygen levels ranging from 1.41 mg/l to 1.90 mg/L (10/20/2019). In the case of York Clay we propose the low flow conditions allow the waters to reach saturation fairly quickly as the water remains stagnant in the system for a longer time. Conversely, at Esco mine our sampling point located at 0 meters was the first accessible location to sample from and the true mine cavity exit is located tens of meters further in the overhang giving the oxygen depleted waters a greater amount of time to interact with the O₂ content of the air.

The ranges we note with Pine Run and Sines No. 2 mine are 0.25 mg/L to 0.65 mg/L (10/23/2019) and 1.08 mg/L to 1.36 mg/L (10/20/2019) respectively. In the case of Pine Run, the mine entrance is tens of meters further within a cavity sealed by a bat gate with some time to interact with the oxygen in the air before reaching our sampling site at 0 meters. The explanation for why dissolved oxygen concentrations are lowest here can

be attributed to the large accumulation of precipitate at the base of the effluent forming a false bottom. While this system has a larger discharge than any other the velocity of the effluent is much slower and the sensor for the YSI probe can easily be inundated with precipitate and read DO concentration more representative of the top layer of the precipitate or sediment and the effluent flowing just above the bottom of the channel. To mitigate this, attempts were made to minimize the submersion of the sensor however all of these factors combined contributed to overall low DO readings. Sines No. 2 mine showed low DO concentrations as it was a low discharge and flow effluent collected from the 0-meter sampling point. Although these levels are low, by the 8 meter mark the effluent is shown to have reached a mostly saturated state.

Temperature

Spatial variability in temperature was recorded for each mine location and remained largely constant along the flow path (Figure 83). Values were averaged from the readings taken from the Myron meter and the YSI probe the encompass the deep and superficial temperatures of the systems. Variation along the flow path was only represented by small changes and largely remained constant. Temperatures were also compared to the ambient temperature of that day as well as the average annual temperature for the nearest city. Average annual temperature was plotted to serve as reference for what temperature the groundwater is with respect to the samples.

One of the notable variations of the overall trend were Pine Run mine, which was collected on the 23rd of October rather than the 20th, and had a lower ambient temperature than the rest of the study sites.

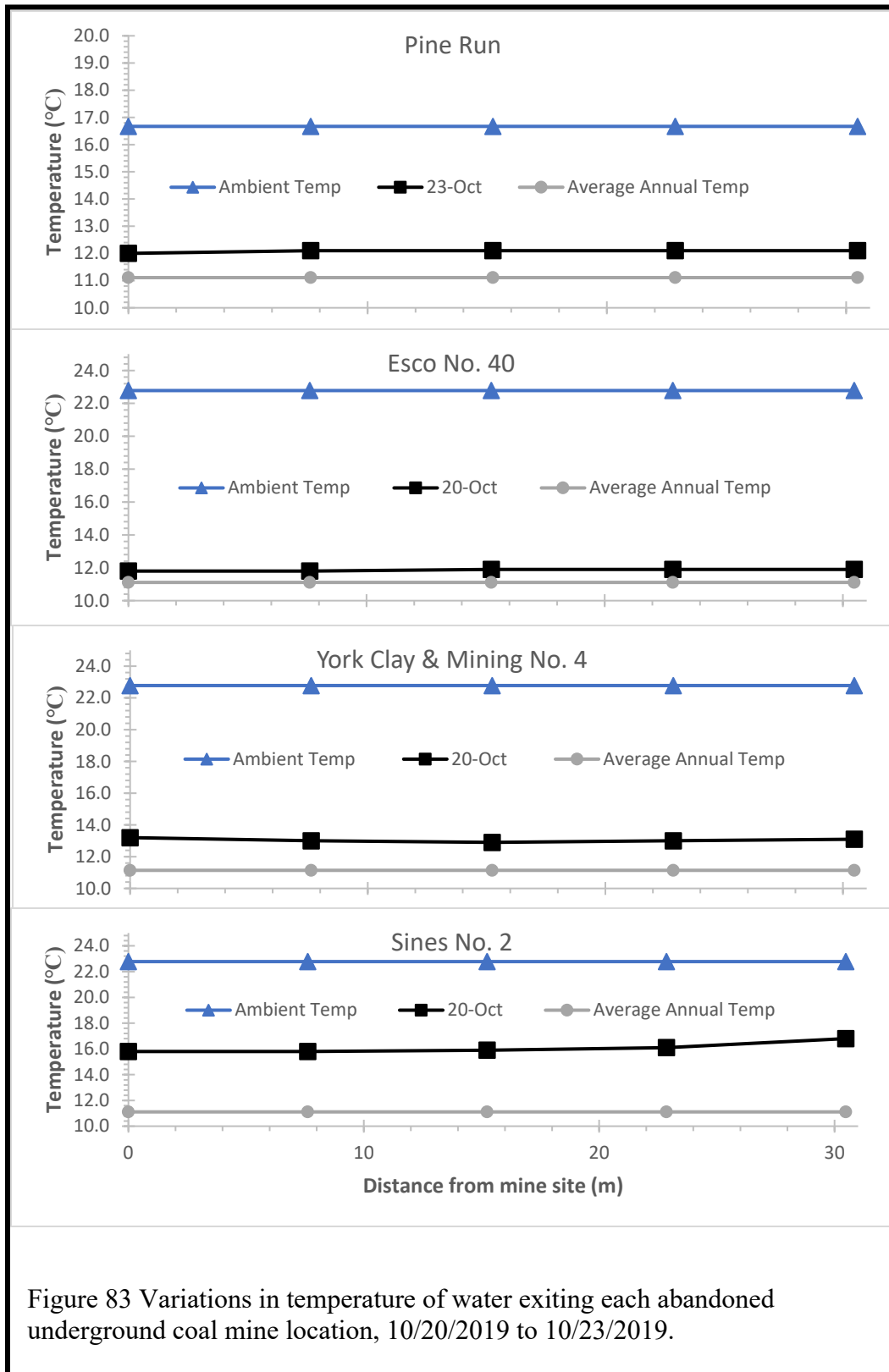


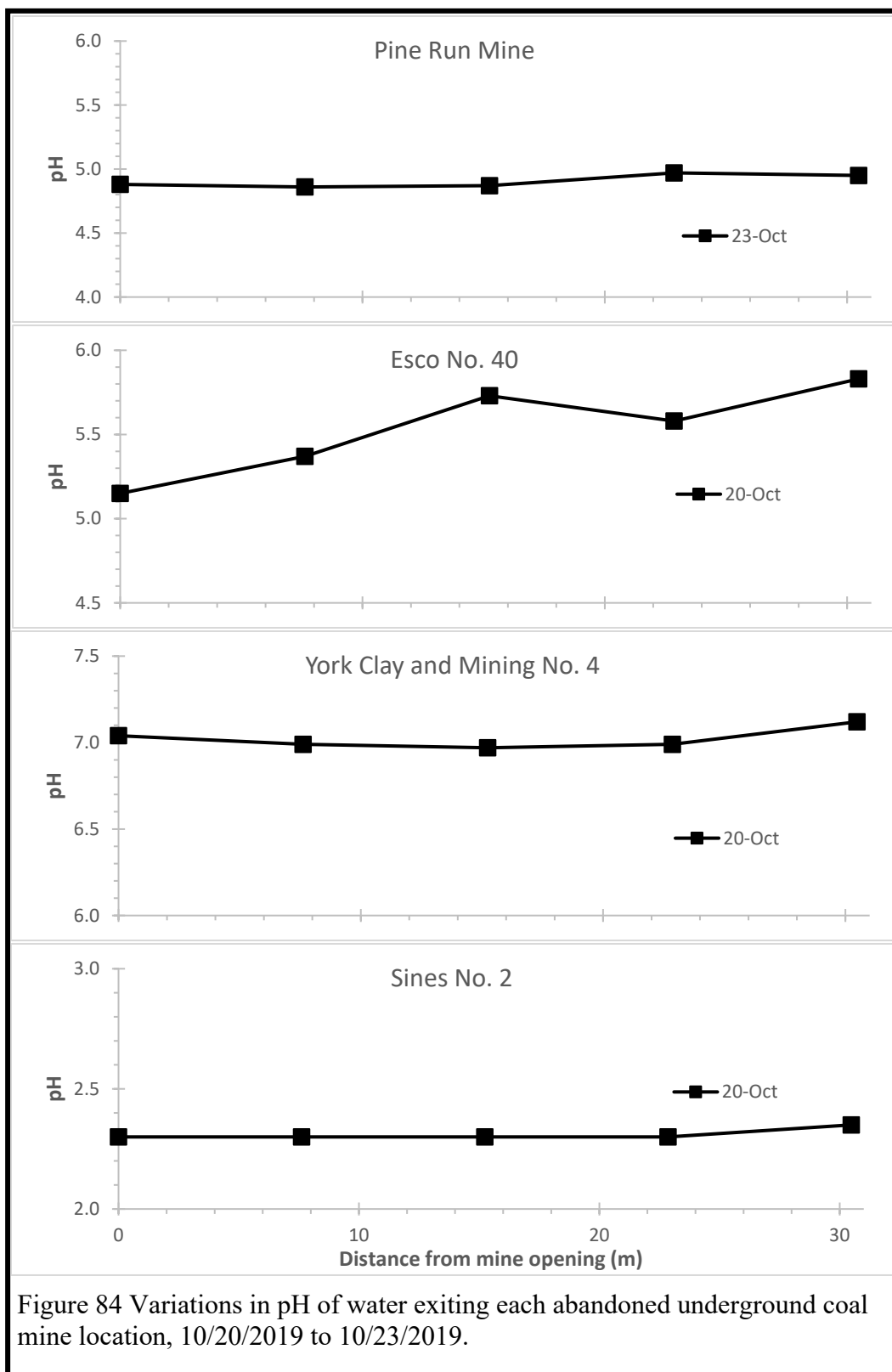
Figure 83 Variations in temperature of water exiting each abandoned underground coal mine location, 10/20/2019 to 10/23/2019.

Another point worth acknowledging is the elevated effluent temperatures recorded at Sines No. 2 mine ($\sim 16^{\circ}\text{C}$). These temperatures call into question whether the sampling point that appeared to be the immediate exit was the true exit or a reemergence located further along the flow path. Apart from Sines No. 2, all other sampled mine sites are within $1\text{-}2^{\circ}\text{C}$ of the average annual temperature for the region.

Of the mines sampled, Esco No. 40 had the lowest effluent temperatures ranging from $11.8\text{-}11.9^{\circ}\text{C}$, followed by Pine Run mine ranging from $12\text{-}12.1^{\circ}\text{C}$, and York Clay mine ranging $12.9\text{-}13.2^{\circ}\text{C}$. The highest temperatures of all any of the mines was Sines No. 2 mine which ranged from $15.8\text{-}16.8^{\circ}\text{C}$. This order may be indicative of how close in proximity the 0-meter collection point was to the true mine exit as the most equilibrated mine water would likely exhibit temperatures closest to $11.11\text{-}11.14^{\circ}\text{C}$.

pH

Variability in pH along the flow path was collected for each of the four mine locations. Figure 84 displays the recorded values for pH for the dates 10/20/2019 or 10/23/2019. When considering spatial variability in pH for each sample site, it is assumed that the discharge and temperature should remain constant from 0-30 meters and there generally should be a decrease in pH to accompany the elevation of dissolved oxygen. Based on the introduction of oxygen, the conversion from ferrous to ferric iron will influence the pH of the effluent. This trend is modest at best within Pine Run mine and York Clay mine, and in others such as Sines No. 2 mine and Esco No. 40 mine is absent.



The most apparent drop in pH can be noted in York Clay mine of Figure 6-3, where the pH steadily drops from 7.04 to 6.97 over 15 meters. Pine Run mine shows a slight drop from 4.88 to 4.86 over the first 8 meters of the flow path, then begins to rise and level off over the remaining measured path. Sines No. 2 mine exhibits a constant pH of 2.3 from 0 to 23 meters. Esco No. 40 mine shows a steady rise in pH from the exit to the entrance of the culvert at 15 meters and drops slightly once it exits the culvert at 23 meters. Overall, Esco mine shows a rising pH trend spanning 5.15 to 5.83.

Solute Chemistry

This section will present spatial trends of individual chemical species that were examined in this study with a basic description of those variations. A more in-depth discussion of these trends are presented in the discussion as this is only a cursory look at the solute data collected from the mine drainage samples. The chemical data presented in this section are in the form of dissolved species or particulates less than 0.45 μm . As the concentrations of each species were completed via IC or ICP-MS, standard deviations for each of the determined values can be found in the appendicized materials.

Fe concentrations for each location can be noted in Figure 85. Fe was the most elevated at Pine Run and Esco sharing an almost completely negative relationship with flow velocity. This negative trend is also somewhat reflected in York Clay and Sines, however, the velocity measurements were at the lowest possible reading for the velocity probe (0.003 m/s) so this should be considered when looking at the Fe vs velocity relationship. In terms of spatial variability at Pine Run we note an overall decrease of total Fe in the water along the 30-meter flow path. The lowest Fe concentration at Pine is

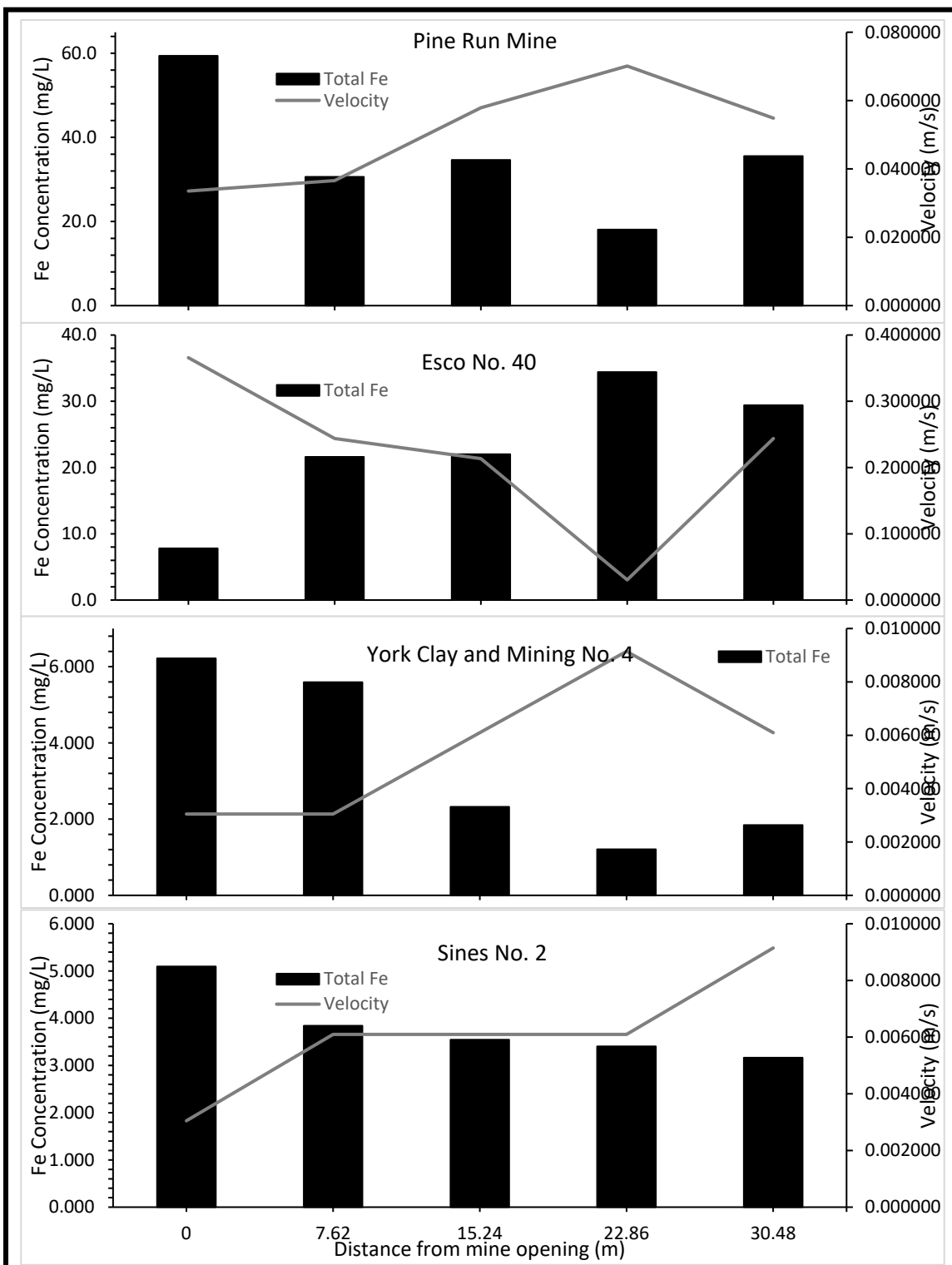


Figure 85 Variability in total iron concentrations of water exiting each abandoned underground mine effluent along flow path, 10/20/2019 or 10/23/2019

still rather elevated in comparison to any of the other mine sites. Esco follows Pine as the second most Fe contaminated mine site with a decreasing overall trend. Finally, York Clay and Sines had lower overall total Fe levels, and both had a general decreasing trend. This trend may be due to Fe oxidation and its translation into the sediment phase.

Concentrations of Al are shown in Figure 86. This Al content is likely sourced from the the shales inside the mine. Al concentration shows an almost opposite spatial trend to that of Fe, with Sines dominating as the most contaminated followed by that of York Clay. The mine drainage from Sines ranged in the upper forties in terms of concentration and an overall decrease in concentration with distance, suggesting precipitation of aluminum minerals.

York Clay fell largely in the 4 to 10 mg/L range with an overall increase in concentration along the flow path. Conversely, Esco and Pine experienced concentrations that never exceeded 2.5 mg/L. Notably there is a decrease in Al concentration at site 4 of Esco and the increase in velocity is likely due to the action of Thiobacillus precipitating hydroxylated-alumino sulfate minerals. Pine Run experienced an overall increase in concentration with the maximum concentration occurring at site 5 (30 meters). For the other sites, Esco stayed the same with the exception of a small spike in concentration at site 3 (15 meters).

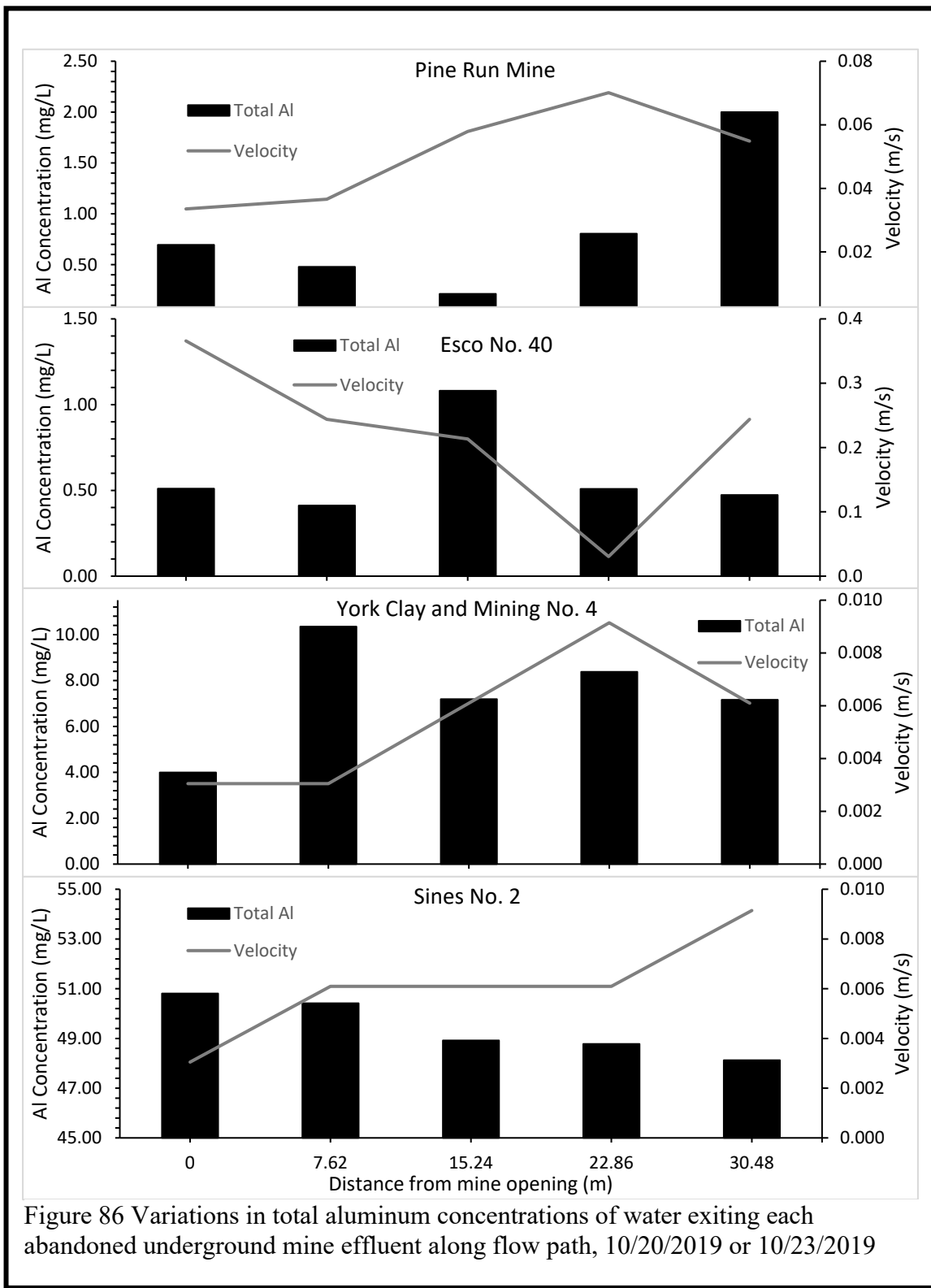
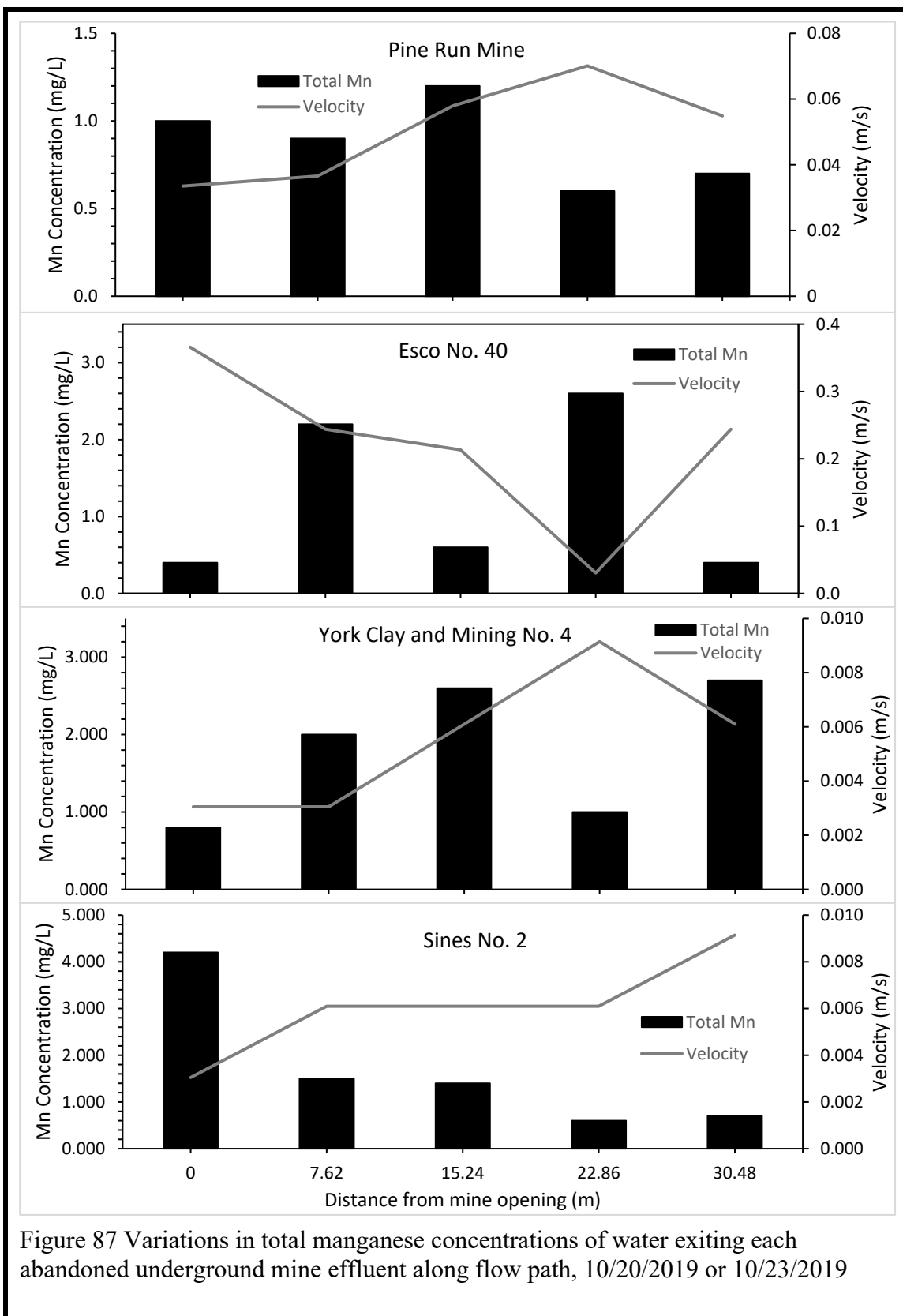
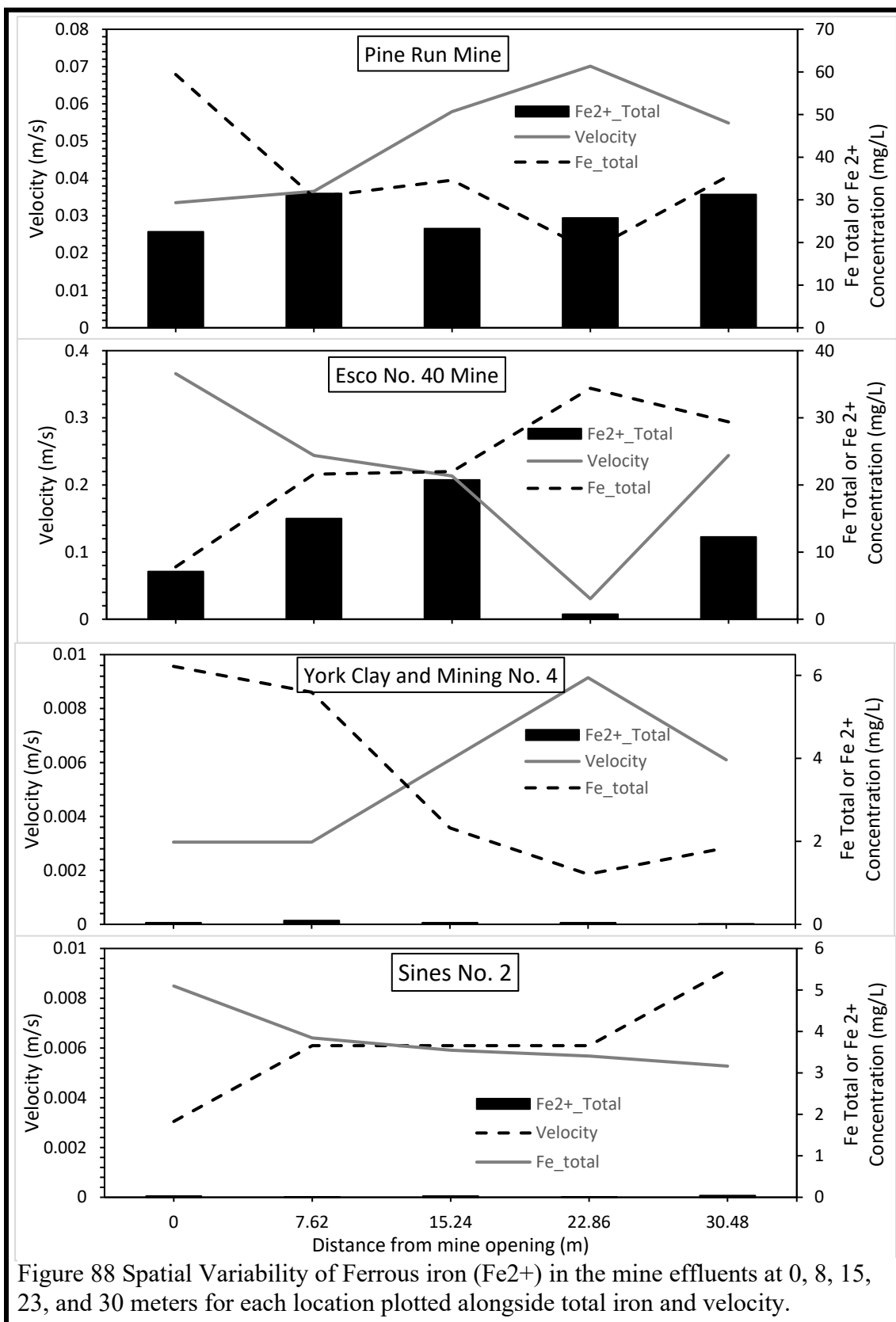


Figure 86 Variations in total aluminum concentrations of water exiting each abandoned underground mine effluent along flow path, 10/20/2019 or 10/23/2019

Concentrations of Mn are presented in Figure 87. Mn concentrations were relatively similar at each site but were proportionately larger with relation to the other primary contaminants at York Clay. Sines and Esco shared similar concentrations of Mn to that of York Clay. York Clay was the only location that exhibited an overall increase in concentration of Mn. Alternatively, Sines and Pine Run experienced overall decreases in Mn concentrations along the flow path and Esco had a variable trend that shows a wider range on concentrations and no change in Mn overall.

Ferrous Iron or Fe^{2+} concentrations are presented in Figure 88. Sines and York Clay samples never exceeded 0.04 and 0.09 mg/L respectively and showed little notable change along the flow path. Esco and Pine contain the most elevated levels of Fe^{2+} among the tested samples. Fe^{2+} ranges from below 1 mg/l to 21 mg/L at Esco with site 4 (where a post culvert pool is located) being the minimum value. These low values for Sines and York Clay suggest that the water had been already oxidized inside the mine with Fe^{2+} already oxidized to Fe^{3+} .



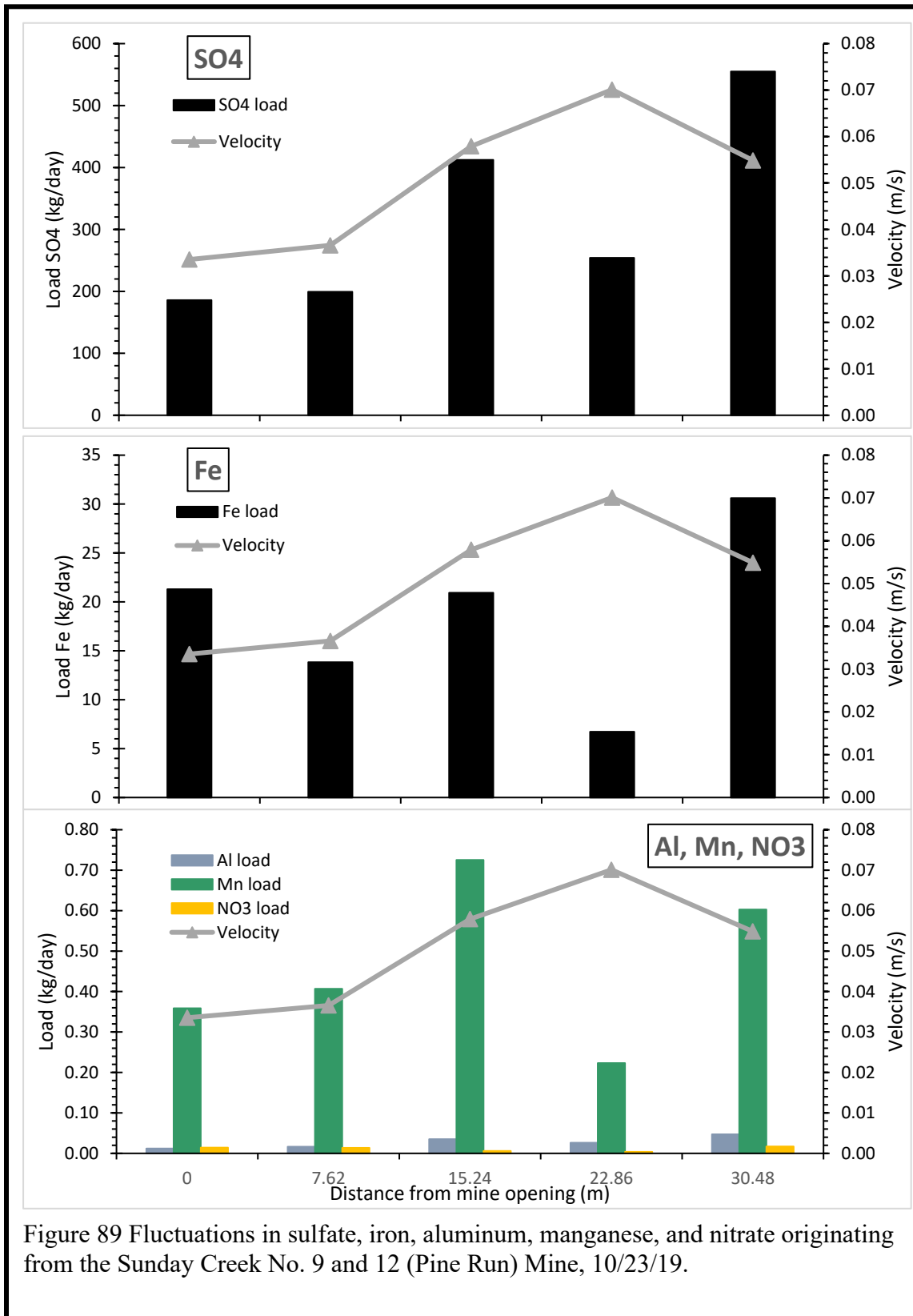


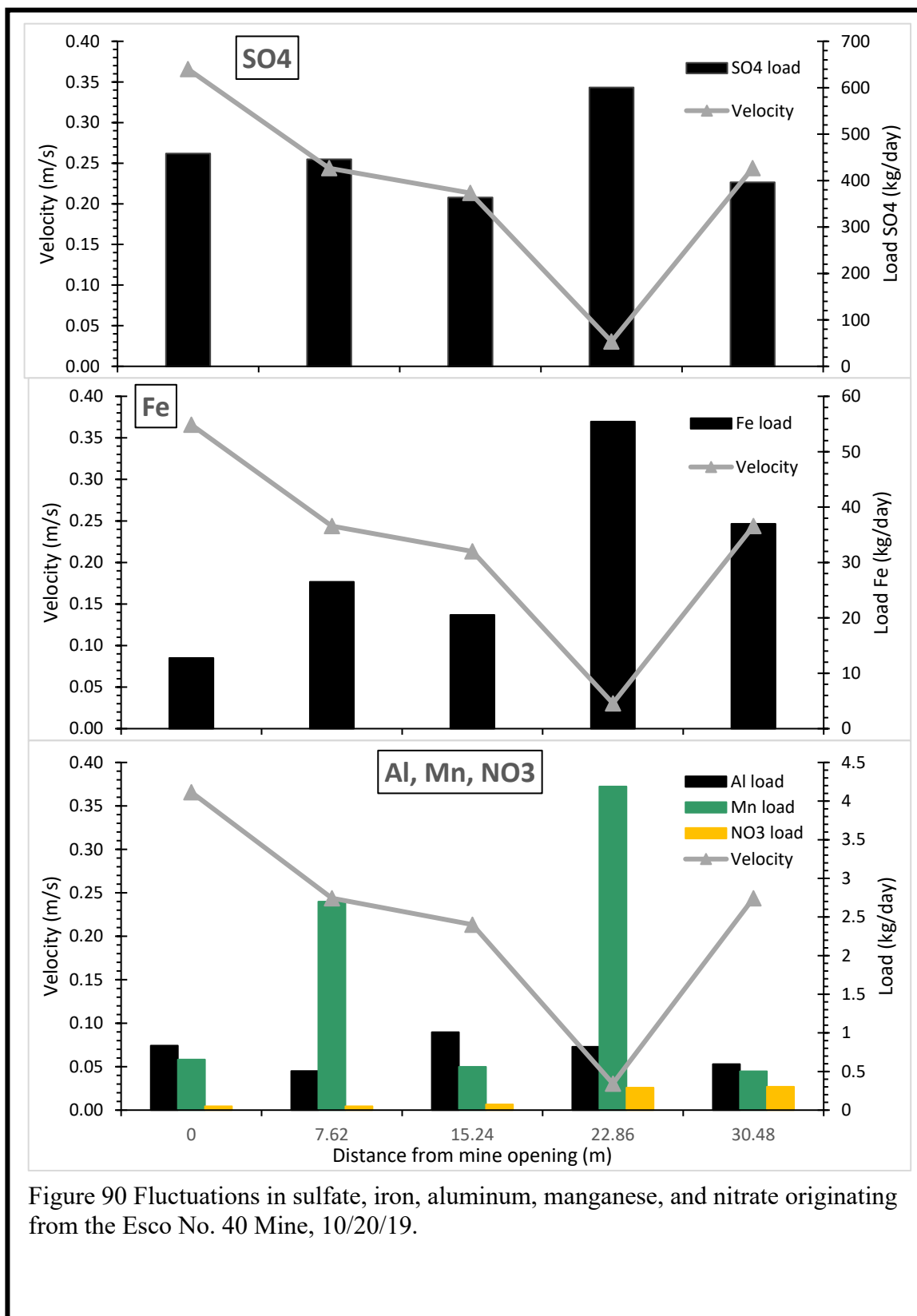
At Esco, Fe^{2+} loosely shares a positive correlation with velocity and a slightly negative relationship with total Fe. Pine run Fe^{2+} concentrations range from roughly 22.5 to 31 mg/L overall. Pine Run shows a variable trend with an overall slight rise, and also negatively correlates with total Fe.

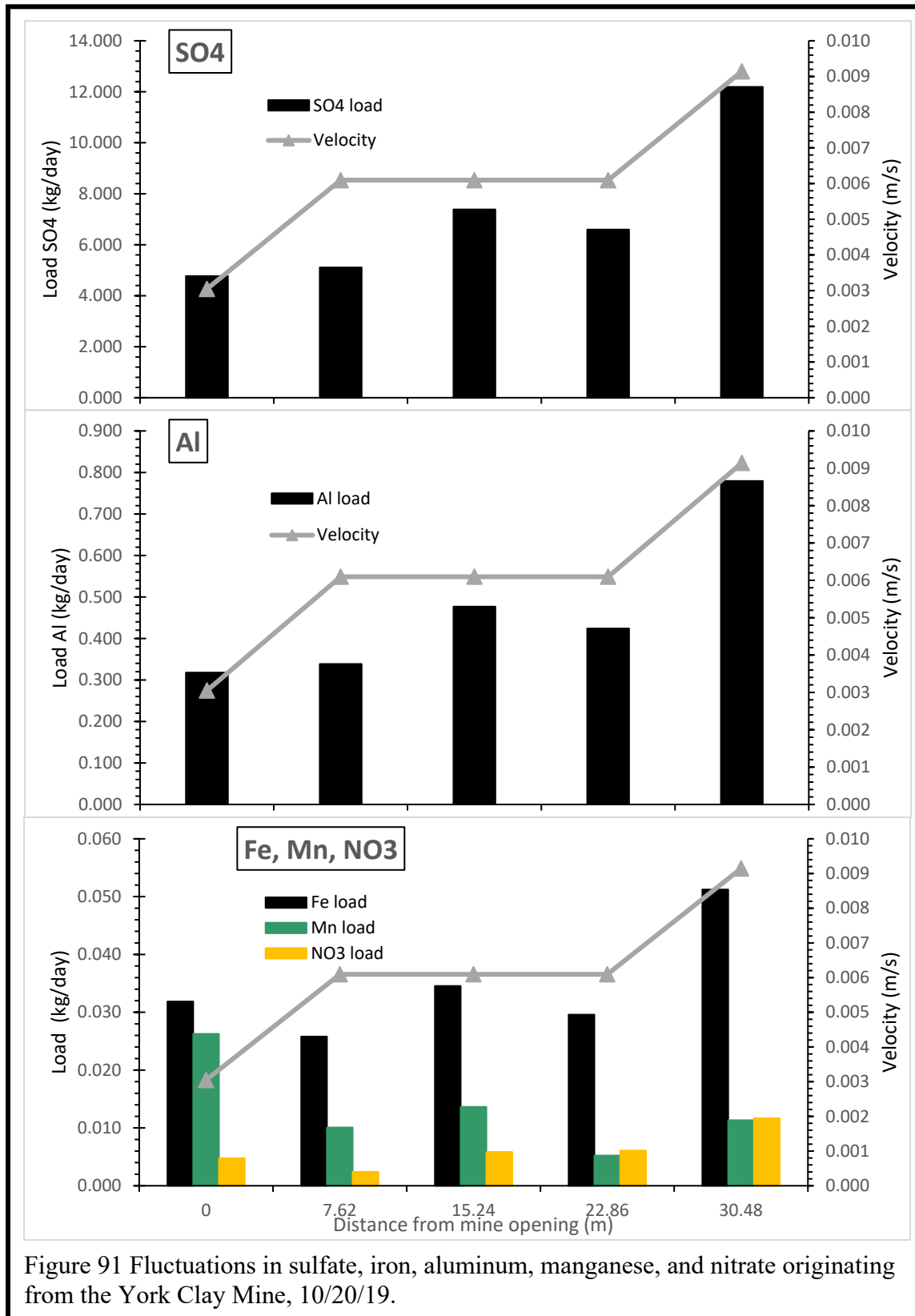
Solute Loadings in Water

Figures 89 through 92 depict the solute loadings for Pine Run, Esco, York Clay, and Sines, respectively. All four mine sites displayed fluctuations for SO_4 , Fe, Al, Mn, and NO_3 loadings in kg/day in decreasing order from the top of each Figure. Chemical loadings are the product of concentrations and discharge. Pine Run and Esco discharge calculations were largely influenced by the discharge component. York Clay and Sines had low discharge which lead to similar loading figures to that of the solute chemistry.

The largest contributions of SO_4 came from Esco and Pine Run which contributed as much as 600 and 550 kg/day of sulfate at their maximum. Maximum SO_4 contributions were around 12 and 8.5 kg/day for York Clay and Sines maximum values, respectively. The second most abundant loadings varied as Pine Run and Esco experienced higher loadings of total Fe and York Clay and Sines had elevated loadings for Al.







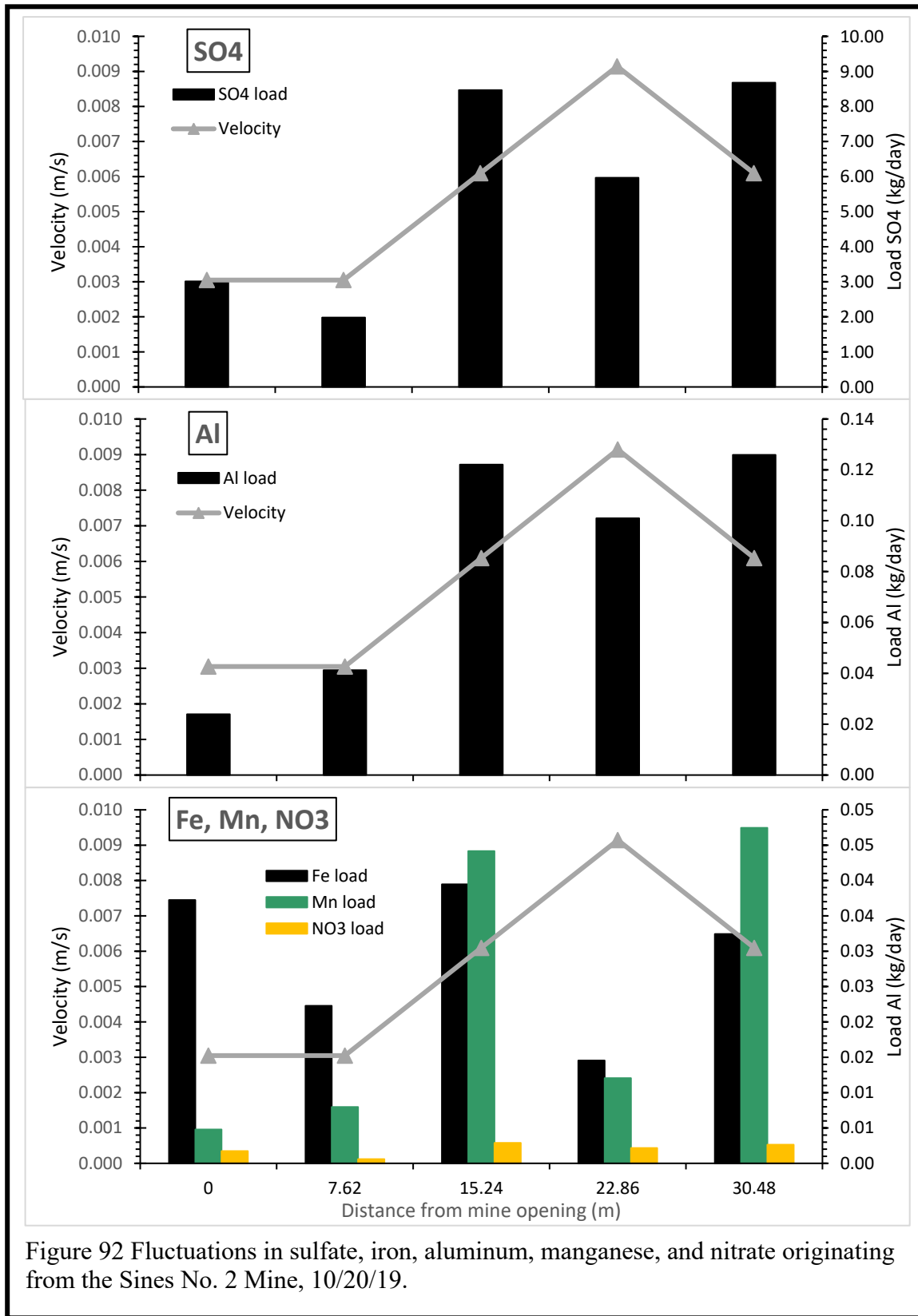


Figure 92 Fluctuations in sulfate, iron, aluminum, manganese, and nitrate originating from the Sines No. 2 Mine, 10/20/19.

Mn loadings at Esco also ranged from 0.5 to 4 kg/day depending on the spatial variability. Remaining contaminant loadings for Pine Run, Esco, York Clay, and Sines all had loadings less than 1 kg/day. From these loadings we can note that loadings for SO₄, Fe, and Al and Mn were the largest at Esco and Pine Run or sites with the largest discharge influenced loadings.

The variability along the flow path in the solute concentrations and loads reflect the fact that mineral precipitation and dissolution occurs along the flow path and it is different at the different studied sites, there is not a unique trend. Each site behaves in a different way probably because the dissolution and precipitation of minerals along the path is affected by different parameters such as fluid velocity, population of bacteria, temperature, and composition of the water discharged from the mine.

Figure 93 depicts graphs for each mine location of percent finer by mass and grain size for each sub-site along the flow path. Table 26 shows all significant relationships between the mean, minimum, and maximum grain sizes versus all recorded values in a Spearman's correlation matrix.

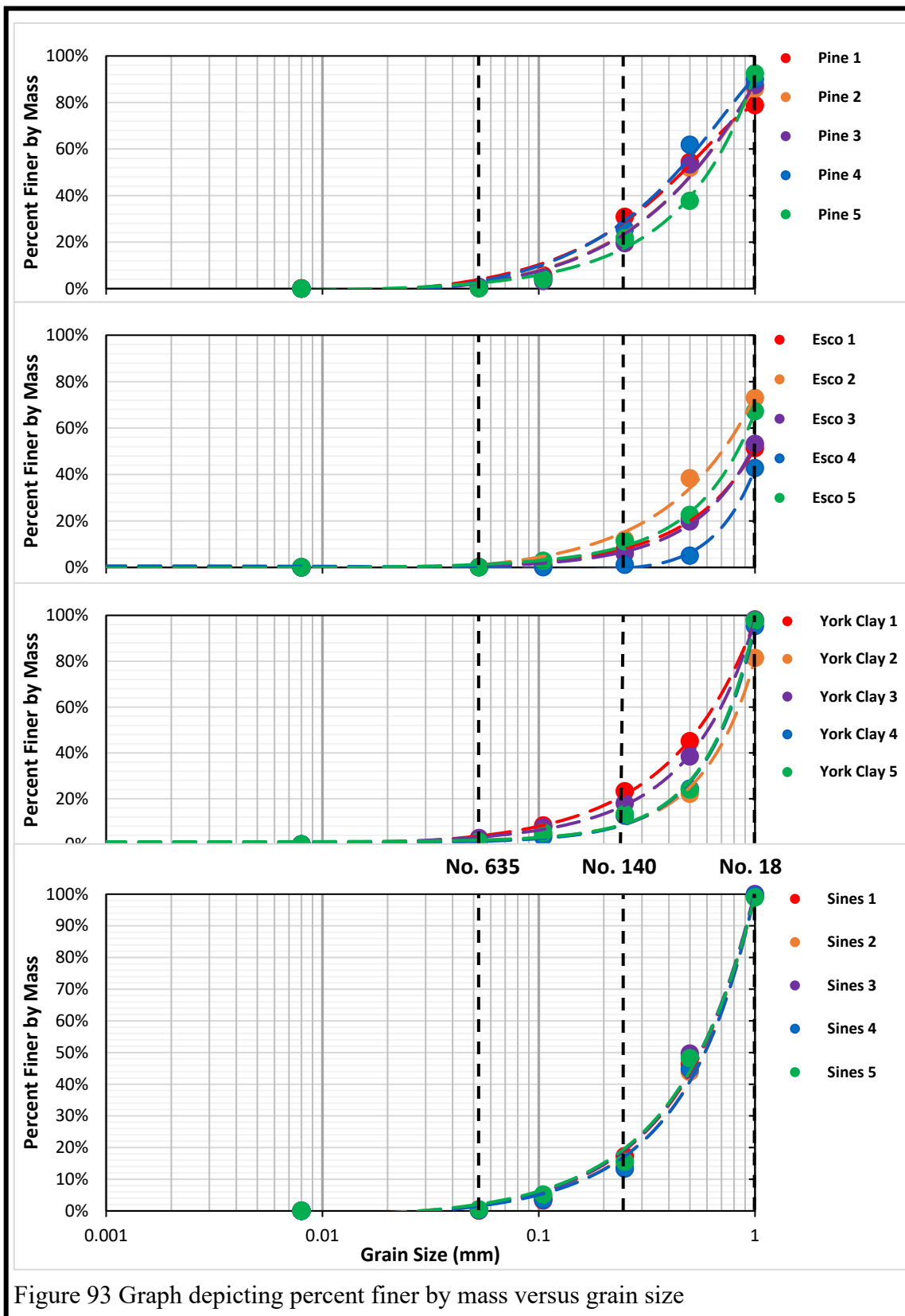


Figure 93 Graph depicting percent finer by mass versus grain size



OHIO
UNIVERSITY

Thesis and Dissertation Services